5 March 2010 $10

Science

AAAS

SIGMA Life Science Where bio begins™

SIGMA Life Science Where bio begins™

cell sciences®

ultra pure cytokines

Produced in barley, these proteins are animal, bacterial, and viral free, and are ultra pure, with extremely low endotoxin.

www.cellsciences.com

Cell Sciences offers innovative, unique growth factors and hard-to-produce recombinant proteins, bypassing the use of bacterial or animal cell systems. These ultra pure proteins contain no contamination from other growth factors and negligible amounts of endotoxin.

Background: barley endosperm

The host organism, barley, with its specialized endosperm storage tissue, provides many unique features including proficient protein machinery, with eukaryotic folding, and a distinct route for long-term protein protection and storage. A biochemically inert environment, void of endotoxins, low protease activity and secondary metabolite content, and a simple protein profile, aid in downstream processing. Barley has also a G.R.A.S. (generally recognized as safe) status from the FDA.

Cell Sciences ultra pure growth factors and cytokines are produced for use in basic and applied medical scientific research, cell culture media and diagnostics.

- serum free
- animal, bacterial & viral free
- extremely low endotoxin (<0.005 ng/ug)
- highly biologically active
- easier regulatory clearance
- perfect for cell culture, drug development, stem cell research, animal research
- for use in all *in vitro* cellular studies
- for use in all *in vivo* animal studies

Ultra pure cytokines & growth factors

FGF1, human
FGF2, human
FLT3 ligand, human
GCSF, human
IFNA2, human
IFN gamma, human
IGF1, human
IL1-alpha, human
IL2, human
IL3, human
IL4, human
IL5, human
IL6, human
IL7, human
IL9, human
IL16, human
IL22, human
KGF, human
M-CSF, human
NRG1/HRG beta 2, human
SCF, mouse
SF20/IL25, human
TNF-alpha, human
TNF-beta, human
VEGF121, human
VEGF165, human

CELL SCIENCES INC • 480 NEPONSET STREET, BUILDING 12A, CANTON, MA 02021 • INFO@CELLSCIENCES.COM

TOLL FREE: (888) 769-1246 • TEL: (781) 828-0610 • FAX: (781) 828-0542 • WEB WWW.CELLSCIENCES.COM

GE Healthcare
Life Sciences

Cell analysis just got easier

The new IN Cell Analyzer 2000 makes previously challenging cell analysis a thing of the past by offering significant throughput gains compared to typical lamp based imaging systems, while still delivering enabling features for your research assays.

From organelles to cells, to tissues and whole organisms – from fixed end-point assays to extended live cell studies – from manual microscopy to automated high-content screening, IN Cell Analyzer 2000 offers you the performance you need for all your screening and research – making your cell analysis faster and easier.

At GE Healthcare Life Sciences, our focus is on helping scientists achieve even more, faster. It's a commitment we have in our genes. And all this is backed by the service, support, and investment for the future that being part of GE can bring.

Cell analysis just got easier. Find out more. **Visit www.gelifesciences.com/incell**

| ÄKTA | Amersham | Biacore | **IN Cell Analysis** | Whatman | GE Service |

INtroducing the new IN Cell Analyzer 2000

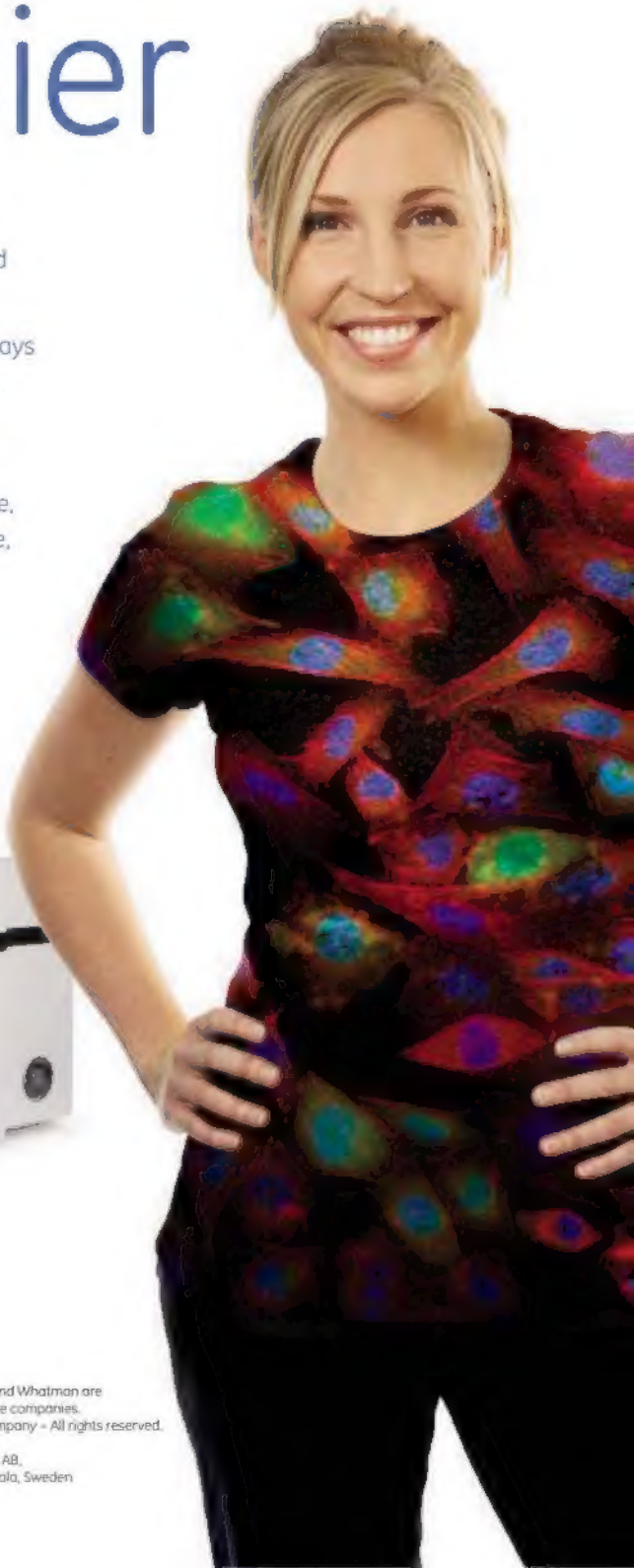

imagination at work

EDITORIAL

NEWS OF THE WEEK

NEWS FOCUS

LETTERS

BOOKS ET AL.

POLICY FORUM

PERSPECTIVES

CONTENTS continued >>

page 1194

page 1207

COVER

Scanning electron micrograph of the fruit fly *Drosophila melanogaster* (magnification 80×, eyes pseudo-colored). Sestrin, an evolutionarily conserved protein, helps protect fruit flies from age-related pathologies, including fat accumulation, muscle degeneration, and heart failure. See page 1223.

Image: T. Deerinck and M. Ellisman/National Center for Microscopy and Imaging Research, University of California, San Diego

DEPARTMENTS

Choose QIAGEN for detection

Detection platforms, assays, and analysis software by QIAGEN

Use QIAGEN® solutions from sample to result, and benefit from sensitive and reliable detection systems:

- **Quantitative, real-time PCR detection**
- **Automated analysis of DNA fragments and RNA**
- **Pyrosequencing® sequence-based DNA detection and quantification**
- **Optimized, ready-to-use assays and reagents**

Making improvements in life possible — www.qiagen.com

QIAGEN®

Sample & Assay Technologies

REVIEW

RESEARCH ARTICLES

REPORTS

CONTENTS continued >>

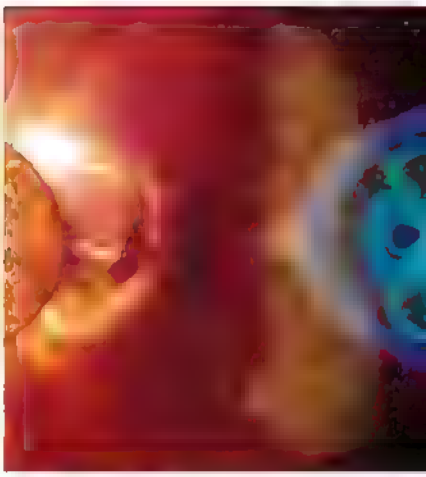

pages 1206 & 1238

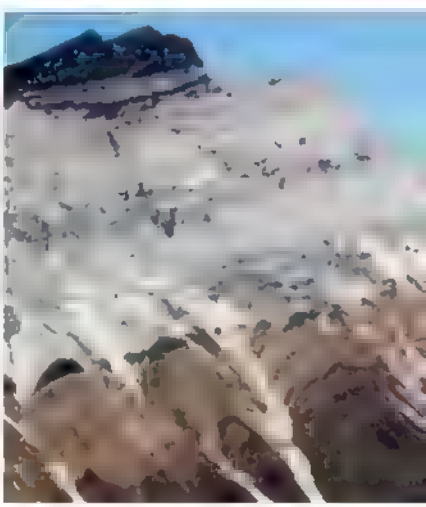

pages 1186 & 1241

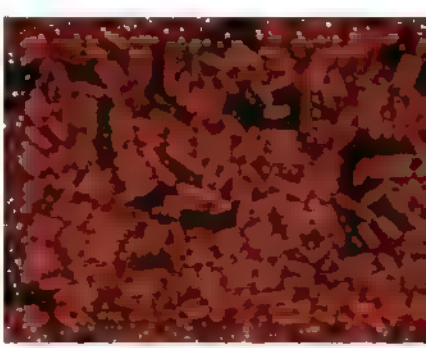

page 1258

"My **amplifriendly** qPCR gets along with everyone in my lab."

Real-time PCR for any need.

Bio-Rad's CFX96™ real-time PCR system combines user-friendly software with innovative optics and unparalleled thermal cycler performance to accommodate any user's unique real-time PCR needs.

- Save samples and reagents by running low sample volumes and 5-target multiplex reactions
- Save time by optimizing reactions for reliable results in a single run using the thermal gradient
- Get results faster with convenient and flexible software packages for qPCR, gene expression and High Resolution Melt Curve analysis

Bring our 20 years of experience in PCR to your discovery. Visit **www.bio-rad.com/ad/amplifamily/** or contact your Bio-Rad sales representative to learn more.

Research. Together.

ad Genomics

To find your local sales office, visit **www.bio-rad.com/contact/** in the U.S., call toll free at 1-800-4BIORAD (1-800-424-6723)

Visit us at **www.bio-rad.com**

BIO-RAD

SCIENCEONLINE

SCIENCEXPRESS
www.sciencexpress.org

Observation of an Antimatter Hypernucleus
The STAR Collaboration

Nuclei composed of antimatter are found to form in the high-energy collisions of gold ions.
10.1126/science.1183980

Iron-Clad Fibers: A Metal-Based Biological Strategy for Hard Flexible Coatings
M. J. Harrington et al.

Marine mussel byssal threads have an outer coating in which proteins are linked to metal ions.
10.1126/science.1181044
>> Science *Podcast*

Solvent-Mediated Electron Hopping: Long-Range Charge Transfer in IBr (CO_2) Photodissociation
L. Sheps et al.

The presence of an intervening CO_2 molecule dramatically changes the electron transfer probability between two halogen atoms.
10.1126/science.1184616

Metabolic Syndrome and Altered Gut Microbiota in Mice Lacking Toll-Like Receptor 5
M. Vijay-Kumar et al.

The innate immune system may promote metabolic health through effects on gut microbes.
10.1126/science.1179721

Cryptic Sex-Ratio Bias Provides Indirect Genetic Benefits Despite Sexual Conflict
R. M. Cox and R. Calsbeek

Female lizards improve their fitness by biasing the sex ratio of their progeny on the basis of sire body size.
10.1126/science.1185550

TECHNICAL COMMENTS

Comment on "Movement Intention After Parietal Cortex Stimulation in Humans"
H.-O. Karnath et al.

full text at www.sciencemag.org/cgi/content/full/327/5970/1200-c

Response to Comment on "Movement Intention After Parietal Cortex Stimulation in Humans"
A. Singu et al.,

full text at www.sciencemag.org/cgi/content/full/327/5970/1200-d

SCIENCENOW
www.sciencenow.org
Highlights From Our Daily News Coverage

Early Polar Bear Discovered in Arctic Tundra

Researchers say fossil represents one of the first members of the species.

Appetite Suppressor Could Be an Alternative to Insulin

Hunger-regulating hormone leptin helps diabetic mice control blood sugar.

Global Warming Didn't Kill the Golden Toad

Researchers find more mundane explanation for demise of colorful amphibian.

SCIENCESIGNALING
www.sciencesignaling.org
The Signal Transduction Knowledge Environment

RESEARCH ARTICLE: Polycomb Group Proteins as Epigenetic Mediators of Neuroprotection in Ischemic Tolerance
M. Stapels et al.

Polycomb group proteins protect neurons from injury through a mechanism involving decreased potassium channel function.

RESEARCH ARTICLE: Characterization of a Domain that Transiently Converts Class 2 DYRKs into Intramolecular Tyrosine Kinases
R. Kinstrie et al.

An N-terminal region of a dual-specificity kinase temporarily enables it to phosphorylate a tyrosine rather than a serine or threonine residue.

RESEARCH ARTICLE: Crystal Structure of the α-Kinase Domain of *Dictyostelium* Myosin Heavy Chain Kinase
Q. Ye et al.

Structural analysis identifies features of atypical serine-threonine kinases that may account for their different activities when compared to those of conventional kinases.

PERSPECTIVE: Allosteric Protein Kinase Regulation by Pseudokinases—Insights from STRAD
T. Rajakulendran and F. Sicheri

A kinase becomes activated when it binds as the "substrate" of a pseudokinase.

GLOSSARY

Find out what CD4, TEM8, and SLK mean in the world of cell signaling.

SCIENCECAREERS
www.sciencecareers.org/career_magazine
Free Career Resources for Scientists

Taken for Granted: Labor Unions and Postdoc Disputes
B. L. Benderly

A former University of Massachusetts postdoc sues his college, as postdocs on three UMass campuses unionize.

Perspective: Keep Working (Even If You Don't Get Paid)
B. Allen

When you are unemployed, it is essential to keep your skills and connections fresh.

***Science* Careers Facebook Fan Page**
Science *Careers Staff*

Join the discussion on topics affecting your next job at www.facebook.com/sciencecareers.

SCIENCETRANSLATIONAL MEDICINE
www.sciencetranslationalmedicine.org
Integrating Medicine and Science

PERSPECTIVE: Fighting Back—Peptidomimetics as a New Weapon in the Battle Against Antibiotic Resistance
A. Bragonzi

Agents that target bacterial outer-membrane synthesis effectively tackle antibiotic-resistant infections.

PERSPECTIVE. Of Mice and Men—How an Oncogene Transgresses the Limits and Predisposes to T Cell Acute Lymphoblastic Leukemia
T. Hoang

The *Lmo2* oncogene confers self-renewal potential to nonrenewing thymocyte progenitors.

RESEARCH ARTICLE: Safety and Efficacy of Subretinal Readministration of a Viral Vector in Large Animals to Treat Congenital Blindness
D. Amado et al.

After gene therapy to correct retinal degeneration in one eye, treatment of the second eye is effective—even when immunity to the vector is present.

RESEARCH ARTICLE: Blood Gene Expression Signatures Predict Invasive Candidiasis
A. K. Zaas et al.,

The development and validation of a gene expression signature is shown to be effective for the diagnosis of *C. albicans* blood stream infection.

SCIENCEPODCAST
www.sciencemag.org/multimedia/podcast
Free Weekly Show

Download the 5 March *Science* Podcast to hear about natural methane venting to the atmosphere, strong and stretchy mussel fibers, and challenges for stem cell science.

SCIENCEINSIDER
blogs.sciencemag.org/scienceinsider
Science Policy News and Analysis

SCIENCE (ISSN 0036-8075) **is published weekly on Friday, except the last week in December, by the American Association for the Advancement of Science, 1200 New York Avenue, NW, Washington, DC 20005.** Periodicals Mail postage (publication No. 484460) paid at Washington, DC, and additional mailing offices.

Domestic individual membership and subscription (51 issues): $146 ($74 allocated to subscription). Domestic institutional subscription (51 issues): $910; Foreign postage extra: Mexico, Caribbean (surface mail) $55, other countries (air assist delivery) $85. First class, airmail, student, and emeritus rates on request. Canadian rates with GST available upon request, GST #1254 88122 Publications Mail Agreement Number 1069624. **Printed in the U.S.A.**

Change of address: Allow 4 weeks, giving old and new addresses and 8-digit account number. **Postmaster:** Send change of address to AAAS, P.O. Box 96178, Washington, DC 20090–6178. **Single-copy sales:** $10.00 current issue, $15.00 back issue prepaid includes surface postage; bulk rates on request. **Authorization to photocopy** material for internal or personal use under circumstances not falling within the fair use provisions of the Copyright Act is granted by AAAS to libraries and other users registered with the Copyright Clearance Center (CCC) Transactional Reporting Service, provided that $20.00 per article is paid directly to CCC, 222 Rosewood Drive, Danvers, MA 01923. The identification code for *Science* is 0036-8075. *Science* is indexed in the *Reader's Guide to Periodical Literature* and in several specialized indexes.

AAAS
ADVANCING SCIENCE SERVING SOCIETY

STUNNING QUALITY

Reagents for Sample Preparation

Sequencing coverage map of the *E. coli* genome after using NEBNext™ DNA Sample Prep Reagent Set 1 for Sample Preparation

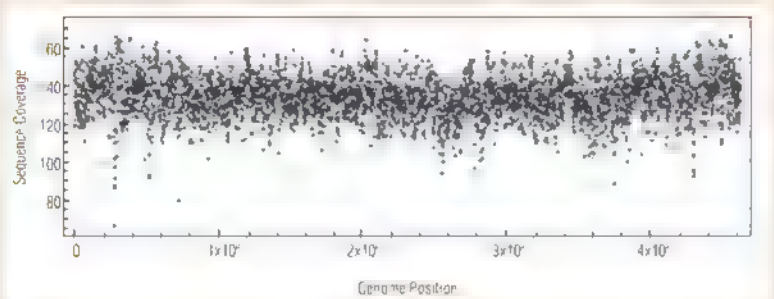

E. coli strain MG1655 gDNA was prepared with NEBNext DNA Sample Prep Reagent Set 1 and sequenced on an Illumina Genome Analyzer II.

Now available:
NEBNext™ dsDNA Fragmentase™
an enzyme-based solution for the fragmentation of DNA

CELEBRATING 35 YEARS

NEW ENGLAND BioLabs Inc
enabling technologies in the life sciences

EDITED BY STELLA HURTLEY

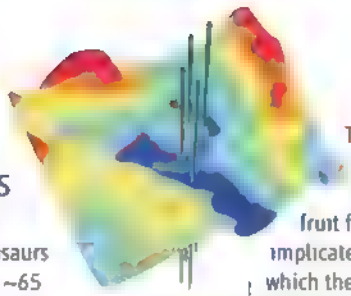

The Fall of the Dinosaurs

According to the fossil record, the rule of dinosaurs came to an abrupt end ~65 million years ago, when all non-avian dinosaurs and flying reptiles disappeared. Several possible mechanisms have been suggested for this mass extinction, including a large asteroid impact and major flood volcanism. **Schulte *et al.*** (p. 1214) review how the occurrence and global distribution of a global iridium-rich deposit and impact ejecta support the hypothesis that a single asteroid impact at Chicxulub, Mexico, triggered the extinction event. Such an impact would have instantly caused devastating shock waves, a large heat pulse, and tsunamis around the globe. Moreover, the release of high quantities of dust, debris, and gases would have resulted in a prolonged cooling of Earth's surface, low light levels, and ocean acidification that would have decimated primary producers including phytoplankton and algae, as well as those species reliant upon them.

Sestrin and the Consequences of Aging

The protein kinase TOR (target of rapamycin) plays key roles in the control of fundamental biological processes, including growth, metabolism, aging, and immune function. Sestrin proteins show increased abundance in response to stress and have been implicated in control of TOR activity. **Lee *et al.*** (p. 1223; see the Perspective by **Topisirovic and Sonenberg**) characterized *Drosophila* fruit flies lacking sestrins. Sestrins were implicated in a negative feedback loop in which the abundance of sestrins is controlled by TOR activity with sestrins concomitantly also inhibiting activity of TOR. Furthermore, flies lacking sestrins showed accumulation of fat, muscle degeneration, and heart abnormalities similar to those that plague aging humans with a sedentary life-style.

Early Origin of Earth's Magnetic Field

Earth's magnetic field protects us from stellar winds and radiation from the Sun. Understanding when, during the Earth's formation, the large-scale magnetic field was established is important because it impacts understanding of the young Earth's atmosphere and exosphere. By analyzing ancient silicate crystals, **Tarduno *et al.*** (p. 1238; see the Perspective by **Jardine**) demonstrate that the Earth's magnetic field existed 3.4 to 3.45 billion years ago, pushing back the oldest record of geomagnetic field strength by 200 million years. This result combined with estimates of the conditions within the solar wind at that time implies that the size of the paleomagnetosphere was about half of that typical today, but with an auroral oval of about three times the area. The smaller magnetosphere and larger auroral oval would have promoted loss of volatiles and water from the early atmosphere.

Aging Snowball Earth

Earth's glacial cycles have varied dramatically over time; at one point glaciers may have covered nearly the entire planet. Correlating various paleoclimate proxies such as fossil and isotope records from that time hinges on the ability to acquire precise age estimates of rocks deposited around the time of this so-called "Snowball Earth." **Macdonald *et al.*** (p. 1241) report new high-precision U-Pb dates of Neoproterozoic strata in the Yukon and Northwest Territories, Canada, to calibrate the timing of carbon isotope variation in rocks from other locations around the globe. Based on the estimated past positions of where these rocks were deposited, glaciers probably extended to equatorial latitudes. The overlap with the survival and, indeed, diversification of some eukaryotes in the fossil record suggests that life survived in localized ecological niches during this global glaciation.

Little Things Do Matter

Gas-phase sulfuric acid is important during atmospheric particle formation, but the mechanisms by which it forms new particles are unclear. Laboratory studies of the binary nucleation of sulfuric acid with water produce particles at rates that are many orders of magnitude too small to explain the concentration of sulfuric acid particles found in the atmosphere. **Sipilä *et al.*** (p. 1243) now show that gas-phase sulfuric acid does, in fact, undergo nucleation in the presence of water at a rate fast enough to account for the observed abundance of sulfuric acid particles in the atmosphere. These particles, which contain

Continued on page 1177

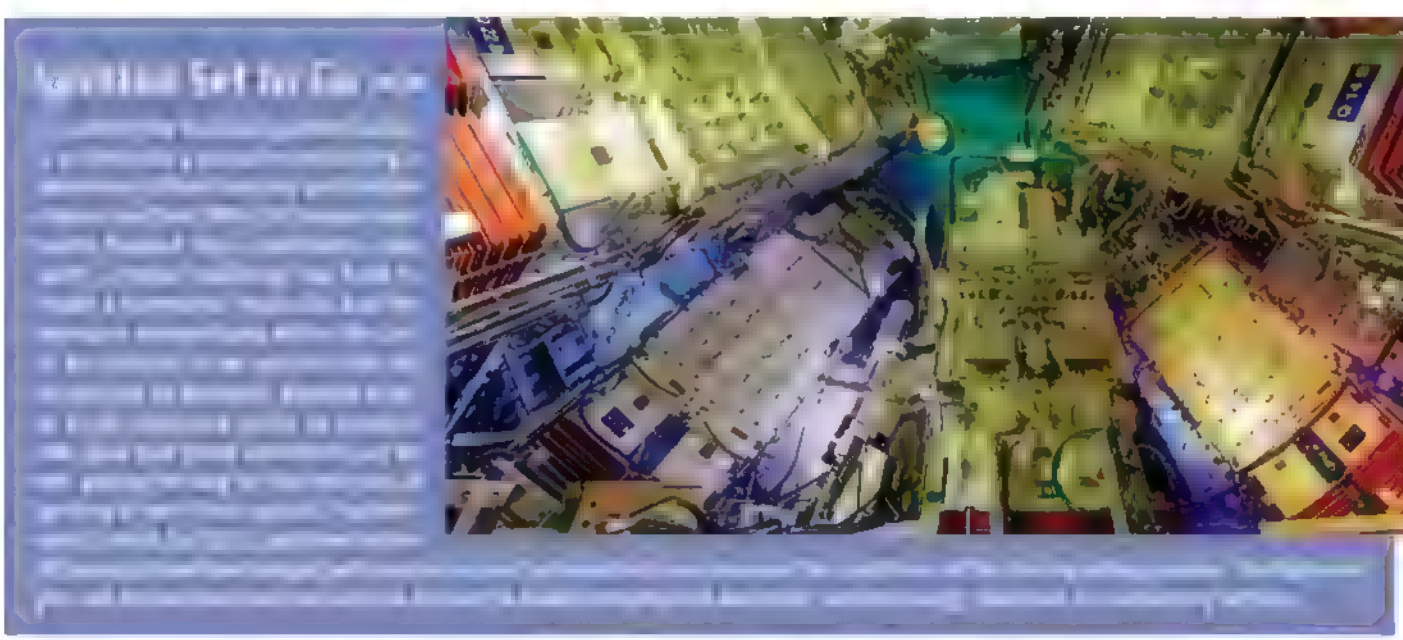

CREDITS (TOP TO BOTTOM): TOBIAS SAUGE AND PETER SCHULTE, WORK PERFORMED FOR DOE/NNSA BY LAWRENCE LIVERMORE NATIONAL LABORATORY

abcam®

We do proteins too!

Over 8,000 proteins and peptides available, with 150 new products added every month.

All supported by industry leading datasheets providing detailed application and technical data, just one click away!

- Bioactive proteins and enzymes
- Immunogen peptides for blocking studies
- Both recombinant and purified native formats
- Variety of expression systems

Many more available at **www.abcam.com/proteins**

NEW! Our Proteins catalog is now available

Contact us to receive a hardcopy for your lab:
www.abcam.com/protein resources

Abcam Inc.
1 Kendall Square, Ste 341
Cambridge, MA 02139-1517
USA

Tel: 1-617-225-2272
Toll free: 1-888-77-ABCAM
Toll free Fax: 1-866-739-9884

Continued from page 1175

1 to 2 sulfuric acid molecules each, were not detectable previously, owing to their small size, with diameters as small as 1.5 nanometers.

Bubble, Bubble, Warming and Trouble

Vast quantities of methane are stored in ocean sediments, mostly in the form of clathrates, but methane is also trapped in submerged terrestrial permafrost that was flooded during the last deglaciation. There is thus concern that climate warming could warm ocean waters enough to release methane cryogenically trapped beneath the seabed, causing even more warming. **Shakova *et al.*** (p. 1246; see the Perspective by **Heimann**) report that more than 80% of the bottom water, and more than 50% of the surface water, over the East Siberian Arctic Shelf, is indeed supersaturated with methane that is being released from the sub-sea permafrost, and that the flux to the atmosphere now is as great as previous estimates of that from the entire world ocean.

Reexamining Glial Function

In the last 20 years glial cells have been elevated from being considered as passive elements during neuronal transmission. By eliciting astroglial calcium rises, so-called gliotransmitters such as glutamate, ATP, or D-serine can be released and the activity of neighboring neurons modulated. However, this emerging picture has been challenged. **Agulhon *et al.*** (p. 1250; see the Perspective by **Kirchhoff**) reexamined these questions using two previously characterized mouse models. Calcium elevations induced selectively in astrocytes caused no change in multiple measures of synaptic activity. Furthermore, in mutant mice unable to elevate intracellular calcium, all synaptic measures were at wild-type levels. Astrocytic calcium signaling activity was thus not tied to the release of gliotransmitters and didn't affect synaptic transmission, short and long-term synaptic plasticity.

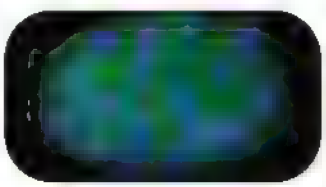

Corpse-Sorting Machinery

Phagocytosis of apoptotic cells is an integral part of the cell death program and plays critical roles in tissue remodeling, suppression of inflammation, and regulation of immune responses. The clearance of cell corpses requires their engulfment and subsequent degradation by phagocytic cells. During this process, receptors of the CED-1 family play a central role in recognizing cell corpses, transducing engulfment signals, and initiating the maturation of phagosomes containing apoptotic cell corpses. Retromer is a multisubunit protein complex conserved from yeast to mammals that mediates retrograde transport of transmembrane cargo from the endosome to the trans-Golgi network. Failure in recycling these proteins leads to their delivery to lysosomes where they are degraded. **Chen *et al.*** (p. 1261, published online 4 February) report that the *Caenorhabditis elegans* retromer complex is essential for the phagocytosis of CED-1 and thus for the clearance of apoptotic cells

Managing Crossovers

In all sexual eukaryotes a special type of cell division called meiosis produces gametes or spores. For chromosomes to segregate properly to the daughter cells during meiosis, DNA crossovers must occur between every pair of homologous chromosomes. The position and number of these crossovers, which help to hold the homologous chromosomes together, is carefully controlled, in part by the condensin I complex. **Youds *et al.*** (p. 1254) show that in the nematode, *Caenorhabditis elegans*, crossovers are regulated at a second level by the anti-recombinase RTEL-1 (regulator of telomere elongation helicase–1). RTEL-1 prevents crossovers occurring too close to each other, and ensures that only one occurs per pair of homologous chromosomes.

Carboxysomes in a Row

The carboxysome is an organelle-like proteinaceous microcompartment that sequesters the enzymes of carbon fixation from the rest of the cytoplasm in cyanobacteria. Cyanobacterial carbon fixation is a major component of the global carbon cycle. **Savage *et al.*** (p. 1258) now show that carboxysomes are linearly arranged within the cytoplasm in a process that involves the bacterial cytoskeleton. This arrangement is important in carboxysome partitioning during cell division. When carboxysome partitioning is disrupted by interfering with the bacterial cytoskeleton, carbon fixation is impaired.

CREDIT: CHEN ET AL.

It becomes you.

Introducing the 3500 Series Genetic Analyzer.

Get ready to make an amazing discovery: the new 8-capillary and 24-capillary 3500 Series Genetic Analyzers take DNA analysis to an entirely new level of performance. A level where your daily workflow seems like a natural extension of your own intuition. Where precise, quality-assured data inspires greater confidence. And where a new consumables design and intuitive software interface keep you current and in control.

Take a closer look, and you'll find the new 3500 and 3500xL Genetic Analyzers are like second nature. Which is our first priority when it's your data.

Discover the 3500 System at **www.appliedbiosystems.com/3500Series**

Easy-to-Use Consumables

Control at Your Fingertips

Quality-Assured Data

applied biosystems
part of Life technologies

Julia Marton-Lefèvre is the director general of the International Union for Conservation of Nature, Gland, Switzerland.

Biodiversity Is Our Life

2010 IS THE INTERNATIONAL YEAR OF BIODIVERSITY, IN RECOGNITION OF LIFE ON EARTH. EIGHT years ago, more than 190 countries agreed, through the United Nations Convention on Biological Diversity, to reduce biodiversity loss by 2010. This October, the Convention will meet in Nagoya, Japan, to evaluate progress and agree on new biodiversity targets for the world. Shortly before that, the UN General Assembly will address the biodiversity crisis for the first time.

It is clear from many indices of biodiversity that the world has failed to meet the 2010 target. For example, in its Red List of Threatened Species, the International Union for Conservation of Nature documents the extinction risk of 47,677 species. 17,291 are threatened, including 12% of birds, 21% of mammals, 30% of amphibians, 27% of reef-building corals, and 35% of conifers and cycads. Tracking extinction risk over time through this index reveals even worse news, with dramatic declines in many groups, notably amphibians and corals. The Living Planet Index reveals that populations of wild species have declined by 30% since 1970; mangrove forests have lost a fifth of their area since 1980, and 29% of seagrass beds are gone.

This biodiversity loss has grim consequences for humanity. According to The Economics of Ecosystems and Biodiversity study in 2009, half the welfare of the world's 1.1 billion poorest people flows directly from nature, through benefits including wild harvest, crop pollination, disaster mitigation, clean water provision, and maintenance of traditional cultures. The study estimates the total global annual economic cost of biodiversity loss, where it can be measured, to be between 1.35 and 3.1 trillion U.S. dollars. In addition, destruction of tropical forests (shrinking by 6 million hectares each year) is responsible for nearly a fifth of greenhouse gas emissions, driving climate change. Biodiversity loss deprives our descendants of currently unknown but potentially vast benefits. And in the sense that it cuts off humanity from the wonders of nature, the loss ultimately makes us less human.

However, rays of hope pierce this gloom. Conservation has centuries-old roots, and it works. The recent toll of bird extinctions would have been 25% greater in the absence of conservation action.* Protected areas are expanding worldwide, and they can prevent or reverse natural habitat destruction. The world's zoos, aquaria, botanic gardens, and gene banks provide insurance for species and genetic diversity.

The key challenge in Nagoya will be to establish a new plan for scaling up and mainstreaming these successes. The plan must have a long-term vision, aimed at 2050, to maintain and restore biodiversity. It must also establish an immediate mission and time frame: to stop biodiversity loss by 2020. To achieve this goal in 10 years, necessary actions will need to be in place by 2015, providing timely synergy with the United Nations Millenium Development Goals. These actions should be explicit, defining the ultimate drivers of biodiversity losses, the proximate threats, the benefits that conservation provides, and the scientific, political, economic, and social response mechanisms necessary to deliver this conservation.

To help drive this mission, a strengthened global science-policy interface is needed, such as the proposed Intergovernmental Platform on Biodiversity and Ecosystem Services. And new biodiversity targets will require new financial support, especially for developing countries. Innovative funding mechanisms for ecosystem services — such as climate change mitigation through forest conservation [known as Reducing Emissions from Deforestation and Forest Degradation (REDD)] offer enormous new opportunities. But much more is needed. For example, each of the 30 member countries of the Organization for Economic Cooperation and Development should contribute 0.2% of its gross domestic product for biodiversity conservation in developing countries, in addition to its 0.5% commitment for development assistance. Such funding could be freed up through the removal of misappropriated economic and environmental subsidies, and would yield several hundred billion dollars annually. Only through such explicit financial commitment can we ensure that biodiversity will survive, for the benefit of all people, and for nature itself. —**Julia Marton-Lefèvre**

10.1126/science.1188424

*A. S. L. Rodrigues, *Science* **313**, 1051 (2006)

EDITED BY GILBERT CHIN AND JAKE YESTON

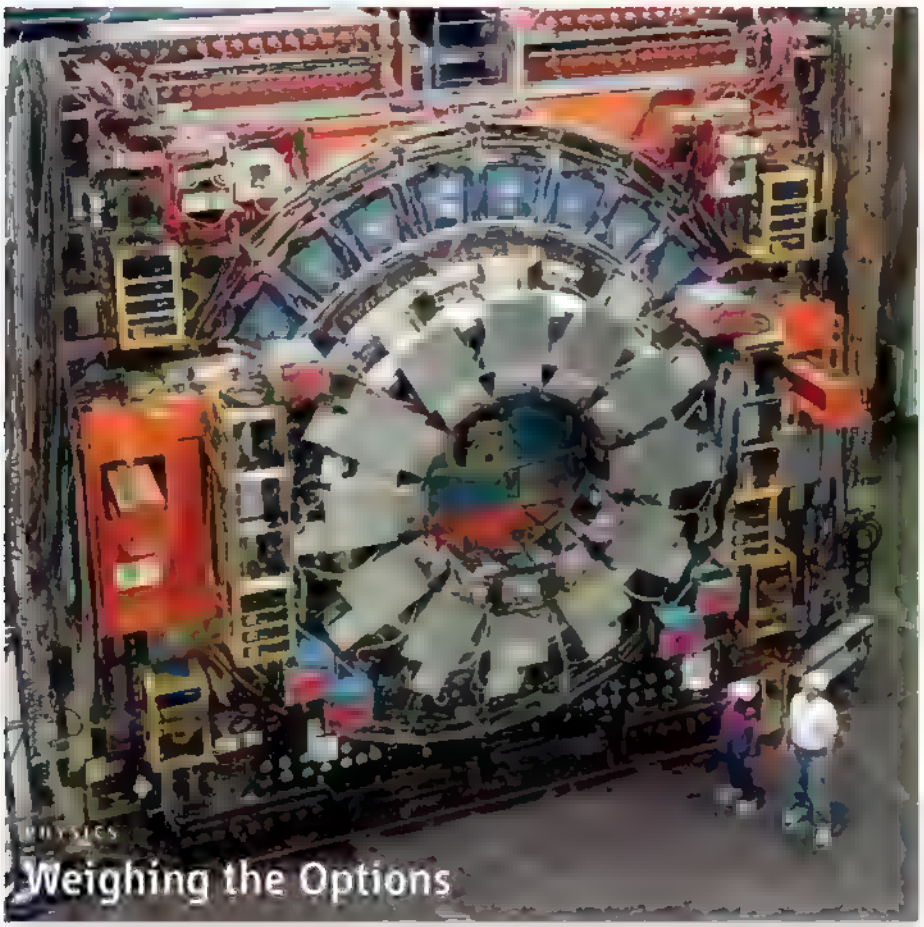

PHYSICS

Weighing the Options

Ever since the theoretical discovery of the Higgs mechanism, which endows particles with mass, the experimental evidence for the existence of the elusive Higgs boson has been a prime objective of particle physics. As the Standard Model does not predict the mass of the Higgs boson, the search has had to be undertaken in a wide parameter space, which has since been constrained to between approximately 115 and 190 GeV as a result of both direct (using the large electron positron collider at CERN) and indirect measurements. Now, Aaltonen *et al.* have combined the searches for the Higgs at the two multipurpose detectors at the Tevatron facility, CDF and D0. To detect the Higgs, they concentrated on the decay channel resulting in one positive and one negative W boson (the mediators of the weak interaction), which is favored if the Higgs mass is above 130 GeV; all Higgs production channels were taken into account. Even though they did not observe the Higgs boson, they were able to exclude a region of Higgs mass between 162 and 166 GeV using sophisticated neural network algorithms to distinguish between observed signal and background events. These analyses were performed with approximately 5 fb^{-1} worth of data; the Tevatron is scheduled to close when 12 fb^{-1} has been reached, so more results are yet to come. — JS

Phys. Rev. Lett. **104**, 061802 (2010)

MOLECULAR BIOLOGY

Acting Out of Character

The steroid receptor coactivator 3 gene, *SRC-3*, was identified in a region on chromosome 20 that was frequently amplified in breast cancer. The SRC-3 protein was shown to act in the nucleus to regulate the transcription of genes involved in growth and development. Long *et al.* report that the *SRC-3* transcript can undergo alternative splicing to produce two proteins with distinct personalities. In comparison to the full-length protein, SRC-3Δ4 lacks exon 4, which encodes the DNA-binding domain and a nuclear localization signal. Like SRC-3, the SRC-3Δ4 isoform is overexpressed in breast cancer and other tumors, but it localizes to the plasma membrane and acts as a cytoplasmic signaling coactivator by mediating epidermal growth factor (EGF)–induced cell migration. SRC-3Δ4 couples the EGF receptor to one of its downstream signaling effectors, focal adhesion kinase. EGF is known to promote cancer cell migration and metastasis, and overexpression of SRC-3Δ4 in breast cancer cells induced metastasis to the lymph node and lung in mice. Thus, both SRC-3 and its close relative SRC-3Δ4 are linked to breast cancer, but likely via completely distinct pathways. — HP

Mol. Cell **37**, 321 (2010)

PALEONTOLOGY

Moving by Mistake

Large macroscopic animal fossils first appear in the Ediacaran, the period just before the Cambrian, about 600 million years ago. Although there are some clear trackways closer to the Cambrian, and several purported reports of earlier tracks, most of these fossils seem to have been sessile organisms. One of the most diverse megafossil assemblages, and one of the oldest, is at Mistaken Point, Newfoundland, dating to 565 million years ago. A variety of leaf-like forms extending up to several tens of centimeters are thought to represent early suspension feeders. Liu *et al.* now report the presence of several tracks in these rocks, implying that mobile animals were also present. The tracks range up to more than 1 cm in width and extend for tens of centimeters. It seems that, together with the diverse macrofossils, Mistaken Point preserves a diverse marine benthic ecosystem at this time. — BH

Geology **38**, 123 (2010)

MICROBIOLOGY

A Home Within a Home

Ion-motive ATP synthases are the primary producers of ATP in mitochondria, chloroplasts, bacteria, and archaea. They convert a transmembrane gradient of ions (H^+ or Na^+) into cytoplasmic ATP, and hence can only operate—in concert with the ion gradient–generating enzymes—in membranes that are relatively impermeant to H^+ or Na^+. In the cases of mitochondria, chloroplasts, and Gram-negative bacteria, this is the inner membrane; the outer membrane is too leaky to support the establishment of ion gradients. Küper *et al.* report that in the archaeon *Ignicoccus hospitalis*, both the ATP synthase and

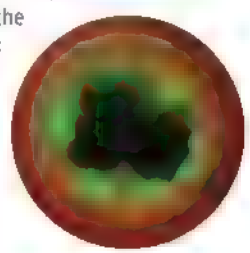

ATP synthase (green) in the outer membrane.

CREDITS (TOP TO BOTTOM): FRED JULICH/FERMILAB; KÜPER *ET AL.*, *PROC. NATL. ACAD. SCI. U.S.A.* **107**, 3152 (2010)

the H_2:sulfur oxidoreductase are located in the outer membrane. *Ignicoccus* obtains energy by reducing elemental sulfur with molecular hydrogen, and its inner membrane encloses the customary complement of DNA and ribosomes. Unlike the aforementioned organelles and cells, however, the intermembrane compartment is as large as the inner membrane–bounded cytoplasm. This sizable periplasmic space likely supports ATP-consuming metabolic reactions such as the fixation of CO_2, the sole carbon source for *Ignicoccus*. The authors point out that in an earlier age, engulfed bacteria might have found this environment hospitable. — GJC

Proc. Natl. Acad. Sci. U.S.A. **107**, 3152 (2010).

PSYCHOLOGY

How Hard Is Hard?

Rankings of incommensurable entities are often equated to comparisons of apples and oranges, the implication being that no objective answer exists. Nevertheless, subjective answers do exist, as can be demonstrated simply by asking people for their judgments. Keil *et al.* have developed a battery of 30 questions representing phenomena in the disciplines of physics, chemistry, biology, psychology, and economics; they posed these questions to students in kindergarten, the second, fourth, sixth, and eighth grades, and college. They did not ask for answers, but instead asked how hard it would be to explain these phenomena and whether they would need to consult an expert to do so. By these measures, psychology was rated as less difficult than the hard sciences and easier to learn about on one's own, although these differentials decreased with age. Economics was at first perceived to be like the hard sciences, but its ranking approached that of psychology in older students, perhaps reflecting a shift from seeing it as relying on mathematics to regarding it as a spectrum of human behaviors. — GJC

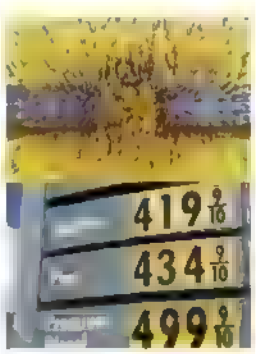

J. Exp. Psychol. Gen. **139**, 1 (2010)

MOLECULAR BIOLOGY

Spreading Barrier

DNA methylation generally functions to silence gene expression, and is most often targeted to parasitic and repeated sequences in the genome. Like other epigenetic marks, DNA methylation may be self-propagating, which can result in its inappropriate spreading into and silencing of nearby active genes. Clearly, barriers are needed to corral such silencing marks, and in yeast these consist of specific DNA sequences. In the filamentous fungus *Neurospora*, DNA methylation is found at AT-rich repeat sequences, including transposon relics and repetitive DNA, and Honda *et al.* show that spreading of DNA methylation into GC-rich regions that contain active genes is strictly limited by the protein DNA methylation modulator 1 (DMM1) and its binding partner DMM2. DDM1 and DMM2 are concentrated at the edges of methylated and silenced regions, and this localization depends on heterochromatin protein 1 (HP1) and histone H3 trimethylated on lysine 9 (H3K9me3), both of which are also implicated in silencing. DMM1 contains a Jumonji-C domain, which is known to direct histone demethylation in other Jumonji-C–containing proteins, and critical catalytic residues are required for the barrier activity of DMM1, suggesting that it might limit spreading by removing ectopic H3K9me3 marks, which recruit HP1, at the edges of methylated silencing domains. — GR

Genes Dev. **24**, 10.1101/gad.1893210 (2010)

CLIMATE SCIENCE

Ski While You Can

Contemporary global climate change is a phenomenon defined in large part by the rapid and substantial warming it includes. During the last glacial period, the climate of the Northern Hemisphere experienced numerous rapid, large warming episodes, termed Dansgaard-Oeschger (DO) events after the Danish and Swiss researchers who documented them through ice-core studies. Can the past be used to help us understand what other impacts modern global warming may bring? In an attempt to garner such insight for the American Southwest, Asmerom *et al.* present oxygen isotopic data from a well-dated stalagmite recovered from central New Mexico. The oxygen isotopic composition of calcite in this speleothem is a proxy for the relative amounts of summer precipitation (from the Gulf of Mexico) and winter precipitation (from the Pacific Ocean) received at the sample site. What the authors find is an excellent match to the record of DO events, which they interpret as a result of a shift of the polar jet stream and Northern Intertropical Convergence Zone to the north during warm periods. This change in turn causes a reduction in winter precipitation and consequently greater aridity. If that same response to warming occurs in the future, an already drought-prone region could become even drier, with significant consequences for the population that lives there. — HJS

Nat. Geosci. **3**, 114 (2010)

CREDITS: PHOTOS.COM

www.sciencemag.org

Science

1200 New York Avenue, NW
Washington, DC 20005
Editorial: 202-326-6550, FAX 202-289-7562
News: 202-326-6581, FAX 202-371-9227

Bateman House, 82-88 Hills Road
Cambridge, UK CB2 1LQ
+44 (0) 1223 326500, FAX +44 (0) 1223 326501

Subscription Services For change of address, missing issues, new orders and renewals, and payment questions: 866-434-AAAS (2227) or 202-326-6417, FAX 202-842-1065. Mailing addresses: AAAS, P.O. Box 96178, Washington, DC 20090-6178 or AAAS Member Services, 1200 New York Avenue, NW, Washington, DC 20005

Institutional Site Licenses please call 202-326-6755 for any questions or information

Reprints: Author inquiries 800-635-7181
Commercial inquiries 803-359-4578

Permissions 202-326-7074, FAX 202-682-0816

Member Benefits AAAS/Barnes&Noble.com bookstore, www.aaas.org/bn; AAAS Online Store, www.apisource.com/aaas/, code MKB6; AAAS Travel: Betchart Expeditions 800-252-4910, Apple Store, www.apple.com/eppstore/aaas, Bank of America MasterCard 1-800-833-6262 priority code FAA3YU, Cold Spring Harbor Laboratory Press Publications, www.cshlpress.com/affiliates/aaas.htm, GEICO Auto Insurance, www.geico.com/landingpage/go51.htm?logo=17624, Hertz 800-654-2200 CDP#343457, Office Depot, https://bsd.officedepot.com/portal_login.do; Seabury & Smith Life Insurance 800-424-9883, Subaru VIP Program 202-326-6417; VIP Moving Services, www.vipmayflower.com/domestic/index.html, Other Benefits: AAAS Member Services 202-326-6417 or www.aaasmember.org

science_editors@aaas.org	(for general editorial queries)
science_letters@aaas.org	(for queries about letters)
science_reviews@aaas.org	(for returning manuscript reviews)
science_bookrevs@aaas.org	(for book review queries)

Published by the American Association for the Advancement of Science (AAAS). *Science* serves its readers as a forum for the presentation and discussion of important issues related to the advancement of science, including the presentation of minority or conflicting points of view, rather than by publishing only material on which a consensus has been reached. Accordingly, all articles published in *Science*—including editorials, news and comment, and book reviews—are signed and reflect the individual views of the authors and not official points of view adopted by AAAS or the institutions with which the authors are affiliated.

AAAS was founded in 1848 and incorporated in 1874. Its mission is to advance science, engineering, and innovation throughout the world for the benefit of all people. The goals of the association are to: enhance communication among scientists, engineers, and the public; promote and defend the integrity of science and its use; strengthen support for the science and technology enterprise; provide a voice for science on societal issues; promote the responsible use of science in public policy; strengthen and diversify the science and technology workforce; foster education in science and technology for everyone; increase public engagement with science and technology; and advance international cooperation in science.

Information for Authors
See pages 352 and 353 of the 15 January 2010 issue or access www.sciencemag.org/about/authors

Small Dog Story

Mexico may claim the Chihuahua and Tibet the shih tzu, but a new genetic study indicates that all small dogs have their origins in the Middle East.

Mitochondrial DNA studies suggest that dogs—descendants of gray wolves—were first domesticated in East Asia between 5000 and 16,000 years ago. But it's a matter of debate, as dog remains as old as 31,000 years have been found in Europe and the Middle East.

Now, a team led by evolutionary geneticist Melissa Gray of the University of California, Los Angeles, has examined different versions of a gene called *insulin-like growth factor-1* (*IGF-1*)—which is strongly associated with canine skeleton size—in big dogs, small dogs, and wild canids from around the world. The team found that the small dogs share an *IGF-1* variant very similar to that found in Middle Eastern gray wolves. That means the common ancestor of all small dogs probably lived there and that the gene must have evolved shortly after dogs were first domesticated, the researchers reported last week in *BMC Biology*. It's a "strong indication" that the region "has played a significant role in the early history of domestic dogs," says Gray. She says farmers may have bred small dogs because they ate less and needed less room.

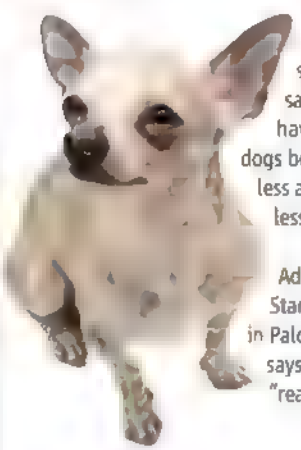

Geneticist Adam Boyko of Stanford University in Palo Alto, California, says the study "really pokes a hole in the argument of this relatively simple domestication in East Asia, … which people have been arguing based on mitochondrial DNA."

Mosquito Buzzer Won't Fly

A Dutch medical entomologist is crusading to stop airlines from selling an electronic gadget that promises to keep mosquitoes away. Bart Knols, who runs a Web site called MalariaWorld, discovered the €17 product, called MozStop, in KLM Royal Dutch Airlines's duty-free catalog while en route to a malaria meeting. Many travelers to malaria-infested regions "think they're buying protection from mosquito-borne diseases, but they're not," says Knols.

MozStop's manufacturer, Akita Electronics in Tokyo, claims it repels mosquitoes "by emitting a high pitch sound that is unbearable to mosquitoes but inaudible to the human ear and family pets." MozStop and similar devices are claimed to imitate the noise of male mosquitoes' wingbeat; that supposedly is a big turnoff for the biting females, which mate only once. But that idea is controversial because the females have poor hearing. A 2009 literature review by Paul Garner of the Liverpool School of Tropical Medicine in the U.K. showed that the buzzers have no effect on them. Nonetheless, Garner says, "people instinctively seem to like the pseudoscience behind it."

A couple of calls and e-mails were enough to persuade KLM—which was selling 1000 MozStops a month—to drop the product. Now, Knols is working on British Airways and Singapore Airlines, which also carry it. Akita did not respond to requests for comment.

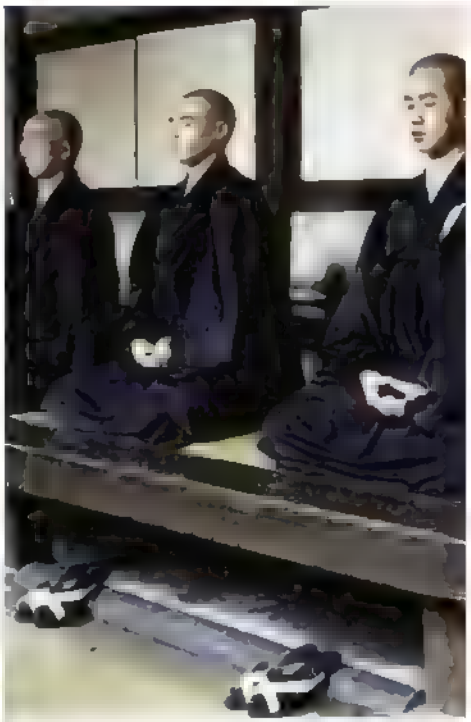

Saying 'Om' Instead of 'Ow'

The pain-relieving benefits of meditation aren't merely in people's minds but in their brains, too, according to a new study.

Neuroscientists at the University of Montreal in Canada turned up the heat on a metal cube applied to the legs of 17 male and female Zen meditation practitioners between the ages of 22 and 57, and 18 matched controls. On average, the meditators, who had between 2 and 30 years of daily practice, tolerated an extra 2°C before saying they were in moderate pain. The team then took MRI scans of the subjects and measured the thickness of certain pain-processing regions in the cerebral cortex. The meditators had greater thickness in a region of the anterior cingulate cortex (ACC), an area thought to mediate pain's unpleasantness. Thicker ACCs were also correlated with less sensitivity to pain in the leg test, the team reported last month in the journal *Emotion*.

The study's lead author, Joshua Grant, says that although physical activities are known to change brains, "I don't know if it's ever been shown that a mental activity—placing your attention on something"—can cause physical changes in that organ. The study "demonstrates convincingly the impact of meditation practice on pain perception," says Bogdan Draganski, a neuroscientist at University College London. "The idea of training the 'emotional muscle' … is very tempting."

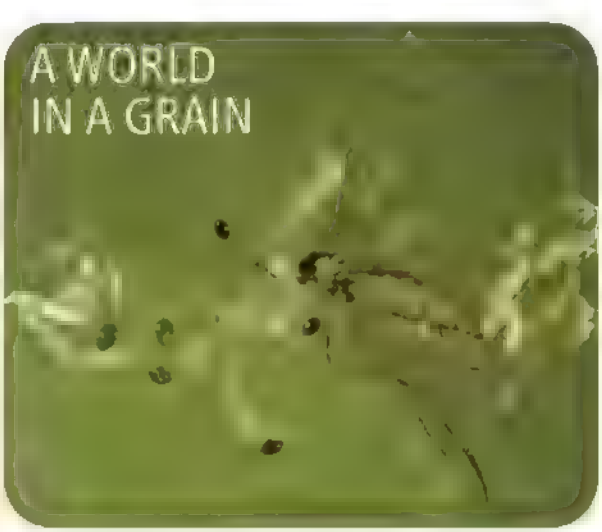

Last month's winners of the U.K. Biotechnology and Biological Sciences Research Council's first science photo competition included this image of mites, springtails, and other insects collected from a soil sample—"the poor man's rainforest." The photo by Felicity Crotty, a Ph.D. student at North Wyke Research in Okehampton, U.K., won in the agriculture, food, diet and health category.

CREDITS (TOP TO BOTTOM): ROBERT WALLIS/CORBIS; SOURCE: AKITA ELECTRONICS; PHOTOS.COM; SOURCE: BBSRC/©FELICITY CROTTY

Testing nutritional claims 1189

Sequencing with a chip 1190

SEISMOLOGY

Two Years Later, New Rumblings Over Origins of Sichuan Quake

BEIJING—When experts suggested that the disastrous 2008 Wenchuan earthquake might have been triggered by the reservoir behind the Zipingpu Dam, establishment scientists in China remained largely silent (*Science*, 16 January 2009, p. 322). Now they've weighed in, ruling out reservoir triggering. But many earth scientists don't buy their arguments.

No large quake had ruptured the Beichuan-Yinxiu fault in southwestern China's Sichuan Province in at least a millennium or two. Then engineers built Zipingpu Dam on the Min River just 500 meters from the fault and in late September 2005 began filling it with upward of 900 million tons of water. Two-and-a-half years later, the magnitude-7.9 Wenchuan earthquake got started 5 kilometers from the reservoir.

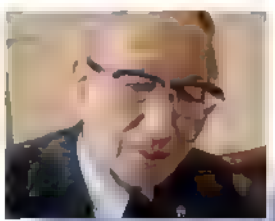

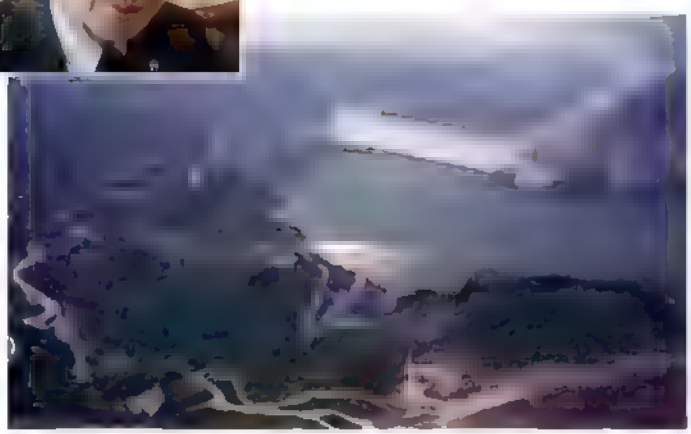

Trickle-down theory. Did filling the Zipingpu Dam trigger the magnitude-7.9 Wenchuan earthquake? Chen Houqun (*inset*) says no

In the January issue of *International Water Power and Dam Construction*, three dam engineers at the China Institute of Water Resources and Hydropower Research here argue that the Zipingpu-Wenchuan situation was so unlike that of the four largest known reservoir-triggered earthquakes—all in the magnitude-6 range—that there could not have been a connection between reservoir and quake. The authors, led by structural engineer Chen Houqun, who has co-authored China's design code for building earthquake resistance into dams, contend that the timing was mere coincidence.

Unlike the four big triggered quakes, the authors point out, the Wenchuan quake occurred on a thrust fault: One block of crust is pushed up the inclined fault over the other block. According to the authors, the reservoir's weight lies on a "relatively stable region" of the footwall, or underlying block.

In addition, the 300-kilometer Wenchuan rupture began 18.8 kilometers beneath the surface, according to new data from a team led by geophysicist Liu Qiyuan of the China Earthquake Administration's Institute of Geology in Beijing. The reservoir's water pressure could not have driven water that far down through cracks and pores, Chen argues. Such water infiltration over months or years is thought to weaken a fault by pushing its sides apart.

Finally, Chen and his colleagues note, in the four cases, filling a dam's reservoir led to an increasing number of temblors until a large earthquake struck. But a seismic-monitoring network around Zipingpu reservoir established 13 months before impoundment began showed only "normal variation" of seismic activity between impoundment and the quake, the group writes. "All of these factors rule out triggering," says Chen.

Martin Wieland, chair of the International Commission on Large Dams' committee on seismic aspects of dam design, says the paper makes a persuasive case. And Liu adds that the Wenchuan quake's focal depth by itself discounts a link to Zipingpu. But neither categorically rejects a role for Zipingpu. There are too many uncertainties, says Wieland, an earthquake engineer at Poyry Energy in Zurich, Switzerland.

Many seismologists say the *Water Power* authors overstate their case. "I don't think [triggering] has been put to rest yet," says seismologist Arthur McGarr of the U.S. Geological Survey (USGS) in Menlo Park, California, who co-authored a review of reservoir-triggered seismicity (RTS) in 2002. The problem, many seismologists say, lies in comparing Wenchuan to the four big RTS earthquakes. "Wenchuan doesn't fit the pattern? What pattern?" asks seismologist Ross Stein of USGS Menlo Park. "The [four] examples are all over the map as to how seismicity has responded to dam impoundment. It shows just how little we know about this process." Although RTS does tend to be shallow, McGarr says, the high Aswan Dam caused a magnitude-5.3 event in 1981 at a depth of 18 kilometers, similar to Wenchuan's depth. And a magnitude-4.5 RTS quake in Tajikistan struck in a region of thrusting as did Wenchuan.

Last October, hydrogeologist Shemin Ge of the University of Colorado, Boulder, and colleagues presented modeling evidence in *Geophysical Research Letters* that water infiltration from Zipingpu "potentially hastened the occurrence of the Wenchuan earthquake by tens to hundreds of years." Other researchers see Zipingpu's fingerprints all over the seismic data. One of the most vocal advocates for a dam-quake link, geologist Fan Xiao of the Sichuan Bureau of Geology and Mineral Resources in Chengdu (*Science*, 8 May 2009, p. 714), says swarms of small quakes struck the region near Zipingpu 3 months before the Wenchuan earthquake. "The fact is, there were obvious foreshocks," Fan says. Chen says he welcomes "scientific debate"—but he is sticking to his guns.

What researchers still want almost 2 years after the earthquake is wide dissemination of the raw data from the Zipingpu monitoring. Until such data sets become commonplace, says geophysicist Evelyn Roeloffs of USGS in Vancouver, Washington, "it's always going to be this kind of story."

–RICHARD A. KERR AND RICHARD STONE

CREDITS: WANGCH NA (INSET); R. STONE/SCIENCE

Redefining childhood psychiatric disorders
1192

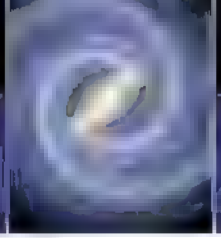

Probing the history of the Milky Way
1194

PHARMACOLOGY

Growth Hormone Test Finally Nabs First Doper

On 22 February, Terry Newton became perhaps the world's best-known rugby player—but not for any accomplishment on the field. UK Anti-Doping last week announced that Newton is the first athlete caught by a blood test designed to detect doping with human growth hormone (HGH) to boost muscle mass. The positive test, for which Newton has accepted a 2-year ban from rugby, represents a warning to athletes who may have thought HGH use was undetectable, and it also erases lingering doubts about the test among scientists. "It's a great success," says Mario Thevis of the Center for Preventive Doping Research at the German Sport University in Cologne. "We were always confident in principle that the test would work."

At the same time, this first successful detection of HGH doping underscores the challenge scientists face as they race to keep up with cheating athletes (*Science*, 30 July 2004, p. 632). The current HGH blood test made a limited debut at the 2004 Athens Olympics, but because of a variety of difficulties, the assay is only now being used widely. And a second HGH test that should stand a better chance of nabbing doped athletes remains on the sidelines as researchers struggle to overcome problems that have stalled its validation.

The test that caught Newton vindicates an idea that endocrinologist Christian Strasburger of Charité-University Medicine Berlin and colleagues proposed in 1999 in an article in *The Lancet*. At the time, illicit use of the hormone was considered unstoppable, as the synthetic form of HGH is identical to the 22-kilodalton protein naturally made by the pituitary gland. But the German group noted that the pituitary makes other forms, notably a 20-kd HGH, and that analyzing the HGH isoform ratios in a blood sample could reveal if someone had spiked themselves with non-natural HGH. After several years of study, the World Anti-Doping Agency (WADA) approved the isoform test, initially screening a small number of athletes at the 2004 and 2006 Olympic Games.

Yet until last week, not a single HGH-doping infraction had been declared, puzzling doping researchers. "There has been concern that there haven't been any positive tests," says endocrinologist Richard Holt of Southampton General Hospital in the United Kingdom.

Banned. Professional rugby player Terry Newton was caught by a HGH blood test.

The likely reason: The test only spots abnormal isoform ratios within a day or so after HGH use, so athletes probably stopped taking the hormone a few days before an event. For that reason, the isoform assay was always planned as an unannounced, out-of-competition test—the way Newton was caught—but supplying enough test kits and validating regional testing labs proved difficult. The tests used in 2004 and 2006 were made by Strasburger's lab, but plans for a commercial manufacturer to take over fell through. Strasburger says the firm's parent company ultimately decided that the market for a doping test was too small, and it had legal concerns. Finally, a new supplier signed on, making the test more available. And because this wasn't a simple urine test, WADA had to develop rigorous procedures for collecting and storing blood samples. It "has been the most complex test ever put into place," says Olivier Rabin, WADA's science director.

Based on data he's seen, Strasburger says WADA could have accused other athletes of HGH doping, but out of caution, the agency refrained. After years of studying HGH isoform ratios in elite athletes—more than 1500 tests have now been conducted—WADA "has gotten a better idea of what's normal. … Now all the legal concerns are out of the way," Strasburger says. Rabin confirms there have been other "suspicious" tests but says, "we really want to make sure we catch the cheater and not someone who had a peak of growth hormone."

This first success of the HGH isoform test has prompted the U.S. National Football League and Major League Baseball to declare interest in its use, although the players' unions are wary of blood, rather than urine, tests. Despite years of research on it, an HGH urine test remains far away, say doping scientists.

For now, WADA is pushing to ready a second blood test that could catch athletes up to a month after they've doped themselves with HGH. It's based on the idea that injections of synthetic HGH—or of HGH from cadavers, which the isoform test would miss—dependably change blood concentrations of other substances. A major effort to identify such HGH biomarkers began in 1996, and Holt and other researchers settled on insulin-like growth factor 1 (IGF-1) and type III pro-collagen. But validating the biomarkers hasn't been easy.

The biggest stumbling block has been the use of commercial immunoassays, antibody-based detection kits, for IGF-1. After scientists gathered years of data on IGF-1 with certain immunoassays, those kits were withdrawn from the market. "We're at the mercy of the manufacturers of immunoassays," Rabin says.

Rabin says WADA has lined up seemingly stable suppliers of the new immunoassays for the HGH biomarker test, and Holt and his colleagues are comparing IGF-1 measurements from the old and new assays. They're also evaluating the new IGF-1 assay in 500 elite U.K. athletes, hoping to amass enough data to persuade WADA. Meanwhile, a group at King's College London is exploring measuring IGF-1 levels in blood with a mass spectrometer.

WADA will soon review the latest data and decide whether to launch the HGH biomarker test for the 2012 Olympics in London. "We're working toward that date," says Holt.

–JOHN TRAVIS

PALEOCLIMATOLOGY

Snowball Earth Has Melted Back To a Profound Wintry Mix

In 1998, a handful of geoscientists at Harvard University breathed new life into a daring idea: that Earth froze over from pole to pole more than a half-billion years ago, threatening life with extinction but perhaps prodding it to greater evolutionary heights (*Science*, 28 August 1998, p. 1342). On page 1241 of this issue, geoscientists report evidence that the tropics also hosted glaciers more than 100 million years before that supposed global freeze. Such low-latitude glaciation is a hallmark of so-called hard snowball Earth scenarios, in which a kilometer of ice sealed off the world ocean.

But despite the new work, the much-studied hypothesis has fallen on hard times. "In many people's minds, the hard snowball is dead," says geochemist Michael Arthur of Pennsylvania State University (PSU), University Park, who was not involved in the new work. Earth was profoundly cold in those geologically weird days, many agree—a "slushball" of a planet, perhaps. But sealed in ice? Unlikely.

The new contribution to the snowball debate comes from Harvard geologist Francis Macdonald and colleagues at Harvard and elsewhere. They dated volcanic ash layered within deposits of the so-called Sturtian glacial era to an age of 716.5 million years. That's the same age as rocks whose paleomagnetic record places them and the Sturtian glaciers in the tropics.

Researchers speculated about possible ancient tropical glaciers for several decades before geobiologist Joseph Kirschvink of the California Institute of Technology in Pasadena coined the term "snowball Earth" in 1992. But the hard-snowball concept gained ground only after geologist Paul Hoffman—then at Harvard University and now retired—and three colleagues boosted it in the 1998 *Science* paper. Drawing on simple climate modeling, the authors concluded that any ice that reached tropical latitudes during the Marinoan glaciation, about 650 million years ago, would not have stopped there. Instead, once the highly reflective ice covered enough area, a climatic feedback would inevitably drive the ice to the equator and create global glaciation: a hard snowball.

Some more-recent paleoclimate modeling, however, suggests that the leap from low-latitude glaciation to a hard snowball may be difficult or even impossible. "We can get ice on land," says climate modeler Mark Chandler of the Goddard Institute for Space Studies in New York City. "It's the ocean we can't freeze over." Model oceans can hold lots of heat and move it around in currents, frustrating a complete freeze-over, Chandler says. A few years ago, "the pattern was that the more sophisticated the model, the less likely you'd get a hard snowball result," he says. Discouraged, Chandler and others moved on to other projects.

Definitely chilly. Clear signs of glaciation, such as rocks dropped to the sea floor from icebergs (*inset*), show up in tropical deposits (dark peak)

Atmospheric physicist James Kasting of PSU now favors a slightly more modest "thin ice" snowball. He and climate modeler David Pollard of PSU have considered how a continent poleward of an inland sea might hold off thick ice intruding from higher latitudes and preserve small areas of thin ocean ice, thin enough to let sunlight through for marine plants. "We think the thin-ice solution satisfies all the constraints better than the other models."

But almost all geologists now reject any worldwide freeze, says geologist Philip Allen of Imperial College London. "When the snowball came up, the [geological] community was very open to it," he says. Now, "it's my impression that 90% of the geological community is quite hostile to the idea."

Allen and other geologists went to the field to study glacial deposits from about the time of the proposed Marinoan hard snowball. Instead of stagnation, the sediments recorded signs of water and ice in motion: ice moving, ocean currents flowing, and waves moving on an open sea. "We do not have a hard snowball Earth," says Allen. Hoffman hasn't disputed such interpretations, but he has argued that they could reflect conditions either just before or after a hard snowball

Most geochemists aren't sold on a hard snowball either. Key to the Harvard group's argument was the contention that a bizarre chemical deposit found on the top of glacial deposits—the cap carbonate formation could have formed after a glacial period only if the world ocean had been sealed off from the atmosphere for millions of years. Only rare cracks in the ice or open water maintained by volcanic hot spots kept the biota going, the group maintained. Geologist Alan Jay Kaufman of the University of Maryland, College Park, a co-author of the 1998 *Science* paper, has shifted his stance. After studying the isotopic records of carbon, strontium, and sulfur, he now supports the slushball view. The sulfur isotopes in particular, he says, suggest "that there was more than cracks in the ice."

Hoffman is unperturbed. Resistance to the hard snowball "is really typical of scientific controversy," he says. "The problem is the experts reach a quick judgment and dig themselves into a position." The idea of a recent ice age, he notes, took 40 years and a new generation of scientists to win acceptance in the 19th century. In his view, "the evidence [for a hard snowball] is getting stronger and stronger." He cites oxygen isotope findings published last year supporting the existence of extremely high atmospheric carbon dioxide concentrations predicted by the hard snowball Still, Hoffman says, "I don't expect to live to see the conclusion on Snowball Earth, though I think I know how it will turn out."

–RICHARD A. KERR

CREDITS: FRANCIS A. MACDONALD

After the volcano. Toba's caldera is today a calm lake.

CREDIT: NICK PEARCE

ARCHAEOLOGY

Of Two Minds About Toba's Impact

OXFORD, U.K.—About 74,000 years ago, Mount Toba on the Indonesian island of Sumatra erupted in the most cataclysmic volcanic event of the past 2 million years. An estimated 2800 cubic kilometers of magma spewed forth, at least 2000 times that ejected during the 1980 eruption of Mount St. Helens. Wind-blown volcanic ash spread thousands of kilometers across Asia, blocking sunlight and triggering what some researchers have called a global "volcanic winter."

How did this gigantic eruption affect modern humans? Did Toba decimate previously thriving *Homo sapiens* populations in Africa and create a genetic "bottleneck" from which our species nearly failed to recover, as advocated by archaeologist Stanley Ambrose of the University of Illinois, Urbana-Champaign, and others? Or was the eruption, albeit dramatic, no match for the survival skills of our ancestors? Debate has raged for more than a decade. And some think the answer lies not in Africa but in Asia, right in the path of the volcano's wrath. If modern humans survived there relatively unscathed, African populations would likely have fared even better. But the resolution hinges on an even more hotly debated question: Was *Homo sapiens* even in Asia at the time?

Key evidence that modern humans might have made it to Asia before the eruption, and that they came through it, comes from excavations since 2003 at Indian sites that show evidence of sophisticated stone tools both above and below the 74,000-year-old Toba ash layers (*Science*, 9 October 2009, p. 224). Many members of the dig team, led by archaeologists Michael Petraglia of the University of Oxford and Ravi Korisettar of Karnatak University in Dharwad, India, think modern humans made both sets of tools.

But these findings conflict with recent mitochondrial DNA (mtDNA) studies suggesting that our ancestors probably left Africa after the eruption—perhaps between 55,000 and 70,000 years ago, according to a paper in the *American Journal of Human Genetics* last June by geneticist Martin Richards of the University of Leeds in the United Kingdom and his co-workers. The mtDNA data make a pre-Toba exodus from Africa "very unlikely," says Richards. If modern humans hadn't reached Asia yet, a different hominin must have made those pre-Toba tools.

At a meeting* here last month on the impact of the Toba eruption, geneticists Stephen Oppenheimer of Oxford and Robin Allaby of the University of Warwick in the United Kingdom provided some maneuvering room for both camps. The timing of the molecular clock is too uncertain to rule out a pre-Toba African exodus, they argued. Genetic data "neither includes nor excludes a pre-Toba exit," Oppenheimer said.

The archaeological evidence remains equivocal too, although Petraglia's team presented several papers at the meeting that may bolster their case. For example, the ▶

*Toba Super-Eruption: A Critical Moment in Human Evolution?, 20–21 February 2010, Oxford, U.K.

*Science*Insider

From the *Science* Policy Blog

The Intergovernmental Panel on Climate Change and its parent organization, the United Nations Environment Programme, will request an independent review of IPCC in the wake of unprecedented criticisms of the panel. The terms of reference will be set by the organization that conducts the review. Working Group II co-chair Chris Field told *Science* that a respected scientific organization would be tasked with the job, which he hopes will help end "a crisis of confidence" plaguing IPCC. http://bit.ly/98s]NN

Meanwhile, embattled climate scientist **Phil Jones of the University of East Anglia** gave testimony before the U.K. House of Commons Science and Technology Committee for the first time since roughly 1000 e-mails between climate scientists were made public in late 2009. No new revelations were made under tough questioning from members of Parliament, and lawmakers seemed unmoved by arguments by some that the e-mails undermine the scientific consensus on climate change. http://bit.ly/9vXwBw

A new report suggests that **Britain produces a disproportionately large number of top-ranked scientific publications**, but U.K. researchers are not adept at translating that research into new inventions. http://bit.ly/aZN0is

Some bloggers are up in arms over National Institutes of Health (NIH) Director **Francis Collins's new book**, *Belief: Readings on the Reason for Faith*, which addresses the question "Is there a God?" Collins, an evangelical Christian, has been involved in the past with science-religion outreach but said he would curtail such work when he took his job at NIH. http://bit.ly/c33TSF

The **European Southern Observatory's** telescopes in northern Chile escaped damage from the magnitude-8.8 earthquake that devastated Concepción and nearby towns and villages in the south. http://bit.ly/aiHefn

For the full postings and more, go to **blogs.sciencemag.org/scienceinsider.**

so-called Middle Paleolithic tools below and above the Toba ash at several sites in the Jurreru River Valley of southern India are similar, said archaeologist Chris Clarkson of the University of Queensland in Australia; the tools include sophisticated artifacts such as flakes, blades, points, and scrapers.

Clarkson compared the detailed features of the stone cores from which the Indian tools were made with more than 800 cores made by both modern humans and earlier hominins at other sites. His study, an expanded version of a similar one reported in *Science* in 2007 (*Science*, 6 July 2007, p. 114), found that both the pre- and post-Toba tools clustered with those apparently made by modern humans in Australia, southern Africa, and Southeast Asia, whereas tools made by Neandertals and other nonmodern humans were statistically distinguishable. Clarkson concluded that his study made a "good case" that modern humans were present in India before 74,000 years ago and also supported continuity of modern human occupation before and after Toba's supposed volcanic winter.

Archaeologist Robin Dennell of the University of Sheffield in the United Kingdom calls the study "pretty convincing." Clarkson, Dennell adds, "seems to have found a way of distinguishing tools made by *Homo sapiens* and Neandertals," both of whom made Middle Paleolithic artifacts.

But other researchers think tools alone can't pinpoint the identity of their makers. "Artifacts are not diagnostic of [hominin] species," says Ambrose, who was not at the meeting. Archaeologist Paul Mellars of the University of Cambridge in the United Kingdom agrees; he suspects that Neandertals made the pre-Toba tools. If so, it would be the first sighting of Neandertals in south Asia.

> ***"This is the most important fieldwork in Paleolithic archaeology of the last 10 years."***
>
> **—PAUL MELLARS, UNIVERSITY OF CAMBRIDGE**

As for the dates of the tools, Petraglia's group was struck by a bombshell at the meeting from a member of their own team, geochronologist Richard "Bert" Roberts of the University of Wollongong in Australia. The 2007 *Science* paper cited optically stimulated luminescence (OSL) dates from a site called Jwalapuram locality 3, of 77,000 years just below the Toba ash and 74,000 years just above it, with error margins of plus or minus 6000 to 7000 years. But Roberts presented new OSL dates from nine Indian sites and found that the pre-Toba dates came out at 74,000 years or earlier, as expected, but nearly all of the post-Toba dates were about 55,000 years or younger. These results, Roberts told *Science*, put "a question mark over" the 74,000-year, post-Toba date reported in the *Science* paper.

Roberts obtained the pre-Toba dates by OSL dating of single quartz grains. But the 74,000-year post-Toba date was determined by an Oxford lab using multiple quartz grains, which Roberts considers less accurate. Roberts and the team now plan to redate the sample using the single-grain technique.

Meanwhile, Petraglia's team continues to explore Toba's effects in India. At the meeting, Oxford archaeologist Michael Haslam reviewed the evidence, including the team's studies of the ancient Indian landscape, and concluded that "we can't say that Toba caused anything other than a lot of ash." Humans were able to survive in many refugia—particularly the river valleys where archaeological sites have been found and where ash was more quickly flushed out by water flows, he said. The team's recent studies of carbon and oxygen isotopes in sediments above and below the ash suggest that the pre-Toba mix of woodland and grassland quickly recovered, Petraglia says.

Ambrose agrees that there could have been refugia in India, but not necessarily for modern humans, whom he is not convinced had made it to the region that early. Mellars is also skeptical but says the ongoing Indian digs will help find the answer. "This is the most important fieldwork in Paleolithic archaeology of the last 10 years," he said at the meeting.

–MICHAEL BALTER

ScienceNOW.org

From *Science*'s Online Daily News Site

Early Polar Bear Discovered in Arctic Tundra
Digging in the frozen tundra of Norway's Svalbard archipelago, scientists have uncovered the remains of the most ancient polar bear ever found. DNA analyses reveal that the bear—a mature male—lived about 120,000 years ago, at a time when wooly mammoths were also roaming the land. The work also shows that this bear represents something very rare in the fossil record: an evolutionary snapshot of one species turning into another.
http://bit.ly/earlybear

An Alternative to Insulin?
In 1922, a Toronto teenager with diabetes became the first person to be saved by insulin treatment, and since then injections have sustained millions of diabetics, who don't make their own hormone. But are there alternatives to a lifetime of insulin therapy? A new study suggests that an appetite-suppressing hormone called leptin is just as effective as insulin at controlling diabetes in mice.
http://bit.ly/leptin

Engraved Eggs Suggest Early Symbolism
What does *Homo sapiens* have that our hominid ancestors did not? Many researchers think that the capacity for symbolic behaviors—such as art and language—is the hallmark of our species. A team working in South Africa has now discovered what it thinks is some of the best early evidence for such symbolism: a cache of ostrich eggshells dated to about 60,000 years ago and etched with intricate geometric patterns.
http://bit.ly/eggshells

Global Warming Didn't Kill Golden Toad
The golden toad was last seen in 1989 in the Costa Rican cloud forest of Monteverde—and 5 years later, its disappearance was the first extinction to be blamed on human-induced global warming. New evidence, however, suggests that humans may not have been at fault after all.
http://bit.ly/goldentoad

Read the full postings, comments, and more on **sciencenow.sciencemag.org**.

CREDITS: U.S. FISH AND WILDLIFE SERVICE

NUTRITION SCIENCE

European Food Watchdog Slashes Dubious Health Claims

BRUSSELS—Do antioxidants prevent premature aging? Do dried plums help maintain normal bowel function? Does lutein help your vision; does chewing sugarless gum prevent plaques; and does fermented whey improve gut health?

The answers: No, no, no, no, and no, according to Europe's food safety watchdog, which on 25 February issued a scientific mass-verdict on more than 400 so-called health claims, the promises that food producers make on their labels and in advertisements. The opinions come from the European Food Safety Authority (EFSA), based in Parma, Italy, which also rejected purported health benefits of certain peptides, honey, black and green teas, and a raft of other substances.

The decisions are the latest installment in a gargantuan and controversial effort by EFSA to validate more than 4000 health claims used by the food industry across the continent. More than a year behind schedule, the agency has more than 3000 claims to go—but so far, it has rejected more than 80% of those it has looked at. The food industry may eventually have to stop using those claims.

Some hail the process, required by European Union (E.U.) legislation passed in 2006, as a timely new way to protect European consumers. "Finally, there's a bright scientific light on the somewhat shady world of food and supplements," says nutrition scientist Martijn Katan of the VU University in Amsterdam, the Netherlands. But many in the food industry and some academic researchers say that EFSA has put the scientific bar so high that it may stifle food research in the long run.

In the past decade, European companies have invested millions in so-called functional foods that they say offer health benefits; if EFSA rejects most of their claims, research on such products may lose its appeal. "I'm getting really worried about all the rejections," says Glenn Gibson, a food microbiologist at the University of Reading in the United Kingdom who studies probiotics, or "healthy bacteria"—an area in which EFSA has so far rejected every claim it has reviewed. "My ultimate concern is that much of the food research in Europe will be lost." Some company representatives vented their frustration at EFSA at a meeting here last week organized by Cantox Health Sciences International, a company that helps food and supplement producers prepare their dossiers for the regulatory mill.

The high rejection rate is partly an artifact of the way the regulation was set up—a typical, tortured E.U. compromise. Member countries wanted to ensure an easy way through the process for food components already known to contribute to some function of the human body—such as vitamin C and iron. Under Article 13.1 of the regulation, such "function" claims can be filed with just a list of scientific references as evidence.

But rather than "regulation-lite," Article 13.1 has become a graveyard of health claims. Except for cases that are literally in the textbooks—mostly vitamins and minerals—EFSA found that there was little consensus. Judging the claims was often "very difficult" because they were poorly stated and the literature cited was often incomplete or irrelevant, says nutrition scientist Albert Flynn of University College Cork in Ireland, the chair of the 21-member Panel on Dietetic Products, Nutrition and Allergies, which issues the rulings. Nigel Baldwin, a regulation specialist at Cantox, says the 13.1 procedure, forced upon EFSA by the E.U. bureaucracy, was flawed from the beginning.

There is another way through the maze. Applicants can make their arguments for a product in a full scientific dossier—including a narrative about why they think it works and some products rejected in the first round may yet win approval by this path, says Flynn. But industry observers say that the EFSA panel is putting the bar very high here, too. The panel puts little stock in animal studies, for instance, and as for human data, it heavily favors randomized, controlled, blind clinical trials, which are far less common in nutrition than pharmaceutical research.

A big company recently stumbled, for example, even though it came with clinical data. On 4 February, EFSA rejected Danone's claim that Immunofortis, a mixture of oligosaccharides added to infant formula, strengthens babies' immune systems. "There's 10 years of science behind this product," says Danone spokesperson Agnès Berthet-d'Anthonay; indeed, the company had 30 studies, including 25 with human data, to prove it. But the panel was unimpressed. Only one trial in 259 infants addressed the benefit directly, it concluded, but it had "considerable weaknesses": it wasn't clear how infections had been diagnosed, for instance. Danone is still awaiting a verdict on several other claims, including its probiotic drinks Actimel and Activia.

Katan disputes that the EFSA panel is particularly stringent. "This is not draconian. It's just standard, mainstream science," he says. The industry's problem is that convincingly proving a benefit is extremely difficult. Because many ingredients can't be patented, the sector can't afford the kinds of large, rigorous studies that the pharmaceutical industry funds.

Does it work? Regulators have yet to decide whether Danone's Actimel "helps strengthen your body's natural defenses," as the company claimed

EFSA Senior Scientific Officer Juliane Kleiner also insists that the agency's scientific assessments aren't more demanding than, say, those of the U.S. Food and Drug Administration (FDA). But analysts point out that several features in the U.S. system make life easier for companies. As a result of a freedom of speech lawsuit, for instance, FDA also admits "qualified claims" for food products when there's some evidence but no scientific consensus. (A label could say, for instance, that there is "limited evidence" that a product may reduce the risk of disease.) The E.U. system doesn't allow that way out.

It may be years before health claims actually start disappearing from labels and TV commercials, however. EFSA can't ban their use itself, that's up to the European Commission and the European Parliament, which have yet to decide what to do with most of the rejections. E.U. politicians are subject to intense lobbying by the industry to soften the blow, Katan says—"but I can't imagine that they'll throw all of these opinions in the garbage bin."

–MARTIN ENSERINK

CREDIT: LUCAS SCHIFRES/LANDOV

GENOMICS

Semiconductors Inspire New Sequencing Technologies

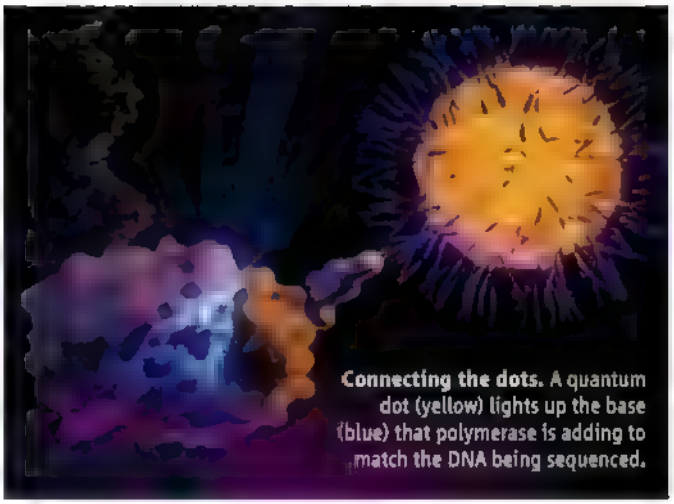

Connecting the dots. A quantum dot (yellow) lights up the base (blue) that polymerase is adding to match the DNA being sequenced.

MARCO ISLAND, FLORIDA—Fifteen years ago, gels and fluorescent dyes lay at the heart of every machine that sequenced DNA. Bases cost a dollar or more to sequence, and deciphering a human genome would take years. The expense of decoding DNA has now plummeted, and new human genomes appear in quick succession thanks to advances in DNA-sequencing technologies and a growing roster of sequencer manufacturers. Whereas one company dominated the industry 6 years ago, about a half-dozen companies now produce DNA-sequencing machines—and novel technologies come onto the scene almost annually. Attesting to this revolution was a packed house at the final Saturday session of a genome meeting here, where silicon wafers and quantum dots were the DNA-sequencing technologies du jour.

Although neither approach is yet able to fulfill the dream of the $1000 human genome, these newcomers have the potential to change the face of DNA sequencing and expand the ability of researchers, and eventually clinicians, to incorporate DNA into their work. "It's pretty exciting that the field has opened up as much as it has," says Elaine Mardis of the Genome Center at Washington University in St. Louis, Missouri. At the same time, labs pursuing a sequencing project face ever more choices and tradeoffs between speed, accuracy, and cost. With so many technologies to choose from, "it's confusing," says Eric Green, director of the National Human Genome Research Institute (NHGRI) in Bethesda, Maryland.

Silicon sequencer. This Ion Torrent chip decodes DNA using voltage detection.

This year's upstart at the annual Advances in Genome Biology and Technology meeting here was Ion Torrent Systems Inc., based in Guilford, Connecticut. Started 2 years ago by Jonathan Rothberg, who founded and sold the sequencing company 454 to Roche in 2007, Ion Torrent offers a DNA-sequencing strategy that's "a radically different proposal," says Edward Rubin, director of the Department of Energy Joint Genome Institute (JGI) in Walnut Creek, California.

In current "next generation" DNA sequencers, such as those made by 454, the machine decodes a strand of DNA by using it as a template to synthesize a matching strand, where base additions are signaled by the emissions of photons of light. A camera records each base, revealing the corresponding one on the template DNA. In most cases, the original DNA must be cut into small pieces that are copied many times over before being sequenced. Those pieces are anchored on beads or slides, and sequencing is done in a massively parallel fashion, achieving rates unthinkable with the gel-based technology used to decode the first human genome.

In contrast, Ion Torrent's sequencer is a silicon chip, built the same way as a semiconductor and etched with an array of nanoscopic wells—400 per the width of a human hair. The wells sit on top of an ion-sensitive layer—a pH meter of sorts—below which is the layer that transmits electrical current. The DNA to be deciphered goes into the wells. Polymerase, the enzyme that builds up a matching strand, is added, along with each of the four different bases, one type of base at a time. When the polymerase finds the right base in the well and attaches it to the new DNA, the reaction releases a hydrogen ion that the chip detects as a voltage change. If the base in the well is wrong and isn't added, no voltage change happens. Then unattached bases are washed out and another type of base is added. Ultimately, the series of electrical pulses recorded by the chip translates into a readout of the DNA being sequenced.

To date, Ion Torrent has sequenced the genomes of only a virus and a bacterium. But according to Rothberg, each took about an hour, 100 times faster than some of the next-generation machines now on the market. At this point, the chip-based system cannot do high-volume sequencing, says NHGRI's Jeffery Schloss, "but it has the potential of filling a very important niche" for small-scale, quick-turnaround jobs.

Rothberg expects to greatly increase the density of the wells and thus the efficiency of sequencing. According to Ion Torrent, its machines will be for sale by the end of the year, priced to put them in reach of many smaller biology labs. "It's one of the best marketed and coolest concepts of where sequencing could potentially go," says Len Pennacchio of JGI.

But it wasn't the only concept to create a buzz at Marco Island. Life Technologies in Carlsbad, California, has in the wings a new strategy aimed at sequencing a single DNA molecule—most other technologies must analyze multiple copies of the DNA to be deciphered. Life Technologies' approach involves tethering a nanocrystal semiconductor called a quantum dot to a DNA polymerase. A laser excites the dot, which then transfers energy to fluorescent dye-tagged bases, but only when the polymerase adds a base to the DNA chain being built from the template being sequenced. A camera detects each added base by the color emitted from its dye, immediately translating that data into the sequence of the template.

At this point, says Joseph Beechem of Life Technologies, the company has tried the technology only on humanmade test DNA strands. And the approach is not perfect, as the quantum-dot nanocrystals blink on and off and might miss a base addition, says Mardis. Still, she and others agree that the technology has the potential to decipher long stretches of DNA in a single sweep. Life Technologies' machine might eventually challenge a single-molecule sequencer produced by Pacific Biosciences, based in Menlo Park, California. But the latter has a head start: At the meeting, it unveiled its first commercial machine with much fanfare, including fireworks on the beach. **–ELIZABETH PENNISI**

CREDITS (TOP TO BOTTOM): COURTESY OF LIFE TECHNOLOGIES CORP AND DIGIZYME INC.; ION TORRENT SYSTEMS INC.

STEM CELLS

Reprogrammed Cells Come Up Short, for Now

Stem cell research offers an ever-shifting battlefield, with vested interests and biologists squabbling over the political, ethical, and scientific merits of different types of cells. Some of the fiercest skirmishes once took place between advocates and opponents of fetal cells. Then along came human embryonic stem cells, opening several fronts, including not-so-civil wars among hES researchers and fans of various adult stem cells. Now two recent papers have dragged the new kid on the block, induced pluripotent stem (iPS) cells, into the fray.

Those papers offer some of the first side-by-side comparisons of human iPS and hES cells as they differentiate into various kinds of cells. In both papers, researchers report that iPS cells can form desired cell types, but they do so with less efficiency than hES cells. Robert Lanza of Advanced Cell Technology, a biotech company based in Worcester, Massachusetts, who co-authored one of the studies, doesn't mince words about iPS cells: "These cells are pretty screwed up," he says.

Not so fast, say other researchers, who contend that not all iPS cells are equal. "The differences are real, but one shouldn't overinterpret them," says James Thomson of the University of Wisconsin, Madison, who is a co-author of the second paper. "When you go back and tweak the conditions, [iPS cells] seem to have the same potential" as ES cells, he says. The differences, Thomson and others explain, are probably due to imperfections in the reprogramming process that occur when scientists activate several genes to convert a differentiated adult cell into an iPS cell. "There's going to be a lot of noise" in the data as scientists work to diagnose and overcome reprogramming's weak spots, Thomson says.

The latest stem cell skirmish started on 12 February with an online paper in *Stem Cells* in which researchers including Lanza and Shi-Jiang Lu of Stem Cell and Regenerative Medicine International, another biotech company based in Worcester, compared the ability of eight human iPS cell lines and 25 hES cell lines to differentiate into several kinds of blood and endothelial cell types. In one test, the hES cells made more than 1000 times more of the desired cells than the iPS cell lines. They also found that, in contrast to cells derived from hES cells, various cell types produced by iPS cells started to undergo cellular aging and programmed death after a short time in culture. Such observations are especially worrisome, Lanza says, as scientists hope to use stem cells in industrial quantities—either for drug testing or for eventual cell therapies. (Most of Advanced Cell Technology's intellectual property portfolio focuses on ES cells and nuclear transfer techniques.)

In the second study, Su-Chun Zhang, Thomson, and their colleagues at the University of Wisconsin, Madison, compared the differentiation of hES and iPS cells into neuronal cells. The two stem cell types behaved very similarly as they became neurons and glia, expressing the same genes at the same time, the researchers reported online 16 February in the *Proceedings of the National Academy of Sciences*. And both hES- and iPS-derived cells acted like normal brain cells in lab tests. But more than 90% of the hES cells responded to the chemical recipe for making neural cells, whereas the iPS cells' response was more variable: In some lines, only 15% of cells turned into neuronal cells, in another, 79%.

In contrast to the Wisconsin group's results, Hans Schöler, a stem cell biologist at the Max Planck Institute for Molecular Biomedicine in Münster, Germany, says he and his colleagues have noticed no differences between ES and iPS cells as they differentiated into neural stem cells. But, he adds, a member of his lab did try unsuccessfully for nearly 3 years to prompt murine iPS cells to form a healthy live-born mouse—the ultimate test of pluripotency that mouse ES cells achieve without a problem. Other groups succeeded, but the efficiency was still low, he notes. In addition, several groups have already reported differences in global gene expression between hES and human iPS cells.

Such observations highlight that cellular reprogramming is still an inexact science. Like Thomson and other stem cell scientists, Schöler thinks that incomplete reprogramming still mars many iPS cells. The first iPS techniques involved using viruses to insert extra copies of reprogramming genes into target cells, but the inserted genes may affect the cells' behavior after reprogramming. Indeed, Lanza says that more-recent studies by his colleagues suggest that cells reprogrammed with newer virus-free techniques are better at differentiating.

Shinya Yamanaka of Kyoto University in Japan, who was the first to successfully reprogram mature mouse cells into iPS cells, says that he has also observed that the differentiation performances of iPS and hES cells vary from line to line. But his lab has not seen systematic differences between the cell types. He and his colleagues are searching for a way to accurately identify more fully reprogrammed iPS cell lines. He predicts that adding additional factors to the reprogramming mix should produce more dependable iPS cells.

Clearly, these findings do not settle the debate, says Miodrag Stojkovic of the Prince Felipe Research Centre in Valencia, Spain. "We're all very excited to work with iPS cells," he says. "But first the science has to determine how they are similar and what is different." **–GRETCHEN VOGEL**

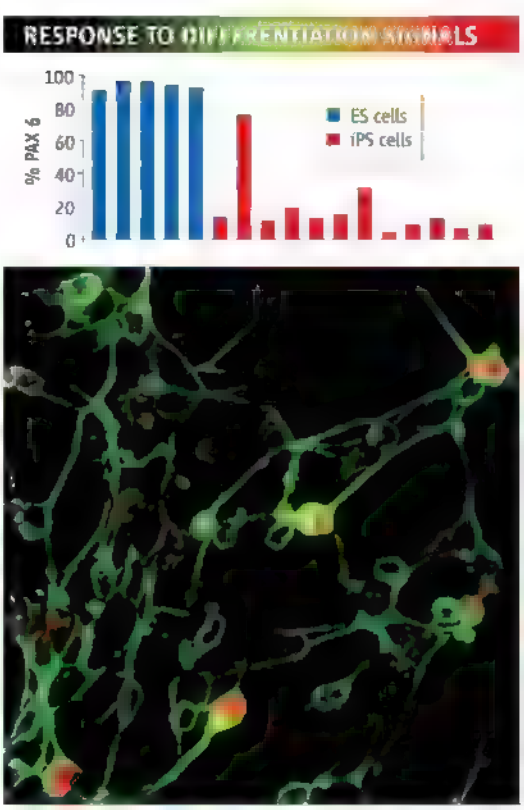

Work in progress. iPS cells can differentiate into functional neurons (*above*), but analysis of PAX6 gene expression shows they are less responsive than human ES cells to neuron-making cues (chart).

Anything But Child's Play

An alternative to juvenile bipolar disorder and a reorganization of autism-related disorders are among the controversial changes proposed for DSM-V

Just a tantrum? Revisions to *DSM* try to define psychiatric conditions without pathologizing children's normal mood swings

CREDIT: LAURENCE MONNERET

DIAGNOSES OF MENTAL DISORDERS IN children and adolescents rose dramatically during the past 2 decades. Juvenile cases of bipolar disorder, once thought to strike only in adulthood, jumped 40-fold between 1993 and 2004 in the United States, according to one widely cited study. Autism estimates leapt from 1 in 1500 to as high as 1 in 90 over a similar time period. Such figures have fueled an intense debate about whether the surge is real or reflects a trend toward overzealous diagnoses and a tendency to pathologize normal youthful behavior.

Against this backdrop, the clinicians and researchers working on revisions to the psychiatrists' bible, the *Diagnostic and Statistical Manual of Mental Disorders* (*DSM*), have been wrestling with how to improve the diagnosis of mental disorders in these age groups. It's not clear how their suggestions, released last month (*Science*, 12 February, p. 770), would affect the prevalence of mental disorders if adopted, but they are already altering the discussion

The most substantial proposals include a reclassification of autism spectrum disorders, a new diagnosis of post-traumatic stress disorder (PTSD) tailored to preschool children, and a brand-new diagnosis called temper dysregulation disorder with dysphoria (TDD) that members of the *DSM* work group hope will stem what they see as a false epidemic of juvenile bipolar disorder.

Reaction to the proposed changes for the fifth edition of *DSM*, slated for publication in 2013, is decidedly mixed. In a recent editorial in *Psychiatric Times*, Allen Frances, a professor emeritus of psychiatry at Duke University in Durham, North Carolina, branded TDD "a new monster." Frances led the previous *DSM* revision and has been a dogged critic of the current revision process. Researchers also disagree about proposals to eliminate several conditions, including Asperger syndrome, and merge them into a single diagnosis of autism spectrum disorder and to stop using IQ scores to grade the severity of intellectual disabilities. "The trouble is that some of these things actually made good sense," says Fred Volkmar, who directs the Yale Child Study Center.

Acting out

For years, researchers have been arguing about the causes and consequences of the explosion of juvenile bipolar disorder (*Science*, 11 July 2008, p. 193). In the mid-1990s, Harvard University psychiatrists Joseph Biederman and Janet Wozniak proposed that many children diagnosed with conduct disorder or attention-deficit hyperactivity disorder (ADHD) may instead have a juvenile form of bipolar disorder. The idea "took the clinical community by storm," says Gabrielle Carlson, director of child and adolescent psychiatry at Stony Brook University School of Medicine in New York state, who is not involved in the current revisions. "What you've got is a lot of kids with very severe problems with explosive outbursts, and the categories that we had to explain their behavior were not very satisfying," Carlson says.

But as the popularity of the bipolar diagnosis grew, Carlson and others became concerned that too many children were being prescribed antipsychotic and mood-stabilizing drugs with serious side effects and unknown long-term effects on the developing brain. They began to question whether bipolar disorder was really the right diagnosis after all. In adults, bipolar disorder is defined by alternating episodes of depression and elevated mood, often typified by grandiose and reckless behavior. That's not what's seen in most children diagnosed with bipolar disorder, says David Shaffer, a child psychiatrist at Columbia University and a member of the *DSM* work group on child psychiatry "What those cases mainly consist of is kids who may or may not be chronically depressed who have intermittent exacerbations when they become extremely irritable and lose their temper," Shaffer says. "We feel quite confident that these kids are a distinct group

. . and [that] it is a disservice to them and leads perhaps to inappropriate treatment to call them juvenile bipolar."

Instead, Shaffer's work group has proposed TDD, which is characterized by "severe recurrent temper outbursts in response to common stressors" accompanied by dysphoria, or persistently negative mood, such as irritability, anger, or sadness.

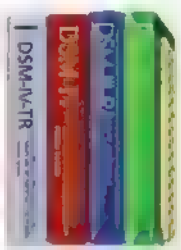

DSM-V
Fourth in a series

"It makes more sense than calling them bipolar, absolutely," says Jon McClellan, a psychiatrist at the University of Washington, Seattle, who is not involved with the *DSM* revisions. For one, McClellan says, it lacks the perceived permanence of a bipolar diagnosis, which in adults carries the expectation of a lifetime of medication and a heightened risk of suicide.

A shift away from bipolar disorder could lead to improved treatment for some patients, says Carlson. For example, she says she sees many children previously diagnosed with bipolar disorder who have untreated ADHD. That's because many psychiatrists are reluctant to prescribe the stimulants used to treat ADHD for fear of provoking a manic episode, Carlson says. That might change if these children's disorders were reclassified.

At the same time, Carlson thinks the new diagnosis of TDD would apply only to about one-third of children who currently receive a bipolar diagnosis. In her view, the requirement of dysphoria makes the diagnosis too restrictive. "Most of the kids aren't like that," Carlson says. "Their mood is fine until they won't do something you ask them to do or won't stop doing something you don't want them to do." Mani Pavuluri, who runs the pediatric mood disorders clinic at the University of Illinois, Chicago, thinks TDD may capture up to two-thirds of children now diagnosed with bipolar disorder. But she sees the potential for trouble if the diagnosis is applied too broadly. McClellan has similar concerns: "It's part of normal childhood to have some temper tantrums," he notes.

Some parents have qualms as well, says Susan Resko, executive director of the Child & Adolescent Bipolar Foundation in Evanston, Illinois. The word "temper" in the name of the disorder reminds some parents of the days when doctors blamed childhood behavioral problems on bad parenting, Resko says: "It conjures images of inept mothers who cannot control their bratty kids." Her group is lobbying for "mood" or "affect" to be used instead. Whatever it comes to be called, however, Resko says she's hopeful that the new diagnosis will foster more research on these kinds of problems.

Fewer distinctions

Also contentious is the proposal for *DSM-V* to combine autism spectrum disorders. *DSM-IV* contained separate diagnoses for autism, Asperger syndrome (considered by many to be a milder form of autism), childhood disintegrative disorder, and the catchall diagnosis of pervasive developmental disorder not otherwise specified. These distinctions attempt to "cleave meatloaf at the joints," the neurodevelopmental work group writes in explaining its rationale on the *DSM-V* Web site (www.dsm5.org). "Behaviorally, these groups cannot be distinguished … except in terms of severity," says group member Catherine Lord of the University of Michigan, Ann Arbor.

The elimination of Asperger syndrome has offended some advocates, who take pride in a diagnosis associated in popular culture if not clinical fact with socially awkward but brilliant figures such as Albert Einstein and Andy Warhol. People can continue to identify themselves as having Asperger, says Lord: "We don't want to take that away, but what we're saying is that scientifically it isn't a reliable diagnosis."

Lord's group also proposes doing away with using IQ to grade the severity of mental retardation, which would now officially be renamed intellectual disability, terminology long preferred by advocates. As with autism spectrum disorders, the group's rationale was that the existing demarcations artificially carve up what is really a continuum.

But those distinctions—both in autism and intellectual disability—have practical value for clinicians and researchers, says Volkmar. "You can argue that these [IQ] tests aren't very precise, but the other side of it is that a person with an IQ of 20 has substantially different needs than someone with an IQ of 65," Volkmar says. He also worries that the elimination of distinctions could complicate research, making it difficult to compare studies that use the new criteria with older studies. Volkmar resigned in frustration from the *DSM-V* work group on neurodevelopmental disorders last year. "There's an apparent lack of peer-reviewed data to justify these changes," he says.

Childhood trauma

The new PTSD diagnosis for preschool children (age 6 or younger) seems to have sparked less debate. It's based largely on studies led by Michael Scheeringa of Tulane University in New Orleans, Louisiana. "Very young children who are severely traumatized develop lots of post-traumatic symptoms, but very few meet the criteria for PTSD" outlined in *DSM-IV*, says Charles Zeanah, a child psychiatrist at Tulane who collaborates with Scheeringa and served on the *DSM* work group for childhood disorders. Adults often describe reliving the traumatic event in flashbacks, for example, but children may not be able to verbalize this, Zeanah says. "What's clear is that they will repeatedly reenact their trauma during play."

Similarly, an adult suffering from PTSD following a car accident is likely to exhibit an aversion to driving or riding in a car, but a child may have no choice to get in the car when told to by his or her parents. The new diagnosis explicitly lists play reenactment as a possible symptom and makes avoidance behavior a possible symptom rather than a requirement, as it is for adults.

Under the umbrella. This boy with autism and others with less severe disorders would fall under one diagnosis in *DSM-V*.

Helen Egger, a child psychiatrist at Duke, supports the new diagnosis. She says epidemiological studies by her group and others suggest that about one-third of very young children with PTSD don't meet the *DSM IV* requirements for a PTSD diagnosis but would meet the new criteria. "Of all the changes that are proposed, this is one that has some good evidence backing it up." **–GREG MILLER**

PHOTO L. REDIT © ABRAHAM MENASHE INC./PHOTOTAKE/NEWSCOM

ASTRONOMY

Unwinding the Milky Way

For a generation, researchers have sought clues to our galaxy's origins in the rare stars whose compositions most closely approach the purity of the primeval universe

As Beatriz Barbuy explains it, she took up astronomy because she couldn't handle philosophy. With a philosopher father and a sociologist mother, Barbuy grew up in São Paolo, Brazil, amid a background hum of intellectual debate. But when she tried to read Hegel as a teenager, the German thinker's ruminations on mind, spirit, and logic made Barbuy's head spin. Instead, Barbuy found inspiration in the Russian cosmologist George Gamow's classic popular-science book *One, Two, Three . . . Infinity*. She asked for a telescope for her 16th birthday and took to rising at 4 a.m. to gaze at the stars.

Growing up in Göttingen, Germany, 2 decades later, Anna Frebel, too, was fascinated by "glowing gas balls up in the sky." And the same fascination led Daniella Carollo to spend hours perched on the balcony of her house in Turin, Italy, neck craned skyward, at the age of 9. "I simply couldn't stop thinking about stars and galaxies," says Carollo, who is completing her Ph.D. at Mount Stromlo Observatory in Australia.

Today, all three women are professional astronomers seeking answers to a centuries-old question that has occupied philosophers and physicists alike: How did the Milky Way originate and evolve into what it is today? For decades, researchers have become increasingly convinced that our galaxy did not develop in isolation but rather grew at least in part by pulling in stars and even whole galaxies that formed outside its borders. But which parts of the galaxy are endemic and which exotic? Where did such alien interlopers come from, and when did they arrive?

For answers, Barbuy, a professor at the University of São Paolo; Frebel, a postdoctoral researcher at Harvard University; and Carollo have devoted themselves to finding and studying stars in the Milky Way that contain vanishingly low quantities of elements heavier than hydrogen and helium. Most of the universe's hydrogen and helium came into being within a few hundred thousand years after the big bang. But heavier elements—sweepingly referred to as "metals"—form by nuclear reactions inside stars and have been steadily building up in the cosmos for billions of years. As a result, astronomers infer that low-metallicity, or "metal-poor," stars formed in the distant past and thus can serve as a fossil record of the events that shaped our galaxy billions of years ago.

Burning slowly. A group led by Anna Frebel (*left*) has spotted a metal-poor star in the Sculptor satellite galaxy that is about 13 billion years old and resembles stars on our galaxy's fringe.

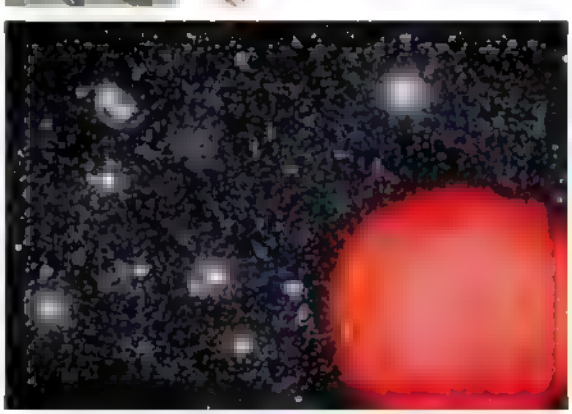

In the late 1980s, for example, Barbuy found chemical evidence that metal-poor stars in the Milky Way's halo—the huge, diffuse ball of stars that surrounds and dwarfs the galactic disk—formed in the wake of explosions of massive progenitor stars known as type II supernovae. The work reaffirmed the usefulness of metal-poor stars as a tool for stellar archaeology and prompted a push to find stars of ever-lower metallicities to reach further back in time.

In recent years, Frebel and her colleagues have done exactly that by discovering metal-poor stars in the Milky Way dating back to within a few hundred million years of the big bang. This week in *Nature*, Frebel and two co-authors report finding such a star, a slow-burning red giant nearly 13 billion years old, in the Sculptor Dwarf Galaxy—a satellite galaxy to the Milky Way. And in a recent paper published in *Astronomy and Astrophysics*, Barbuy and colleagues have used metallicity analysis to identify what could be the most ancient globular clusters in the central bulge of the Milky Way.

From these and other findings, researchers are starting to piece together how our galaxy grew from the assembly of smaller galaxies. "The picture is growing more richly detailed as we go along," says Jason Tumlinson, a theorist at the Space Telescope Science Institute in Baltimore, Maryland.

Alien invaders

The reason astronomers favor the Milky Way galaxy, simply enough, is that they have ringside seats. Although advanced telescopes can see out to the edge of the universe, researchers can get "relatively little information" from those images, notes Timothy Beers, an astronomer at Michigan State University (MSU) in East Lansing. "They'll have colors of stars, maybe some

CREDITS (TOP TO BOTTOM): NASA, JPL-CALTECH; COURTESY OF ANNA FREBEL; DAVID AGUILAR, CFA

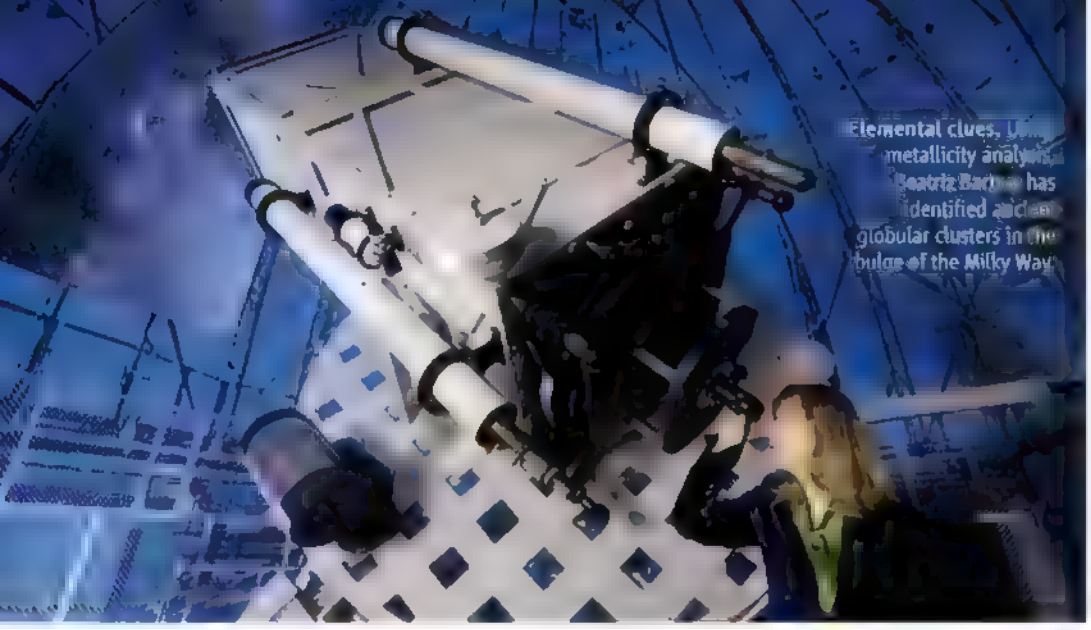

Elemental clues. [illegible] metallicity analysis [illegible] has identified ancient globular clusters in the bulge of the Milky Way.

CREDIT: MICHELINE PELLETIER/FONDATION L'ORÉAL/IAU

kind of spectral signature," he says. "In the Milky Way, we can get enough information that we can tell the whole story."

That story has been evolving. In the 1960s, when Barbuy was still a schoolgirl stargazing from the top of a plum tree in her parents' garden, astronomers theorized that the Milky Way had originated from the rapid collapse of a gigantic cloud of gas and dust. In this "monolithic collapse model," the galaxy formed over a few hundred million years more or less in one piece. In 1978, Leonard Searle of the Carnegie Observatories and Robert Zinn of Yale University proposed a different idea: that the Milky Way didn't come together all at once but had gradually "accreted" by the merger of smaller structures—a process that is continuing today. This accretion scenario has become the dominant model of our galaxy's evolution.

Barbuy, who was in graduate school when Searle and Zinn's paper appeared, has focused mainly on the history of star formation well inside the Milky Way. For her doctoral research at the University of Paris, she developed a more sensitive method of measuring trace elements in star spectra and used it to determine that most metal-poor stars in the halo have a high ratio of oxygen to iron. In 1987, 5 years after finishing her doctorate, Barbuy confirmed that finding with observations at the European Southern Observatory's Very Large Telescope in northern Chile. "I was lucky to get to observe for 7 nights in a row," she says.

From the high oxygen-to-iron ratio, Barbuy inferred that the metal-poor halo stars had formed from material blasted into space by type II supernovae—the most efficient process for producing oxygen. Type II supernovae are the death throes of stellar objects 10 to 500 times as massive as the sun and made up of almost pure hydrogen and helium. Because the high pressures inside such stars give them extremely short life spans of only a few million years, those precursor stars had to have exploded early in the galaxy's history. Barbuy's result confirmed that metal-poor stars were reliable markers of the past. The work helped nail down a key piece of the Milky Way's evolutionary puzzle: the conditions under which the earliest generations of more lasting, stable stars had formed.

In the 1990s, Barbuy and colleagues turned their attention to the bulge at the center of the Milky Way. By measuring the oxygen-iron ratio of hundreds of stars, they identified collections of stars known as globular clusters that were more than 10 billion years old. At the time, they were the oldest globular clusters to be discovered in the bulge; Barbuy has since found even older ones. The age of the clusters suggested that the bulge of the Milky Way—or at least parts of it—had formed early on in galactic history.

New twists in the plot

Meanwhile, stellar metallicity was helping other researchers probe broader questions of the Milky Way's evolution. A key recent insight has come from the work of Carollo. Carollo came to low-metal stars by chance. After finishing the Italian equivalent of a master's degree in physics, she took a staff position at the Turin Observatory. But she says she felt stifled there and began writing to astronomers at institutes around the world in search of other research projects. When Beers offered her a stint as a visiting researcher in his group at MSU, Carollo jumped at the chance. When she arrived, she says, Beers gave her a data set of some 20,000 stars from the Sloan Digital Sky Survey (SDSS) and said "Work on it"—that is, check how metallicity varied in this population.

Measuring the velocity and the metallicity of individual stars, Carollo saw a pattern. In the inner parts of the Milky Way's halo—about as far out as the edge of the 100,000-light-year-wide galactic disk—stars of relatively high metallicity traveled around the galactic center clockwise, the same direction as the disk itself. Farther out, however, the most metal-poor stars in the halo were moving counterclockwise. In a 2007 paper in *Nature*, Carollo, Beers, and their colleagues reported this finding as evidence that the halo has two counter-rotating components—an inner halo and an outer halo—that formed at different times.

The discovery, which Tumlinson calls a "gem," gave a fillip to the idea of galactic mergers, which had been gaining ground since Searle and Zinn proposed it 3 decades earlier. "The outer halo is most likely associated with the debris of what are probably ancient dwarf galaxies that have been torn up as they merged with the core of the Milky Way," Beers says. The researchers say an analysis of a larger sample of stars, in press at the *Astrophysical Journal*, confirms their interpretation.

A recent discovery, reported this week in *Nature*, supports that view of the galaxy's outskirts. Lead author Frebel, a young astronomer with a knack for finding ancient stars, reports that she and colleagues have identified an extremely metal-poor red giant star about 13 billion years old in the Sculptor Satellite Galaxy. The star, christened S1020549, has a chemical profile very similar to that of extremely metal-poor stars in the outer halo of the Milky Way. "If the outer halo was assembled from accreted dwarf galaxy stars, you would exactly expect such a chemical similarity," Frebel says.

Despite such recent advances, researchers still have far to go in piecing together the galaxy's history, notes Roger Cayrel, an astronomer at the Paris Observatory who has had an ultra–metal-poor star named in his honor. "In an accretion assembly scenario, we would like to be able to have a complete list of the events with the epoch of occurrence, the mass and former chemical evolution of each accreted small galaxy, and so on," he says.

The answers may lie in the multitude of low-metal candidates identified in the SDSS. "The high-resolution follow-up of SDSS stars is just starting," Beers says. "My expectation is that the numbers of low-metallicity stars will be greatly expanded." That should help develop an account of Milky Way formation that's sufficiently rich and precise to make astronomers proud and philosophers envious.

–YUDHIJIT BHATTACHARJEE

The Ins and Outs of HIV

Researchers first isolated HIV 27 years ago and arguably know more about how it behaves than they do any other virus. But presentations here challenged the most basic notions of how HIV enters and exits cells.

As landmark studies first revealed in 1996, HIV initiates an infection by binding to two receptors on the cell surface (*Science*, 10 May 1996, p. 809). But how that bound HIV then penetrates the cell membrane has remained murky. Many researchers believed that HIV sticks a protein into the cell membrane and then directly fuses with it. But HIV—and other viruses that have an outer coat made from a mishmash of its own proteins and cellular membrane—can enter via endocytosis.

In endocytosis, the membrane invaginates and pinches off to form an endosome—a bubble of membrane with the virus inside. The virus fuses with the endosome only after the bubble is floating in the cell. Biophysicist Gregory Melikian of the Institute of Human Virology at the University of Maryland School of Medicine in Baltimore presented provocative evidence that HIV primarily relies on the endocytic pathway.

In test tube studies with HIV and human cells, Melikian introduced a peptide that blocks direct fusion with the cell membrane. If endocytosis was a primary mechanism, the viruses already inside of endosomes could dodge the peptide. As a control, he used low temperature to block both direct fusion and fusion that occurs inside endosomes. Low temperature blocked fusion more potently than the peptide, indicating that many viruses were inside of endosomes and could proceed with the infection process. The block on direct fusion had no impact on the virus inside endosomes.

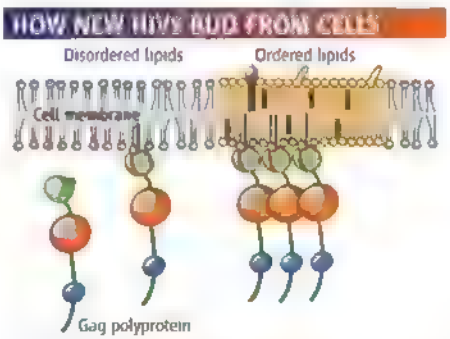

Self-coated. HIV selects specific lipids from membranes as it leaves the human cell.

This doesn't rule out the possibility that some virus enters by direct fusion, but in another experiment, Melikian made movies in which he labeled the virus with a fluorescent protein and recorded the infection process. HIV readily fused with the endosomes and initiated an infection, while the process of direct fusion aborted before the virus could unload its genetic cargo into the cell. In all, these data suggest that "the overwhelming majority of viruses are entering through endocytic pathways," Melikian concluded. "And with endocytosis, you hide the virus much sooner, narrowing the opportunities for antibodies."

Virologist Hans-Georg Kräusslich of the University of Heidelberg in Germany, whose lab first showed the importance of HIV endocytosis in 2004, said Melikian's work "certainly takes it further" but cautioned that it remains controversial whether that mechanism is an exclusive entry route.

Kräusslich presented data that tackled the other, often ignored end of the process: how HIV exits cells. "People thought the virus simply blebs out," said Kräusslich. "It doesn't. The virus controls the process." Over the past 6 years, Kräusslich's lab, along with several other groups—including Eric Freed of the U.S. National Cancer Institute in Frederick, Maryland; Michael Summers of the University of Maryland, Baltimore County; and Wes Sundquist of the University of Utah in Salt Lake City—have shown in exquisite detail

Treatment as Prevention

An ambitious idea to slow the HIV/AIDS epidemic is gaining traction. Test everyone for the virus and immediately start all HIV-infected people on treatment. But the test-and-treat scheme has epidemic modelers battling it out, with some insisting it's feasible, both financially and practically, and others denouncing it as a pipe dream and warning that it could increase drug resistance. At the meeting, two groups presented some of the firmest data yet to support the concept.

Although it's logical that if drugs reduce the amount of virus in individuals (the "viral load"), they then become less likely to transmit HIV, until now, the population data supporting the idea has remained sparse. Deborah Donnell of the Fred Hutchinson Cancer Research Center in Seattle, Washington, described a study of 3381 "discordant" heterosexual couples in seven sub-Saharan countries in which only one partner was infected with HIV at the outset. Over 2 years, Donnell and co-workers analyzed 103 new infections in which they could prove through genetic sequencing that the infecting virus came from the person's long-term partner. Of these, only one person who became infected had a partner who was receiving anti-HIV drugs, showing that treatment reduced the risk of transmission by 92%. "I think it's the single most important presentation here," said virologist Mark Wainberg of McGill University in Montreal, Canada.

Others cautioned that treatment might not have as powerful an effect with other transmission routes. But Julio Montaner, a key proponent of test-and-treat who directs the B.C. Centre for Excellence in HIV/AIDS at the University of British Columbia, Vancouver, in Canada, presented compelling data from one of the most susceptible groups, injecting drug users (IDUs). Test-and-treat is more feasible and possible to track in Canada because it has a national medical system with centralized, local control, he added.

Earlier, Montaner's group showed that as

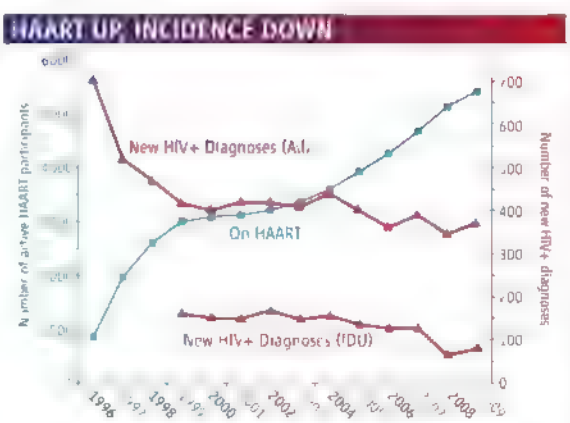

All together now. As more people received highly active antiretroviral treatment (HAART) in British Columbia, new infections plummeted, even in IDUs.

CREDITS (TOP TO BOTTOM): MICHAEL F. SUMMERS/HHMI/UMBC; JULIO MONTANER/BC CENTER FOR EXCELLENCE IN HIV/AIDS, MODIFIED FROM MONTANER *ET AL.* CROI 2010

the structure and function of HIV's Gag polyprotein, which orchestrates the exit process with help from the cell

Cell membranes consist of two sheets of many different types of lipids, including cholesterol. Kräusslich showed that new virions do not—as cartoons used by many in the field often suggest—bleb through the membrane and then randomly dress themselves in a coat made of these cellular lipids. Rather, HIV's Gag selects specific lipids to form the viral coat.

The lipid bilayer has two microdomains with different degrees of rigidity. The more rigid microdomain is "ordered" into "rafts" of regularly packed lipids that are straight and lined up like soccer players forming a wall to block a penalty kick. The other one is "disordered" with lipids that have kinks in them (see illustration). Gag selects lipids in the rafts—in particular, favoring one called PIP for short or gathers other lipids to form its own rafts.

Using fluorescence microscopy, Kräusslich's lab showed the process of budding and release, detailing how the virus co-opts cellular proteins to pinch itself off from the cell. "What's remarkable about these new studies is what appeared to be such a simple process is so complex, and it shows how this virus interacts intimately with the machinery of the cell," said molecular virologist Nathaniel Landau of New York University School of Medicine in New York City. "It's one of the major advances in understanding HIV molecular biology."

–JON COHEN

2500 people started antiretroviral drugs (ARVs) between 1996 and 1999, new infections in their steadily expanding testing program dropped by 50%. The analysis presented here examined data from 2004 to 2009, when the number of treated people doubled to about 5000; many were IDUs. New infections fell, and although the drop wasn't as dramatic as before, there was a concomitant decline in viral load in the treated people. A subset analysis of IDUs also showed a particularly sharp reduction in new infections.

Several studies around the world will soon begin to evaluate the test-and-treat strategy. "It's a very challenging concept," said Anthony Fauci, head of the U.S. National Institute of Allergy and Infectious Diseases (NIAID) in Bethesda, Maryland, who described obstacles, including the feasibility of conducting widespread, voluntary testing. But NIAID is funding a study of the concept at two U.S. sites that will start in June. "It's a bold, high-risk but high-return project that we are going to push the envelope on," said Fauci. **–J.C.**

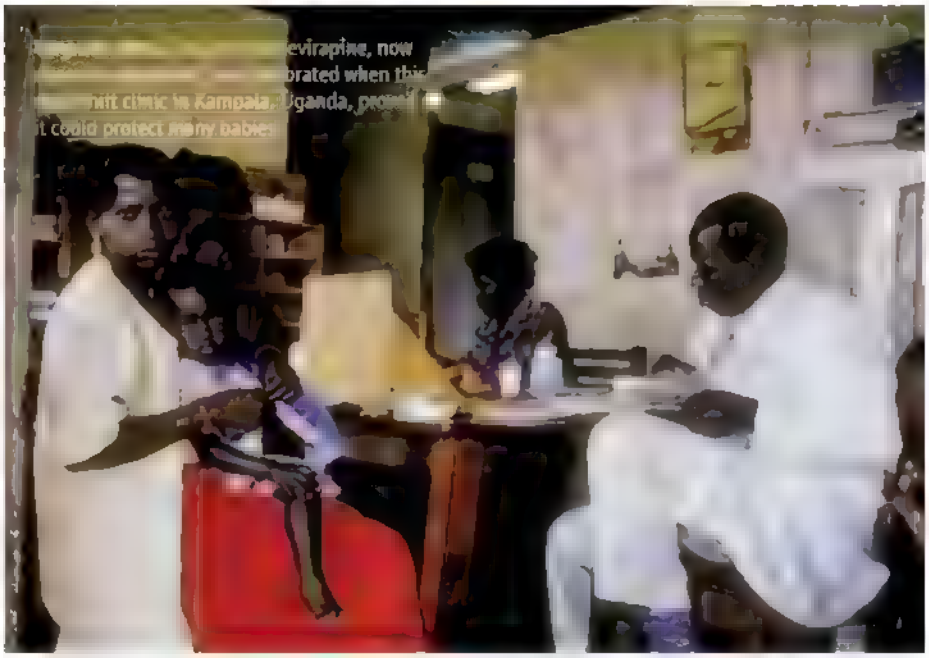

CREDIT: MALCOLM LINTON

Limits of Success

Huge disparities in access to proven methods to thwart HIV still exist between rich and poor countries. Prevention of mother-to-child transmission (PMTCT) efforts are a case in point, explained pediatrician Elaine Abrams of Columbia University. In wealthy countries, where HIV-infected pregnant women receive cocktails of antiretroviral drugs (ARVs) and do not breastfeed, fewer than 2% transmit the virus to their babies. That's a drop from as high as 40% of the women who receive no treatment and breastfeed. "New pediatric infections have virtually been eliminated," said Abrams. "In contrast, the pediatric epidemic rages overseas." According to the best estimates, 480,000 babies worldwide became infected in 2008, with a mere 21% of pregnant women receiving an HIV test and only 45% of those who tested positive receiving drugs to prevent infection—and that treatment was often suboptimal.

The most commonly used intervention for PMTCT in developing countries is a single dose of the drug nevirapine given to the mother in labor and the baby at birth. This strategy, which first proved its worth in a Ugandan study that ended in 1999, is cheap and simple and cuts transmission rates in half—and, before the arrival of cheap ARVs, it was the only option for many poor women. But, said Abrams, abundant data now show the dangers of the "overreliance on single-dose nevirapine." Not only are cocktails of ARVs more effective at preventing transmission, but as many as 50% of pregnant, infected women have suffered severe immune destruction and need combination treatment for their own health. What's more, the single dose of nevirapine fuels the emergence of resistant strains, compromising the ability of mothers and their babies, if they do become infected, to benefit from that entire class of drugs—a key component of cocktails in developing countries.

Some countries now add another ARV or two for a short time before labor and during breastfeeding to reduce the risk of resistance emerging, and even when resistance does develop, it wanes over about a year's time. Still, the different standards of care for poor and rich are unacceptable, many researchers said at the meeting. "Our responsibility is to come up with consistent, across-the-board ARV recommendations," said pediatrician Arthur Ammann, who heads Global Strategies for HIV Prevention, a nonprofit based in San Rafael, California, that does PMTCT in the Democratic Republic of the Congo and Liberia.

Catherine Wilfert, a pediatrician emeritus at Duke University in Durham, North Carolina, stressed that the costs of ARVs are not the main roadblock. "The real funding challenge is the training," said Wilfert.

But if single-dose nevirapine is the only option available, it remains much better than doing nothing, said infectious disease specialist Nicholas Hellman, who heads medical and scientific affairs at the Elizabeth Glaser Pediatric AIDS Foundation: "We have to be careful not to throw out the baby with the bath water." **–J.C.**

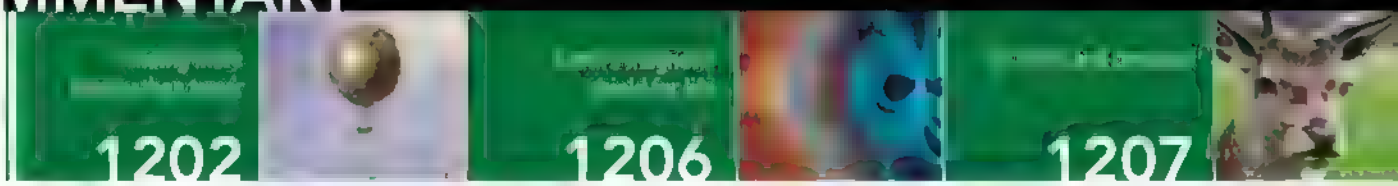

LETTERS

edited by Jennifer Sills

A Greener Future for China's Cities

IN THEIR PERSPECTIVE "CLEAN AIR FOR MEGACITIES" (30 OCTOBER 2009, P. 674), D. D. Parrish and T. Zhu highlighted the opportunities and challenges that exist for megacities to address air quality and climate change issues. In China, only 60.5% of the 287 large cities monitored in 2007 had air quality that met the standard of the Ministry of Environmental Protection of China (*1*). However, there is encouraging evidence that China is striving to build more low-carbon cities. In early 2008, the World Wildlife Fund collaborated on pilot programs with Shanghai and Baoding, focusing on how to implement low-carbon development in China's urban areas (*2*). Afterward, Beijing, Shanghai, Tianjin, Shenyang, Wuhan, Hangzhou, and Shenzhen all laid out their respective low-carbon road maps (*3*–*6*).

The World Exposition Expo to be held in May 2010 will offer a glimpse of a greener future for Shanghai. During the construction of the Shanghai Expo Park, energy use efficiency and low greenhouse gas emissions were prioritized in activities such as planning, building, and transportation. For example, 4.5 MW integrated solar systems will be used to power buildings in the Expo Park. The use of this clean power is expected to save an estimated 4100 tons of carbon dioxide emissions annually, compared with coal-fired electric power (*7*).

Addressing air pollutants and climate-forcing agents in Chinese cities will require strategic urban planning, large-scale inputs of finances and technology, new regulations, and lifestyle changes. The carbon emissions during the development of low-carbon cities (mostly existing district-level and larger cities) must also be taken into account. New regulations (*8*) have recently been issued in China to eradicate the corrupt inflation in statistics (*9*) associated with the development of low-carbon cities. If these are carefully implemented, we have every reason to look forward to more low-carbon cities in China.

ZONGMING WANG[1] AND JING MING CHEN[2]*

[1]Northeast Institute of Geography and Agro-Ecology, Chinese Academy of Sciences, Changchun 130012, China
[2]Department of Geography, University of Toronto, Toronto, ON M5S 3G3, Canada

*To whom correspondence should be addressed. E-mail: chenj@geog.utoronto.ca

References and Notes

1. B. Fu, *Science* **321**, 611 (2008)
2. WWF China, "Shanghai and Baoding to become China's low-carbon city pilots" (2008); www.wwfchina.org/english/loca.php?loca=502
3. Xinhu News Agency, "Beijing established carbon sequestration office" (Xinhua News Agency News, 2010); http://news.xinhuanet.com/fortune/2010-01/26/content_12875941.htm [in Chinese]
4. China Government Affairs Net, "Building low-carbon cities: Race each other" (China Government Affairs News, 2009); www.ccgov.net.cn/aspx/zzNewsdata.aspx?id=5377&cateid=30 [in Chinese]
5. Agency of China Economy Times, "Establishment of low-carbon cities in Shanghai, Hangzhou, etc." (China Economy Times, 2009); www.zjjmw.gov.cn/qgjmxx/2009/12/17/2009121700005.shtml [in Chinese]
6. Xinhu News Agency, "Shenzhen are exploring new development pattern" (Xinhua News Agency News, 2010); http://news.xinhuanet.com/politics/2010-01/17/content_12822879.htm [in Chinese]
7. Xinhu News Agency, "Low-carbon-emission technologies will become highlights of the World Expo 2010 Shanghai" (Xinhua News Agency News, 2009) http://news.xinhuanet.com/tech/2009-10/30/content_12361624.htm [in Chinese]
8. J. Liu, H. Yang, *Science* **325**, 675 (2009)
9. Xinhu News Agency, "Investigation and consideration on construction of low-carbon cities in China" (Xinhua News Agency News, 2009), http://news.xinhuanet.com/fortune/2009-09/16/content_12063569.htm [in Chinese]

We acknowledge support from the key project of the Chinese Academy of Sciences (grant KZCX2-YW-341)

CREDIT: WIKIMEDIA COMMONS

Bioenergy: Counting on Incentives

THE SUGGESTION BY T. D. SEARCHINGER *et al.* ("Fixing a critical climate accounting error," Policy Forum, 23 October 2009, p. 527) to account for CO_2 by "tracing the actual flows of carbon" appears to promote an approach to carbon accounting in which emissions and removals from a forest are determined on the basis of gross atmospheric fluxes between the forest, or forest products, and the atmosphere. This contrasts with the current "stock-change" approach, in which the annual removals or emissions from a country's forest are assumed to be equal to the net change in carbon stocks in biomass and soils of the forest estate.

We share the concern of the authors that a "critical climate accounting error" exists within the Kyoto protocol and could undermine greenhouse gas (GHG) reduction goals. However, we feel that their solution would create new, unintended disincentives for the sustainable use of biomass.

The practical problem in the current accounting framework is that some countries do not have commitments under the Kyoto Protocol, and they are therefore not obliged to account for emissions from loss of terrestrial carbon. Furthermore, some countries with commitments choose not to account for some sources of emissions (for example, conversion of natural to managed forest, conversion of grassland to cropland). Therefore, loss of carbon stock associated with the supply of biomass for bioenergy may not be accounted for

Applying the atmospheric-flow accounting approach would not solve this problem. The importing country would account only for the carbon contained in the biomass used for bioenergy, even though the carbon stock losses in the cleared forest, especially if growing on peatland, could be many times greater than the quantity of carbon contained in the imported biomass (*1*). Replacing the current stock-change accounting approach with the proposed atmospheric-flow–based accounting approach would also lead to unintended incentives. For instance, combustion of biomass may appear in national GHG accounting with higher CO_2 emissions than coal combustion (because the energy content per unit of carbon is higher for coal than for biomass), even if biomass is harvested on a sustainable basis without reducing the biological carbon stock. This would make all imported bioenergy uncompetitive with fossil fuels. The negative impacts of the atmospheric-flow approach have been discussed in depth (*2*–*5*); the conclusions favoring a stock-change based approach, which is applied in the existing GHG accounting framework, remain valid. Rather than abandoning the current approach and implementing the atmospheric-flow based strategy that they advocate, we suggest retaining the existing stock-change–based accounting framework for biomass while extending the end-user's responsibility to include the terrestrial carbon stocks.

The "end-user country" would be required to take full or partial responsibility for changes in the terrestrial carbon stocks in the "producer country." Quantifying the change in carbon stocks attributable to bioenergy is difficult, especially given that bioenergy is not the only driver of land-use change. (For example, the food industry is also a rapidly growing market for vegetable oils.) Development of feasible accounting rules is thus a challenging task. However, it is critical that policy measures do not create disincentives for bioenergy from sustainable sources.

KIM PINGOUD,[1]* ANNETTE COWIE,[2]* NEIL BIRD,[3] LEIF GUSTAVSSON,[4] SEBASTIAN RÜTER,[5] ROGER SATHRE,[4] SAMPO SOIMAKALLIO,[1] ANDREAS TÜRK,[3] SUSANNE WOESS-GALLASCH[3]

[1]VTT Technical Research Centre of Finland, Post Office Box 1000, 02044 VTT, Finland. [2]University of New England, Armidale, NSW 2351, Australia. [3]Joanneum Research, Elisabethstrasse 5, A-8010 Graz, Austria. [4]Mid Sweden University, S-831 25 Östersund, Sweden. [5]Johann Heinrich von Thünen-Institute (vTI) German Federal Research Institute for Rural Areas, Forestry and Fisheries, Leuschnerstrasse 91, 21029 Hamburg, Germany

*To whom correspondence should be addressed. E-mail: kim.pingoud@vtt.fi; annette.cowie@une.edu.au

References

1. J. Fargione *et al.*, *Science* **319**, 1235 (2008)
2. B. Lim *et al.*, *Environ. Sci. Pol.* **2**, 207 (1999)
3. UNFCCC, "Estimating, reporting, and accounting of harvested wood products" (Technical Paper FCCC/TP/2003/7, 27 October 2003); http://unfccc.int/resource/docs/tp/tp0307.pdf
4. A. Cowie *et al.*, *Clim. Pol.* **6**, 161 (2006)
5. M. Apps *et al.*, "Accounting system considerations: CO_2 emissions from forests, forest products, and land-use change—A statement from Edmonton" (1997); www.ieabioenergy-task38.org/publications/publication1.htm

Response

PINGOUD *ET AL.* AGREE WITH US THAT A carbon accounting error underestimates greenhouse gas emissions from bioenergy. Our Policy Forum offers a narrower solution than their Letter because we focus on a narrower source of the problem.

Pingoud *et al.* focus on the Kyoto Protocol decision not to limit most land-based emissions, which is equally true of many European and U.S. laws. Just as this decision leaves out most emissions from agriculture and forestry, it also means that emissions from the production and use of bioenergy could potentially exceed those saved from fossil fuels, particularly over decades. This deliberate omission reflects measurement challenges, resistance by landowners, and the difficulty of distinguishing human from natural causes of many land-based emissions. We agree that some increased accountability for land-based emissions would be desirable, but worldwide enforceable limits are unlikely to come into effect soon. Incentives are likely to remain the main tool for reducing land-based emissions.

The decision to exempt most land-use emissions does not require the separate decision to exempt CO_2 emitted by using bioenergy from limits that are applied to energy emissions. Our Policy Forum focuses on the undercounting of net greenhouse gas emissions created by this exemption. Land use is affected because this energy rule incorrectly rewards activities that cut down forests or otherwise reduce carbon stocks to make bioenergy.

CORRECTIONS AND CLARIFICATIONS

News: "Armed and dangerous" by E. Pennisi (Special Section on Food Security, 12 February, p. 804). The potato blight leaf photo showed early blight, not late blight. Late blight is shown here. The image has been corrected in the HTML version online.

Random Samples: "Loading springs" (29 January, p. 507). The term "radioisotopes" should have been "environmental isotopes." Also, K. Shivanna is an isotope hydrologist.

Reports: "$^{238}U/^{235}U$ variations in meteorites: Extant ^{247}Cm and implications for Pb-Pb dating" by G. A. Brennecka *et al.* (22 January, p. 449). There was an error in the numerator of the expression on the left-hand side of Eq. 1. The correct expression is here. $\frac{^{207}Pb^*}{^{206}Pb^*}$

News Focus: "From medfly to moth: Raising a buzz of dissent" by I. Chen (8 January, p. 134). Light brown apple moth larvae have been observed feeding on only around 265 species, not more than 2000 plant species, as the story and photograph caption stated. The higher number is the agriculture agencies' estimate of all potential plant hosts for the pest, including relatives (such as cypress trees) in the same genera as those 265 species. Critics say that the larger figure is unsubstantiated.

TECHNICAL COMMENT ABSTRACTS

COMMENT ON "Movement Intention After Parietal Cortex Stimulation in Humans"

Hans-Otto Karnath, Svenja Borchers, Marc Himmelbach

Desmurget *et al.* (Reports, 8 May 2009, p. 811) applied direct electrical stimulation (DES) to the human cortex to study the origin of movement intention. Their interpretation assumed that DES causes cortical activation, whereas it is possible that it actually evokes deactivation. The lack of certain knowledge about the true effects of DES limits its use for validation of cognitive models.

Full text at www.sciencemag.org/cgi/content/full/327/5970/1200-c

RESPONSE TO COMMENT ON "Movement Intention After Parietal Cortex Stimulation in Humans"

Angela Sirigu, Carmine Mottolese, Michel Desmurget

Karnath *et al.* argue that the behavioral effects observed in our study after direct parietal and premotor electrical stimulation (DES) could reflect a decrease of local cortical activity. If so, intention and awareness would not reflect the activity of the stimulated area but the recruitment of remote regions. Although tenable, this view does not seem to be the most plausible.

Full text at www.sciencemag.org/cgi/content/full/327/5970/1200-d

Our solution is to count the CO_2 from all energy use but then to reward bioenergy to the extent it results from "additional" biomass i.e., carbon that would not otherwise be stored in plants or soils. This approach does not treat liquid and solid biofuels as automatically equivalent to coal but credits them to the extent they truly offset energy emissions. This solution would not control land-based emissions spurred by economic factors or policies, as Pingoud *et al.* would wish, but it would properly count energy emissions and avoid creating inaccurate incentives to clear land and release carbon through the laws aimed at reducing global warming

Letters to the Editor

Letters (~300 words) discuss material published in *Science* in the previous 3 months or issues of general interest. They can be submitted through the Web (www.submit2science.org) or by regular mail (1200 New York Ave., NW, Washington, DC 20005, USA). Letters are not acknowledged upon receipt, nor are authors generally consulted before publication. Whether published in full or in part, letters are subject to editing for clarity and space.

Our proposal does not imply using carbon fluxes instead of stock changes to measure carbon or otherwise change the accounting used in the U N Framework Convention on Climate Change (UNFCCC). Under that approach, emissions from land-use change are counted in the countries where they occur for international reporting purposes, not where timber or crops are consumed. By definition, the "carbon stock" approach can work only in a legal regime like the UNFCCC that counts changes in carbon stock i.e., land-use emissions. The problem we identified is found in laws and treaties that do not legally "count" land-use emissions.

Our modest fix does not require "end-user responsibility" for land-use emissions, as suggested by Pingoud *et al.*, or any other direct or indirect regulation of those emissions. Instead, our approach is about accurately counting energy emissions and offsetting sinks. It treats bioenergy in the same way that the Kyoto Protocol and many other climate laws already treat agricultural and forestry activities. Although most of their land-use emissions are unregulated, land-use activities can only receive credits for offsetting energy emissions when net effects are counted; thus, only "additional carbon" receives credits. The same approach should apply whether the offset involves sequestering carbon in forests or generating biomass for energy

TIMOTHY D. SEARCHINGER,[1]* STEVEN P. HAMBURG,[2]* JERRY MELILLO,[3] WILLIAM CHAMEIDES,[4] PETR HAVLIK,[5] DANIEL M. KAMMEN,[6] GENE E. LIKENS,[7] MICHAEL OBERSTEINER,[5] MICHAEL OPPENHEIMER,[1] G. PHILIP ROBERTSON,[8] WILLIAM H. SCHLESINGER,[7] RUBEN LUBOWSKI,[9] G. DAVID TILMAN[10]

[1]Woodrow Wilson School, Princeton University, Princeton NJ 08544, USA. [2]Environmental Defense Fund, Boston, MA 02108, USA. [3]The Ecosystems Center, Marine Biological Laboratory, Woods Hole, MA 02543, USA. [4]Nicholas School of Environment, Duke University, Durham, NC 27708, USA. [5]International Institute for Applied Systems Analysis, Laxenburg 2361, Austria [6]Energy and Resources Group, University of California at Berkeley, Berkeley, CA 94720 USA. [7]Cary Institute of Ecosystem Studies, Millbrook NY 12545, USA. [8]WK Kellogg Biological Station, Michigan State University, Hickory Corners, MI 49060, USA. [9]Environmental Defense Fund, Washington, DC 20009, USA. [10]Department of Ecology, Evolution and Behavior, University of Minnesota, St. Paul, MN 55108, USA.

*To whom correspondence should be addressed. E-mail: tsearchi@princeton.edu (T.D.S.); shamburg@edf.org (S.P.H.)

HISTORY OF SCIENCE

Romantics in the English Manner

Robert J. Richards

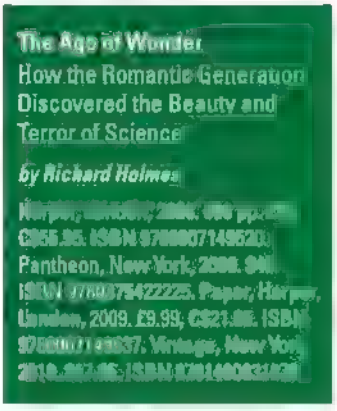

The designation "Romantic science" might refer to a special kind of science or to the particular personalities who engage in science. In *The Age of Wonder: How the Romantic Generation Discovered the Beauty and Terror of Science*, Richard Holmes succeeds admirably in pursing the latter meaning, though he has ambitions also to explore the former. Holmes, a biographer of Shelley, Coleridge, and Dr. Johnson, has woven together several tales of English scientists who ventured to exotic lands, flung themselves into love affairs, and wrote sonnets to science. The likes of Joseph Banks, William and Caroline Herschel, Mungo Park, and Humphry Davy displayed, in the calmer English manner (even if the Herschels stemmed from Hanover), the kind of personalities that discovered the "beauty," if not exactly the "terror," of science. Holmes dishes up the faux terror in his chapter on Mary Shelley's *Frankenstein*, although the wilder opinions of Samuel Taylor Coleridge, who passes through his pages in a drug-induced ramble, are unsettling enough. The lives of the individuals whose accomplishments Holmes depicts are bracketed by James Cook's first voyage to the South Pacific (1768–1771) and Darwin's *Beagle* adventure (1831–1836). With dexterity and considerable but unobtrusive scholarship, Holmes goes far to reveal "the scientific process by which a mind of acknowledged power actually proceeds in the path of successful enquiry." That last line comes from David Brewster's *Life of Sir Isaac Newton* (1831). The minds Holmes depicts, however, stand deep in the shadow of the standard by which Brewster gauged scientific power.

Joseph Banks, botanist and long-time president of the Royal Society, serves Holmes as his Virgil, helping to link together the lives of his other protagonists. Banks gained his scientific reputation as a botanist on Cook's first voyage, though Holmes only touches lightly on the botanical work. He rather lingers, as a deft biographer might, over the scientist's shedding of English inhibitions while in the Tahitian islands, where he danced naked with native women and took as his lover one of the queen's servants. The young Banks stands in sharp contrast to the very image of John Bull that he later assumed as president of the Royal Society.

The story of the astronomical work of William Herschel and his sister Caroline forms the spine and intellectual pith of Holmes's narrative. In 1766, William came to Bath, England, where he had been appointed organist and choirmaster at the Octagon Chapel. Between giving music lessons and composing, he began reading astronomical works and mathematics. His passion for astronomy led him to construct his own reflecting telescopes. In 1773, he built a five-foot reflector, for which he cast and ground his own mirror, a six-inch concave "metal speculum," the first of its size and precision. As his ambition grew, so did the size of his telescopes, which he began manufacturing for other astronomers. In the spring of 1781, with his seven-foot reflector he watched a new planet swim into his ken. This discovery of Uranus (the first new planet observed since the time of Ptolemy), along with his numerous papers on original sightings of comets and nebulae, won Herschel election to the Royal Society and its Copley Gold Medal.

Herschel brought his sister Caroline to Bath principally to emancipate her from the vapid life in Hanover but also to act as his housekeeper and general secretary. Gradually she was inducted into the manufacture of telescopes, and then to sweeping the sky with her brother and aiding him in the necessary calculations. Two individuals were needed when Herschel deployed his 20-foot and then his 40-foot telescopes, from the towers of which he would shout his observations to his sister. These dazzling instruments allowed them to resolve nebulae into individual stars and to speculate that these clouds were the "laboratories of the universe," the cradle of new stars and their planets. Holmes obviously means to secure due recognition for Caroline's extraordinary talent, which she exercised well into her nineties.

As an agile writer, Holmes understands that an extended narrative about the work of the Herschels might grind down the less committed reader. He thus lightens his story through an interlude on competitive ballooning, with the English and the French vying to be first to cross the channel. The chapter

The First Balloon Crossing of the English Channel, 7 January 1785. E. W. Cocks's painting (c. 1840) depicts the hydrogen balloon flown by Blanchard and Jeffries leaving the Dover coast.

CREDIT: SCIENCE MUSEUM PICTORIAL

The reviewer is in the Departments of History, Philosophy, and Psychology, University of Chicago, 1126 East 59th Street, Chicago, IL 60637, USA. E-mail: r-richards@uchicago.edu

devoted to Mary Shelley's *Frankenstein* serves a similar function, dividing up two long chapters on Humphrey Davy, one on his search for therapeutic gases (and his use of nitrous oxide for pain relief), the other on his invention of a miner's lamp that would not ignite coal gases.

Davy probably comes closest to developing something like a distinctive Romantic conception, or at least his poetry had the kind of dark, melancholic tincture that sometimes passes for romantic. He had a gift for lecturing on the delights and utilities of science to public audiences at the Royal Institution. Nearly 500 people attended his final lecture of the London season in 1801. As he wrote a friend: "There was Respiration, Nitrous Oxide, and unbounded Applause. Amen!" But as a grounded Englishman, he did not expect the advance of science to bring mankind to the state sought by the French Revolutionists. He would not entertain "delusive dreams concerning the infinite improveability of man." Nitrous oxide, mediocre poetry, and English good sense, it must be said, do not a Romantic make.

In order to suggest that the English science of this period is Romantic science, Holmes has to construct walk-on roles for Keats, Coleridge, Percy Shelley, and Mary Shelley's monster. The latter did seem to have a notion of the Romantic: at least one of the books by which he became schooled in human feeling and with whose main character he identified was Goethe's *Sorrows of Young Werther*.

Early German Romanticism stands in the background of the scientifically anemic English brand. Friedrich Schlegel, one of the architects of the German movement, declared: "all art should become science and all science art; poetry and philosophy should be made one." Goethe, Humboldt, Herder, Novalis, Ritter, Schelling, the brothers Schlegel, and the femme fatale Caroline Böhmer-Schlegel-Schelling forged, in the framework provided by Kant and Fichte, the union of science and art and demonstrated that nature still retained the kind of moral and aesthetic values evacuated from an English mechanical universe. Their organic conception of nature had a decided impact on that scientist who could stand up to the measure of Newton, namely Charles Darwin. Holmes's *Age of Wonder* displays more the skill of the accomplished biographer than the beauty and fear of an English Romantic science.

10.1126/science.1181808

HISTORY OF SCIENCE

Far More Than Mere Transmission

Laurel Brown

In *Science and Islam: A History*, Ehsan Masood presents a clear, interesting, and nonspecialist account of a much-overlooked piece of the history of science. Although not perfect, the short book excellently portrays the importance of Islamic science.

Written to accompany a BBC television series of the same name, the book focuses on "the scientific revolution that took place during the empires created by Islam, between the 8th and the 16th centuries." During this period, science flourished and grew from mostly Greek origins into a system of unprecedented accomplishment. Despite several centuries of important advances, modern scientists and historians have long overlooked the contribution of the Islamic world to the sciences.

The book begins with a solid overview of the "classical narrative" of science in Islam, according to which scientists of the Islamic world focused on the translation and transmission of sciences that remained Greek in all essentials. This narrative further holds that, after a brief period of activity terminated by the triumph of religion over reason, Islam simply passed on the Greek sciences to a ready and willing Europe. Although several decades of historical research have laid siege to this interpretation, Masood rightly notes that it continues to hold sway. Insisting that the classical narrative cannot be the whole story, he offers instead a rich history of innovative Islamic science.

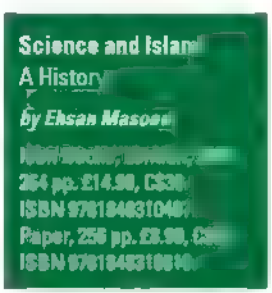

Still, Masood (a London-based science journalist and writer) does not appear to have had the historical resources required to break free of the classical narrative. He gives examples of scientific advancements (including the development of algebra and trigonometry, the discovery of the lesser circulation of blood, and the overhaul of Greek astronomy) but frequently falls back on the classical perspective when specific evidence is lacking. Masood mentions, for example, the work of al-Razi, a ninth-century physician who drew attention to particular problems with Galen's medical system. Despite discussing later physicians who shared al-Razi's qualms and advanced further arguments against Galen, Masood states, "No-one really followed up al-Razi's doubts about the entire system of humours, … and it was another thousand years before it was seriously challenged." Such an insistence that Islamic science continued to rely only on the original Greek tradition stems directly from the classical narrative. The narrative reoccurs throughout the book in the face of the concurrent challenge of Masood's evidence for scientific advancement and originality.

Masood follows his prologue on theories and misconceptions with a concise but excellent overview of the political, religious, and intellectual history of early Islam. This serves as a springboard for surveying the early achievements of Islamic science, especially the rapid translation of Greek scientific texts into Arabic and the flowering of scientific centers such as Baghdad and Muslim Spain.

The book's central section, "Branches of Learning," may be its strongest. Masood adeptly details breakthroughs and advances of Islamic scientists in the areas of medicine, astronomy, mathematics, chemistry, and engineering. Considering that some of these discoveries—including astronomical techniques later used by Copernicus and surgical tools we still use—are integral to the history of our modern science, Masood's work is particularly welcome.

The final section, "Second Thoughts," proves somewhat problematic. Its first chapter inexplicably covers optics, the formation of universities, the European reception of Islamic science, and theories of evolution in rapid succession. Masood discusses each topic clearly and carefully, but, with no explanation given for this grouping, readers may find it difficult to keep matters straight.

The last two chapters deal primarily with Islam's loss of scientific preeminence from the 1500s on. Masood covers the possible influences on the "decline," including economic woes, self-identity crises within Islam, and European colonization. Given the dearth of studies on later-period science, it is not surprising that he offers little on scientific continuity within the Islamic Ottoman and Mughal empires after the 16th century.

Masood makes good use of recent scholarship in the area of Islamic science. Interested readers will find the book an excellent first foray into the field. *Science and Islam* definitely does not shut the door on the unfortunate classical narrative. But it does provide the tools that may begin to move the history of science in the Muslim world in a different and hopefully more productive—direction.

The reviewer is at 8317 South Lake Stevens Road, Everett, WA 98205, USA. E-mail: laurel.a.brown@gmail.com

10.1126/science.1187158

ENERGY

Behavior and Energy Policy

Hunt Allcott[1]* and Sendhil Mullainathan[2]

Investment in scalable, non–price-based behavioral interventions and research may prove valuable in improving energy efficiency.

Many countries devote substantial public resources to research and development (R&D) for energy-efficient technologies. Energy efficiency, however, depends on both these technologies and the choices of the user. Policies to affect these choices focus on price changes (e.g., subsidies for energy-efficient goods) and information disclosure (e.g., mandated energy-use labels on appliances and autos). We argue that a broader approach is merited, one that draws on insights from the behavioral sciences. Just as we use R&D to develop "hard science" into useful technological solutions, a similar process can be used to develop basic behavioral science into large-scale business and policy innovations. Cost-effectiveness can be rigorously measured using scientific field-testing. Recent examples of scaling behaviorally informed R&D into large energy conservation programs suggest that this could have very high returns.

Behavioral Research in Energy Efficiency

The focus on price and information derives from traditional economic models of rational choice. Behavioral research, however, suggests a more complex, less idealized, view. People procrastinate; attention wanders. Peripheral factors subconsciously influence perceptions and decisions. These behavioral tendencies influence real-world outcomes and can inform interventions. For example, we often resist actions with clear long-term benefits if they are unpleasant in the short run. Programs that allow people to commit in advance to such actions—e.g., saving money or exercising—have proven quite popular, even when that commitment is costly (*1*, *2*). Default ("no-action") options strongly influence choices [e.g., when choosing between 401(k) plans], even when an alternative option is markedly better and switching appears easy (*3*, *4*). Small changes in context ("nudges") can affect behavior as much as large price changes (*5*). Such findings are striking in a cost-benefit framework; psychological cues typically cost very little compared with price changes.

In terms of energy efficiency, many studies suggest that people fail to adopt existing technologies that would save them money by using less energy, such as better insulation, fuel-efficient vehicles, and efficient appliances and lighting (*6*). For example, a recent consulting report concluded that many households and businesses in the United States have yet to take such relatively straightforward measures, even though doing so could reduce energy consumption by 23% from baseline and, thus, earn $1.2 trillion at an up-front cost of $520 billion (*7*). Although there are multiple explanations for this finding (*8*) and more evidence is needed, some barriers may be behavioral.

This suggests a potential role for non-price-based, behavioral interventions. Many such ideas have been studied in a large body of ongoing research on social approval, consumption feedback, goal setting, commitment, and other mechanisms (*9*, *10*). Although many of these were small-scale, short-term pilot studies on nonrepresentative populations, they do show proof of concept (*11*).

Recent work by a company called OPOWER, informed by academic work showing the power of social comparisons in environmental conservation (*12*), suggests that behavioral programs can be cost-effectively scaled to millions of households. OPOWER sends home energy-use reports to electricity and gas consumers that display the household's energy consumption, compare it with that of similar households, and provide energy conservation tips. Using randomized, controlled trials with hundreds of thousands of utility customers across the United States, these reports have been shown to reduce electricity consumption in the average household by over 2% (*13*).

As shown in the table, right, an OPOWER-like program costs an electric utility 2.5¢ per kilowatt-hour (¢/kWh) saved (*14*). This compares favorably with estimates of the average cost of other energy-efficiency programs, which in two recent studies range from 1.6¢ to 3.3¢ (*15*) and 5.5¢ to 6.4¢/kWh (*16*). If scaled nationwide, a program like this could reduce U.S. carbon dioxide (CO_2) emissions from electric power by 0.5%, while actually saving $165 per metric ton of reductions. This compares very favorably with other, more traditional strategies to reduce carbon emissions; wind power, carbon capture, and storage added to new coal power plants, and plug-in hybrid vehicles are estimated to cost $20, $44, and $15 per metric ton of CO_2 abated (*17*). The table shows that a comparable intervention scaled across the United States would net $2.2 billion per year over the program's life.

Systematically Structuring Interventions

Although laboratory studies and small-scale pilots demonstrate academic insights and proofs-of-concept, scalable behavioral interventions require in situ testing. OPOWER illustrates this: It would be difficult to predict the effects without randomized, controlled field trials in a representative population. Fortunately, randomized field experiments have become increasingly feasible. Large-scale social science field experiments began 40 years ago and are now used by businesses (*18*), governments, development agencies, electric utilities (*19*), and other organizations

COSTS AND BENEFITS OF BEHAVIORAL INTERVENTIONS IN THE UNITED STATES*

Cost-effectiveness of behavioral program	
Reduction in electricity consumption (%)	2.7
Average household electricity consumption (kWh/year)	11,232
Savings (kWh/household-year)	305
Program cost to the utility ($/household-year)	$7.48
Cost effectiveness (¢/kWh)	2.5
Comparison: other efficiency programs (¢/kWh)	1.6–6.4
Cost per ton of carbon abatement	
Long-run marginal cost of electricity (¢/kWh)	8.0
Net savings from behavioral program (¢/kWh)	5.5
Marginal carbon intensity (metric tons/MWh)	0.34
Carbon abatement cost ($/metric ton CO_2)	−$165
Comparison: Wind, carbon capture, hybrids	$20, $44, $15
Value of a comparable intervention, scaled across entire U.S.	
Annual carbon abatement (MMT CO_2/year)	12.7
Assumed value of CO_2 reduction ($/metric ton)	$10
Total value of CO_2 reduction (millions of $/year)	$127
Value of electricity saved (millions of $/year)	$3,020
Total cost to the utility (millions of $/year)	$927
Net value of intervention (millions of $/year)	$2,220

* See supporting online material for data sources and analysis details.

[1]Department of Economics, Massachusetts Institute of Technology, Cambridge, MA 02142, USA. [2]Department of Economics, Harvard University, Cambridge, MA 02138, USA.
*Author for correspondence. E-mail: allcott@mit.edu

in the United States and around the world (*20*). In our own work testing behaviorally informed interventions, we have seen how the long-understood insight of randomization can be made practical. Useful techniques include randomizing letter content across groups, encouragement designs that simultaneously evaluate program marketing and the program itself, and phased implementation (*21*). In some settings, outcomes can be measured with little additional cost; utilities, for example, already record their customers' energy consumption. In the OPOWER example, it is straightforward to send letters to a study group and not to a group of controls, and effects are measured simply by comparing the two groups' electricity bills.

Careful design must ensure external validity: that estimated treatment effects apply beyond the experimental sample. Dynamic electricity-pricing experiments in France and the United States illustrate this. Randomization over representative samples (*22*), rather than those who express interest in a program, (*23*, *24*) is essential, because the interested are likely more motivated and engaged and, therefore, have different treatment effects. Similar electricity-pricing experiments have been carried out in different geographic areas, informing whether results from one program can generalize to others.

As in other R&D processes, behavioral experiments benefit from iterative design, testing, and refinement, which suggests long-term partnerships between researchers and implementing businesses (*25*). Of course, randomized field trials are only one tool; other approaches, such as laboratory experiments and qualitative interviews, are invaluable in the iterative design of behavioral interventions.

Policy Implications

Our argument has three key policy implications. First, governments can provide funding for potentially high-impact behavioral programs as part of their broader support for energy innovation. A bill under consideration in the U.S. House of Representatives, HR 3247, would establish a program at the Department of Energy to understand behavioral factors that influence energy conservation and speed the adoption of promising initiatives.

Criteria for funding such behavioral research should be similar to those used for allocating resources to engineering and "hard-science" research. In those domains, promising technologies are theory-driven; similarly, successful behavioral interventions have typically drawn on existing theoretical and empirical work. Behavioral interventions should also have clearly measurable outcomes; projects should include careful testing protocols, including randomized field trials when possible. Perhaps most important, promising interventions must be scalable; although basic behavioral science questions and theoretical nuances are also important, here we are advocating for ideas that have large effects on energy consumption and can cost-effectively be scaled to millions of consumers. As such, R&D that brings together scientific knowledge and industry testing and scaling capacity can be particularly powerful.

Second, through market incentives, policy-makers can encourage—or fail to encourage—private-sector firms to generate and utilize behavioral innovations that "nudge" consumers to make better choices. Historically, economists and policy-makers have focused on how regulation affects relative prices—for example, how emissions caps or taxes on pollution-intensive goods affect the prices firms set. In practice, however, firms interact with consumers in many ways in addition to pricing. Utilities, for example, can give consumers clear or opaque information about energy-efficient goods, can make it easy or difficult to find out about energy-efficiency promotions, and can otherwise nudge consumers in ways that cause them either to increase or decrease consumption. Regulatory changes such as "decoupling," which separate electricity retailers' profits from quantities sold, are one mechanism that could encourage firms to nudge consumers toward reducing energy use (*26*).

Third, government agencies often provide independent information disclosure, such as vehicle and appliance energy-efficiency ratings. This helps catalyze private-sector innovation by allowing firms to credibly convey the financial value of energy efficiency to consumers. The effect of information on choices, however, depends critically on how the information is conveyed, and government agencies should carefully consider behavioral factors in the disclosures they control. For example, rating fuel economy in miles per gallon (MPG) can mislead consumers, most people approach MPG as a linear indicator of the cost of fueling a vehicle, whereas, in reality, annual fuel costs will scale nonlinearly in MPG (*27*).

Nuanced research into human behavior and energy-use decisions is not new, nor is the idea that energy efficiency may be generally cost-effective. What has been missing is a concerted effort by researchers, policy-makers, and businesses to do the "engineering" work of translating behavioral science insights into scaled interventions, moving continuously from the laboratory to the field to practice. It appears that such an effort would have high economic returns.

References and Notes

1. R. Thaler, S. Benartzi, Save More Tomorrow *J. Polit. Econ.* **112**, (suppl. 1), S164 (2004)
2. N. Ashraf, D. Karlan, W. Yin, *Q. J. Econ.* **121**, 635 (2006).
3. E. J. Johnson, D. Goldstein, Medicine. *Science* **302**, 1338 (2003)
4. B. Madrian, D. Shea, Behavior *Q. J. Econ.* **116**, 1149 (2001)
5. M. Bertrand *et al.*, Discussion paper 968 (Yale Univ. Economic Growth Center, New Haven, CT 2009) www.econ.yale.edu/growth_pdf/cdp968.pdf
6. J. Hausman, *Bell J. Econ.* **10**, 33 (1979)
7. H. C. Granade *et al.*, *Unlocking Energy Efficiency in the U.S. Economy* (McKinsey & Co., New York, 2009), www.mckinsey.com/clientservice/electricpowernaturalgas/downloads/US_energy_efficiency_full_report.pdf.
8. A. Jaffe, R. Stavins, *Resour. Energy Econ.* **16**, 91 (1994).
9. W. Abrahamse *et al.*, *J. Environ. Psychol.* **25**, 273 (2005).
10. Before 1980, there were 20 experiments on energy-use feedback alone (*28*); these and more recent information provision experiments reduced electricity use by between 5 and 20% (*29*, *30*)
11. D. Charles, *Science* **325**, 804 (2009)
12. J. M. Nolan *et al.*, Normative social influence is underdetected. *Pers. Soc. Psychol. Bull.* **34**, 913 (2008)
13. H. Allcott, *Social Norms and Energy Conservation* (Working paper, Massachusetts Institute of Technology (MIT), Cambridge, MA, 2009); http://web.mit.edu/allcott/www/papers.html.
14. Program cost and treatment effects represent a scaled program, with monthly reports targeted at the 60% of users with highest baseline use and quarterly reports for the remaining 40%. Note that "cost to the utility" somewhat understates total social costs, because the costs consumers incur are not known.
15. K. Friedrich *et al.*, American Council for an Energy-Efficient Economy (ACEEE) report no. U092 (ACEEE Washington, DC, 2009); www.aceee.org/pubs/u092.htm.
16. T. Arimura, R. Newell, K. Palmer, Discussion paper 09-48 (Resources for the Future, Washington, DC, 2009), www.rff.org/RFF/Documents/RFF-DP-09-48.pdf
17. J. Creyts *et al.*, *Reducing U.S. Greenhouse Gas Emissions: How Much and at What Cost?* (McKinsey & Co., New York, 2008), www.mckinsey.com/clientservice/ccsi/pdf/US_ghg_final_report.pdf
18. T. Davenport, *Harv. Bus. Rev.* **87**, 68 (2009)
19. D. Aigner, *J. Econom.* **26**, 1 (1984)
20. S. Levitt, J. List, *Eur. Econ. Rev.* **53**, 1 (2009).
21. For more detail on these techniques, see http://ideas42.iq.harvard.edu/files/ideas42/Behavioral.ScienceandEnergyPolicy.pdf
22. F. Wolak, Working paper 151 (Center for the Study of Energy Markets, Univ. of California Energy Institute Berkeley, CA, 2006), ftp://zia.stanford.edu/pub/papers.anaheim_cpp.pdf
23. C. Aubin *et al.*, *J. Appl. Econ.* **10**, (suppl. 1), S171 (1995)
24. H. Allcott, *Rethinking Real-Time Electricity Pricing* (Working paper, MIT, Cambridge, MA, 2010), http://web.mit.edu/allcott/www/papers.htm.
25. A. Banerjee, E. Duflo, National Bureau of Economic Research (NBER) working paper 14467 (NBER, Cambridge, MA, 2008), www.nber.org/papers/w14467.pdf
26. T. Brennan, Discussion paper 08-27 (Resources for the Future, Washington, DC, 2008), http://ideas.repec.org/p/rff/dpaper/dp-08-27.html.
27. R. P. Larrick, J. B. Soll, *Science* **320**, 1593 (2008)
28. G. Shippee, *Environ. Manage.* **4**, 297 (1980)
29. P. Stern, *Am. Psychol.* **47**, 1224 (1992)
30. C. Fischer, *Energ. Effic.* **1**, 79 (2008)

31. This work was supported by the Hewlett Foundation and the Russell Sage Foundation.

Supporting Online Material

www.sciencemag.org/cgi/content/full/327/5970/1204/DC1

10.1126/science.1180775

ASTRONOMY

Sunscreen for the Young Earth

Dating the establishment of Earth's magnetic field has implications for identifying conditions when life could take hold.

Moira Jardine

What were the conditions on the young Earth that allowed life to form? The obvious one, the presence of water, has driven the search for extrasolar planets whose orbits lie in the so-called habitable zone. A less well known requirement, however, is the need for Earth to generate a large-scale magnetic field to shield it from the high-energy radiation and wind from the Sun. Without such a magnetic field, the atmosphere would have been exposed to ionization and erosion by the charged particles in the solar wind, and any form of early life would have been irradiated by the intense x-ray and high-energy ultraviolet emission from the young Sun. On page 1238 of this issue Tarduno *et al.* (*1*) show that an appreciable magnetic field had developed as early as 3.45 billion years ago (Ga). The timing—not long after the Late Heavy Bombardment (3.90 Ga) but before the development of an oxygen-rich atmosphere (2.30 Ga)—suggests that the magnetic field may predate the establishment of life. The measured field strengths, while less than that of the present-day Earth, may have been sufficient to shroud the Earth in a protective shield.

Not all planets in the solar system can generate and maintain a magnetic field. To do so, they must rotate about their axis, but more crucially they need a liquid core that is both electrically conducting and convecting. These convective motions can be triggered as the interior cools from its initial hot state after formation but a decline in cooling may shut off convection and the magnetic field with it. This is one hypothesis for the loss of Mars' ancient magnetic field (*2*). The evolution of Earth's internal structure is therefore a crucial factor in determining the time scale over which a magnetic field can be generated and sustained.

At the same time as Earth's interior was cooling, however, the solar dynamo was also changing. Observations of young solar-like stars show that they rotate much more rapidly than the Sun does today. This faster rotation powers an interior dynamo that generates enough magnetic flux to pepper almost the entire stellar surface with star spots. Energy stored in this magnetic field leaks into the outer atmosphere, producing a corona similar to that seen during eclipses of the present-day Sun, but with a greater x-ray luminosity. Some of this million-degree gas escapes, carrying away mass and angular momentum in a powerful wind. Over time, this process has spun the Sun down to its present leisurely rotation rate, such that its dynamo produces less magnetic flux and its wind has subsided to a comparatively gentle breeze. Even today, however, the solar wind is capable of buffeting and compressing Earth's magnetic field (see the figure). The enhancements in the solar wind (coronal mass ejections) that sometimes accompany a large solar flare can temporarily shift Earth's magnetic pole by several degrees.

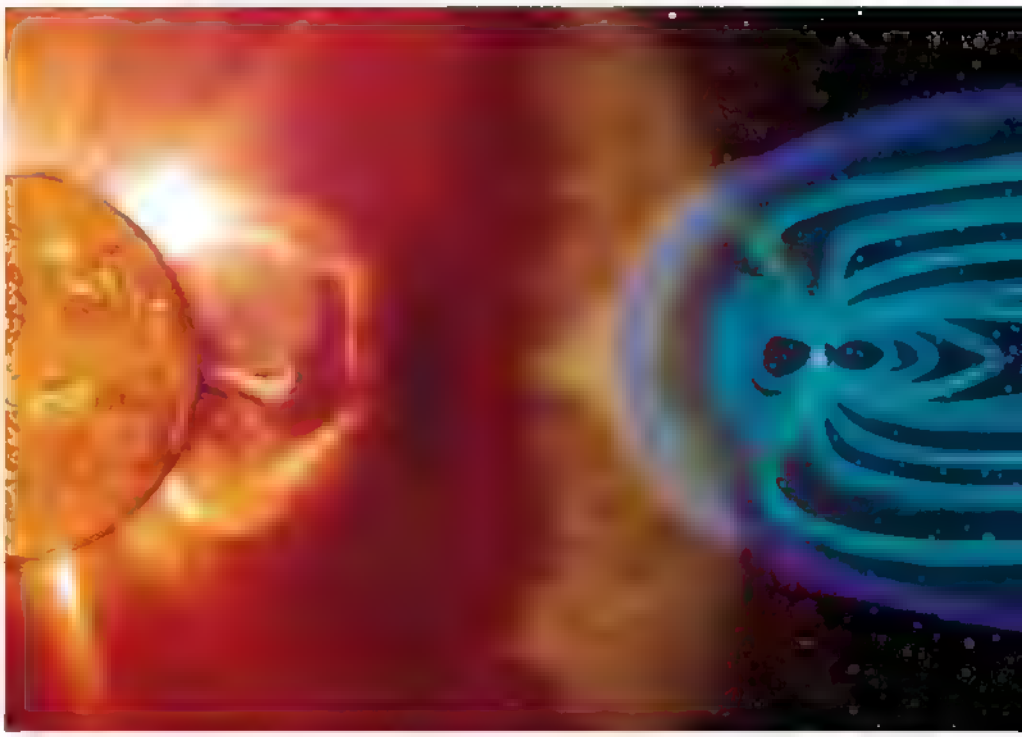

Shelter from the storm. Clouds of hot gas called coronal mass ejections are often ejected by the Sun when there is a large solar flare. It takes about 3 days for them to reach the distance of Earth's orbit. If they collide with Earth, the impact compresses and buffets Earth's protective magnetic field and can produce spectacular aurorae.

CREDIT: STEELE HILL/NASA

Whereas the measurements of Tarduno *et al.* provide us with an essential data point in the evolution of Earth's magnetic field, we have no such data for the Sun. Studies of young solar analogs have improved our understanding of the magnetic fields of young stars (*3*), but their winds cannot be directly observed. What can be detected, however, is the edge of the bubble that forms around the star as the wind ploughs into the interstellar medium. An ingenious method has been developed (*4*) to measure the absorption of starlight by this ridge of compressed gas from which its density and the ram pressure of the stellar wind that produced it can then be inferred. The method depends on some assumptions about the wind, however, principally that it has the same terminal velocity as the present-day solar wind. If the Sun had a higher-speed, lower-pressure wind in the past, it may have exerted a lower ram pressure on the young Earth than this approach implies (*5*).

Even given the uncertainties involved in extrapolating back in time, the measurement by Tarduno *et al.* suggests that as early as 3.45 Ga, Earth may have had a magnetosphere that extended out to about 5 Earth radii—comparable to values experienced during coronal mass ejection events today. The area of the polar hole, where Earth's magnetic field lines are open and allow solar energetic particles to penetrate the atmosphere, would have been about a factor of 3 higher than present-day values. This estimate, however, does not allow for the greater frequency and mass loss rate seen in coronal mass ejections from young stars. These may have been powerful

Department of Physics and Astronomy, University of St. Andrews, St. Andrews, KY16 9SS, UK. E-mail: mmj@st-andrews.ac.uk

enough to crush the magnetosphere of the young Earth.

This suggests that for some time after planets form, they may suffer from the intense magnetic activity of their young star, even if their internal structure and composition enable them to develop and maintain a large-scale magnetic field. Only once the stellar wind has lessened can a planetary magnetic field shield the atmosphere from irradiation and erosion. This casts a new light on the suitability of low-mass stars as hosts for life-bearing planets. These stars are numerous—much more so than solar-mass stars but they are also much cooler than the Sun. To be hot enough to have liquid water on the surface, a planet needs to be closer to a low-mass star than Earth is to the Sun. This presents an immediate problem, however, as these low-mass stars are notoriously active, with magnetic flares that may be three orders of magnitude more powerful than that of the present-day Sun. We do not know what type of planetary magnetic field would be needed to provide a shield against such activity. The measurement by Tarduno *et al.*, however, lays down a crucial data point in Earth's history that adds to our understanding of the factors necessary for the establishment of life.

References

1. J. A. Tarduno *et al.*, *Science* **327**, 1238 (2010)
2. D. J. Stevenson, *Nature* **412**, 214 (2001)
3. J.-F. Donati *et al.*, *Mon. Not. R. Astron. Soc.* **380**, 1297 (2007)
4. B. E. Wood, J. L. Linsky, H. R. Müller, G. P. Zank, *Astrophys. J.* **547**, L49 (2001)
5. V. Holzwarth, M. Jardine, *Astron. Astrophys.* **463**, 11 (2007)

10.1126/science.1187051

ECOLOGY

The Seven Ages of *Pan*

Decades-long field studies require unusual dedication but provide unique insight into animal behavior and ecology

Tim Clutton-Brock[1] and Ben C. Sheldon[2]

Imagine yourself as a latter-day Jane Goodall, establishing your camp on the edge of the rainforest, eager to document the behavior and ecology of a previously unstudied ape. As months pass, the animals stop scrambling away as soon as they see you and you can catch occasional glimpses of them as they feed. Stick at it for a year or two and, if you are lucky, you will be able to recognize individuals and spot interesting new behavior patterns. But to understand the network of social relationships between individuals, you need to know their ages, kin relations, and relative dominance rank. That will take at least one decade or, more likely, two. However, other important questions will take three or four decades of systematic data collection, how and why groups increase or decline in size; how genetic differences interact with environmental factors to affect breeding success and survival; how population density is regulated. During all this time you will need to withstand the vicissitudes of funding, political disturbances, and the demands of your career and family.

For long-lived species, the time scale outlined above is no exaggeration. After Jane Goodall started to study the chimpanzees at Gombe in 1960, it took her and her collaborators 50 years to obtain the data required to fully describe the life histories of chimpanzees—a quantitative Seven Ages of *Pan*—and answer important questions (*1*–*5*). For example, the research on female reproductive success shows that although their fecundity declines with increasing age, female chimpanzees (unlike female humans) show no evidence of menopause. Similarly, the study of male success shows that dominance is important for the number of offspring fathered by individual males but that younger males and low-ranking males are more successful than predicted by simple models based on priority of access. With the basic structure of the life history in place, future studies will be able to investigate the social, ecological, and genetic factors affecting breeding success and survival.

Not all primates are as long-lived as chimpanzees. Studies of primate species with shorter life spans, like some lemurs, can make more rapid progress. But even in these cases, data usually need to cover more than a decade to answer many behavioral and ecological questions. Without records that span life histories of individuals, it is seldom possible to assess how events at one stage of the life span affect the behavior, breeding success, or survival at other stages. Furthermore, the costs and benefits of different reproductive strategies vary widely as food availability fluctuates between years and can be strongly influenced by rare events like droughts or epidemics, so that attempts to compare their payoffs based on data from one or two seasons can be very misleading.

[1]Department of Zoology, University of Cambridge, Cambridge CB2 3EJ, UK. [2]Edward Grey Institute, Department of Zoology, University of Oxford, Oxford OX1 3PS, UK. E-mail: tmcb@cam.ac.uk; ben.sheldon@zoo.ox.ac.uk

CREDITS: (RED DEER) MEHMET KARATAY/WIKIMEDIA COMMONS; (GREAT TIT) JOE TOBIAS; (CHIMPS) STOCKPHOTOS.COM

The value of long-term studies. Individual-based studies of red deer, great tits, and chimpanzees now extend over more than 30 years, spanning the full life histories of large numbers of individuals. These studies provide reliable estimates of the factors affecting reproduction and survival that offer unique insights into the operation of natural selection and the causes of fluctuations in population size and structure.

As a result, successful long-term field studies, like those of chimpanzees at Gombe and Mahale (*6*), gorillas at Karisoke (*7*), savannah baboons at Amboseli (*8*), and Japanese macaques at Arashiyama (*9*), provide many of the best opportunities for novel, innovative research on primate ecology and behavior. Many of these studies are now collaborative ventures involving multiple scientists from separate disciplines and universities, who can together draw on detailed records of the life histories of large samples of individuals. The protracted presence of scientists at particular sites also contributes to the conservation of study populations and their habitats (*10*).

Long-term, individual-based studies are not restricted to primates; however, most involve birds or mammals (see the figure), and only a few have focused on fish, reptiles, and amphibians (*11*). Despite extensive interest in the evolution of insect societies, few studies of social insects have yet been able to track the full careers of reproductive individuals; the first study to explore the extent and causes of individual differences in lifetime breeding success in social insects was published only last year (*12*). The longest-running field studies are of passerine birds and were started in the Netherlands in the 1930s (*13*). Several long-term studies of seabirds, wildfowl, ungulates, carnivores, and primates have been running since the late 1950s and early 1960s, producing vital insights into the causes of population declines and responses to climate change (*14*). Among mammals other than primates, long-term individual-based studies of African lions, elephant seals, wild sheep, African elephants, red deer, and marmots have been running for over three decades.

Compared to primates, many other mammals are relatively easy to catch and mark and (with the exception of elephants) have shorter life spans. As a result, some studies now provide records of the full life histories of several thousand individuals spanning multiple generations and offer opportunities to investigate biological questions that are not yet accessible in primates. Multigenerational pedigrees that can be used to assess the relative contributions of genotype and environment to individual differences now exist for an increasing number of birds and mammals (*15*), and modern genomic approaches have also started to yield new insights. However, their application requires the existence of extensive phenotypic and ecological data, and there are no short-cuts to obtaining these data (*16*).

Long-term field projects are often at risk to bandits or rebels because they are usually located in isolated areas. Several have lost staff and some have had to close. Poaching and human encroachment are common problems and are often exacerbated by political instability. But the greatest problem faced by long-term studies is their need for continuous funding. Most long-term individual-based studies are run by universities and rely on short-term research grants for support. These studies will eventually face a rejection and interruption in the collection of data. For studies of long-lived species, this may mean abandoning the study or starting from scratch. Protection for the continuity of long-term studies has been elusive, and even the most productive studies spend much of their lives teetering on the brink of closure.

References and Notes

1. J. Goodall, *Anim. Behav. Monogr.* **1**, 165 (1968)
2. R. W. Wrangham, *Soc. Sci. Inf. (Paris)* **18**, 336 (1979)
3. J. Goodall, *The Chimpanzees of Gombe. Patterns of Behavior* (Harvard Univ. Press, Harvard, 1986)
4. M. Emery Thompson *et al.*, *Curr. Biol.* **17**, 2150 (2007).
5. E. E. Wroblewski *et al.*, *Anim. Behav.* **77**, 873 (2009)
6. T. Nishida *et al.*, *Am. J. Primatol.* **59**, 99 (2003)
7. A. H. Harcourt, K. J. Stewart, *Gorilla Society* (Univ. Chicago Press, Chicago, 2007).
8. M. J. E. Charpentier, R. C. van Horn, J. Altmann, S. C. Alberts, *Proc. Natl. Acad. Sci. U.S.A.* **105**, 1988 (2008)
9. N. Koyama, Y. Takahata, M. A. Huffman, K. Norikoshi, H. Suzuki, *Primates* **33**, 33 (1992)
10. A. E. Pusey, L. Pintea, M. L. Wilson, S. Kamenya, J. Goodall, *Conserv. Biol.* **21**, 623 (2007)
11. O. R. Jones, T. Clutton-Brock, T. Coulson, H. C. J. Godfray, *J. Anim. Ecol.* **77**, 612 (2008)
12. C. Lopez-Vaamonde *et al.*, *J. Evol. Biol.* **22**, 983 (2009).
13. H. N. Kluijver, *Ardea* **39**, 1 (1951).
14. A. Charmantier *et al.*, *Science* **320**, 800 (2008)
15. L. E. B. Kruuk, J. Slate, A. J. Wilson, *Annu. Rev. Ecol. Evol. Syst.* **39**, 525 (2008).
16. H. Ellegren, B. C. Sheldon, *Nature* **452**, 169 (2008)
17. Some of our discussion is based on talks at the VII Gottinger Freilandtage on "Long-term field studies of primates," 8 to 11 December 2009, organized by the Department of Behavioral Ecology and Sociobiology, Deutsches Primatenzentrum, Gottingen.

10.1126/science.1187796

PHYSICS

Controlling Implosion Symmetry Around a Deuterium-Tritium Target

Fusion power is a step closer with the demonstration of control over the extreme thermal radiation pressure created by high-power laser beams within a cavity.

Peter A. Norreys

One of the goals of 21st-century physics—controlling the implosion of a target and initiating nuclear fusion has its origins in one of the puzzles of 19th-century physics. The understanding of thermal radiation emitted from a cavity ("blackbody radiation"), which is an important component of the fusion problem, began by abandoning classical physics and adopting the revolutionary idea of energy quantization. Thermal radiation has reappeared in the fusion problem because the powerful megajoule-class lasers do not implode their targets directly instead, they create intense radiation pressure within a cavity. On pages 1231 and 1228 of this issue, Li *et al.* (*1*) and Glenzer *et al.* (*2*) show that the distribution of radiation inside a cavity can be accurately controlled to create a symmetrical implosion, thereby removing major obstacles to the realization of fusion energy in the laboratory. These new insights promise another revolution in physics in the near future, one that provides access to new states of matter with unprecedented energy densities.

Central Laser Facility, Science and Technology Facilities Council, (STFC) Rutherford Appleton Laboratory, Didcot, Oxfordshire OX11 0QX, UK, and Blackett Laboratory, Imperial College London, Prince Consort Road, London SW7 2BZ, UK. E-mail: peter.norreys@stfc.ac.uk

The ideal limit of a thermal emitter, a "black body," absorbs all incoming radiation. In practice, the best black body to study is a small hole in an enclosed cavity; almost all incoming light will be absorbed on its walls before finding a reflecting pathway back out (see the figure, panel A). Classical physics accounted for thermal emission from an object as a continuous process resulting from accelerating electrical charges and predicted that more radiation would be emitted as the wavelength of light decreased. The classical theory not only failed to account for the intensity of thermal emission peaking at some frequency, but also suffered from the "ultraviolet catastrophe" a

black body, or any other object with a temperature, would emit an infinite amount of energy

The solution would lie with the concept that light is emitted in packets, or quanta, as pioneered by Max Planck in 1900. His new theory accurately predicted the intensity and the frequency spectra of blackbody radiation as a function of temperature. In doing so, Planck reconciled electromagnetism with statistical mechanics, which describes the energy distribution of a gas in thermal equilibrium.

Unlike molecules in a gas, radiation in a cavity does not come to equilibrium by experiencing collisions in the middle of the box. Energy can shift from one frequency mode to another by charge oscillations induced in the wall material. Energy can then be transferred to other charges in the wall, and these will oscillate and radiate at different frequencies. Eventually, the radiation inside the box comes to thermal equilibrium, which can be measured when it eventually escapes the cavity through the hole.

This old problem received a new lease on life with the invention of lasers in the second half of the 20th century. It was quickly realized that these devices can deliver immense energy densities to a small target. If that energy could be captured and enclosed in a cavity similar to Planck's black box, called a hohlraum, then the resulting blackbody radiation would have its maximum at frequencies in the soft x-ray regime, which corresponds to cavity temperatures of millions of kelvin. This value is many orders of magnitude more powerful than anything that Planck considered Indeed, this blackbody radiation is so powerful that it can then be used to implode a small shell of material containing fusion fuel (deuterium and tritium, the isotopes of hydrogen) to high velocity. The resulting density and temperature increase at peak compression would be sufficient to create conditions where large numbers of fusion reactions take place (*3*).

However, if the release of fusion energy is to exceed the energy of the input laser beams, a number of criteria must be met simultaneously. The energy coupling to the cavity generating the blackbody radiation must be high The number of fast electrons generated from so-called parametric instabilities must be minimized to prevent preheating of the fuel as it implodes. The soft x-ray drive that surrounds the shell must be sufficiently symmetric. The high-pressure shock waves, which must converge at the center of the pellet at peak compression, must be timed accurately. Finally, hydrodynamic instabilities that are seeded by imperfections (residual mass perturbations in the original shell) must be controlled (*4*, *5*).

The radiation temperature needed for fusion is at least 3 million kelvin, which would require nearly a megajoule of laser energy delivered in several nanoseconds, corresponding to peak powers of 500 TW. Given that the entire world's electricity generation output is 17 TW, the energy density delivered to the cavity in that short time would be enormous. This megajoule energy requirement demands the use of many overlapping laser beams that create quite complex structures inside the hohlraum. This is beautifully demonstrated by Li *et al.* in their proton radiographs of the converging shell in a scaled-down experiment performed at the University of Rochester's OMEGA laser facility (*6*), which showed the formation and evolution of spoke-like electric field structures inside the cavity on a nanosecond time scale. The complex structure inside the cavity does not appear to have influenced the compression performance of the shell. Furthermore, striations previously observed with direct laser illumination of shell targets are absent with the soft x-ray drive (*7*).

The worry is that these structures could affect both the energy absorption (via laser beam scattering or self-focusing) and parametric instability growth in the larger targets needed for fusion energy gain that will be used at the National Ignition Facility (*8*). Fortunately, this is not the case. Indeed, Glenzer *et al.* demonstrate greater than 90% energy coupling to the hohlraum (see the figure, panel B). They also show that the fraction of laser energy converted to hot electrons is in the range of 1 to 2%, well within acceptable limits. They provide conclusive proof that they have achieved blackbody radiation temperatures of 3.3 million kelvin. Finally, in an extraordinary tour de force, they demonstrate the control the symmetry of the x-ray drive at the center of the cavity Control is achieved by forming a novel plasma diffraction grating in the beam-crossing area near the laser entrance holes, which tunes the wavelength of the two outer cones of beams with respect to the two inner cones of beams (see the figure, panel C).

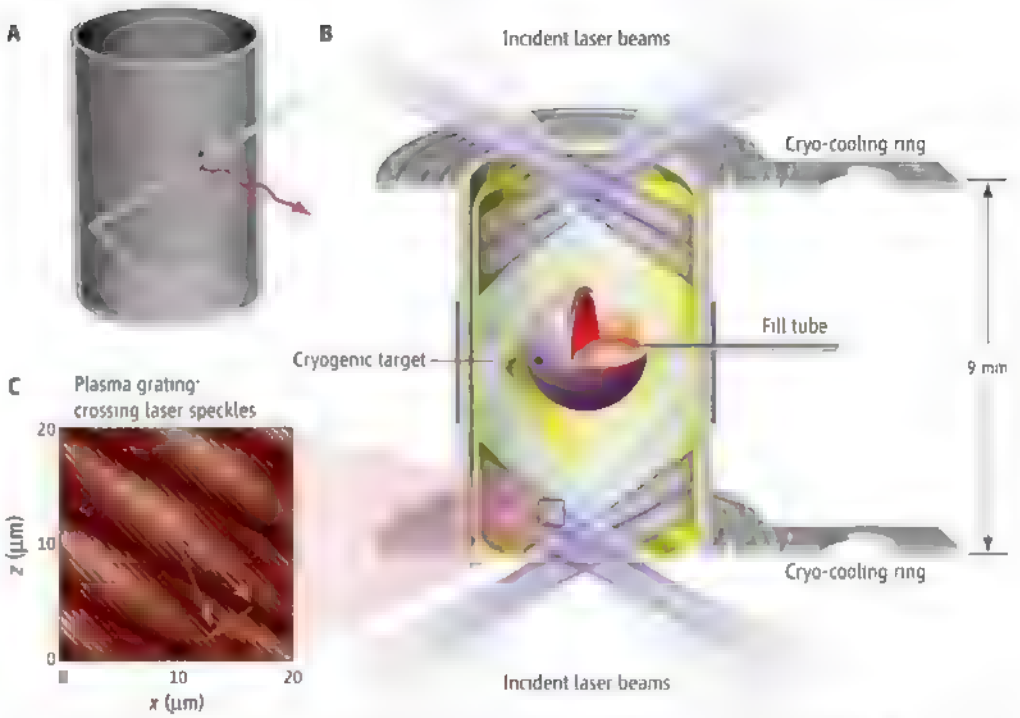

Thermal radiation, then and now. (**A**) The classical blackbody source is a hole in a blackened cavity. Light coming in (shown in blue) will absorb as it bounces around; the emission (red) is thermal radiation from the cavity walls. (**B**) A schematic illustration of the radiation cavity, or hohlraum, containing the shell that has a layer of deuterium-tritium fusion target frozen on its inner surface The cavity is kept at cryogenic temperatures by two cooling rings at the top and bottom; laser radiation will increase the temperature above 3 million kelvin. The 192 laser beams of the National Ignition Facility enter the hohlraum from both the top and bottom of the chamber. They are arranged in four cones of beams. The radiation symmetry is controlled by adjusting the wavelength of the two inner cones with respect to the outer two cones. (**C**) An expanded view of the overlap point of the beams, which combine to form a plasma diffraction grating The arrows depict how the wave vectors of the beams (long arrows) combine to generate the wave vector of the grating (short arrow).

These remarkable observations suggest that the remaining obstacles to fusion energy gain are now surmountable. These results also herald a new era in physics, that of high-energy-density science. It is truly fitting that this 21st-century frontier (*9*) can trace some of its origins back to the humble radiation cavity of the 19th century.

References and Notes

1. C. K. Li *et al.*, *Science* **327**, 1231 (2010); published online 28 January 2010 (10.1126/science.1185747)
2. S. H. Glenzer *et al.*, *Science* **327**, 1228 (2010); published online 28 January 2010 (10.1126/science.1185634)
3. J. Nuckolls, L. Wood, A. Thiessen, G. Zimmerman, *Nature* **239**, 139 (1972)
4. For a comprehensive review, see (*5*) and references therein.
5. J. D. Lindl *et al.*, *Phys. Plasmas* **11**, 339 (2004)
6. T. R. Boehly *et al.*, *Opt. Commun.* **133**, 495 (1997)
7. J. R. Rygg *et al.*, *Science* **319**, 1223 (2008)
8. E. I. Moses, C. R. Wuest, *Fusion Sci. Technol.* **47**, 314 (2005)
9. E. I. Moses *et al.*, *Phys. Plasmas* **16**, 041006 (2009).

10.1126/science.1187275

CELL BIOLOGY

Burn Out or Fade Away?

A protein whose expression is turned on by stress delays the onset of age-related pathologies.

Ivan Topisirovic[1,2] and Nahum Sonenberg[1,2]

The target of rapamycin (TOR) kinase plays an evolutionarily conserved role, from yeast to human, in controlling metabolic activity in response to intracellular cues and extracellular stimuli (*1*). It stimulates anabolic processes that engender cell growth and proliferation by increasing protein synthesis and lipogenesis. TOR also inhibits autophagy, which is a major catabolic process. Persistent activation of TOR causes an imbalance between anabolic and catabolic processes, resulting in the accumulation of damaging reactive oxygen species (ROS), which favors the development of age-related disorders. Indeed, the inhibition of TOR by the drug rapamycin increases organism life span and reduces the incidence of age-related pathologies (*2*). On page 1223 of this issue, Lee *et al.* report that sestrin proteins prevent excessive TOR activation and delay the onset of age-related pathologies through a negative-feedback mechanism (*3*).

Sestrins are a family of highly conserved cytoplasmic proteins that contain a redox-active domain, and whose expression is induced by stress (*4*). There are three sestrins in mammals, but only one in the fly *Drosophila melanogaster*, making the latter an optimal model system for studying the physiological functions of sestrins. Activation of *Drosophila* TOR (dTOR) increases transcription of the gene encoding *Drosophila* sestrin (dSesn) through a signaling pathway that is not fully understood, but involves the enzyme c-Jun N-terminal kinase (JNK) and the forkhead box O (FOXO) transcription factor. In turn, increased abundance of dSesn inhibits dTOR signaling by activating adenosine monophosphate–activated protein kinase (AMPK) and tuberous sclerosis complex 2 (TSC2) proteins (see the figure).

Lee *et al.* report that the loss of dSesn results in chronic activation of dTOR, leading to the induction of anabolic processes and inhibition of autophagic degradation of dysfunctional mitochondria. This causes ROS accumulation and development of a variety of age-related pathologies in *Drosophila*, including muscle degeneration, cardiac arrhythmia, and lipid accumulation. Deletion of the gene encoding dSesn resulted in a 50% decrease in AMPK activity and a 50% increase in dTOR activity. Strikingly, feeding dSesn-deficient flies with pharmacological activators of AMPK (e.g., metformin), or the TOR inhibitor rapamycin, prevented the age-related phenotypes.

How does dSesn antagonize premature aging in flies? It has been proposed that aging is caused by the accumulation of stochastic molecular damage, which is mainly induced by mitochondrial ROS production (*5*). Treatment of flies lacking dSesn with the natural antioxidant vitamin E ameliorated most of the age-related pathologies, suggesting that they depend on ROS accumulation, and that the dSesn-induced negative feedback on TOR activity prevents ROS buildup. Although sestrins can eliminate ROS production in vitro (*4*), Lee *et al.* demonstrate that the intrinsic redox activity of dSesn is not critical for sup-

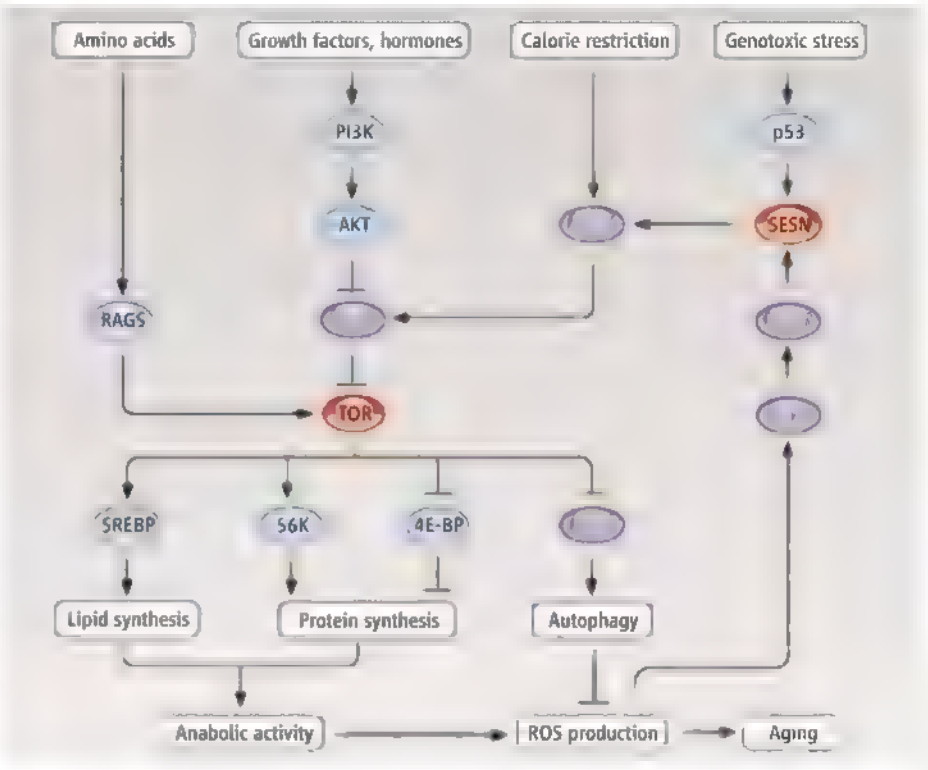

CREDIT: Y. GREENMAN, SCIENCE

Metabolic network. Sestrins control the effects of TOR, in a complex network of pathways that regulate anabolism, catabolism, and the development of age-related pathologies. ATG1, authphagy-specific gene 1; PI3K, phosphatidylinositol 3-kinase, RAGS, Ras-related GTP-binding protein; SREBP, sterol regulatory element-binding protein.

[1]Department of Biochemistry, McGill University, Montreal, Quebec, H3A 1A3, Canada. [2]Goodman Cancer Research Centre, McGill University, Montreal, Quebec, H3A 1A3, Canada. E-mail: nahum.sonenberg@mcgill.ca

pressing the observed age-related phenotypes, which are almost exclusively mediated through dSesn-AMPK-TSC2 signaling pathway that inhibits dTOR. This is consistent with the previously established role for mammalian sestrins 1 and 2 in blocking mammalian TOR (mTOR) signaling (and aging phenotypes) in reponse to genotoxic stress through a pathway that involves the tumor suppressor protein p53 and the same Sesn-AMPK-TSC2 cascade (*6*)

Caloric restriction blunts aging and delays the onset of age-related pathologies in many organisms (*7*). The TOR pathway has emerged as a prime candidate for mediating these effects. Lee *et al.* underscore TOR's role in aging by uncovering a feedback mechanism that keeps dTOR activity in check, thereby maintaining the integrity of mitochondria, a major ROS source. Several targets of TOR have been implicated in affecting mitochondrial function. For example, in response to caloric restriction in *Drosophila*, the eIF4E-binding protein (d4E-BP) can prolong life span by promoting the translation of messenger RNAs (mRNAs) that encode components of the mitochondrial electron transport chain (thus boosting mitochondrial functional capacity) (*8*). In mammalian cells, a complex of proteins containing mTOR (mTORC1) stimulates mitochondrial biogenesis and oxidative metabolism by promoting the association of two proteins, peroxisome proliferator-activated receptor-γ coactivator 1 -α and yin-yang 1 (*9*) Thus, sestrins would presumably keep this association in check.

In addition to the effect of sestrins on mitochondria, TOR also controls two cellular processes that affect mitochondrial function and integrity and are intimately linked to aging: protein synthesis (mRNA translation) and autophagy. Inhibition of autophagy abates life-span extension by caloric restriction in the nematode *Caenorhabditis elegans* (*10*) and decreases longevity in yeast (*11*). TOR stimulates mRNA translation by inhibiting 4E-BPs and activating S6 kinases (S6K) (*1*). Reduced S6K activity extends life span in the nematode (*12*), the fruit fly *Drosophila melanogaster* (*13*), and mice (*14*). Depletion of an eIF4E isoform (eIF4E is a protein inhibited by 4E-BPs) extends life span in *C. elegans* (*15*), and loss of d4E-BP reduces longevity in flies (*8*).

Lee *et al.* demonstrate that sestrins and TOR act as central nodes of the complex regulatory network that controls aging by linking genotoxic and oxidative stress with the control of metabolic activity. Although it remains to be determined whether this pathway is evolutionarily conserved, recent findings that the FOXO transcription factor increases Sesn3 abundance in mammalian cells (*16*) implies that a similar mechanism functions in mammals. Accordingly, aberrant mTOR activity underlies several human age-related disorders, including diabetes, obesity, heart disease, muscle degeneration, and cancer. As sestrins appear to amend the age-related effects of excessive TOR signaling, developing molecular mimics of sestrin could open new therapeutic avenues to target age-related pathologies.

References

1. S. Wullschleger *et al.*, *Cell* **124**, 471 (2006).
2. D. E. Harrison *et al.*, *Nature* **460**, 392 (2009)
3. J. H. Lee *et al.*, *Science* **327**, 1223 (2010)
4. A. V. Budanov *et al.*, *Science* **304**, 596 (2004)
5. T. B. Kirkwood, S. N. Austad, *Nature* **408**, 233 (2000)
6. A. V. Budanov, M. Karin, *Cell* **134** 451 (2008)
7. M. D. Piper, A. Bartke, *Cell Metab.* **8**, 99 (2008)
8. B. M. Zid *et al.*, *Cell* **139**, 149 (2009)
9. J. T. Cunningham *et al.*, *Nature* **450**, 736 (2007).
10. K. Jia, B. Levine, *Autophagy* **3**, 597 (2007).
11. A. L. Alvers *et al.*, *Aging Cell* **8**, 353 (2009)
12. M. Hansen *et al.*, *Aging Cell* **6**, 95 (2007)
13. P. Kapahi *et al.*, *Curr. Biol.* **14**, 885 (2004)
14. C. Selman *et al.*, *Science* **326**, 140 (2009)
15. P. Syntichaki *et al.*, *Nature* **445**, 922 (2007)
16. V. Nogueira *et al.*, *Cancer Cell* **14**, 458 (2008)

10.1126/science.1187497

CLIMATE CHANGE

How Stable Is the Methane Cycle?

Ship and satellite data help to elucidate how methane emissions from sources such as wetlands may change in a warming climate.

Martin Heimann

Methane is, after water vapor and carbon dioxide, the third most important greenhouse gas in the atmosphere. Its concentration in the atmosphere has more than doubled since preindustrial times. Human energy production and use, landfills and waste, cattle raising, rice agriculture, and biomass burning are considered responsible for this increase (*1*). However, ~40% of current global methane sources are natural. Most natural emissions come from anaerobic decomposition of organic carbon in wetlands, with poorly known smaller contributions from the ocean, termites, wild animals, wildfires, and geological sources. Two observational studies now shed light on how these natural sources are changing in today's changing climate (*2*, *3*).

Ice core studies have shown that the natural methane sources must have changed substantially during the glacial cycles. How stable are they under global warming? Wetlands and permafrost soils, including the sub-sea permafrost under the Arctic Ocean, contain at least twice the amount of carbon that is currently in the atmosphere as carbon dioxide. Release of a sizable fraction of this carbon as carbon dioxide and/or methane would lead to warmer atmospheric temperatures, causing yet more methane to be released It would thus create a positive feedback loop that amplifies global warming However, observational evidence for such release on regional and global scales has been elusive.

On page 1246 of this issue, Shakhova *et al* (*2*) report convincing evidence of methane outgassing from the Arctic continental shelf off northeastern Siberia (Laptev and East Siberian Sea), based on painstaking repeated surveys using Russian ice breakers between 2003 and 2008 In this region, the relatively shallow continental shelf extends up to 1000 km north of the coastline. The seabed consists of relict permafrost from the last glaciation (*4*), when sea levels were considerably lower than today. The permafrost layer contains substantial amounts of organic carbon and also traps methane seeping up from underneath. In the permafrost, the methane forms relatively stable methane hydrates, but warming of the seawater or a decrease in pressure by a reduction in sea level will destabilize the hydrates, releasing methane into the ocean waters (*5*).

Shakhova *et al.* now document large areas with surface waters that are highly supersaturated in methane; in some places, methane concentrations are more than 100 times as high as expected in equilibrium with the ambient atmosphere. Based on their extensive data set, the authors estimate an annual outgassing to the atmosphere of ~8×10^{12} grams of carbon (8 Tg C) as methane from the East Siberian Arctic Shelf waters Consistent with this, concurrent atmospheric concentration measurements on the ship and with a helicopter document methane levels up to four times as high as recorded elsewhere in the Arctic basin.

Max-Planck-Institut für Biogeochemie, Hans-Knöll-Strasse 10, 07745 Jena, Germany. E-mail: martin.heimann@bgc-jena.mpg.de

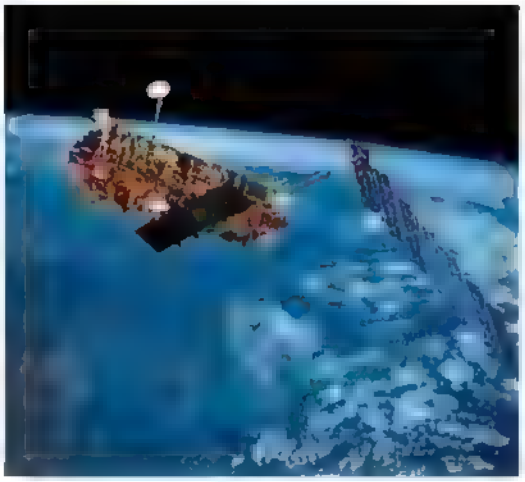

Complementary strategies. In situ data from ships such as this Russian icebreaker (**above**) and remote-sensing data from satellites such as Envisat (**right**) are indispensable for understanding how natural methane emissions are changing under global warming.

Another observational window into the natural methane cycle has been opened by remote sensing from space. Since 2003, the Scanning Imaging Absorption Spectrometer for Atmospheric Chartography (SCIAMACHY) instrument on the Envisat satellite has provided global atmospheric methane column measurements over land. In a recent issue of *Science*, Bloom *et al.* (*3*) compared the methane satellite data from the years 2003 to 2005 with surface temperatures from a weather prediction model and with water table elevation estimates derived from the Gravity Recovery and Climate Experiment (GRACE) satellite. Water table and surface temperature are considered the key controlling variables for methane emissions from wetlands and rice paddies (*6*).

Mostly in the tropics, Bloom *et al.* find a tantalizing correlation between water table and atmospheric methane. In contrast, at high latitudes, methane concentrations appear to be better correlated with surface temperatures. These findings are consistent with previous inverse atmospheric modeling studies (*7*). Using their results to calibrate a simple methane emission model, Bloom *et al.* estimate that methane emissions from temperate Northern Hemisphere latitude wetlands rose by ~6 Tg C per year between 2003 and 2007.

How important are these fluxes in the global methane cycle? Considering the global emissions of ~440 Tg C as methane per year (*1*), the Siberian Arctic Ocean emissions and the changes in northern wetland emissions are negligible. This is good news, implying that current climate change does not affect the natural methane cycle in a globally important way. But will this persist into the future under sustained warming trends? We do not know. Current modeling studies indicate that the climate-methane feedback from wetlands and permafrost will not be catastrophic but that there will be sustained methane leakages from wetlands and permafrost areas in coming decades (*8*). Keeping track of these leakages is indispensable for quantifying the climate-methane feedback on a global scale.

The two studies (*2*, *3*) exemplify complementary strategies for observing the modern Earth system (see the figure). The east Siberian ocean methane measurements are a beautiful example of diligent, high-quality in situ measurements that, together with an expanded atmospheric network, are vital for understanding climate, even though such on-the-ground monitoring is part of what Nisbet has called "Cinderella science" (*9*). On the other hand, Bloom *et al.*'s study illustrates the power of new remote sensing techniques to probe the globe in unprecedented detail. The SCIAMACHY instrument is restricted to daytime surface-reflected solar radiation; active remote sensing techniques (such as light detection and ranging) are needed to capture the high-latitude permafrost methane emissions. Both approaches are indispensable and need to be used in synergy to monitor and ultimately predict the natural methane cycle over coming decades.

References

1. K. L. Denman *et al.*, in *Climate Change 2007: The Physical Science Basis. Contribution of Working Group I to the Fourth Assessment Report of the Intergovernmental Panel on Climate Change*, S. Solomon *et al.*, Eds. (Cambridge Univ. Press, Cambridge, UK and New York, 2007), pp. 499–587
2. N. Shakhova *et al.*, *Science* **327**, 1246 (2010)
3. A. A. Bloom *et al.*, *Science* **327**, 322 (2010)
4. N. N. Romanovskii *et al.*, *Geo-Mar. Lett.* **25**, 167 (2005)
5. G. K. Westbrook *et al.*, *Geophys. Res. Lett.* **36**, L15608 (2009)
6. B. P. Walter, M. Heimann, *Global Biogeochem. Cycles* **14**, 745 (2000)
7. P. Bousquet *et al.*, *Nature* **443**, 439 (2006)
8. D. Archer, *Biogeosciences* **4**, 521 (2007)
9. E. Nisbet, *Nature* **450**, 789 (2007)

10.1126/science.1187270

NEUROSCIENCE

Questionable Calcium

Frank Kirchhoff

The mechanism of calcium signaling in astrocytes is part of the debate on the role of glia at neuronal synapses.

Astrocytes constitute the major glial cells of the mammalian central nervous system, but they were long regarded as passive elements, providing only structural and nutritional support to neurons. Over the past 25 years, another view has emerged in which astrocytes directly affect neuron function. Just as a neuron releases molecules to signal to another neuron (at a junction called the synapse), astrocytes also transmit molecules to affect neuronal communication, and it is thought that the same release mechanism is used (*1*–*6*). However, conflicting data continue to raise debate about this view, including the contradictory results of mouse studies reported recently (*7*, *8*) and by Agulhon *et al.* on page 1250 of this issue (*9*). Can this controversy be resolved?

Department of Neurogenetics, Max Planck Institute of Experimental Medicine, 37075 Göttingen, Germany, and Institute of Physiology, University of Saarland, 66421 Homburg/Saar, Germany. E-mail: frank.kirchhoff@uks.eu

Thin astrocyte processes wrap tightly around synaptic neurons, and there is good evidence for signaling between these cells at the synaptic junction. Astrocytes respond to the stimulation of nearby neurons with an increase in intracellular calcium (Ca^{2+}) concentration. This increase triggers the release of transmitter molecules such as glutamate, which can potentiate the synaptic activity of neighboring neurons (*1*, *3*), or adenosine triphosphate (ATP), which reduces synaptic transmission (*4*). In addition, restricting the intracellular Ca^{2+} concentration in astrocytes can prevent the release of transmitters, as shown for D-serine, thus inhibiting modulation of neurotransmission at closely located synapses (*5*). These findings support a model (see the figure) in which a presynaptic

neuron releases transmitters that activate receptors at the postsynaptic neuron and astrocytes. In asytrocytes, this causes the liberation of Ca^{2+} from the endoplasmic reticulum (ER) and the subsequent release of transmitter molecules that control neurotransmission

Although this may explain how astrocytes directly affect neuron function, there are concerns as to whether such "gliotransmission" is merely an experimental artifact. For instance, intracellular vesicles harboring transmitter molecules, and the molecular machinery required for their release (in response to intracellular Ca^{2+}), have rarely been detected in astrocytes.

These concerns are now boosted by recent observations using different mouse models (*7*–*9*). One mouse model was genetically engineered to allow for astrocyte-specific increases in intracellular Ca^{2+}. For that purpose, expression of the metabotropic receptor MrgA1, which is normally not expressed in the brain, was induced in astrocytes. The MrgA1 ligand was used to selectively increase the concentration of the intracellular signaling molecule inositol 1,4,5-trisphosphate (IP_3). IP_3 triggers the liberation of Ca^{2+} from the ER. The other mouse model was engineered to prevent any IP_3-mediated Ca^{2+} liberation from the ER by deletion of the gene encoding IP3R2, the only astrocyte receptor (expressed on the ER) that responds to IP_3. Thus, astrocytes cannot evoke this increase of intracellular Ca^{2+}. Collectively, the studies show that in both paradigms, neurotransmission and synaptic plasticity (long-term potentiation) in hippocampal neurons were unaffected, thus challenging the role of Ca^{2+} transients (induced by IP_3) for gliotransmission.

Differences in experimental setups or method-intrinsic artifacts may be responsible for the divergent results. For example, overexpression of the MrgA1 receptor in mice might not include appropriate receptor localization and embedding in astrocyte signaling pathways. But rather than focus on methodological reasons, it is perhaps more profitable to consider these results in light of several commonly accepted facts: Astrocytes express receptors that respond to neuronal activity; activation of these receptors causes transient increases in intracellular Ca^{2+}; astrocytes release gliotransmitters from intracellular vesicles; these gliotransmitters modulate neuronal activity. However, the data obtained by Agulhon *et al.* in mice lacking an IP_3 receptor suggest that other molecules involved in Ca^{2+} signaling should be considered, such as voltage-gated Ca^{2+} channels or transient receptor potential (TRP) channels. TRP channels are Ca^{2+}-permeable, nonselective cation channels that are gated by diverse stimuli such as phospholipids, oxidants, cell volume changes, acidity, or osmolarity (*10*). In addition, unlike neurons, astrocytes do not necessarily require a process for priming transmitter-containing vesicles for rapid release. The composition and properties of the release machinery also may be different from their neuronal counterparts (*11*). And the requirements for Ca^{2+} in releasing gliotransmitters may vary in different subcellular regions of an astrocyte. Perisynaptic astrocyte processes can be thinner than 50 nm. It is conceivable that Ca^{2+} transients in these regions have been missed by the largely somatic Ca^{2+} recordings of Agulhon *et al.* Perhaps TRP or voltage-gated Ca^{2+} channels, which are both expressed in astrocytes, mediate Ca^{2+} entry (*12*).

Technological advancements could help to resolve the mechanism of gliotransmission. More sensitive imaging that operates at submicrometer resolution would allow recording of Ca^{2+} signals from astrocyte processes just outside the synapse that have thus far been missed. Also, genetic mouse models in which proteins involved in the release of gliotransmitters can be visualized by fluorescence would demonstrate release machinery in astrocytes. Finding out where astrocytic Ca^{2+} comes from and how it supports gliotransmission is an important step in settling the debate

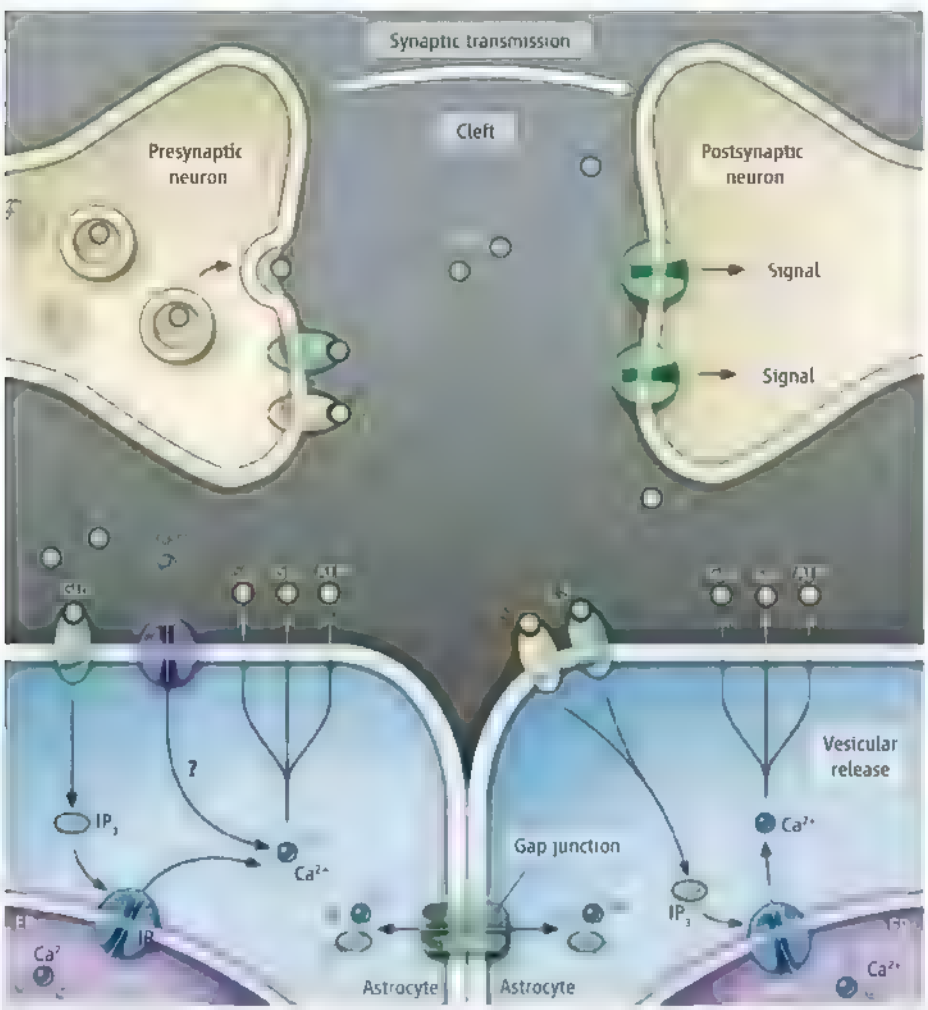

CREDIT: V. GREENMAN/SCIENCE

Calcium trigger. Glutamate (Glu), ATP, and D-serine (Ser) are gliotransmitters that affect synaptic activity [through ionotropic receptors (postsynaptic neuron) and metabotropic receptors (presynatic neuron and astrocytes)]. Their release is triggered by intracellular Ca^{2+}, but where does the Ca^{2+} come from?

References and Notes

1. G. Perea, A. Araque, *Science* **317**, 1083 (2007).
2. P. Bezzi *et al.*, *Nat. Neurosci.* **7**, 613 (2004).
3. P. Jourdain *et al.*, *Nat. Neurosci.* **10**, 331 (2007).
4. O. Pascual *et al.*, *Science* **310**, 113 (2005).
5. C. Henneberger *et al.*, *Nature* **463**, 232 (2010).
6. G. Perea *et al.*, *Trends Neurosci.* **32**, 421 (2009).
7. J. Petravicz *et al.*, *J. Neurosci.* **28**, 4967 (2008).
8. T. A. Fiacco *et al.*, *Neuron* **54**, 611 (2007).
9. C. Agulhon *et al.*, *Science* **327**, 1250 (2010).
10. R. Inoue, *Curr. Pharm. Des.* **11**, 1899 (2005).
11. M. M. Halassa *et al.*, *Neuropharmacology* **57**, 343 (2009).
12. J. D. Cahoy *et al.*, *J. Neurosci.* **28**, 264 (2008).

13. I thank N. Brose and S. Wichert for discussions. Supported by the Max Planck Society, the MPI for Experimental Medicine, the European Union (FP7 Neuroglia, EdU-Glia), and the Deutsche Forschungsgemeinschaft (CMPB, SPP 1172, TRR 43).

10.1126/science.1187420

The Chicxulub Asteroid Impact and Mass Extinction at the Cretaceous-Paleogene Boundary

Peter Schulte,[1]* Laia Alegret,[2] Ignacio Arenillas,[2] José A. Arz,[2] Penny J. Barton,[3] Paul R. Bown,[4] Timothy J. Bralower,[5] Gail L. Christeson,[6] Philippe Claeys,[7] Charles S. Cockell,[8] Gareth S. Collins,[9] Alexander Deutsch,[10] Tamara J. Goldin,[11] Kazuhisa Goto,[12] José M. Grajales-Nishimura,[13] Richard A. F. Grieve,[14] Sean P. S. Gulick,[6] Kirk R. Johnson,[15] Wolfgang Kiessling,[16] Christian Koeberl,[11] David A. Kring,[17] Kenneth G. MacLeod,[18] Takafumi Matsui,[19] Jay Melosh,[20] Alessandro Montanari,[21] Joanna V. Morgan,[9] Clive R. Neal,[22] Douglas J. Nichols,[15] Richard D. Norris,[23] Elisabetta Pierazzo,[24] Greg Ravizza,[25] Mario Rebolledo-Vieyra,[26] Wolf Uwe Reimold,[16] Eric Robin,[27] Tobias Salge,[28] Robert P. Speijer,[29] Arthur R. Sweet,[30] Jaime Urrutia-Fucugauchi,[31] Vivi Vajda,[32] Michael T. Whalen,[33] Pi S. Willumsen[32]

The Cretaceous-Paleogene boundary ~65.5 million years ago marks one of the three largest mass extinctions in the past 500 million years. The extinction event coincided with a large asteroid impact at Chicxulub, Mexico, and occurred within the time of Deccan flood basalt volcanism in India. Here, we synthesize records of the global stratigraphy across this boundary to assess the proposed causes of the mass extinction. Notably, a single ejecta-rich deposit compositionally linked to the Chicxulub impact is globally distributed at the Cretaceous-Paleogene boundary. The temporal match between the ejecta layer and the onset of the extinctions and the agreement of ecological patterns in the fossil record with modeled environmental perturbations (for example, darkness and cooling) lead us to conclude that the Chicxulub impact triggered the mass extinction.

Paleontologists have long recognized the global scale and abruptness of the major biotic turnover at the Cretaceous-Paleogene (K-Pg, formerly K-T) boundary ~65.5 million years ago (Ma). This boundary represents one of the most devastating events in the history of life (*1*) and abruptly ended the age of the dinosaurs. Thirty years ago, the discovery of an anomalously high abundance of iridium and other platinum group elements (PGEs) in the K-Pg boundary clay led to the hypothesis that an asteroid ~10 km in diameter collided with Earth and rendered many environments uninhabitable (*2*, *3*).

The occurrence of an impact is substantiated by the recognition of impact ejecta including spherules, shocked minerals, and Ni-rich spinels in many K-Pg boundary event deposits [e.g., (*4*, *5*)]. The ejecta distribution points to an impact event in the Gulf of Mexico–Caribbean region; this prediction is reinforced by the discovery of the ~180- to 200-km-diameter Chicxulub crater structure on the Yucatan peninsula, Mexico (*6*). Modeling suggests that the size of the crater and the release of climatically sensitive gases from the carbonate- and sulfate-rich target rocks could have caused catastrophic environmental effects such as extended darkness, global cooling, and acid rain (*7*–*9*). These effects provide an array of potential mechanisms for the ecologically diverse but selective abrupt extinctions (Fig. 1) (*10*–*13*).

Notwithstanding the substantial evidence supporting an impact mechanism, other interpretations of the K-Pg boundary mass extinction remain. Stratigraphic and micropaleontological data from the Gulf of Mexico and the Chicxulub crater have instead been used to argue that this impact preceded the K-Pg boundary by several hundred thousand years and therefore could not have caused the mass extinction [e.g., (*14*)]. In addition, the approximately one-million-year-long emplacement of the large Deccan flood basalts in India spans the K-Pg boundary (Fig. 1), the release of sulfur and carbon dioxide during these voluminous eruptions may have caused severe environmental effects (*15*) that have also been proposed as triggers for the mass extinction at the K-Pg boundary (*16*).

Here, we assess the observational support for these divergent interpretations by synthesizing recent stratigraphic, micropaleontological, petrological, and geochemical data from the globally distributed K-Pg boundary event deposit. Impact and volcanism as extinction mechanisms are evaluated in terms of their predicted environmental perturbations and, ultimately, the distribution of life on Earth before and after the K-Pg boundary

What Is the Evidence for Correlating the Impact with the K-Pg Boundary?

The Upper Cretaceous and lower Paleogene sediments bracketing the K-Pg boundary event deposits are among the most intensively investigated deposits in the geological record. More than 350 K-Pg boundary sites are currently known, and these sites show a distinct ejecta distribution pattern related to distance from the Chicxulub crater (Fig. 2 and table

[1]GeoZentrum Nordbayern, Universität Erlangen-Nürnberg, Schlossgarten 5, D-91054 Erlangen, Germany. [2]Departamento de Ciencias de la Tierra e Instituto Universitario de Investigación de Ciencias Ambientales de Aragón, Universidad de Zaragoza, Pedro Cerbuna 12, E-50009 Zaragoza, Spain. [3]Department of Earth Sciences, University of Cambridge, Cambridge CB2 3EQ, UK. [4]Department of Earth Sciences, University College London, Gower Street, London WC1E 6BT, UK. [5]Department of Geosciences, Pennsylvania State University, University Park, PA 16802, USA. [6]Institute for Geophysics, Jackson School of Geosciences, University of Texas at Austin, J.J. Pickle Research Campus, 10100 Burnet Road 196-ROC, Austin, TX 78759, USA. [7]Earth System Science, Vrije Universiteit Brussel, Pleinlaan 2, B-1050 Brussels, Belgium. [8]Centre for Earth, Planetary, Space and Astronomical Research, Open University, Milton Keynes MK7 6AA, UK. [9]Earth Science and Engineering, Imperial College London, London SW7 2BP, UK. [10]Institut für Planetologie, Universität Münster, D-48149 Münster, Germany. [11]Department of Lithospheric Research, University of Vienna, Althanstrasse 14, A-1090 Vienna, Austria. [12]Tsunami Engineering Laboratory, Disaster Control Research Center, Graduate School of Engineering, Tohoku University, 6-6-11-1106 Aoba, Aramaki, Sendai 980-8579, Japan. [13]Programa de Geología de Exploración y Explotación, Dirección de Investigación y Posgrado, Instituto Mexicano del Petróleo, Eje Lázaro Cárdenas No. 152, C.P. 07730, Mexico City, México. [14]Earth Sciences Sector, Natural Resources Canada, Ottawa, Ontario K1A 0E4, Canada. [15]Research and Collections Division, Denver Museum of Nature and Science, 2001 Colorado Boulevard, Denver, CO 80205, USA. [16]Museum für Naturkunde, Leibniz Institute at the Humboldt University Berlin, Invalidenstrasse 43, D-10115 Berlin, Germany. [17]Center for Lunar Science and Exploration, Universities Space Research Association–Lunar and Planetary Institute, 3600 Bay Area Boulevard, Houston, TX 77058–1113, USA. [18]Department of Geological Sciences, University of Missouri, Columbia, MO 65211, USA. [19]Planetary Exploration Research Center, Chiba Institute of Technology, 2-17-1 Tsudanuma, Narashino, Chiba 275-0016, Japan. [20]Earth and Atmospheric Sciences, Purdue University, 550 Stadium Mall Drive, West Lafayette, IN 47907–2051, USA. [21]Osservatorio Geologico di Coldigioco, 62021 Apiro (MC), Italy. [22]Department of Civil Engineering and Geological Sciences, 156 Fitzpatrick Hall, University of Notre Dame, Notre Dame, IN 46556, USA. [23]SIO Geological Collections, 301 Vaughan Hall, MS-0244, Scripps Institution of Oceanography, La Jolla, CA 92093–0244, USA. [24]Planetary Science Institute, 1700 East Fort Lowell Road, Suite 106, Tucson, AZ 85719, USA. [25]Department of Geology and Geophysics, School of Ocean and Earth Science and Technology, University of Hawaii, Manoa, Honolulu, HI 96822, USA. [26]Unidad de Ciencias del Agua, Centro de Investigación Científica de Yucatán, A.C., Calle 8, No. 39, Mz. 29, S.M. 64, Cancún, Quintana Roo, 77500, México. [27]Laboratoire des Sciences du Climat et de l'Environnement, Institut Pierre et Simon Laplace, Commission à l'Énergie Atomique/CNRS/Université de Versailles Saint Quentin en Yvelines–UMR 1572, Avenue de la Terrasse, F-91198 Gif-sur-Yvette Cedex, France. [28]Bruker Nano GmbH, Schwarzschildstraße 12, D-12489 Berlin, Germany. [29]Department of Earth and Environmental Sciences, K.U. Leuven, Box 2408, Celestijnenlaan 200E, 3001 Leuven, Belgium. [30]Natural Resources Canada, Geological Survey of Canada Calgary, 3303 33rd Street NW, Calgary, AB T2L 2A7, Canada. [31]Laboratorio de Paleomagnetismo y Paleoambientes, Programa Universitario de Perforaciones en Oceanos y Continentes, Instituto de Geofísica, Universidad Nacional Autonoma de México (UNAM), DF 04510 Mexico, Mexico. [32]Department of Earth and Ecosystem Sciences, Lund University, Sölvegatan 12, 223 62 Lund, Sweden. [33]Department of Geology and Geophysics, University of Alaska, Fairbanks, AK 99775, USA.

*To whom correspondence should be addressed. E-mail: schulte@geol.uni-erlangen.de. The remaining authors contributed equally to this work.

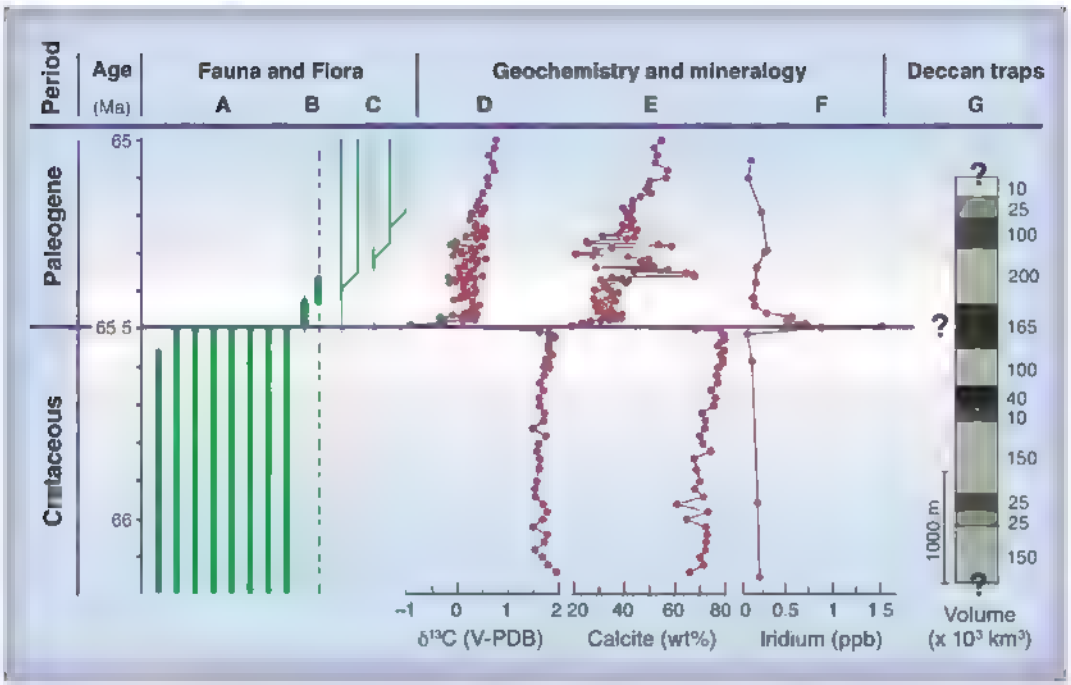

Fig. 1. Stratigraphy and schematic record of biotic events across the K-Pg boundary correlated to the chemical and mineralogical records of a core from the North Atlantic [Ocean Drilling Program (ODP) Leg 207] and the major eruptive units of the Deccan flood basalt province, India. Many (>60%) Cretaceous species experienced mass extinction at the boundary (A), whereas successive blooms of opportunistic species (B) and radiation of new species (C) occurred in the Early Paleogene. V-PDB indicates the Vienna Pee Dee Belemnite; wt %, weight %; and ppb, parts per billion. The mass extinction coincides with a major perturbation of the global carbon cycle as indicated by a negative $\delta^{13}C$ anomaly (D), a major drop of carbonate sedimentation in the marine realm (E), and the enrichment of PGEs in Chicxulub ejecta deposits (F) (*25*, *26*). Composite stratigraphic column of the formations of the main Deccan Trap flood basalt province showing their cumulative thickness and estimated basalt volumes (G) (*15*). Note that the exact stratigraphic onset and end of the main Deccan flood basalt sequence and the precise position of the K-Pg boundary in the formations have yet to be determined, as indicated by the question marks (*16*). However, the onset of the main eruption phase is ~400 to 600 thousand years before the K-Pg boundary as is also shown by Os isotope data (*38*).

S1) (*17*, *18*). Accordingly, the K-Pg boundary sites can be divided into four groups (Fig. 2 and table S1): (i) In very proximal settings up to 500 km from Chicxulub, impact deposits are quite thick. Cores recovered close to the crater rim inside the Chicxulub impact structure include a >100-m-thick impact-breccia sequence, and 1-m- to >80-m-thick ejecta-rich deposits are present in the surrounding Central American region [e.g., (*19*–*21*)]. (ii) In proximal areas around the northwestern Gulf of Mexico from 500 to 1000 km from Chicxulub, the K-Pg boundary is characterized by a series of cm- to m-thick ejecta spherule-rich, clastic event beds indicative of high-energy sediment transport, for example, by tsunamis and gravity flows (*18*, *22*, *23*). (iii) At intermediate distances from Chicxulub (~1000 to ~5000 km), the K-Pg boundary deposit consists of a 2- to 10-cm-thick spherule layer topped by a 0.2- to 0.5-cm-thick layer anomalously rich in PGEs with abundant shocked minerals, granitic clasts, and Ni-rich spinels (Fig. 3) (*12*, *24*–*26*). (iv) In distal marine sections more than 5000 km from Chicxulub, a reddish, 2- to 5-mm-thick clay layer rich in impact ejecta material is usually present at the K-Pg boundary [e.g., (*17*)]. The bedding plane between the impact-ejecta-rich red clay layer and the underlying Cretaceous marls coincident with the abrupt mass extinction in the El Kef section, Tunisia, is also the officially defined base of the Paleogene (fig. S1) (*27*). This definition implies that the impact-generated sediments in the K-Pg boundary interval stratigraphically belong to the Paleogene (Fig. 2).

The pattern of decreasing ejecta-layer thickness with increasing distance from the impact crater is consistent with the Chicxulub impact as the unique source for the ejecta in the K-Pg boundary event deposit (Figs. 2 and 3 and table S1). Additional support for this genetic link derives from the distribution, composition, and depositional mode of the ejecta. First, the size and abundance of spherules and ballistically ejected shocked quartz grains, which are resistant to alteration, decrease with increasing distance from Chicxulub (*18*, *28*). Second, the specific composition [e.g., silicic spherules, shocked limestone, and dolomite and granitic clasts (Fig. 3 and figs. S2 to S4)] (*29*) and age distribution (table S2) of the ejecta match the suite of Chicxulub target rocks. Lastly, the presence of the high-energy clastic unit at proximal K-Pg boundary sites, intercalated between two layers rich in Chicxulub ejecta, suggests that the Chicxulub impact caused a collapse of the Yucatan carbonate platform and triggered mass flows and tsunamis in the Gulf of Mexico and adjacent areas (Fig. 2 and figs. S3 to S8) (*17*, *18*, *30*). Therefore, the K-Pg boundary clastic unit, up to 80 m thick in places, was deposited in the extremely brief period between the arrival of coarse-grained spherules and the subsequent, longer-term deposition of the finer-grained PGE- and Ni-rich ejecta phases (Fig. 2) (*22*).

A contrasting hypothesis is founded on the interpretation that the clastic unit is a long-term depositional sequence genetically unrelated to the Chicxulub impact event (*14*, *31*); lenslike spherule deposits locally present below the clastic unit in Mexico would then correlate to the base of the uppermost Cretaceous planktic foraminiferal zone (*14*, *31*). This interpretation also proposes a latest Cretaceous age for the impact breccia found within the Chicxulub crater with the implication that all intermediate to distal K-Pg boundary sites lack the resolution and completeness to firmly establish a correlation to the Chicxulub impact event (*14*, *32*). Additionally, the assertion that the Chicxulub impact preceded the K-Pg mass extinction by ~300 thousand years predicts that the PGE anomaly at the top of the clastic unit resulted from a second large impact event (*14*). In this scenario, either the second impact event or the Deccan flood basalt eruptions caused the K-Pg mass extinction (*14*).

However, sedimentological and petrological data suggest that the lenslike ejecta deposits in Mexico were generated by impact-related liquefaction and slumping, consistent with the single very-high-energy Chicxulub impact (figs. S5 to S9) (*23*). A range of sedimentary structures and the lack of evidence for ocean floor colonization within the clastic unit in northeastern Mexico indicate rapid deposition (figs. S6 to S8) (*22*, *23*). Moreover, the presence of shallow-water benthic foraminifera in the clastic unit (*33*) contradicts a long-term depositional sequence (*14*); if in situ, their presence requires unrealistically rapid relative sea-level changes of >500 m. Lastly, high-resolution planktic foraminiferal analyses in the southern Mexican sections demonstrate that the Chicxulub-linked clastic unit is biostratigraphically equivalent to the officially defined base of the Paleocene (i.e., the red clay

layer) in the El Kef section, Tunisia (Fig. 2 and fig. S1) (*20*).

A pre–K-Pg boundary age for the Chicxulub event has also been argued on the basis of the sequence at a Brazos River site in Texas and from within the crater. If a 3-cm-thick clay layer interbedded in Upper Cretaceous shales at the Brazos River site originated from the Chicxulub impact, the impact occurred significantly before the K-Pg boundary (*31*). Yet, in this clay layer there are no spherules or shocked minerals that would provide evidence for an impact origin, and its high sanidine and quartz content supports a local volcanic origin similar to ash layers found below the K-Pg boundary in Mexico and Haiti (table S3 and figs S10 to S12).

Within the Chicxulub crater, an ~50-cm-thick dolomitic sandstone unit between the impact breccias and the lower Paleocene postimpact crater infill has been interpreted as undisturbed sediments deposited immediately after the impact (fig. S13) (*32*). Rare uppermost Cretaceous planktic foraminifera within this unit were proposed as evidence that the impact preceded the K-Pg mass extinction (*32*). However, this sandstone unit is in part cross-bedded, contains ejecta clasts (fig. S14), and also includes planktic foraminifera of Early Cretaceous age (figs. S14 and S15) (*34*, *35*). These observations, as well as grain-size data (*36*), indicate that deposition of this sequence was influenced by erosion and reworking after the impact and therefore provide no evidence for a long-term post-impact and pre–K-Pg boundary deposition.

In addition, multiple independent lines of evidence place the Chicxulub event at the K-Pg boundary. Geochronologic data demonstrate that the Chicxulub impact correlates to the K-Pg boundary at ~65.5 Ma (*29*). Detailed investigation of continuous sequences from globally distributed marine and terrestrial sites yield no chemical or physical evidence of a large impact in the last million years of the Cretaceous other than the Chicxulub event (table S1 and fig. S16) (*25*, *37*, *38*). Lastly, orbital cycles in deep-sea sites [(*39*) and references therein] demonstrate that there is neither a proposed global 300-thousand-year gap (*14*) nor a hiatus between the Chicxulub impact and the K-Pg boundary.

What Were the Initial Consequences of the Impact?

Asteroid impact models [e.g., (*40*)] predict that an impact large enough to generate the Chicxulub crater would induce earthquakes (magnitude > 11), shelf collapse around the Yucatan platform, and widespread tsunamis sweeping the coastal zones of the surrounding oceans (*7*). Moreover, models suggest the Chicxulub impact had sufficient energy to eject and distribute material around the globe (*7*), possibly enhanced by decomposition of the volatile-rich carbonate and sulfate sediments (*41*). Near-surface target material was ejected ballistically at velocities up to a few km/s as part of the ejecta curtain. This yielded the thick spherule layer at proximal sites and the basal spherule layer at intermediate distance sites (Fig. 2) (*41*). Parts of the ejecta would be entrained within the impact plume: a complex mixture of hot air;

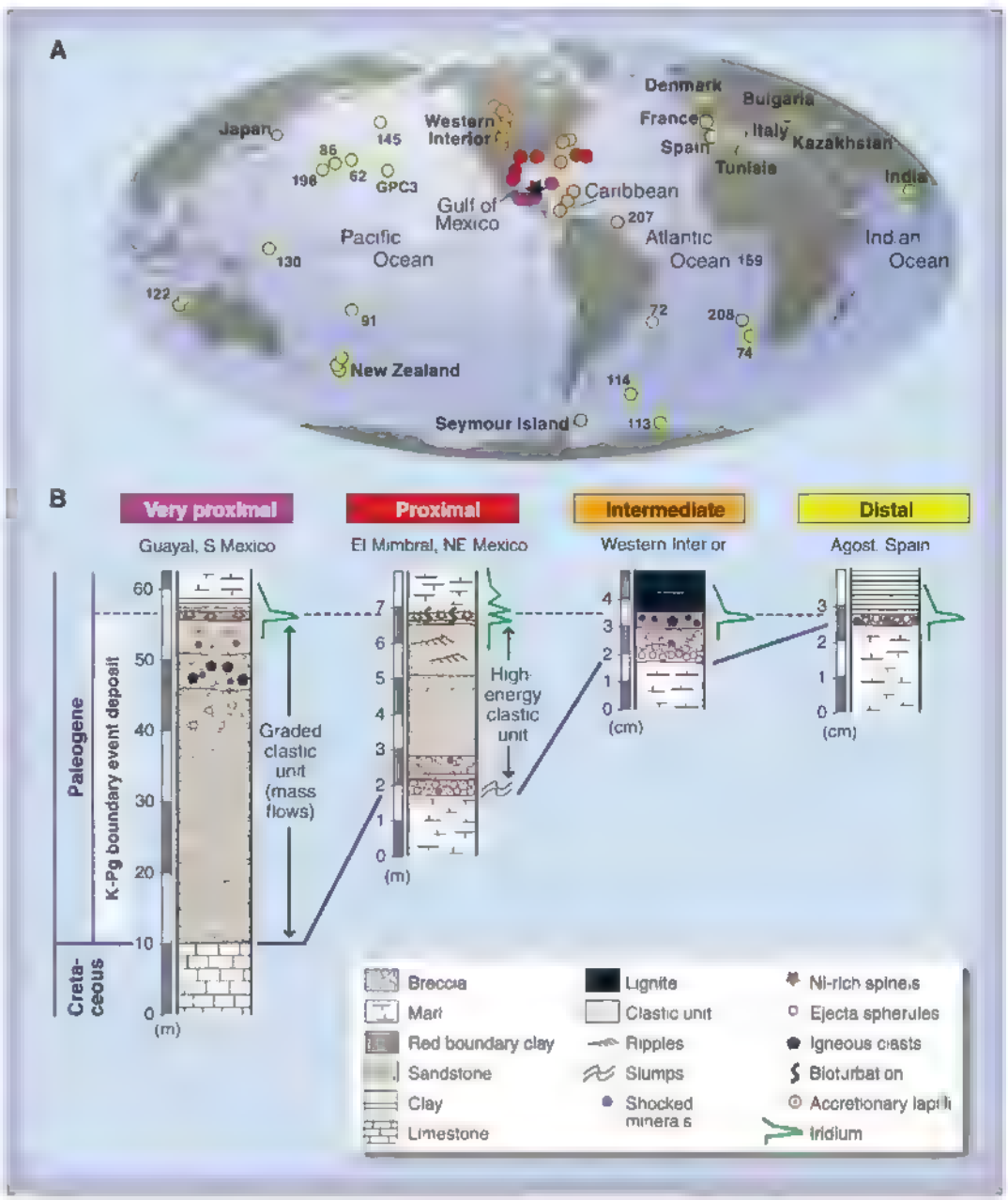

Fig. 2. (**A**) Global distribution of key K-Pg boundary locations. Deep-Sea drill sites are referred to by the corresponding Deep Sea Drilling Project (DSDP) and ODP Leg numbers. The asterisk indicates the location of the Chicxulub impact structure. Colored dots mark the four distinct types of K-Pg boundary event deposit related to distance from the Chicxulub crater (table S1): magenta, very proximal (up to 500 km); red, proximal (up to 1000 km); orange, intermediate distance (1000 to 5000 km); and yellow, distal (>5000 km). Schematic lithologs of the four groups of K-Pg boundary event deposits (**B**) highlighting high-energy event beds (clastic unit) proximal to the crater and the depositional sequence of different materials that originated in one single impact in proximal to distal sites.

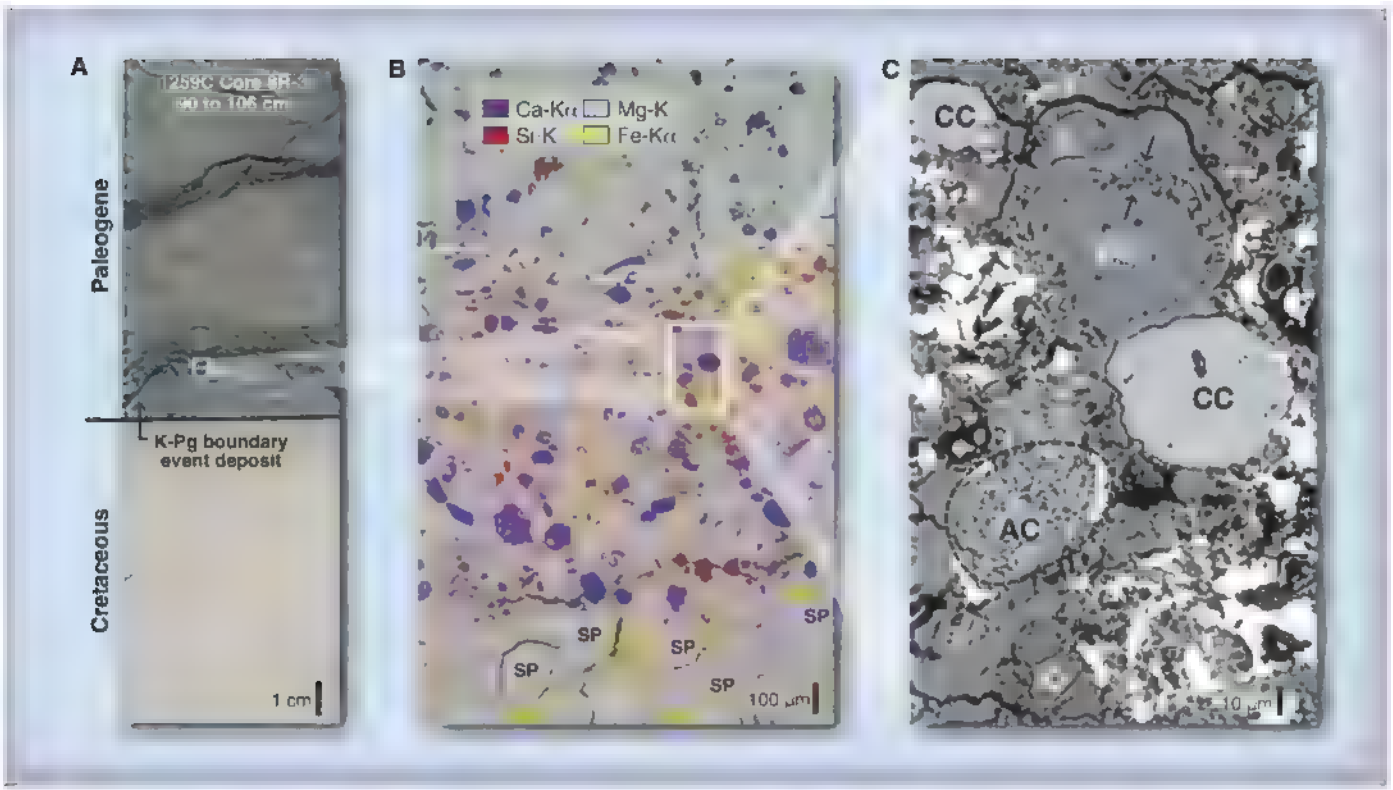

Fig. 3. The K-Pg boundary at ODP Leg 207, western North Atlantic (**A**). An energy-dispersive element distribution map of the box in (A) shows the transition from the top of the spherule-rich graded ejecta sequence (SP) to the lowermost Paleogene sediments (**B**). Note abundant calcite (blue) and dolomite (turquoise) ejecta material as well as occurrence of shocked quartz grains (red) in the uppermost 0.5 mm. A backscattered electron image of the box in (B) shows a rounded dolomite clast (DO) with a Ca-rich clay shell (between arrows), a rounded calcite clast (CC), an accretionary calcite clast (AC), and quartz (Q) interpreted to be of shock-metamorphic origin resulting from the Chicxulub impact (**C**).

projectile material; and impact-vaporized, shock-melted, and fragmented target rocks that expanded rapidly by several km/s up to velocities greater than Earth's escape velocity of 11 km/s. Projectile-rich impact plume deposits form the upper layer in intermediate-distance K-Pg sections and contribute to the single red K-Pg boundary clay layer at distal sites, enriching both in PGEs and shocked minerals (Fig. 2).

Detailed multiphase flow models suggest that the atmospheric reentry of the ejecta spherules may have caused a global pulse of increased thermal radiation at the ground (*42*). Such a thermal pulse is below the lower limits of woody biomass ignition, in agreement with studies yielding no evidence for widespread large wildfires at the K-Pg boundary (*43*), with a possible exception for the Gulf of Mexico region close to the impact site [(*9*) and references therein]. However, the modeled level of radiation is expected to have resulted in thermal damage to the biosphere even if the maximum radiation intensity was only sustained for a few minutes.

Geophysical models indicate that the impact release of large quantities of water, dust, and climate-forcing gases would dramatically alter the climate system (*7*, *8*). The estimated amount of the silicic sub-micrometer-sized dust input of 0.01 to 0.1 Gt (1 Gt = 10^{15} g) is considered to be too low by itself to cause a catastrophic impact winter (*44*). However, abundant sub-micrometer-sized particulate carbonates in the ejecta (*26*) and soot, a strong absorber of short-wave radiation, derived from burning of targeted carbonaceous sediments may have greatly amplified the effects of dust injection (*43*). In addition, there are estimates of at least 100 to 500 Gt of sulfur released nearly instantaneously (*7*, *8*). These figures are likely to be conservative given new larger estimates of the volume of water and sulfur-bearing sediments within Chicxulub's 100-km-diameter transient crater (*45*). The sulfur was probably rapidly transformed to sunlight-absorbing sulfur aerosols with the capacity to cool Earth's surface for years to decades by up to 10°C (*8*, *10*). Temperatures of the deep ocean, however, remained largely unaffected by the impact because of the ocean's large thermal mass (*46*), contributing to a rapid recovery of the global climate. The sulfur release also generated acid rain, which, although not sufficient to completely acidify ocean basins, would have severely affected marine surface waters and/or poorly buffered continental catchments and watersheds (*9*).

Although current models cannot fully assess the combined environmental consequences of the Chicxulub impact (*7*, *9*), the extremely rapid injection rate of dust and climate-forcing gases would have magnified the environmental consequences compared with more-prolonged volcanic eruptions, particularly when compounded by the additional adverse effects of a large impact (e.g., heat wave, soot, and dust release) that are absent during flood basalt volcanism. Specifically, the injection of ~100 to 500 Gt of sulfur into the atmosphere within minutes after the Chicxulub impact contrasts with volcanic injection rates of 0.05 to 0.5 Gt of sulfur per year during the ~1-million-year-long main phase of Deccan flood basalt volcanism (Fig. 1 and fig. S16) (*15*, *16*). Indeed, an only moderate climate change (~2°C warming) during the last 400 thousand years of the Cretaceous has been interpreted to result from Deccan flood basalt volcanism [e.g., (*47*)].

What Does the Fossil Record Reveal About the Global Consequences for Life?

The scale of biological turnover between the Cretaceous and Paleogene is nearly unprecedented in Earth history (*1*). A number of major animal groups disappeared across the boundary (e.g., the nonavian dinosaurs, marine and flying reptiles, ammonites, and rudists) (*48*), and several other major groups suffered considerable, but not complete, species-level extinction (e.g., planktic foraminifera, calcareous nannofossils, land plants) (*12*, *13*, *37*, *49*). Even the groups that showed negligible extinctions exhibited substantial changes in assemblage composition (e.g., benthic foraminifera) (*50*).

For marine phytoplankton, major drivers of ocean productivity, darkness, and suppression of photosynthesis were likely major killing

mechanisms (*9*). There is a clear separation in extinction rate between strongly affected phytoplankton groups with calcareous shells and groups that had organic or siliceous shells. Although the possible effects of surface ocean acidification after the impact may have been an additional stress factor, this selectivity seems to have favored traits contributing to survival of acute stress (*11*, *13*). For example, cyst-forming dinoflagellates persisted through the K-Pg boundary, although assemblage changes suggest a brief cooling phase after the impact [(*51*) and references therein].

The extinction of calcareous primary producers must have caused major starvation higher up in the food chain. This would explain the extinctions of animals relying on plankton as their food source, the survival of organisms living in detritus-based food chains, and the dwarfing in evolutionary lineages observed in marine biota after the K-Pg boundary (*9*, *52*, *53*). The abrupt drop in plankton productivity was apparently short-lived as shown by marine biomarker data (*54*). The negative shift of the stable carbon isotopic value ($\delta^{13}C$) (Fig. 1) and the surface to deep water $\delta^{13}C$ gradient collapse is indicative of a major disruption to marine productivity and the ocean's biological pump (*11*). However, the large magnitude of the $\delta^{13}C$ anomaly suggests that the release of methane, input of soot, or the dependency of the isotopic signal on the metabolism of different species may have contributed to the anomaly (*50*).

On land, the loss of the diverse vegetation and the onset of the fern-spore spike following the K-Pg boundary indicates instantaneous (days to months) destruction of diverse forest communities coincident with deposition of ejecta from the Chicxulub impact (fig. S17) (*12*, *37*, *55*). A shutdown of photosynthesis because of low light levels is also indicated by high abundances of fungal spores in a thin layer of sediment preceding the recovery succession of ferns at a New Zealand K-Pg boundary site (*56*). Analogous to the marine environment, the abrupt elimination of the forest communities may have had similarly catastrophic effects on animals relying on primary producers (e.g., the herbivorous dinosaurs), whereas detritus-based food chains (e.g., in lakes) were apparently less affected (*52*).

Faunal and floral changes during the Late Cretaceous do occur [e.g., (*12*, *47*)] but are clearly distinguishable from the abrupt mass extinction and ecosystem disruption coincident with the K-Pg boundary, as indicated by high-resolution records of marine planktonic microfossils and terrestrial pollen and spores (*12*, *13*, *25*, *37*, *55*, *57*). Productivity proxies (e.g., carbonate content) linked to orbitally tuned stratigraphic time scales provide no evidence for major changes preceding the boundary (*39*). Claims of gradual or stepwise extinctions during the Late Cretaceous culminating in the K-Pg mass extinction (*14*) and survivorship through the K-Pg boundary may be explained by short-term survival with greatly reduced population sizes, sampling artifacts, or reworking of Cretaceous fossils [e.g., (*57*)]. In addition, the global onset of opportunistic species blooms and the evolutionary radiation of new taxa started consistently after the K-Pg boundary mass extinction (Fig. 1 and fig. S17) (*49*, *55*).

What Do We Need to Look at Next?

The correlation between impact-derived ejecta and paleontologically defined extinctions at multiple locations around the globe leads us to conclude that the Chicxulub impact triggered the mass extinction that marks the boundary between the Mesozoic and Cenozoic eras ~65.5 million years ago. This conclusion is reinforced by the agreement of ecological extinction patterns with modeled environmental perturbations. Although the relative importance of the different impact-induced environmental effects on the K-Pg mass extinction is still under scrutiny, alternative multi-impact or volcanic hypotheses fail to explain the geographic and stratigraphic distribution of ejecta and its composition, the timing of the mass extinction, and the scale of environmental changes required to cause it. Future geophysical, geological, and drilling studies of the Chicxulub structure will further constrain the impact process and the amount and nature of environment-altering gases generated by this so far unparalleled combination of a large impact into ~3- to 4-km-thick carbonate- and sulfate-rich target rocks. Research focused on high-resolution studies of the ejected material, integrated climate models, and detailed study of related fossil successions will help reveal the physical and biological mechanisms of the K-Pg mass extinction and may also aid in understanding other mass extinction events in Earth history.

References and Notes

1. J. Alroy, *Proc. Natl. Acad. Sci. U.S.A.* **105** (suppl. 1), 11536 (2008)
2. L. W. Alvarez, W. Alvarez, F. Asaro, H. V. Michel, *Science* **208**, 1095 (1980)
3. J. Smit, J. Hertogen, *Nature* **285**, 198 (1980)
4. A. Montanari *et al.*, *Geology* **11**, 668 (1983)
5. B. F. Bohor, *Tectonophysics* **171**, 359 (1990)
6. A. R. Hildebrand *et al.*, *Geology* **19**, 867 (1991)
7. O. B. Toon, K. Zahnle, D. Morrison, R. P. Turco, C. Covey, *Rev. Geophys.* **35**, 41 (1997).
8. E. Pierazzo, A. N. Hahmann, L. C. Sloan, *Astrobiology* **3**, 99 (2003)
9. D. A. Kring, *Palaeogeogr. Palaeoclimatol. Palaeoecol.* **255**, 4 (2007)
10. K. O. Pope, K. H. Baines, A. C. Ocampo, B. A. Ivanov, *J. Geophys. Res.* **102**, (E9), 21645 (1997)
11. S. D'Hondt, *Annu. Rev. Ecol. Evol. Syst.* **36**, 295 (2005)
12. A. R. Sweet, D. R. Braman, *Can. J. Earth Sci.* **38**, 249 (2001)
13. P. Bown, *Geology* **33**, 653 (2005)
14. G. Keller, W. Stinnesbeck, T. Adatte, D. Stuben, *Earth Sci. Rev.* **62**, 327 (2003)
15. S. Self, M. Widdowson, T. Thordarson, A. E. Jay, *Earth Planet. Sci. Lett.* **248**, 518 (2006)
16. A.-L. Chenet *et al.*, *J. Geophys. Res.* **114**, (B6), B06103 (2009)
17. J. Smit, *Annu. Rev. Earth Planet. Sci.* **27**, 75 (1999)
18. P. Claeys, W. Kiessling, W. Alvarez, *Spec. Pap. Geol. Soc. Am.* **356**, 55 (2002)
19. J. Urrutia-Fucugauchi, L. E. Marín, A. Trejo-Garcia, *Geophys. Res. Lett.* **23**, 1565 (1996)
20. I. Arenillas *et al.*, *Earth Planet. Sci. Lett.* **249**, 241 (2006)
21. K. Goto *et al.*, *Cretaceous Res.* **29**, 217 (2008)
22. J. Smit, W. Alvarez, A. Montanari, P. Claeys, J. M. Grajales-Nishimura, *Spec. Pap. Geol. Soc. Am.* **307**, 151 (1996)
23. P. Schulte, A. Kontny, *Spec. Pap. Geol. Soc. Am.* **384**, 191 (2005)
24. R. D. Norris, B. T. Huber, B. T. Self-Trail, *Geology* **27**, 419 (1999)
25. K. G. MacLeod, D. L. Whitney, B. T. Huber, C. Koeberl, *Geol. Soc. Am. Bull.* **119**, 101 (2007)
26. P. Schulte *et al.*, *Geochim. Cosmochim. Acta* **73**, 1180 (2009)
27. E. Molina *et al.*, *Episodes* **29**, 263 (2006)
28. J. V. Morgan *et al.*, *Earth Planet. Sci. Lett.* **251**, 264 (2006)
29. Materials and methods are available as supporting material on *Science* Online
30. T. J. Bralower, C. K. Paull, R. M. Leckie, *Geology* **26**, 331 (1998)
31. G. Keller *et al.*, *Earth Planet. Sci. Lett.* **255**, 339 (2007)
32. G. Keller *et al.*, *Meteorit. Planet. Sci.* **39**, 1127 (2004)
33. L. Alegret, E. Molina, E. Thomas, *Geology* **29**, 891 (2001).
34. J. A. Arz, L. Alegret, I. Arenillas, *Meteorit. Planet. Sci.* **39**, 1099 (2004)
35. J. Smit, S. V. D. Gaast, W. Lustenhouwer, *Meteorit. Planet. Sci.* **39**, 1113 (2004)
36. T. J. Bralower *et al.*, *Geology*, in press.
37. D. J. Nichols, K. R. Johnson, *Plants and the K-T Boundary* (Cambridge Univ. Press, Cambridge 2008), p. 280
38. N. Robinson, G. Ravizza, R. Coccioni, B. Peucker-Ehrenbrink, R. D. Norris, *Earth Planet. Sci. Lett.* **281**, 159 (2009)
39. T. Westerhold *et al.*, *Palaeogeogr. Palaeoclimatol. Palaeoecol.* **257**, 377 (2008)
40. B. Ivanov, *Sol. Syst. Res.* **39**, 381 (2005)
41. N. Artemieva, J. Morgan, *Icarus* **201**, 768 (2009)
42. T. J. Goldin, H. J. Melosh, *Geology* **37**, 1135 (2009)
43. M. C. Harvey, S. C. Brassell, C. M. Belcher, A. Montanari, *Geology* **36**, 355 (2008)
44. K. O. Pope, *Geology* **30** 99 (2002).
45. S. P. S. Gulick *et al.*, *Nat. Geosci.* **1**, 131 (2008)
46. T. Luder, W. Benz, T. F. Stocker, *J. Geophys. Res.* **108**, (E7), 5074 (2003).
47. P. Wilf, K. R. Johnson, B. T. Huber, *Proc. Natl. Acad. Sci. U.S.A.* **100**, 599 (2003)
48. D. E. Fastovsky, P. M. Sheehan, *GSA Today* **15**, 4 (2005).
49. I. Arenillas, J. A. Arz, E. Molina, C. Dupuis, *Micropaleontology* **46**, 31 (2000).
50. E. Thomas, *Spec. Pap. Geol. Soc. Am.* **424**, 1 (2007)
51. P. S. Willumsen, *Cretaceous Res.* **27**, 954 (2006)
52. P. M. Sheehan, P. J. Coorough, D. E. Fastovsky, *Spec. Pap. Geol. Soc. Am.* **307**, 477 (1996)
53. M. Aberhan, S. Weidemeyer, W. Kiessling, R. A. Scasso, F. A. Medina, *Geology* **35**, 227 (2007)
54. J. Sepulveda, J. E. Wendler, R. E. Summons, K.-U. Hinrichs, *Science* **326**, 129 (2009)
55. V. Vajda, J. I. Raine, C. J. Hollis, *Science* **294**, 1700 (2001)
56. V. Vajda, S. McLoughlin, *Science* **303**, 1489 (2004)
57. C. R. C. Paul, *Palaeogeogr. Palaeoclimatol. Palaeoecol.* **224**, 291 (2005)

58. D.J.N. passed away during the final revision of this paper. His more than 30 years of work on the Cretaceous-Paleogene boundary influenced the data, ideas, and thesis of this paper. This research used samples and photos provided by the Ocean Drilling Program (ODP) and the International Continental Scientific Drilling Program (ICDP) and was funded by the Deutsche Forschungsgemeinschaft, the Austrian Science Foundation (FWF), Danish Carlsberg Foundation, European Social Fund, Research Foundation Flanders, Mexican Consejo Nacional de Ciencia y Tecnología, NASA, Japan Society for the Promotion of Science, Joint Oceanographic Institutions, K.U. Leuven Research Fund, UK Natural Environment Research Council, NSF, the Swedish Research Council (VR) and the Royal Swedish Academy of Sciences through the Knut and Alice Wallenberg Foundation, and the Spanish Ministerio de Ciencia e Innovación. We are grateful to E. Thomas and an anonymous reviewer for valuable comments and thank G. Izett for providing support and photos.

Supporting Online Material

www.sciencemag.org/cgi/content/full/327/5970/1214/DC1
Materials and Methods
SOM Text
Figs. S1 to S17
Tables S1 to S3
References

10.1126/science.1177265

Contributions of Stratospheric Water Vapor to Decadal Changes in the Rate of Global Warming

Susan Solomon,[1] Karen H. Rosenlof,[1] Robert W. Portmann,[1] John S. Daniel,[1] Sean M. Davis,[1,2] Todd J. Sanford,[1,2] Gian-Kasper Plattner[3]

Stratospheric water vapor concentrations decreased by about 10% after the year 2000. Here we show that this acted to slow the rate of increase in global surface temperature over 2000–2009 by about 25% compared to that which would have occurred due only to carbon dioxide and other greenhouse gases. More limited data suggest that stratospheric water vapor probably increased between 1980 and 2000, which would have enhanced the decadal rate of surface warming during the 1990s by about 30% as compared to estimates neglecting this change. These findings show that stratospheric water vapor is an important driver of decadal global surface climate change.

Over the past century, global average surface temperatures have warmed by about 0.75°C. Much of the warming occurred in the past half-century, over which the average decadal rate of change was about 0.13°C, largely due to anthropogenic increases in well-mixed greenhouse gases (*1*). However, the trend in global surface temperatures has been nearly flat since the late 1990s despite continuing increases in the forcing due to the sum of the well-mixed greenhouse gases (CO_2, CH_4, halocarbons, and N_2O), raising questions regarding the understanding of forced climate change, its drivers, the parameters that define natural internal variability (*2*), and how fully these terms are represented in climate models. Here we use a combination of data and models to show that stratospheric water vapor very likely made substantial contributions to the flattening of the global warming trend since about 2000. Although earlier data are less complete, the observations also suggest that stratospheric water contributed to enhancing the warming observed during 1980–2000 [as emphasized in previous studies (*3*–*5*)].

Water vapor is a highly variable gas. Tropospheric water vapor increases in close association with warming (*6*), and this represents a major climate feedback that is well simulated in global climate models (*7*). In sharp contrast, current global models are limited in their representations of key processes that control the distribution and variability of water within the stratosphere, such as the deep convection that affects the temperatures at which air enters the stratosphere and the resulting drying (*8*). Current global climate models simulate lower-stratospheric temperature trends poorly (*9*), and even up-to-date stratospheric chemistry-climate models do not consistently reproduce tropical tropopause minimum temperatures (*10*) or recently observed changes in stratospheric water vapor (*11*). Because of these limitations in prognostic climate model simulations, here we impose observed stratospheric water vapor changes diagnostically as a forcing for the purpose of evaluation and comparison to other climate change agents. However, in the real world, the contributions of changes in stratospheric water vapor to global climate change may be a source of unforced decadal variability, or they may be a feedback coupled to climate change, as discussed further below.

Increases in stratospheric water vapor act to cool the stratosphere but to warm the troposphere, whereas the reverse is true for stratospheric water vapor decreases. Previous studies have suggested that stratospheric water vapor changes might contribute significantly to climate change (*3*–*5*), but there has been debate about the magnitude of the radiative effects (*12*) as well as whether systematic changes in water vapor could be documented, because of calibration issues (*13*) and limited spatial coverage before the mid-1990s. Beginning in 1980, information on trends in stratospheric water was based largely on balloon observations from a single site in Boulder, Colorado (*14*), but high-quality global satellite observations from multiple platforms began in the 1990s. A substantial and unexpected decrease in stratospheric water vapor was documented after the year 2000 (*15*), and lower levels have persisted up to the present (mid-2009, see Fig. 1). Here we use a range of recent observations of stratospheric water vapor coupled with detailed radiative transfer and modeling information to describe the global changes in this important species and to estimate their expected impacts on climate trends.

Recent global stratospheric water vapor changes. Data used to assess global changes in stratospheric water vapor are from the HALogen Occultation Experiment (HALOE) that flew on the Upper Atmosphere Research Satellite (UARS) from late 1991 through November 2005, with coverage extending from the tropopause to the stratopause over 65°S to 65°N (*16*). Figure 1A shows the time series of mid-latitude water vapor in the lower stratosphere based on HALOE and balloon sonde measurements (*17*), along with two additional (and independent) sets of satellite data from the Stratospheric Aerosol and Gas Experiment II (SAGE II) (*18*) and from the Microwave Limb Sounder (MLS) (*19*) instruments. Taken together, these data provide strong evidence for a sharp and persistent drop of about 0.4 parts per million by volume (ppmv) after the year 2000. Observations of lower-stratospheric tropical ozone changes also reveal a sharp change after 2000 (*15*). Before this decrease, the balloon data suggest a gradual mid-latitude increase in lower-stratospheric water vapor of more than 1 ppmv from about 1980 to 2000. The HALOE data as well as other Northern Hemisphere mid-latitude data sets also support increases in lower-stratospheric water vapor during the 1990s of about 0.5 ppmv (*15*, *20*).

Using HALOE data, the annual average water vapor difference before and after the persistent drop at the end of 2000 is contoured in Fig. 1B. Averages were constructed on a seasonal basis for two comparison periods, from 1996–2000 and for 2001.5–2005.5. Only measurements above the tropopause were used, i.e., water vapor changes in the troposphere were not included in the analysis. Figure 1B shows that substantial water vapor decreases after 2000 extend throughout the bulk of the stratosphere, with the largest magnitudes in the lowermost tropical and subtropical stratosphere.

The water vapor content of the stratosphere is controlled by transport through the tropopause region (*21*) and the oxidation of methane within the stratosphere. Transport into the stratosphere occurs mainly as air rises in the tropics and is largely a function of the coldest temperature encountered, or the cold point (*8*, *22*–*24*). The drop in stratospheric water vapor observed after 2001 has been correlated (*25*) with sea surface temperature (SST) increases in the vicinity of the tropical warm pool (Fig. 1C), which are related to El Niño Southern Oscillation, the maximum correlation between stratospheric entry values of water vapor and cold point temperatures was found just to the west of the warmest SSTs (10°N to 10°S; 171° to 200°W). Figure 1C shows that although the water vapor changes appear to be positively correlated with SSTs after about 1997, the behavior is different before that year, at least insofar as short-term variations are concerned, and this is discussed further below. The reduction in stratospheric water vapor remains relatively steady from 2001 through the end of 2007 [with a strong quasi-biennial oscillation (QBO) signal in water also present (*26*)]. Although there is some evidence for a slight increase from mid-

[1]National Oceanic and Atmospheric Administration (NOAA) Earth System Research Laboratory, Chemical Sciences Division, Boulder, CO, USA. [2]Cooperative Institute for Research in Environmental Sciences, University of Colorado, Boulder, CO, USA. [3]Climate and Environmental Physics, Physics Institute, University of Bern, Sidlerstrasse 5, 3012 Bern, Switzerland

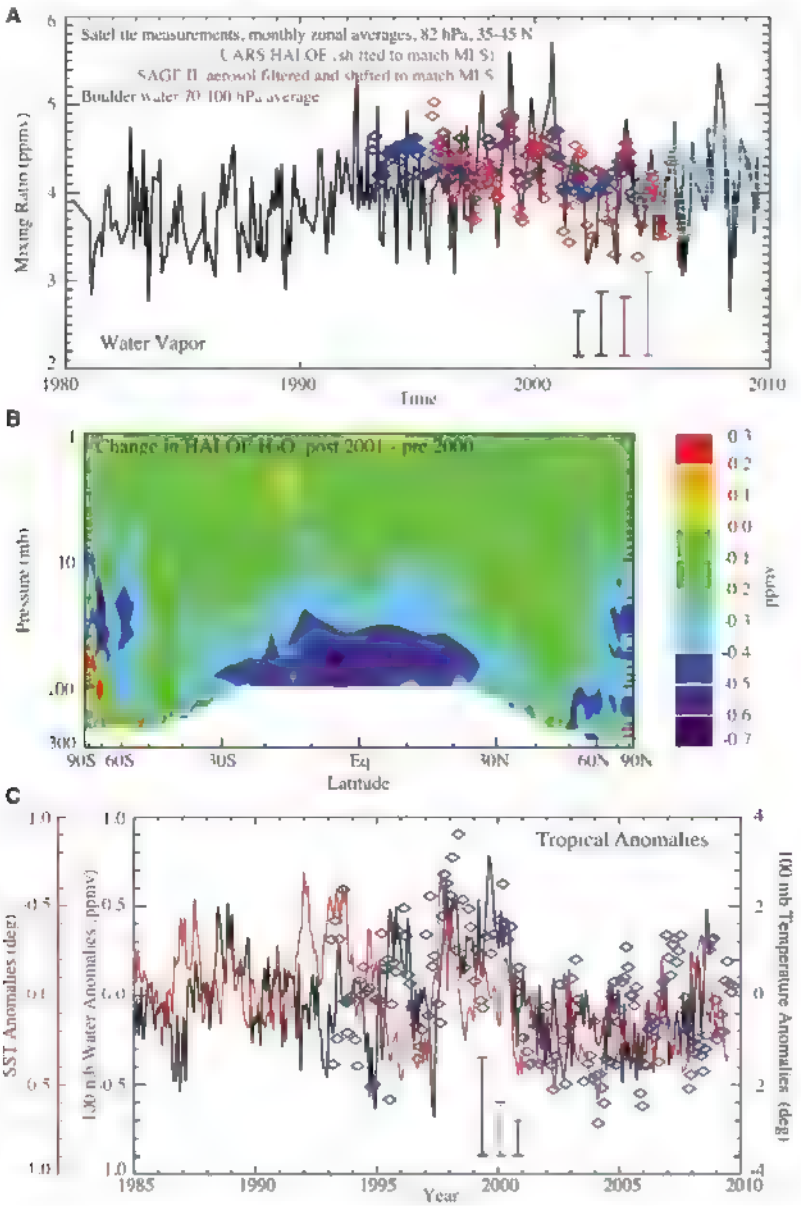

Fig. 1. Observed changes in stratospheric water vapor. **(A)** Balloon measurements of water vapor, taken near Boulder, Colorado (40°N, 105.25°W) along with zonally averaged satellite measurements in the 35° to 45° latitude range at 82 hPa from the Aura MLS (turquoise squares), UARS HALOE (blue diamonds), and SAGE II instruments (red diamonds). The SAGE II and HALOE data have been adjusted to match MLS during the overlap period from mid-2004 to the end of 2005. Representative uncertainties are given by the colored bars; for the satellite data sets, these show the precision as indicated by the monthly standard deviations, while for the balloon data set this is the estimated uncertainty provided in the Boulder data files. **(B)** The altitude/latitude distribution of the drop in HALOE water vapor mixing ratio (in ppmv) in the stratosphere that occurred after 2000. The plot shows the difference between the annual average from June 2001 to May 2005 and the average from January 1996 through December 1999. To extend HALOE data toward the poles, we averaged observations on equivalent latitudes [a coordinate based on potential vorticity that has been used in a variety of satellite studies outside of the subtropics, as in (*36*)], and we then filled any gaps to the pole with the data from the highest equivalent latitude available. **(C)** 10°N to 10°S monthly average anomalies of temperatures and water vapor relative to the period from 1993 to 2006. 100-hPa monthly-averaged temperature anomalies are taken from the Japanese Reanalysis [(*37*), black line], SST anomalies from the Optimal Interpolation Version 2 data obtained from the NOAA Earth System Research Laboratory physical sciences division Web site (www.esrl.noaa.gov/psd) (red line), and 100-hPa water vapor anomalies from the combined UARS HALOE and Aura MLS time series (blue diamonds). Temperatures and SSTs are for longitudinal regions in the Pacific; 139° to 171° for the SSTs, and 171° to 200° for the 100-hPa temperatures, whereas zonal averages are shown for water vapor. Representative uncertainties are given by the colored bars as in (A) above and show the average monthly standard deviations.

2007 to mid-2008, the 5-year running mean of the monthly averaged satellite water anomaly in Fig. 1C is nearly flat from 2001 to late 2009 (within ±0.05 ppmv) and is assumed to be constant here.

Radiative effects of stratospheric water vapor changes. Stratospheric water vapor changes affect the fluxes of longwave (infrared) and (to a lesser extent) shortwave (solar) radiation, and can thereby influence the temperature in the stratosphere and troposphere. Radiative transfer calculations were carried out with a high–spectral resolution model (*27*). This accurate line-by-line radiative transfer model integrates over spectral lines to compute the changes in the radiative fluxes at the tropopause when the stratospheric water vapor changes are imposed (the instantaneous radiative forcing). Stratospheric temperatures are then adjusted to the perturbation, using the fixed-dynamical-heating assumption to give the adjusted radiative forcing. The calculation uses an atmosphere derived from the International Satellite Cloud Climatology Project (ISCCP) climatology for temperatures, tropospheric water, and cloud amounts and fractions (*28*). Clouds have only a small effect on the computed radiative forcing, because the water vapor changes considered are in the stratosphere.

The effects of water vapor changes were probed with two sets of radiative transfer calculations. In the first of these, the satellite-based global stratospheric water vapor distributions as discussed above were seasonally averaged above the tropopause for 1996–2000 and 2001–2005, respectively, to examine the climate impact of the water vapor decrease after 2000. The adjusted radiative forcing of climate from this change was found to be −0.098 W m^{-2}. For comparison, the radiative forcing increase due to the growth of carbon dioxide from 1996 to 2005 was about +0.26 W m^{-2}. In a second case, it was assumed that water vapor had increased uniformly by 1 ppmv at all latitudes and altitudes above the tropopause between 1980 and the 1996–2000 period. A total globally averaged radiative forcing including a stratospheric adjustment of +0.24 W m^{-2} was obtained for this assumed 1-ppmv increase, which is close to the value of +0.29 W m^{-2} reported, for example, in (*3*). This can be compared to the radiative forcing increase due to the growth of carbon dioxide of about +0.36 W m^{-2} from 1980 to 1996. It is clear that carbon dioxide has been increasing for more than a century, whereas the water vapor changes are far shorter in duration, and both the magnitude and time scale of radiative forcing perturbations are important to the resulting surface climate response. The comparison of these radiative forcings nonetheless suggests that the decadal changes in stratospheric water vapor have the potential to affect recent climate, and this is further examined in the next section.

It is informative to investigate the effect of stratospheric water vapor changes at different altitudes on surface climate change by computing

the kernel function for vertical changes (i.e., the radiative forcing per layer). In Fig. 2A we show the kernel function computed using 1-ppmv perturbations of water vapor imposed in 1-km-thick layers. Figure 2A shows that the influence of changes in stratospheric water vapor on shortwave radiation is much smaller than the influence on longwave radiation. Stratospheric adjustment has a large effect on the net radiative forcing in the lowermost stratosphere, where it reduces the impact of local changes there, although they still dominate the profile. Kernel calculations are presented here only for the purpose of illustration, because the full global distributions are used in the detailed radiative calculations discussed above. The kernels should only be considered approximate when convolved with realistic profile changes (comparisons suggest possible errors of between 10 and 25%).

Figure 2A shows that the profile of the kernel function is strongly peaked around the tropopause. The response of surface climate to uniform stratospheric water vapor perturbations would be dominated by this narrow region, at a vertical scale too fine to be captured in many global climate models. Further, the balloon and satellite water vapor records (Figs. 2B and 1) show that the largest observed changes in stratospheric water vapor occurred near the tropopause, so that the shape of the observed stratospheric water perturbation further increases the dominance of the tropopause region in recent radiative forcing. Because of a lack of global data, we have considered only the stratospheric changes, but if the drop in water vapor after 2000 were to extend downward by 1 km, Fig. 2 shows that this would significantly increase its effect on surface climate.

Changes in stratospheric water vapor linked to cold point changes in the tropics are expected to dominate the water vapor variations in the lowermost stratosphere and are transported laterally to mid-latitudes on time scales of months to at most a few years. Thus, the gradual and persistent water vapor increase observed at Boulder from 1980 to 2000 as shown in Fig. 1A should reflect similar changes occurring elsewhere in the altitude range of greatest importance for radiative forcing. Nevertheless, the data before the mid-1990s are limited in space and/or time, and the stratospheric water vapor trends before 2000 should therefore be considered uncertain, whereas the decrease after 2000 is much better characterized by multiple records.

Methane oxidation increases stratospheric water vapor, but its contributions are small near the tropopause (*29*), the region of greatest impact for radiative forcing as shown in Fig. 2. This explains why studies in which methane oxidation is the only adopted source of increasing stratospheric water provide considerably smaller radiative forcings than those shown here. Estimates of the forcing due to methane oxidation have varied widely among different studies (*30*), perhaps because of different shapes of the water profile in the region of greatest sensitivity. Such differences are a source of potential confusion about the influence of stratospheric water vapor changes on surface climate, and they underscore the need to consider the direct input of water vapor at the cold point.

Global temperature response. We used the Bern 2.5CC intermediate complexity model (*31*) to estimate the effect of the decrease in stratospheric water vapor after 2000 on recent global average decadal temperature trends. The model has been extensively compared to other Earth system models of intermediate complexity as well as to atmosphere-ocean general circulation models [AOGCMs (*31*)]. A radiative forcing time series of well-mixed greenhouse gases and tropospheric aerosols from 1760 to 2008 was used to provide a baseline model scenario to which cases including stratospheric water vapor changes are compared (additional forcings such as tropospheric ozone were not considered). The resulting total radiative forcing and calculated temperature changes relative to 1980 are shown in Fig. 3, together with observed annual average surface temperature anomalies from three different global temperature data sets for individual years (*32*), and for the 5-year running mean. Absolute values of the calculated temperature changes are dependent on the model climate sensitivity and transient climate response and are hence somewhat arbitrary. The focus here is therefore not on the detailed match to observed absolute warming but rather on the changes in radiative forcing and their likely implications for relative changes in the decadal rates of warming from 1980 to 2009.

Figure 3 shows the added forcing and estimated warming corresponding to an adopted linear increase of stratospheric water vapor forcing ranging from 0 to +0.24 W m^{-2} from 1980 to 2000 based on the analysis in the previous section. This range brackets the large uncertainty in water vapor trends before 2000. The figure also shows the effect of the observed post-2000 decrease, for which there is much higher confidence as discussed above. Figure 3 shows that the reduced forcing associated with the drop in stratospheric water vapor after 2000 decreased the rate of warming as compared to what would have been expected for well-mixed greenhouse gases alone by about 25% (from about 0.14°C per decade to 0.10°C per decade for this particular model or about a −0.04°C per decade change). Figure 3 also shows that an increase in global stratospheric water vapor at the upper end of the range suggested by the balloon measurements should be expected to have steepened the rate of global warming from 1990 to 2000 by about 30% as compared to a case neglecting stratospheric water changes.

Figure 3 thus shows that the decline in stratospheric water vapor after 2000 should be expected to have significantly contributed to the flattening of the global warming trend in the past decade, and stratospheric water increases may also have acted to steepen the observed warming trend in the 1990s. The transient climate response (TCR) of the model used in Fig. 3 is slightly less than the mean of models assessed by the Intergovernmental Panel on Climate Change (IPCC) (*1*), the "very likely" range of TCR across climate models suggests that the effects of the stratospheric water vapor changes on the warming trends considered here could be greater by about 80% or smaller by about 40%. Our analysis focuses only on estimating the contributions of stratospheric water vapor changes to recent decadal rates of warming,

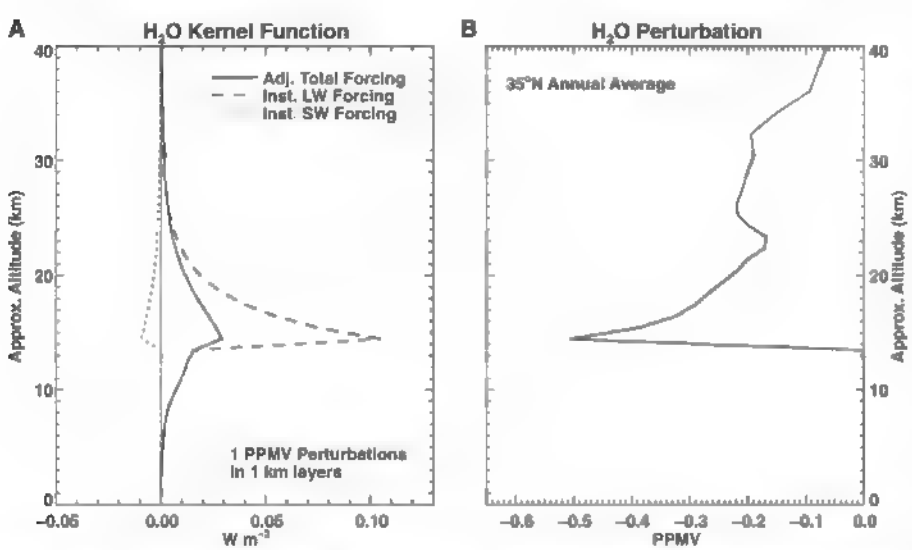

Fig. 2. Effect of stratospheric water vapor changes on radiative forcing of surface climate based on detailed line-by-line calculations. **(A)** Instantaneous longwave (LW) and instantaneous shortwave (SW) radiative forcing, along with the adjusted net total forcing versus altitude at 35°N obtained for a uniform change of 1 ppmv in 1-km layers using a line-by-line radiative transfer model; the largest sensitivity occurs close to the tropopause. **(B)** The observed post-2000 water vapor decrease at 35°N (from Fig. 1B), showing that the largest changes occurred in the most sensitive region.

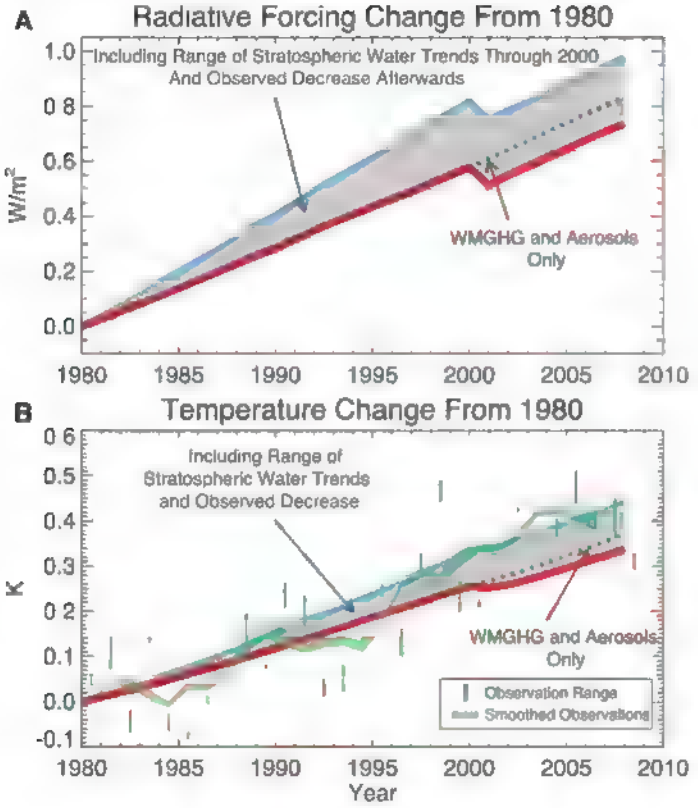

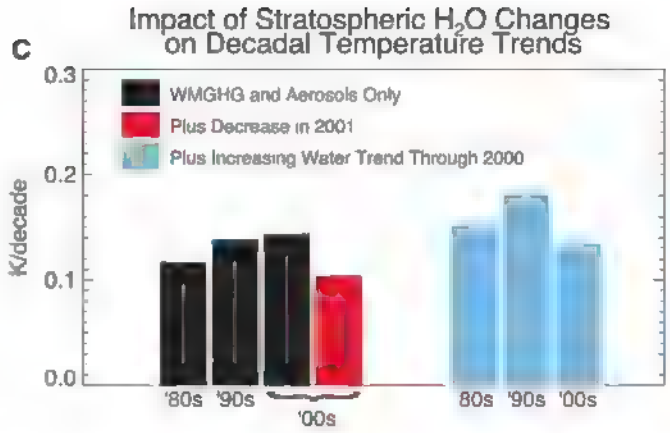

Fig. 3. Impact of changes in stratospheric water vapor on surface climate. **(A)** Time series of the changes in radiative forcing since 1980 due to well-mixed greenhouse gases (WMGHG), aerosols, and stratospheric water vapor. The forcings of CO_2, CH_4, and N_2O are obtained from historical mixing ratios (*38*). The forcing of the Montreal Protocol gases is calculated from their radiative efficiencies and observed mixing ratio time series (*39*). The time dependence of the tropospheric aerosol forcing is taken from Goddard Institute for Space Studies (GISS) model input (http://data.giss.nasa.gov/modelforce/RadF.txt), but scaled so that total aerosol radiative forcing from 1985 to 2004 is −1.1 W m^{-2}, following (*40*). The shaded region shows the stratospheric water contribution calculated from an assumed range of decadal trends from 1980 to 2000 of 0 (red line) to 0.5 ppmv per decade (blue line) along with the observed decline prescribed after 2000. **(B)** Measured and modeled temperature changes relative to 1980. Three different observed global temperature records were used [from the National Climate Data Center (NCDC), Climatic Research Unit (CRU), and GISS records], with the green markers indicating the range across the three data sets in each year. The green shaded line shows the range of the 5-year running mean of the three data sets. **(C)** Decadal warming rates arising from (i) the WMGHG and aerosols alone (black), as well as (ii) that obtained including the stratospheric water decline after 2000 (red) and (iii) including both the stratospheric water vapor decline after 2000 and the increase in the 1980s and 1990s (cyan). Smooth lines show the warmings calculated by the Bern intermediate complexity climate model, which does not simulate internal variability from one year to another. Volcanoes have not been included in the radiative forcing. The climate sensitivity of the model used is 3°C for a doubling of atmospheric CO_2, and the transient climate response is 1.7°C, slightly less than the mean of the range of models assessed by the IPCC (*1*). The colors of the bars in (C) correspond to the respective lines shown in (A) and (B).

additional contributions such as from solar variations (*33*), aerosols, natural variability, or other processes are not ruled out by this study.

Recent observations have suggested a correlation of the post-2000 stratospheric water vapor decrease with SST changes near the tropical warm pool region and associated cooling of the cold point that governs water vapor input to the stratosphere in the tropics (Fig. 1C). However, the relation between SSTs in the warm pool region and stratospheric water vapor changes character (from negative to positive short-term correlations) from 1980 to 2009, suggesting that other processes may also be important or that the correlation may be a transient feature linked to the specific pattern of SSTs at a given time rather than to the average warming of SSTs around the globe. It is therefore not clear whether the stratospheric water vapor changes represent a feedback to global average climate change or a source of decadal variability. Current global climate models suggest that the stratospheric water vapor feedback to global warming due to carbon dioxide increases is weak (*1*, *34*), but these models do not fully resolve the tropopause or the cold point, nor do they completely represent the QBO, deep convective transport and its linkages to SSTs, or the impact of aerosol heating on water input to the stratosphere (*35*). This work highlights the importance of using observations to evaluate the effect of stratospheric water vapor on decadal rates of warming, and it also illuminates the need for further observations and a closer examination of the representation of stratospheric water vapor changes in climate models aimed at interpreting decadal changes and for future projections.

References and Notes

1. IPCC, *Climate Change 2007: The Physical Science Basis*, Contribution of Working Group I to the Fourth Assessment Report of the Intergovernmental Panel on Climate Change, S. Solomon *et al.*, Eds. (Cambridge Univ. Press, Cambridge, 2007).
2. D. R. Easterling, F. M. Wehner, *Geophys. Res. Lett.* **36**, L08706 (2009).
3. P. M. de S. Forster, K. P. Shine, *Geophys. Res. Lett.* **26**, 3309 (1999).
4. C. A. Smith, J. D. Haigh, R. Toumi, *Geophys. Res. Lett.* **28**, 179 (2001).
5. D. T. Shindell, *Geophys. Res. Lett.* **28**, 1551 (2001).
6. K. E. Trenberth, J. Fasullo, L. Smith, *Clim. Dyn.* **24**, 741 (2005).
7. A. E. Dessler, Z. Zhang, P. Yang, *Geophys. Res. Lett.* **35**, L20704 (2008).
8. P. W. Mote *et al.*, *J. Geophys. Res.* **101**, (D2), 3989 (1996).
9. E. C. Cordero, P. M. Forster, *Atmos. Chem. Phys.* **6**, 5369 (2006).
10. A. Gettelman *et al.*, *Atmos. Chem. Phys.* **9**, 1621 (2009).
11. R. R. Garcia, D. R. Marsh, D. E. Kinnison, B. A. Boville, F. Sassi, *J. Geophys. Res.* **112**, (D2), D09301 (2007).
12. V. Oinas, A. A. Lacis, D. Rind, D. T. Shindell, J. E. Hansen, *Geophys. Res. Lett.* **28**, 2791 (2001).
13. D. Kley *et al.*, *SPARC Assessment of Upper Tropospheric and Stratospheric Water Vapour* [WCRP-No. 113,WMO/TD No. 1043S, SPARC Report No. 2, Stratospheric Processes and Their Role in Climate (SPARC) project, World Meteorological Organization, Paris, 2000].
14. S. J. Oltmans, H. Vome., D. J. Hofmann, K. H. Rosenlof, D. Kley, *Geophys. Res. Lett.* **27**, 3453 (2000).
15. W. J. Randel, F. Wu, H. Vomel, G. E. Nedoluha, P. M. D. Forster, *J. Geophys. Res.* **111**, (D12), D12312 (2006).
16. J. E. Harries *et al.*, *J. Geophys. Res.* **101**, (D6), 10205 (1996).
17. M. Scherer, H. Vomel, S. Fueglista.er, S. J. Oltmans, J. Staehelin, *Atmos. Chem. Phys.* **8**, 1391 (2008).
18. D. Rind *et al.*, *J. Geophys. Res.* **98**, (D3) 4835 (1993).
19. A. Lambert *et al.*, *J. Geophys. Res.* **112**, (D24), D24536 (2007).
20. K. H. Rosenlof *et al.*, *Geophys. Res. Lett.* **28**, 1195 (2001).
21. A. W. Brewer, *Q. J. R. Meteorol. Soc.* **75**, 351 (1949).
22. J. R. Holton *et al.*, *Rev. Geophys.* **33**, 403 (1995).
23. S. C. Sherwood, A. E. Dessler, *J. Atmos. Sci.* **58**, 765 (2001).
24. S. Fueglistaler *et al.*, *Rev. Geophys.* **47**, RG1004 (2009).

25. K. Rosenlof, G. C. Reid, *J. Geophys. Res.* **113**, (D6), D06107 (2008)
26. M. A. Geller, X. L. Zhou, M. H. Zhang, *J. Atmos. Sci.* **59**, 1076 (2002)
27. R. W. Portmann *et al.*, *J. Geophys. Res.* **102**, (D8), 9409 (1997)
28. W. B. Rossow, R. A. Schiffer, *Bull. Am. Meteorol. Soc.* **80**, 2261 (1999)
29. S. Rohs *et al.*, *J. Geophys. Res.* **111**, (D14), D14315 (2006)
30. P. Forster *et al.*, in (*1*), pp. 129–234
31. G.-K. Plattner *et al.*, *J. Clim.* **21**, 2721 (2008)
32. K. Trenberth *et al.*, in (*1*), pp. 235–336.
33. J. L. Lean, D. H. Rind, *Geophys. Res. Lett.* **36**, L15708 (2009)
34. N. Stuber, M. Ponater, R. Sausen, *Clim. Dyn.* **24**, 497 (2005)
35. S. Sherwood, *Science* **295**, 1272 (2002)
36. G. Manney *et al.*, *J. Geophys. Res.* **112**, D24550 (2007)
37. K. Onogi *et al.*, *J. Meteorol. Soc. Jpn.* **85**, 369 (2007).
38. J. M. Gregory, P. M. Forster, *J. Geophys. Res.* **113**, D23105 (2008)
39. World Meteorological Organization, *Scientific Assessment of Ozone Depletion: 2006* (Global Ozone Research and Monitoring Project-Report No. 50, Geneva, Switzerland 2007)
40. D. M. Murphy *et al.*, *J. Geophys. Res.* **114**, D17107 (2009)
41. This work was supported by the Atmospheric Composition and Climate Program of the National Oceanic and Atmospheric Administration Climate Program. We appreciate helpful comments on a draft manuscript by K. Shine, M. Geller, A. Gettelman, and A. Dessler

25 September 2009; accepted 12 January 2010
Published online 28 January 2010
10.1126/science.1182488
Include this information when citing this paper

Sestrin as a Feedback Inhibitor of TOR That Prevents Age-Related Pathologies

Jun Hee Lee,[1] Andrei V. Budanov,[1] Eek Joong Park,[1] Ryan Birse,[2] Teddy E. Kim,[3] Guy A. Perkins,[4] Karen Ocorr,[2] Mark H. Ellisman,[4] Rolf Bodmer,[2] Ethan Bier,[3]* Michael Karin[1]*

Sestrins are conserved proteins that accumulate in cells exposed to stress, potentiate adenosine monophosphate–activated protein kinase (AMPK), and inhibit activation of target of rapamycin (TOR). We show that the abundance of *Drosophila* sestrin (dSesn) is increased upon chronic TOR activation through accumulation of reactive oxygen species that cause activation of c-Jun amino-terminal kinase and transcription factor Forkhead box O (FoxO). Loss of dSesn resulted in age-associated pathologies including triglyceride accumulation, mitochondrial dysfunction, muscle degeneration, and cardiac malfunction, which were prevented by pharmacological activation of AMPK or inhibition of TOR. Hence, dSesn appears to be a negative feedback regulator of TOR that integrates metabolic and stress inputs and prevents pathologies caused by chronic TOR activation that may result from diminished autophagic clearance of damaged mitochondria, protein aggregates, or lipids.

Target of rapamycin (TOR) is a key protein kinase that regulates cell growth and metabolism to maintain cellular and organismal homeostasis (*1*–*3*). Insulin and insulin-like growth factors are major TOR activators that operate through phosphoinositide 3-kinase (PI3K) and the protein kinase AKT (*2*). Conversely, adenosine monophosphate–activated protein kinase (AMPK), which is activated upon energy depletion, caloric restriction (CR), or genotoxic damage, is a stress-responsive inhibitor of TOR activation (*2*, *4*). TOR stimulates cell growth and anabolism by increasing protein and lipid synthesis through p70 S6 kinase (S6K), eukaryotic translation initiation factor 4E-binding protein (4E-BP), and sterol response element binding protein (SREBP) (*1*–*3*, *5*) and by decreasing autophagic catabolism through phosphorylation-mediated inhibition of ATG1 protein kinase (*1*, *6*). Persistent TOR activation is associated with diverse pathologies such as cancer, diminished cardiac performance, and obesity-associated metabolic diseases (*1*). Conversely, inhibition of TOR prolongs life span and increases quality of life by reducing the incidence of age-related pathologies (*1*–*3*, *7*). The antiaging effects of CR could be due to inhibition of TOR (*8*).

Sestrins (Sesns) are highly conserved proteins that accumulate in cells exposed to stress, lack obvious domain signatures, and have poorly defined physiological functions (*9*, *10*). Mammals express three Sesns, whereas *Drosophila melanogaster* and *Caenorhabditis elegans* have single orthologs (fig. S1, A and B). In vitro, Sesns exhibit oxidoreductase activity and may function as antioxidants (*11*). Independently of their redox activity, Sesns lead to AMPK-dependent inhibition of TOR signaling and link genotoxic stress to TOR regulation (*12*). However, Sesns are also widely expressed in the absence of exogenous stress, and in *Drosophila*, expression of *Drosophila* sestrin (dSesn) is increased upon maturation and aging (fig. S1C) (*10*). Given the redundancy between mammalian Sesns, we chose to test the importance of Sesns as regulators of TOR function in *Drosophila*. We generated both gain- and loss-of-function *dSesn* mutants (figs. S2 to S4). Analysis of these mutants revealed that dSesn is an important negative feedback regulator of TOR whose loss results in various TOR-dependent, age-related pathologies (*13*).

Prolonged TOR signaling induces dSesn. Persistent TOR activation in wing discs by a constitutively active form of the insulin receptor (InR^{CA}) resulted in prominent dSesn protein accumulation, which is not seen in a *dSesn*-null larvae (Fig. 1, A to C). InR^{CA} also induced accumulation of *dSesn* RNA (Fig. 1, D to F), indicating that dSesn accumulation is due to increased transcription or mRNA stabilization. As dSesn accumulation was restricted to cells in which TOR was activated, the response is likely to be cell autonomous. dSesn was also induced when TOR was chronically activated by overexpression of the small guanine triphosphatase Rheb (Fig. 1G), clonal loss of phosphatase and tensin homolog (PTEN), or tuberous sclerosis complex 1 (TSC1) (Fig. 1, H and I). Dominant-negative PI3K ($PI3K^{DN}$) or TOR (TOR^{DN}) inhibited dSesn accumulation caused by overexpression of InR^{CA}, but inactive ribosomal S6 protein kinase (S6K, $S6K^{DN}$) and hyperactive 4E-BP ($4E\text{-}BP^{CA}$), two downstream TOR effectors, did not (fig. S5). Furthermore, dorsal-specific expression of activated $S6K^{CA}$ or loss of 4E-BP activity failed to induce dSesn expression (Fig. 1, J and K), indicating that TOR regulates expression of dSesn through different effector(s).

TOR signaling generates ROS to induce dSesn. In mammals, transcription of *Sesn* genes is increased in cells exposed to oxidative stress (*9*, *11*), and we observed reactive oxygen species (ROS) accumulation, detected by oxidation of dihydroethidium (DHE), in the same region of the imaginal discs in which InR^{CA} or Rheb were expressed (Fig. 2, A and B). InR^{CA}-induced accumulation of ROS was blocked by coexpression of either $PI3K^{DN}$ or TOR^{DN}, but not $S6K^{DN}$ or $4E\text{-}BP^{CA}$ (Fig. 2B), revealing TOR's role in ROS accumulation. Wing-disc clones in which TOR was activated by loss of TSC1 also exhibited ROS accumulation (Fig. 2C), confirming that TOR-dependent ROS accumulation is cell-autonomous. Expression of the ROS scavengers catalase or peroxiredoxin (*14*) inhibited InR^{CA}-induced accumulation of dSesn

[1]Laboratory of Gene Regulation and Signal Transduction, Departments of Pharmacology and Pathology, School of Medicine, University of California San Diego (UCSD), La Jolla, CA 92093–0723, USA. [2]Development and Aging Program, Neuroscience, Aging and Stem Cell Research Center, Sanford-Burnham Medical Research Institute, La Jolla, CA 92037, USA. [3]Section of Cell and Developmental Biology, UCSD, La Jolla, CA 92093–0349, USA. [4]National Center for Microscopy and Imaging Research and Department of Neurosciences, UCSD, La Jolla, CA 92093-0608, USA.

*To whom correspondence should be addressed. E-mail: ebier@ucsd.edu (E.B.); karinoffice@ucsd.edu (M.K.)

(Fig. 2, D and E). Feeding animals with vitamin E, an antioxidant, also prevented dSesn induction caused by TSC1 loss (Fig. 2F).

Forkhead box O (FoxO) and p53 are ROS-activated transcription factors that control mammalian *Sesn* genes (*9*–*12*, *15*). The *dSesn* locus contains eight perfect FoxO-response elements (fig. S6A), a frequency 25 times higher than that expected on the basis of random distribution. Overexpressed FoxO or p53 could both increase expression of the *dSesn* gene (fig. S6, B to D). However, InR^{CA} caused accumulation of dSesn in a *p53*-null background (fig. S6E), but not in a *FoxO*-null background (fig. S6, F and J), indicating that TOR-activated FoxO (fig. S6, K to M) (*16*) is likely to be the regulator of *dSesn* gene transcription. Accumulation of dSesn in response to Rheb overexpression was also FoxO-dependent (fig. S6, G and H).

In dorsal wing disc cells, where ROS accumulated in response to InR^{CA} (Fig. 2A), c-Jun N-terminal kinase (JNK), a protein kinase that phosphorylates FoxO (*14*, *15*), was also activated (fig. S7, A and B). JNK activation was diminished in cells overexpressing catalase (fig. S7C), suggesting that it depends on TOR-induced accumulation of ROS. Mitogen-activated protein kinase kinase 7 mediated activation of JNK also resulted in accumulation of dSesn (fig. S7, D and E), as did overexpression of mammalian STE20-like kinase 1 (MST1), another protein kinase that phosphorylates FoxO (*17*), (fig. S7F). However,

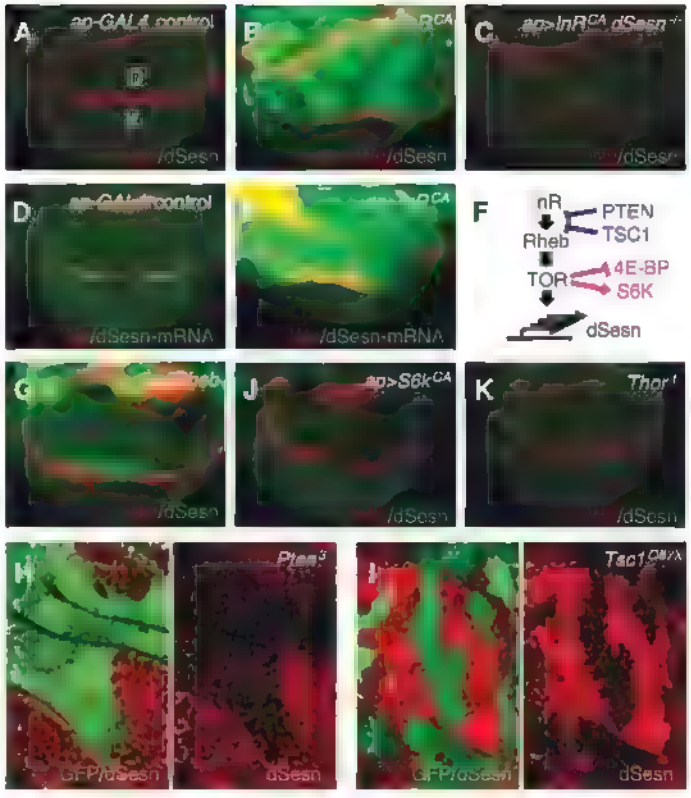

Fig. 1. Increased abundance of dSesn upon TOR activation. Larval wing discs of indicated strains were stained to visualize indicated proteins or mRNA. The dorsal side points upward. Dorsoventral boundary [indicated by D and V in (A)] was visualized by staining with an antibody to the wingless (Wg) protein (red). (**A** to **C**) Expression of dSesn protein (green) in the absence (A) or presence of InR^{CA} in WT (B) and *dSesn*-null (C) strains. (**D** and **E**) Accumulation of dSesn mRNA (green) in response to InR^{CA} detected by in situ hybridization. (**F**) The signaling network controlling TOR activity and expression of dSesn. (**G** to **K**) Accumulation of dSesn (green) in response to Rheb (G) but not $S6K^{CA}$ (J) or loss of 4E-BP (K). $Thor^2$ is a *Drosophila* 4E-BP loss-of-function mutant. (H and I) Accumulation of dSesn after somatic loss of PTEN (H) or TSC1 (I). Absence of green fluorescent protein (GFP) (green) indicates loss of PTEN or TSC1 resulting in dSesn (red) accumulation.

Fig. 2. Chronic TOR activation results in accumulation of ROS and dSesn. Larval imaginal discs of indicated strains were stained as indicated (**A**) ROS accumulation (red) in response to InR^{CA} or Rheb overexpressed in dorsal (upward) wing discs was revealed by DHE staining. (**B**) InR^{CA}-induced ROS (red) accumulation in eye discs was reduced by $PI3K^{DN}$ or TOR^{DN} but not by $S6K^{DN}$ or $4E\text{-}BP^{CA}$. (**C**) DHE staining (red) in TSC1-negative wing disc clones marked by absence of GFP. (**D** and **E**) Inhibition of InR^{CA}-induced accumulation of dSesn (green) in eye and wing discs by expression of catalase or peroxiredoxin (Prx). D-V wing boundary and differentiated eye area were visualized by Wg (red) and Elav (red) staining, respectively. (**F**) dSesn accumulation (red) in TSC1-negative wing disc clones was suppressed by vitamin E feeding. Absence of GFP (green) indicates loss of TSC1. (**G**) Diagram depicting TOR-stimulated production of ROS and expression of dSesn.

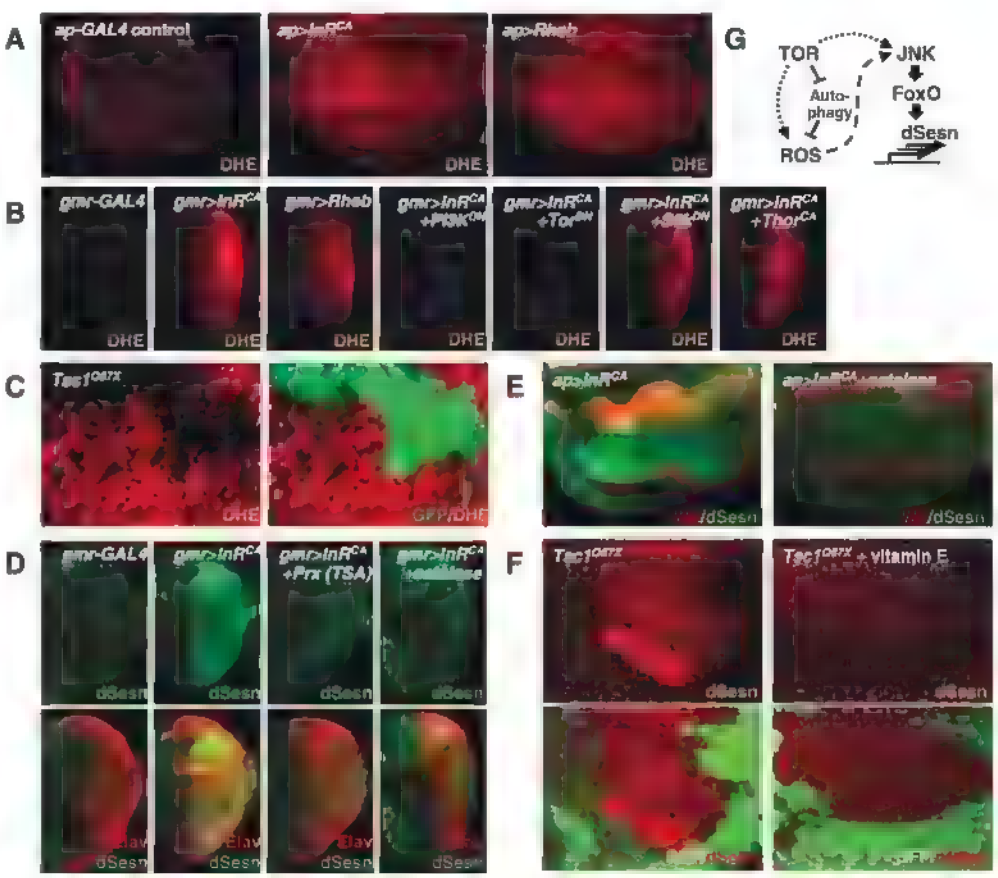

only JNK^{DN} (but not Mst1^{DN}) inhibited InR^{CA}-mediated accumulation of dSesn (fig. S7, G and H). Collectively, these data suggest that *dSesn* transcription is increased upon chronic TOR activation through ROS-dependent activation of JNK and FoxO (Fig. 2G).

dSesn antagonizes TOR-dependent cell and tissue growth. To determine effects of dSesn on cell growth, a major function of TOR (*1*–*3*), we overexpressed dSesn in dorsal wings (fig. S2F). This resulted in a dose-dependent phenotype in which the wing bends upward (fig. S8, A to D), indicating suppressed dorsal tissue growth. A dSesn^{C86S} variant, in which the cysteine required for oxidoreductase activity was mutated (C86S, Cys^{86} → Ser^{86}) (*11*), still conferred this phenotype (fig. S8, E and F) when expressed in amounts similar to those of wild-type dSesn (dSesn^{WT}) (fig. S3, A to D). We measured cell number and size in a dorsal wing region defined by the L3, L4, C1, and C2 veins (shaded in pink in fig. S8, G and H). Although the size of this area was significantly reduced by dSesn expression (fig. S8I), the cell number remained unchanged (fig. S8J), showing that decreased cell size (fig. S8K) can account for dSesn suppression of tissue growth. Overexpression of dSesn also reduced cell size in larval wing discs (fig. S9) and adult eyes (fig. S10). Thus, dSesn inhibits cell growth without affecting cell proliferation and does so independently of its redox activity.

When dSesn was expressed with InR^{CA} or Rheb, it suppressed the hyperplastic phenotypes caused by these TOR activators (Fig. 3, A to F). Both eye and individual ommatidia sizes were significantly reduced (Fig. 3G). dSesn also inhibited InR^{CA}- or Rheb-induced phosphorylation of TOR targets S6K and 4E-BP (Fig. 3H). In mammalian cells, dSesn enhanced AMPK-induced phosphorylation of TSC2 and inhibited S6K activity through TSC2 (fig. S11, A to C), just as mSesn2 does (*12*). In *Drosophila* wings, dSesn-induced growth suppression was attenuated by reduced gene dosage of TSC1, TSC2, or AMPK, although reduced dosage of these genes alone did not affect normal growth (fig. S11, D and E). Expression of mSesn1/2 in flies (fig. S3, E and F) also reduced normal (fig. S12, A to C) and InR^{CA}-induced hyperplastic (fig. S12D) growth.

Expression of InR, constitutively active PI3K (PI3K^{CA}), AKT, or S6K^{CA} in dorsal cells of the

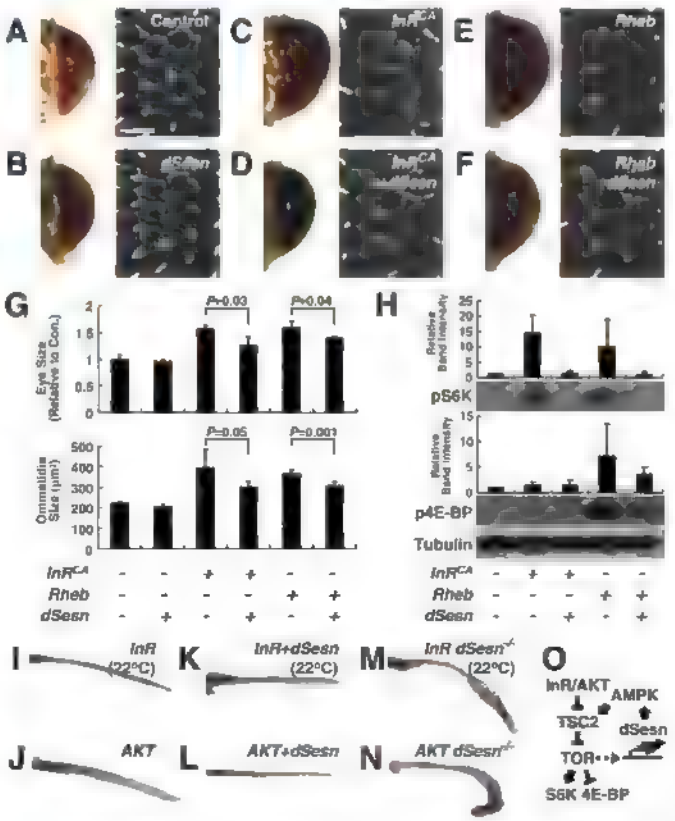

Fig. 3. Antagonism of TOR-stimulated growth by dSesn. (**A** to **F**) Light (left) and scanning electron (right) micrographs of eyes expressing the indicated genetic elements driven by *gmr-GAL4*. Scale bar, 20 μm. (**G**) Quantification of eye and ommatidia sizes measured from frontal and lateral views, respectively. *P* values were calculated by one-way analysis of variance (ANOVA). Error bars indicate SD; $n = 3$ eyes and 5 ommatidia. (**H**) Suppression of TOR signaling by dSesn. Adult heads with eye-specific expression of indicated genetic elements driven by *gmr-GAL4* were subjected to immunoblot analyses with indicated antibodies. Relative band intensities were quantified and are presented as bar graphs. Error bars indicate SD; $n = 3$. (**I** to **N**) Suppression of InR-induced growth by dSesn. Anterior views of wing blades with *apterous-GAL4*–driven expression of indicated genetic elements. Dorsal sides point upward. (**O**) Schematic diagram summarizing genetic interactions between dSesn and TOR signaling components.

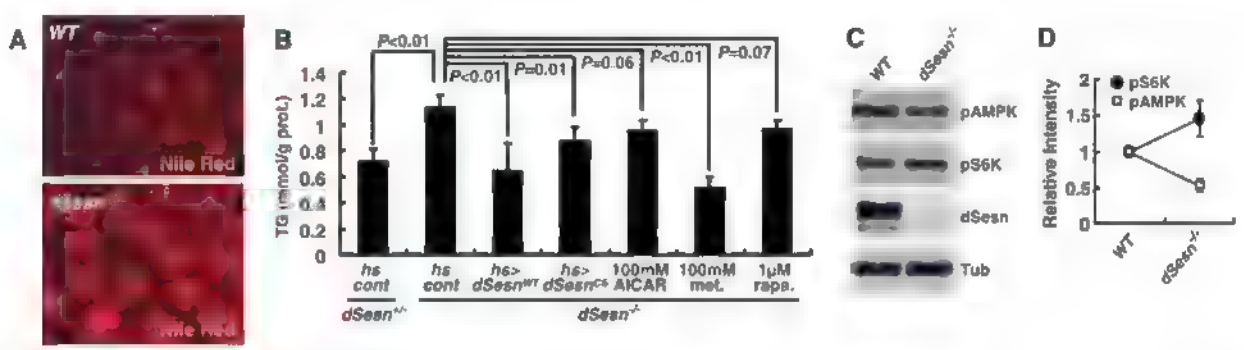

Fig. 4. Effect of dSesn on lipid homeostasis. (**A**) Lipid accumulation in fat bodies examined by Nile red staining (red). (**B**) Total triglycerides were measured in five 10-day-old adult males of the indicated genotypes subjected to the indicated treatments (met, metformin; rapa, rapamycin). *P* values were calculated by one-way ANOVA. Error bars indicate SD; $n \geq 3$. TG, triglycerides. (**C** and **D**) Protein lysates from fat bodies were analyzed by immunoblotting with indicated antibodies. Relative band intensities were quantified and are shown as a bar graph. Error bars indicate SD; $n = 3$. (**E**) Expression of indicated mRNAs in adult flies was examined by quantitative reverse transcription polymerase chain reaction. Fifty 3-day-old adult males of each genotype were used to prepare total RNA. Error bars indicate SD; $n = 3$.

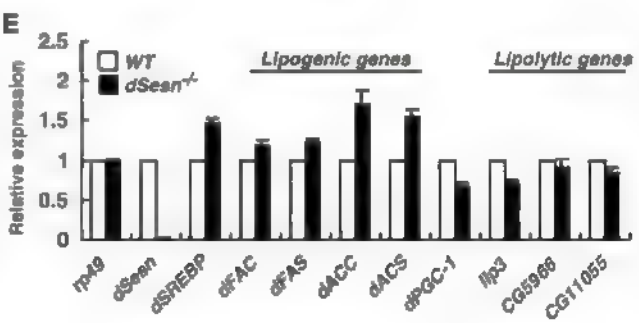

wing caused an overgrowth phenotype in which the wing bends downward (Fig. 3, I and J, and fig. S13, A to D). dSesn expression reversed this effect of overexpressed InR, $PI3K^{CA}$, and AKT, but not that of $S6K^{CA}$ (Fig. 3, K and L, and fig. S13, E to H), suggesting that dSesn inhibits TOR downstream of AKT. Conversely, dorsal wing-specific expression of PTEN and InR^{DN}, $PI3K^{DN}$, or $S6K^{DN}$ caused wings to bend upward (fig. S13, I to L), and this effect was enhanced by dSesn (fig. S13, M to P).

Although *dSesn*-null flies did not exhibit developmental abnormalities, the growth-promoting effect of overexpressed InR or AKT was enhanced in *dSesn*-null background (Fig. 3, M and N, and fig. S14, A and B), suggesting that endogenous dSesn restricts TOR activation and its growth-promoting effect. Loss of dSesn, however, did not enhance S6K-stimulated cell growth (fig. S14, C to F) or decrease growth suppression by overexpressed InR^{DN} or $S6K^{DN}$ (fig. S14, G to J). These findings indicate that Sesn is an evolutionarily conserved inhibitor of TOR signaling that acts via the AMPK-TSC2 axis (Fig. 3O).

dSesn reduces lipid accumulation. Fat bodies from *dSesn*-null third-instar larvae contained more lipids than did those of WT animals (Fig. 4A). *dSesn*-null adults also contained more triglycerides, which were decreased after ectopic expression of $dSesn^{WT}$ or $dSesn^{CS}$ (Fig. 4B and fig. S15). Thus, the TOR-inhibitory function of dSesn, rather than its antioxidant activity, appears to affect metabolic control. Congruently, *dSesn*-null fat bodies showed decreased AMPK and increased TOR activities (Fig. 4, C and D). Pharmacological manipulation strengthened this conclusion; feeding *dSesn*-null mutants with AMPK-activators such as 5-aminoimidazole-4-carboxamide 1-β-D-ribofuranoside (AICAR) or metformin (*4*), or the TOR-inhibitor rapamycin (*2*) reduced triglyceride accumulation (Fig. 4B).

Expression of the gene-encoding transcription factor dSREBP (*5*, *18*) and its targets, which encode fatty acyl coenzyme A (CoA) synthetase, fatty acid synthase, acetyl CoA carboxylase, and acetyl CoA synthetase (*18*), was significantly increased (20 to 70%) in *dSesn*-null mutants (Fig. 4E). However, the peroxisome proliferator activated receptor γ coactivator 1 (dPGC-1) gene and some lipolytic genes showed decreased expression. This is consistent with reports that dSREBP and dPGC-1 are inversely regulated by TOR and AMPK to properly control lipid metabolism (*1*, *2*, *4*, *5*).

dSesn mutants exhibit a decline in cardiac performance. Age-related decline in heart performance is another phenotype associated with TOR hyperactivity in insects and mammals (*19*–*21*). In WT flies, the heart beats in a highly regular manner (Fig. 5A and movie S1), but in *dSesn*-null mutants, heart function was compromised (Fig. 5B and movie S2), as manifested by arrhythmia (Fig. 5C) and decreased heart rate (Fig. 5D). Slowing of heart rate reflected expansion of the diastolic period (fig. S16A), as observed in aged or TOR-activated flies (*19*, *22*). These defects were largely prevented by feeding flies AICAR (Fig. 5E and movie S3) or rapamycin (Fig. 5F and movie S4), indicating that they are caused by low activity of AMPK or high TOR activity. Vitamin E feeding or catalase expression suppressed the arrhythmia caused by loss of dSesn (Fig. 5, C and G), but not the decrease in heart rate (Fig. 5D), suggesting that TOR-induced oxidative stress contributes to the arrhythmic phenotype. Analysis of F-actin revealed structural disorganization of myofibrils in *dSesn*-null hearts (Fig. 5, H and I), suggesting that cardiac muscle degeneration may cause some of the functional defects in *dSesn*-null hearts. Reflecting this structural abnormality, *dSesn*-null

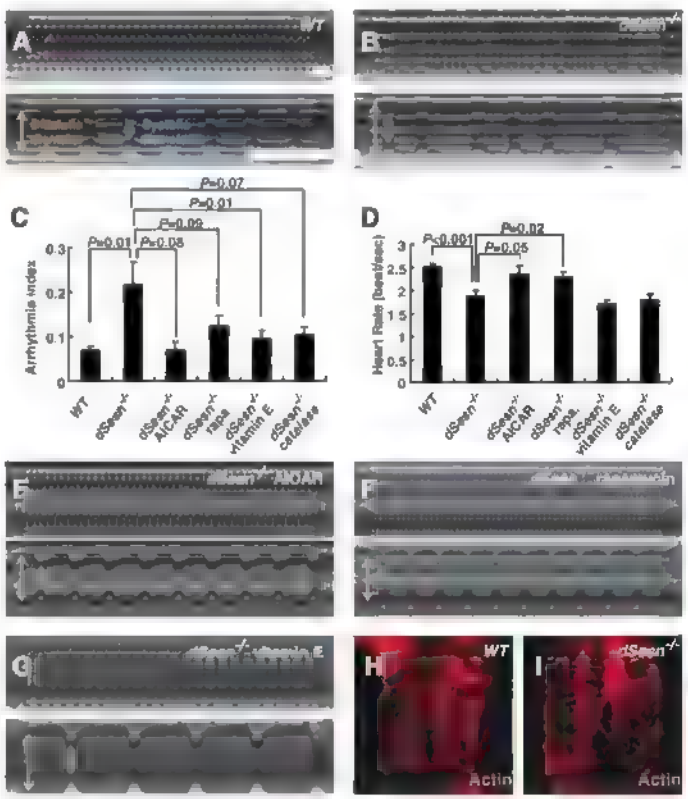

Fig. 5. Effect of dSesn on cardiac function. (**A**, **B**, and **E** to **G**) Representative M mode records of indicated 2-week-old flies fed with or without indicated drugs, showing movement of heart tube walls (*y* axis) over time (*x* axis). Diastolic (orange) and systolic (blue) diameters are indicated. Scale bar, 1 s. (**C** and **D**) Quantification of cardiac function parameters. *P* values were calculated using one-way ANOVA. Error bars indicate SEM; $n > 10$. (**H** and **I**) Actin fibers in WT and *dSesn*-null hearts were visualized by phalloidin staining (red).

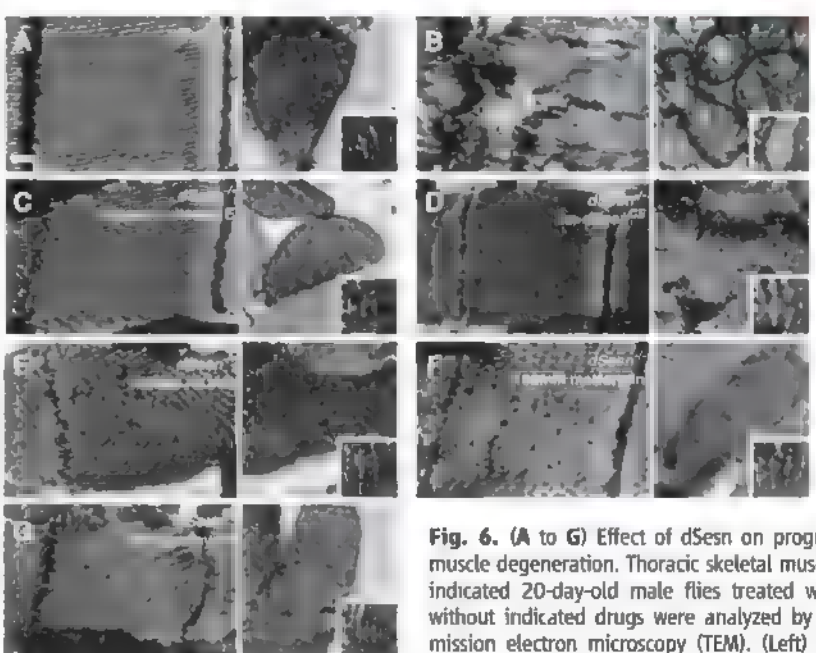

Fig. 6. (**A** to **G**) Effect of dSesn on progressive muscle degeneration. Thoracic skeletal muscles of indicated 20-day-old male flies treated with or without indicated drugs were analyzed by transmission electron microscopy (TEM). (Left) Sarcomeres; (right) mitochondria. Mitochondrial microstructure is shown in the insets (0.15-μm width). Scale bars, 0.2 μm.

hearts were dilated during both the diastolic and systolic phases, and this was prevented by AICAR or rapamycin (fig. S16B).

Heart-specific depletion of dSesn caused cardiac malfunction similar to that seen in *dSesn*-null mutants (fig. S17, A and B, and movies S5 and S6). Heart-specific depletion of AMPK also caused cardiac malfunction, but this was not alleviated by AICAR administration (fig. S17, C to E, and movie S7), supporting the notion that dSesn maintains normal heart physiology through AMPK activation.

Skeletal muscle degeneration and mitochondrial dysfunction caused by loss of dSesn. dSesn mRNA and protein are abundant in the adult thorax (fig. S18), which is mostly composed of skeletal muscle. mSesn1 is also highly expressed in skeletal muscle (*10*). Therefore, we tested whether dSesn has a role in maintaining muscle homeostasis. 20-day-old *dSesn*-null flies showed degeneration of thoracic muscles with loss of sarcomeric structure, including discontinued Z discs, disappearance of M bands, scrambled actomyosin arrays, and diffused sarcomere boundaries (Fig. 6, A and B, and fig. S19, A to H). Such defects are only partially observed in very old WT flies (~90 days) (*23*) and were not found in young (5-day-old) *dSesn*-null muscles (fig. S19, I to L). Thus, the *dSesn*-null skeletal muscle appears to undergo accelerated age-related degeneration.

Despite its normal appearance, muscle from 5-day-old *dSesn*-null flies exhibited mitochondrial abnormalities, including a rounded shape, occasional enlargement, and disorganization of cristae (fig. S19, I to L), which were also observed in 20-day-old mutants (fig. S19, E to H). Mitochondrial dysfunction can result in excessive generation of ROS leading to other abnormalities (*24*). *dSesn*-null muscles exhibited increased accumulation of ROS, revealed by more intense DHE fluorescence and reduced *cis*-aconitase activity (fig. S20, A and B), which was associated with muscle cell death (fig. S20C). Furthermore, the muscle defects were prevented by vitamin E feeding (Fig. 6C), underscoring the role of ROS in muscle degeneration.

Expression of exogenous dSesn^{CS}, devoid of redox activity (*11*), prevented muscle degeneration (Fig. 6D), suggesting again that regulation of AMPK-TOR by dSesn, rather than intrinsic redox activity, is of importance. Feeding animals with AMPK activators prevented muscle degeneration in *dSesn*-null mutants (Fig. 6, E and F), and depletion of AMPK in skeletal muscles caused severe degeneration of mitochondrial and sarcomeric structures (fig. S21, E to H). Treatment of animals with rapamycin also prevented muscle degeneration in *dSesn*-null flies (Fig. 6G). Thus, dSesn-dependent control of AMPK-TOR signaling is essential for prevention of mitochondrial dysfunction and maintenance of muscle homeostasis during aging.

Inhibition of autophagy phenocopies dSesn loss of function. We noticed that *dSesn*-null muscles accumulated polyubiquitin aggregates (fig. S20D), which are hallmarks of defective autophagy (*25*). To test whether decreased autophagy brought about by excessive and prolonged TOR activity (*24*) might cause muscle degeneration, we silenced expression of ATG1, an essential component of the autophagic machinery, which is inhibited by TOR (*1*, *6*). This caused a decline in cardiac performance (Fig. 7, A to C, and movie S8), as well as degeneration and mitochondrial abnormalities in skeletal muscle (Fig. 7D and fig. S21, I to L). These results suggest that TOR up-regulation caused by dSesn loss inhibits autophagy needed to eliminate ROS-producing dysfunctional mitochondria (*26*), which may contribute to muscle degeneration. Consistent with this view, ATG1 silencing resulted in ROS accumulation in wing discs (Fig. 7E).

Discussion. The results described above identify *Sesn* as a negative feedback regulator of TOR function. In mammalian cells, increased expression of mSesns in response to genotoxic stress leads to inhibition of TOR activity through activation of AMPK (*12*). We now show that transcription of the *dSesn* gene is increased upon chronic TOR activation through JNK and FoxO in a manner dependent on ROS accumulation. Although transient InR activation inhibits FoxO through its phosphorylation by AKT (*15*), we find that chronic TOR activation overcomes this inhibition and results in nuclear translocation of FoxO, which increases *dSesn* transcription. In turn, dSesn suppresses metabolic dysfunction and age-related tissue degeneration brought about by hyperactivated TOR. Although dSesn can inhibit TOR-stimulated cell growth, our analysis points to its most important function being the maintenance of metabolic homeostasis and prevention of TOR-induced tissue degeneration. The three major functions of dSesn revealed by this study—suppression of lipid accumulation, prevention of cardiac malfunction, and protection of muscle from age-related degeneration—are adversely affected by obesity, lack of exercise, and aging, which make a disproportional contribution to health problems in developed and rapidly developing societies.

Whereas TOR controls cell growth mostly through inhibition of 4E-BP and activation of S6K kinase (*1*, *3*), its ability to induce dSesn expression depends on ROS accumulation, which our results suggest is a pathophysiological aberration caused by TOR hyperactivation that is normally antagonized by dSesn. However, the previously described redox function of Sesn (*11*) is not required for its protective role. TOR-induced accumulation of ROS was observed in yeast (*27*) and hematopoietic cells (*28*, *29*), but the molecular mechanism underlying this phenomenon and its physiological and pathophysiological importance were unknown. Our results suggest that TOR-stimulated production of ROS, which is needed for accumulation of dSesn, is independent of two of the major TOR targets (4E-BP and S6K) and instead may result from TOR-mediated inhibition of physiological autophagy, a process that eliminates ROS-producing dysfunctional mitochondria (*24*). Nonetheless, inhibition of 4E-BP also contributes to the pro-aging effects of TOR by suppressing translation

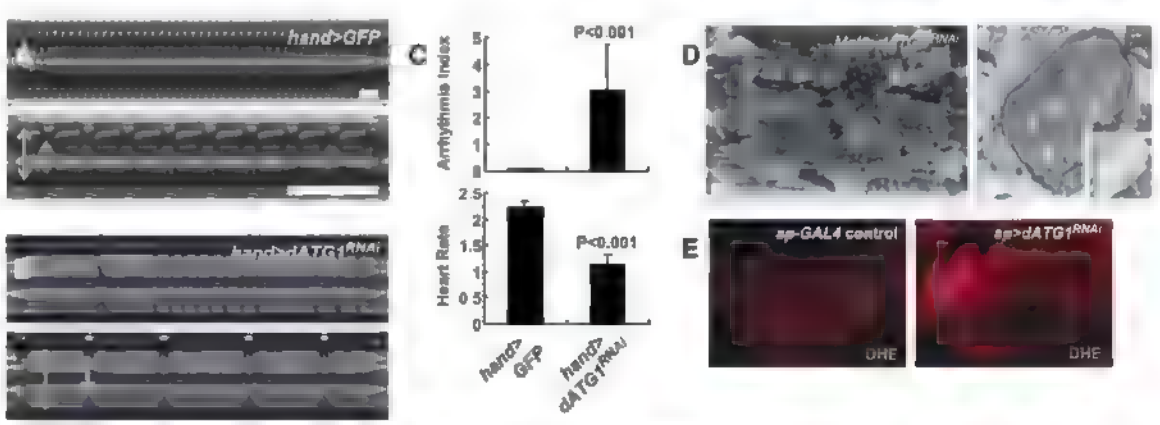

Fig. 7. Phenotypes caused by silencing of dATG1. (**A** and **B**) Representative M mode records of control and *dATG1*^{RNAi}-expressing hearts in 2-week-old adult flies, showing the movement of heart tube walls (*y* axis) over time (*x* axis). RNAi, RNA interference. Diastolic (orange) and systolic (blue) diameters are indicated. Scale bar, 1 s. (**C**) Quantification of cardiac function parameters. *P* values were calculated using one-way ANOVA. Error bars indicate SEM; $n \geq 9$. (**D**) *dATG1*^{RNAi}-expressing thoracic skeletal muscle was analyzed by TEM. (Left) Sarcomeres; (right) mitochondria. Mitochondrial microstructure is shown in the insets (0.15-μm width). Scale bars, 0.2 μm. (**E**) ROS accumulation (red) in response to *dATG1*^{RNAi} expressed in dorsal (upward) wing discs revealed by DHE staining.

of several mitochondrial proteins (*30*) and by accelerating age-related cardiac malfunction at young ages (*21*), which is reminiscent of the observed cardiac defects seen in *dSesn*-null flies. Although TOR activates SREBP (*18*), which may contribute to lipid accumulation in *dSesn*-null flies, autophagy promotes lipid elimination (*31*). Thus, decreased autophagy may also contribute to triglyceride accumulation. Hence, the different degenerative phenotypes exhibited by *dSesn*-null flies are due to the cumulative effects of several biochemical and cell biological defects caused by hyperactive TOR, including reduced autophagy and reduced function of 4E-BP. Both basal physiologic autophagy and 4E-BP function are enhanced by CR, which prevents aging-related pathologies (*32*). In the future, it will be of interest to determine the contribution of Sesn to these antiaging effects.

References and Notes

1. S. Wullschleger, R. Loewith, M. N. Hall, *Cell* **124**, 471 (2006)
2. N. Hay, N. Sonenberg, *Genes Dev.* **18**, 1926 (2004)
3. S. Oldham, E. Hafen, *Trends Cell Biol.* **13**, 79 (2003)
4. M. C. Towler, D. G. Hardie, *Circ. Res.* **100**, 328 (2007)
5. T. Porstmann *et al.*, *Cell Metab.* **8**, 224 (2008)
6. E. Y. Chan, *Sci. Signal.* **2**, pe51 (2009)
7. D. E. Harrison *et al.*, *Nature* **460**, 392 (2009)
8. P. Kapahi, B. Zid, *Sci. Aging Knowl. Environ.* **2004**, pe34 (2004)
9. A. V. Budanov *et al.*, *Oncogene* **21**, 6017 (2002)
10. S. Velasco-Miguel *et al.*, *Oncogene* **18**, 127 (1999)
11. A. V. Budanov, A. A. Sablina, E. Feinstein, E. V. Koonin, P. M. Chumakov, *Science* **304**, 596 (2004)
12. A. V. Budanov, M. Karin, *Cell* **134**, 451 (2008)
13. Materials and methods are available as supporting material on *Science* Online
14. E. Owusu-Ansah, A. Yavari, S. Mandal, U. Banerjee, *Nat. Genet.* **40**, 356 (2008)
15. E. L. Greer, A. Brunet, *Oncogene* **24**, 7410 (2005)
16. K. F. Harvey *et al.*, *J. Cell Biol.* **180**, 691 (2008)
17. M. K. Lehtinen *et al.*, *Cell* **125**, 987 (2006)
18. I. Y. Dobrosotskaya, A. C. Seegmiller, M. S. Brown, J. L. Goldstein, R. B. Rawson, *Science* **296**, 879 (2002)
19. R. J. Wessells, E. Fitzgerald, J. R. Cypser, M. Tatar, R. Bodmer, *Nat. Genet.* **36**, 1275 (2004)
20. N. Luong *et al.*, *Cell Metab.* **4**, 133 (2006)
21. R. Wessells *et al.*, *Aging Cell* **8**, 542 (2009)
22. K. Ocorr *et al.*, *Proc. Natl. Acad. Sci. U.S.A.* **104**, 3943 (2007)
23. A. Takahashi, D. E. Philpott, J. Miquel, *J. Gerontol.* **25**, 222 (1970)
24. W. L. Yen, D. J. Klionsky, *Physiology (Bethesda)* **23**, 248 (2008)
25. T. Hara *et al.*, *Nature* **441**, 885 (2006)
26. Y. Zhang *et al.*, *Autophagy* **3**, 337 (2007)
27. N. D. Bonawitz, M. Chatenay-Lapointe, Y. Pan, G. S. Shadel, *Cell Metab.* **5**, 265 (2007).
28. C. Chen *et al.*, *J. Exp. Med.* **205**, 2397 (2008)
29. J. H. Kim *et al.*, *Blood* **105**, 1717 (2005)
30. B. M. Zid *et al.*, *Cell* **139**, 149 (2009)
31. R. Singh *et al.*, *Nature* **458**, 1131 (2009)
32. R. J. Colman *et al.*, *Science* **325**, 201 (2009)

33. We thank W. McGinnis (UCSD), M. Tatar (Brown Univ.), S. Oldham (Burnham Institute), U. Banerjee (Univ. of California Los Angeles), J. K. Hariharan (Univ. of California Berkeley), J. Brenman (Univ. of North Carolina), O. Puig (Merck), C. Wilson (Oxford Univ.), L. Jones (Salk Institute), M. Miura (Univ. of Tokyo) Developmental Studies Hybridoma Bank (DSHB), *Drosophila* Genomics Resource Center (DGRC) (Indiana), DGRC (Japan), Vienna *Drosophila* RNAi Center (Austria), Cell Signaling Inc., Santa Cruz Biotechnology, and Bloomington and Harvard stock centers for fly strains, reagents, and access to lab equipment. We acknowledge help from J. Kim, M. Yoon, and R. Anderson in electron microscopy analysis; V. Temkin in ROS analysis, and M. Smelkinson, D. Cook, and A. Guichard in histochemistry. We thank M. Kim for suggestions and constructive criticism. This work was supported by grants and fellowships from the NIH and Superfund Research Program (CA118165, ES006376, and P42-ES010337 to M.K., DK082080 to A.V.B.; P41-RR004050 and P30-CA23100 to M.H.E.; and NS29870 and AI070654 to E.B.), NSF (IOS-074462 to E.B.), Korea Research Foundation (KRF-2007-357-C00096 to J.H.L.), Human Frontier Science Program Organization (LT00653/2008-L to J.H.L), and the Natural Sciences and Engineering Research Council of Canada (to E.J.P.). M.K. is an American Cancer Society professor.

Supporting Online Material

www.sciencemag.org/cgi/content/full/327/5970/1223/DC1
Materials and Methods
Figs. S1 to S21
References
Movies S1 to S8

21 September 2009; accepted 6 January 2010
10.1126/science.1182228

REPORTS

Symmetric Inertial Confinement Fusion Implosions at Ultra-High Laser Energies

S. H. Glenzer,[1]* B. J. MacGowan,[1] P. Michel,[1] N. B. Meezan,[1] L. J. Suter,[1] S. N. Dixit,[1] J. L. Kline,[2] G. A. Kyrala,[2] D. K. Bradley,[1] D. A. Callahan,[1] E. L. Dewald,[1] L. Divol,[1] E. Dzenitis,[1] M. J. Edwards,[1] A. V. Hamza,[1] C. A. Haynam,[1] D. E. Hinkel,[1] D. H. Kalantar,[1] J. D. Kilkenny,[3] O. L. Landen,[1] J. D. Lindl,[1] S. LePape,[1] J. D. Moody,[1] A. Nikroo,[3] T. Parham,[1] M. B. Schneider,[1] R. P. J. Town,[1] P. Wegner,[1] K. Widmann,[1] P. Whitman,[1] B. K. F. Young,[1] B. Van Wonterghem,[1] L. J. Atherton,[1] E. I. Moses[1]

Indirect-drive hohlraum experiments at the National Ignition Facility have demonstrated symmetric capsule implosions at unprecedented laser drive energies of 0.7 megajoule. One hundred and ninety-two simultaneously fired laser beams heat ignition-emulate hohlraums to radiation temperatures of 3.3 million kelvin, compressing 1.8-millimeter-diameter capsules by the soft x-rays produced by the hohlraum. Self-generated plasma optics gratings on either end of the hohlraum tune the laser power distribution in the hohlraum, which produces a symmetric x-ray drive as inferred from the shape of the capsule self-emission. These experiments indicate that the conditions are suitable for compressing deuterium-tritium–filled capsules, with the goal of achieving burning fusion plasmas and energy gain in the laboratory.

With the completion (*1*) and commissioning (*2*) of the National Ignition Facility (NIF), the quest for producing a burning fusion plasma has begun (*3*, *4*). The goal of the NIF experiments is to compress matter to densities and temperatures that are higher than those in the interior of the Sun (*5*–*8*), initiating nuclear fusion and the burning of hydrogen isotopes (*9*–*11*). This technique holds promise to demonstrate a highly efficient carbon-free process that will burn milligram quantities of nuclear fuel on each laser shot for producing energy gain in the laboratory.

The NIF consists of 192 laser beams that have been arranged into cones to irradiate a target from the top and bottom hemispheres. This "indirect-drive" laser geometry has been chosen for the first experiments to heat the interior of centimeter-scale cylindrical gold hohlraums (*9*, *12*–*15*) through laser entrance holes (LEHs) on the top and bottom ends of the cylinder (Fig. 1). Hohlraums act as radiation enclosures that convert the optical laser light into soft x-rays, and they are characterized by the radiation temperature T_{RAD}. Present ignition designs operate at temperatures of 270 to 305 eV or 3.1 million to 3.5 million K. The radiation field compresses a spherical fusion capsule, which is mounted in the center of the hohlraum, by x-ray ablation of the outer shell. The ablation process compresses the cryogenically prepared solid deuterium-tritium fuel layer in a spherical rocket implosion. In the final stages, the fuel reaches densities that are 1000 times that of a solid, and the central hot spot temperatures will approach 100 million K to initiate the nuclear burn process.

We have symmetrically imploded 1.8-mm-diameter fusion capsules in cryogenically fielded,

[1]Lawrence Livermore National Laboratory, Post Office Box 808, Livermore, CA 94551, USA. [2]Los Alamos National Laboratory, Los Alamos, NM 87545, USA. [3]General Atomics, San Diego, CA 92121, USA.

*To whom correspondence should be addressed. E-mail: glenzer1@llnl.gov

centimeter-scale hohlraums at 20 K. These experiments show efficient hohlraum heating to radiation temperatures of 3.3 million K. In addition, the large-scale length plasmas that are encountered in these experiments have allowed us to use self-generated plasma optics gratings (*16*, *17*) to control the radiation symmetry (*18*, *19*), and we were able to achieve symmetric fusion capsule implosions.

Figure 2A shows the laser power at the frequency-tripled wavelength of 351 nm versus time for two different pulse shapes. These 11- and 16-ns-long pulses heat 8.4-mm-long, 4.6-mm-diameter hohlraums with 20% helium, 80% hydrogen (atomic) mixtures; and 100% helium gas fill, respectively. The laser peak powers P_L = 220 and 245 TW have been distributed initially among the inner beams at 23.5° and 30° and the outer beams at 44.5° and 50°, with a ratio of about 1:2 as required for a symmetric implosion.

Measurements show that these hohlraums absorb more than 90% of the laser energy. Losses are due to laser backscattering by stimulated Raman scattering (SRS) on the inner beams (*20*, *21*). Stimulated Brillouin scattering and SRS on outer beams are negligible for our conditions. The inner beams interact with the hohlraum fill plasma, the capsule, and the hohlraum wall blow-off plasma, where radiation hydrodynamic simulations (*22*) and laser-plasma interaction calculations (*23*) show amplification gains for SRS of 10 to 20. We observed SRS in the wavelength range of 500 to 650 nm, which is measured spectrally and temporally resolved on two quadrants of beams on the 30° and the 50° cone. The SRS signal propagating back into the focusing lens is transmitted through the final turning mirror and measured with a full-aperture backscatter station (*24*). In addition, light scattered from the hohlraum outside the final optics aperture is observed with a near-backscatter imager that measures the reflection from a scatter plate using gated charge-coupled device cameras (*25*). The experiments show that 21 and 15% of the incident inner beam energy are reflected predominantly at the time of peak laser intensity (Fig. 2A). Because backscattering on the outer beams is negligible, the hohlraums with helium-hydrogen gas mixtures absorb 93% (±2%) of the laser energy, whereas hohlraums filled with only helium gas show a total absorption of 95% (±2%).

With η_{cc} being the conversion efficiency from laser power P_L to soft x-rays, the hohlraum radiation temperature is determined by balancing the absorbed laser power with the x-ray power

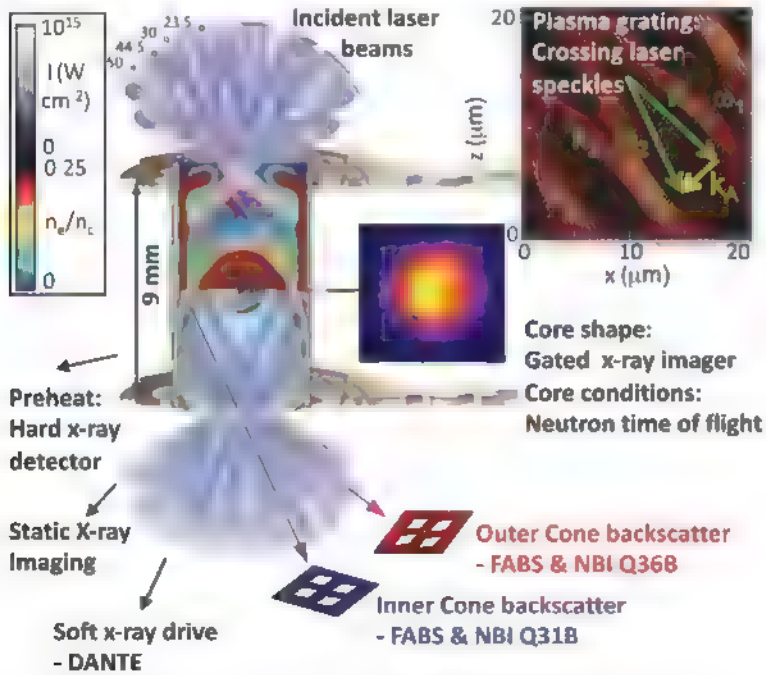

Fig. 1. Schematic of experimental setup. Hohlraums (8.4 mm long, 4.6 mm in diameter, 2.9 mm LEH) that are scaled in size to 78% of a full ignition target are irradiated by 192 high-power laser beams. The beams are arranged in four cones of beams; the beams at 23.5° and 30° to the hohlraum axis make up the inner beams and beams at 44.5° and 50° to the axis are the outer beams. The wavelength of the outer beams can be tuned with respect to the inner beams to control the laser power distribution inside the hohlraum by scattering laser light on a plasma grating in the beam crossing area. An example of the calculated single-quadrant laser intensity in the hohlraum is shown with a black and white color bar reaching peak intensities of 10^{15} W cm^{-2}. The lasers heat and ionize the hohlraum gas fill on their way to the walls, forming a high-temperature, low-density plasma inside the hohlraum. The density contour shows the electron density normalized to the critical density, indicating tamping of the capsule and hohlraum wall blow-off. Laser coupling, x-ray production, and capsule implosion conditions are measured with a suite of optical, x-ray, and neutron detectors.

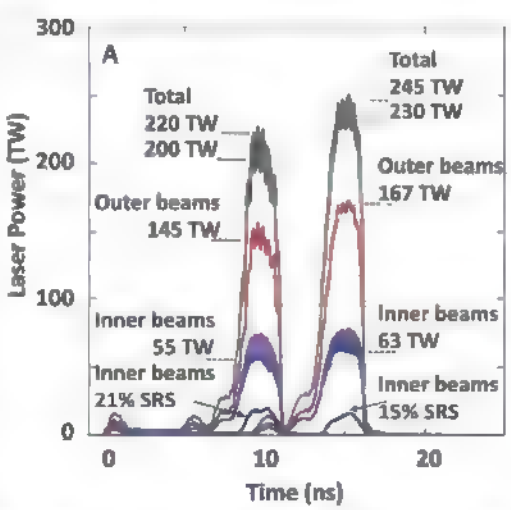

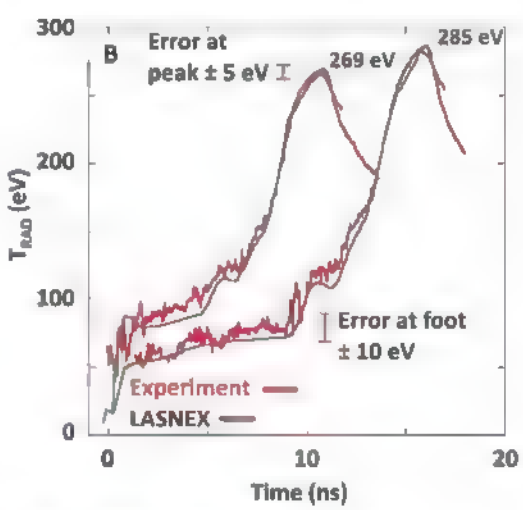

Fig. 2. (**A**) Total laser powers are shown together with power on the outer cone and inner cone and the reflected SRS power on the inner cone. For the 11-ns, 568-kJ pulses, the laser delivers peak powers of 220 TW. SRS losses, indicated as shaded areas, reduce the hohlraum absorbed peak power to 200 TW. For the 16-ns, 664-kJ pulses, the laser delivers peak powers of 245 TW, with 230 TW peak absorbed power in the hohlraum. (**B**) Hohlraums heat to peak radiation temperatures of 269 to 285 eV, in close agreement with radiation-hydrodynamic modeling. The error bar is calculated from uncertainties of the absolute detector calibration and from uncertainties of the LEH area and soft x-ray background signals.

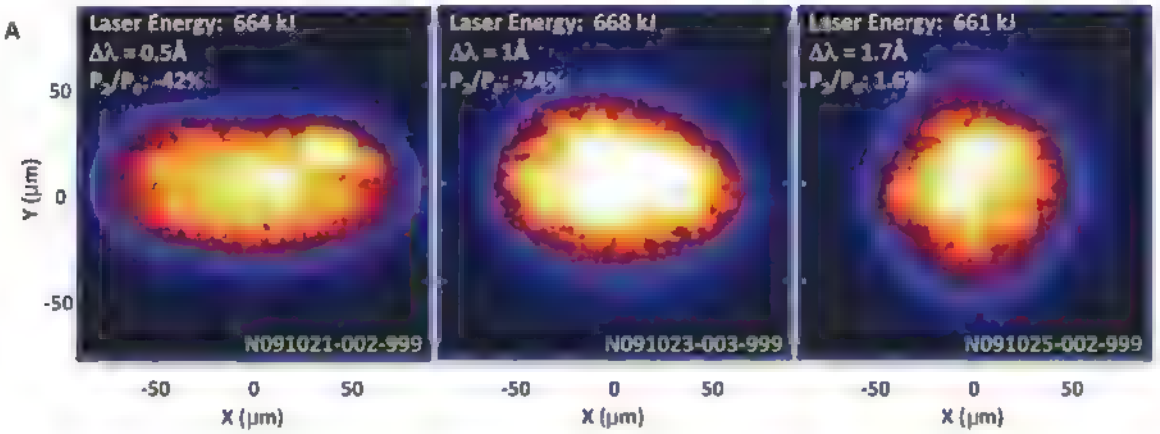

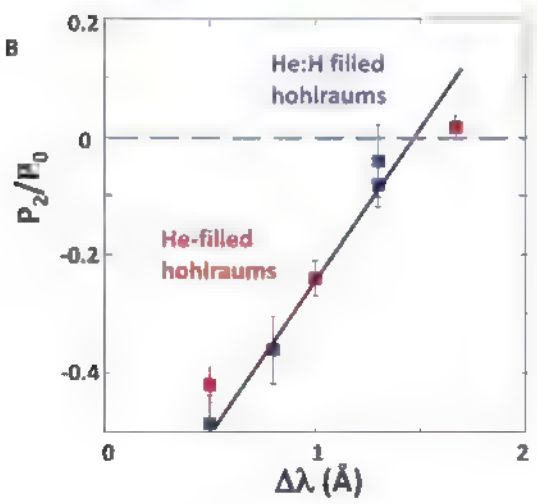

Fig. 3. (**A**) Capsule x-ray emission images at 9-keV energy from helium-filled hohlraums and 16-ns-long pulses are shown as a function of the wavelength difference between the laser beams on the inner and outer cones. Data are shown at peak x-ray emission at t = 18 ± 0.15 ns. The hohlraum axis of symmetry is vertical. (**B**) The low-order, even Legendre polynomial is shown at peak emission for helium-filled hohlraums heated with 16-ns-long laser pulses (red symbols) and hohlraums filled with a mixture of helium and hydrogen heated with a shorter, 11-ns-long pulse (blue symbols). The data indicate a linear scaling in agreement with calculations. The error bar is estimated from determining the Legendre polynomial from multiple simultaneously measured images. The dashed curve indicates a symmetric implosion, and the solid curve is the scaling calculated from two-dimensional radiation hydrodynamic simulations.

radiated into the wall, P_W, that absorbed by the capsule, P_{CAP}, and the power that escapes though the LEH, P_{LEH},

$$\eta_{LE}(P_L - P_{Backscatter}) = P_W + P_{LEH} + P_{CAP} = \sigma T_{RAD}^4[(1-\alpha_W)A_W + A_{LEH} + (1-\alpha_{CAP})A_{CAP}] \quad (1)$$

Here, σ denotes the Stefan-Boltzmann constant and α_W and α_{CAP} are the x-ray albedo of the hohlraum wall and the capsule, respectively. The albedo is defined as the ratio of re-emitted to incident x-rays. Further, A_W, A_{LEH}, and A_{CAP} are the hohlraum wall area, LEH area, and capsule surface area, respectively. Assuming a conversion efficiency of η_{LE} = 0.9 at peak laser power, Eq. 1 indicates peak radiation temperatures of $260 < T_{RAD} < 280$ eV.

The radiation temperature was inferred from the measured total x-ray hohlraum emission and from detailed radiation-hydrodynamic simulations using the code LASNEX (*22*) (Fig. 2B). An absolutely calibrated broadband x-ray spectrometer (Dante) measures the x-ray flux that is emitted from the LEH in the energy range of $0 < E_{x\text{-}ray} < 20$ keV (*26*). The x-ray power in the direction of Dante in units of gigawatt per steradian is determined by $dP/d\Omega = A_{LEH}(t)\cos\theta\,\sigma T_{RAD}^4/\pi$, where θ is the view angle of Dante toward the hohlraum axis. To determine T_{RAD}, we infer the dynamically varying source area from 3- to 5-keV x-ray pinhole camera images of the LEH. The hohlraums reach peak radiation temperatures of 285 eV after going through three low-power steps that drive coalescing shocks in ignition capsules. The experimental data are in excellent agreement with the radiation hydrodynamic modeling at all times, and further agree with the estimate provided by Eq. 1. The calculations indicate peak ablation pressures of 120 to 142 Mbar, resulting in peak implosion velocities of 380 km/s, a capsule convergence of 10 to 15, and in a compressed capsule inner shell diameter of 100 μm.

Figure 3A shows capsule implosion images at the time of peak emission that occurs 1 to 2 ns after the end of the laser drive. The x-ray self-emission is observed through a 500-μm-diameter diagnostic window in the side of the hohlraum. The images are taken using a pinhole array with 15× magnification and a gated microchannel plate detector that is filtered for x-ray energies of 9 keV and that yields temporal resolution of 80 ps (*27*). The capsules have been filled initially with a high-pressure gas mixture of 90% helium and 10% deuterium at 2594 torr (at 20 K). Thus, convergence is limited to a capsule x-ray emission radius of 50 μm with central ion temperatures in excess of T_i ~ 30 million K, as inferred from the D-D neutron time-of-flight spectrum. At these temperatures and densities, the capsule self-emission provides a sensitive measure of the hohlraum soft x-ray drive symmetry (*28*, *29*).

Figure 3 shows that the capsule symmetry is controlled by the laser wavelength settings on the inner and outer cones of beams. In particular, a wavelength difference of Δλ = 1.7 Å results in excellent implosion symmetry as required for ignition experiments. On the other hand, at Δλ = 0.5 Å, we observe an oblate implosion shape, indicating a locally reduced x-ray drive in the hohlraum equatorial plane.

These observations can be quantified by decomposing the soft x-ray flux asymmetry at the capsule into Legendre polynomials P_n. Odd orders (n = 1,3,...) are approximately zero because of the up-down illumination symmetry, and low-order, even modes (n = 2, 4) are the most important asymmetries. Higher-order drive variations are negligibly small and smoothed by the hohlraum radiation environment. Whereas small wavelength differences result in oblate implosions (P_2/P_0 = −0.42 at Δλ = 0.5 Å and P_2/P_0 = −0.24 at Δλ = 1 Å), we obtain a symmetric implosion for sufficiently large

shifts, that is, P_2/P_0 0.02 at $\Delta\lambda$ 1.7 Å. For all cases, we find $P_4/P_0 = 0.09 \pm 0.02$ (here, $P_0 = 50$ μm denotes the radius of the imploded core).

We have achieved symmetric implosions and adequate equatorial x-ray drive without changing the initial inner- and outer-cone laser powers. This tuning mechanism takes advantage of the multiple laser beam interactions (*30*, *31*) with the plasma in the LEH area where all the beams cross. Transferring power into the inner beams allows us to compensate for SRS losses of the inner beams. Although inner beam SRS energy losses of 5 to 7% are energetically small and do not substantially affect radiation temperatures, these losses may affect the local soft x-ray production.

As shown in the inset of Fig. 1, and as indicated by the interference fringes, the crossing lasers in the LEH produce spatial intensity modulations. These intensity modulations further drive plasma electron density modulations that are caused by the ponderomotive force. If these modulations move with the plasma sound speed C_S (in the frame of the plasma), then modulations and laser scattering will grow to large levels, and efficient energy transfer between beams will occur. In the rest frame, the power transfer rate Q is determined by

$$Q \sim [(\omega_1 \quad \omega_2) \quad k_A(C_S \quad V) + i\nu]^{-2} \quad (2)$$

In Eq. 2, V is the plasma flow velocity, $i\nu$ is the Landau damping rate for acoustic fluctuations, and k_A is the wave number. The frequency detuning between pairs of beams is denoted as $\omega_1 \quad \omega_2$. This factor allows us to control the energy transfer between cones of beams in integrated hohlraum experiments, and it can be set to transfer power into either cone of beams. Proper choice of the laser wavelengths is therefore required to obtain the desired x-ray drive symmetry.

P_2/P_0 depends linearly on the wavelength tuning difference $\Delta\lambda$ (Fig. 3). This fact has allowed us to tune the implosion symmetry in three shots. This observation has been expected for the small tuning range (*18*, *19*) and constant SRS levels in this study. A linear scaling further agrees with power-transfer calculations that include the detailed calculated plasma conditions and flow profiles in the LEH region. Although the experimental scaling is reproduced, the P_2 zero crossing is not accurately calculated. A difference of 0.5 Å can be explained by, for example, errors of ~10% in the calculated plasma flow.

Moreover, best agreement is observed when including a model that assumes enhanced inner laser beam absorption in the hohlraum gas fill plasma. This assumption is motivated by observations of increasing levels of hot electrons at the peak of the laser drive with increasing wavelength shift. The hot electron fraction reaches levels between 1 and 2% of the laser energy, indicating finite levels of reabsorbed SRS in the hohlraum. Without the absorption model, the calculated slope increases by 20%.

The demonstration of efficient laser coupling and symmetric capsule implosions in cryogenic hohlraum experiments on the NIF meet simultaneous requirements for laser coupling and symmetry for future ignition shots. The measured insensitivity of SRS losses to the power level of the inner cone beams will motivate future higher radiation-temperature experiments with higher laser intensities and energies.

References and Notes

1. E. Moses, C. R. Wuest, *Sci. Tech. (Paris)* **47**, 314 (2005)
2. C. A. Haynam *et al.*, *Appl. Opt.* **46**, 3276 (2007)
3. D. Clery, *Science* **324**, 326 (2009)
4. J. Nuckolls, L. Wood, A. Thiessen, G. Zimmerman, *Nature* **239**, 139 (1972)
5. R. P. Drake, *High-Energy-Density Physics* (Springer, New York, 2006)
6. B. A. Remington, R. P. Drake, D. D. Ryutov, *Rev. Mod. Phys.* **78**, 755 (2006)
7. R. A. Garcia *et al.*, *Science* **316**, 1591 (2007)
8. D. O. Gough *et al.*, *Science* **272**, 1296 (1996)
9. J. D. Lindl *et al.*, *Phys. Plasmas* **11**, 339 (2004)
10. S. Atzeni, J. Meyer ter-Vehn, *The Physics of Inertial Fusion* (Oxford Univ. Press, New York, 2004)
11. R. L. McCrory *et al.*, *Phys. Plasmas* **15**, 055503 (2008)
12. L. J. Suter *et al.*, *Phys. Rev. Lett.* **73**, 2328 (1994)
13. R. L. Kauffman *et al.*, *Phys. Rev. Lett.* **73**, 2320 (1994)
14. W. J. Krauser *et al.*, *Phys. Plasmas* **3**, 2084 (1996)
15. S. H. Glenzer *et al.*, *Phys. Rev. Lett.* **80**, 2845 (1998)
16. W. L. Kruer, S. C. Wilks, B. B. Afeyan, R. K. Kirkwood, *Phys. Plasmas* **3**, 382 (1996)
17. W. L. Kruer, *The Physics of Laser Plasma Interactions* (Addison-Wesley, New York, 1988)
18. P. Michel *et al.*, *Phys. Rev. Lett.* **102**, 025004 (2009)
19. P. Michel *et al.*, *Phys. Plasmas* **16**, 042702 (2009)
20. B. J. MacGowan *et al.*, *Phys. Plasmas* **3**, 2029 (1996)
21. J. C. Fernandez *et al.*, *Phys. Plasmas* **4**, 1849 (1997).
22. G. B. Zimmerman, W. L. Kruer, *Plasma Phys. Contr. Fusion* **2**, 85 (1975)
23. R. L. Berger, C. H. Still, E. A. Williams, A. B. Langdon, *Phys. Plasmas* **5**, 4337 (1998)
24. D. H. Froula *et al.*, *Rev. Sci. Instrum.* **75**, 4168 (2004)
25. A. J. Mackinnon *et al.*, *Rev. Sci. Instrum.* **75**, 4183 (2004)
26. E. L. Dewald *et al.*, *Rev. Sci. Instrum.* **75**, 3759 (2004)
27. J. A. Oertel *et al.*, *Rev. Sci. Instrum.* **77**, 10F308 (2006)
28. A. A. Hauer *et al.*, *Phys. Plasmas* **2**, 2488 (1995)
29. O. L. Landen *et al.*, *Phys. Plasmas* **6**, 2137 (1999)
30. K. B. Wharton *et al.*, *Phys. Rev. Lett.* **81**, 2248 (1998)
31. R. K. Kirkwood *et al.*, *Phys. Rev. Lett.* **89**, 215003 (2002).

32. This work was performed under the auspices of the U.S. Department of Energy by Lawrence Livermore National Laboratory under contract DE-AC52-07NA27344

7 December 2009; accepted 15 January 2010
Published online 28 January 2010;
10.1126/science.1185634
Include this information when citing this paper

Charged-Particle Probing of X-ray–Driven Inertial-Fusion Implosions

C. K. Li,[1]* F. H. Séguin,[1] J. A. Frenje,[1] M. Rosenberg,[1] R. D. Petrasso,[1] P. A. Amendt,[2] J. A. Koch,[2] O. L. Landen,[2] H. S. Park,[2] H. F. Robey,[2] R. P. J. Town,[2] A. Casner,[3] F. Philippe,[3] R. Betti,[4] J. P. Knauer,[4] D. D. Meyerhofer,[4] C. A. Back,[5] J. D. Kilkenny,[5] A. Nikroo[5]

Measurements of x-ray–driven implosions with charged particles have resulted in the quantitative characterization of critical aspects of indirect-drive inertial fusion. Three types of spontaneous electric fields differing in strength by two orders of magnitude, the largest being nearly one-tenth of the Bohr field, were discovered with time-gated proton radiographic imaging and spectrally resolved proton self-emission. The views of the spatial structure and temporal evolution of both the laser drive in a hohlraum and implosion properties provide essential insight into, and modeling validation of, x-ray–driven implosions.

Understanding and characterizing x-ray drive and capsule implosions is critical to indirect-drive inertial confinement fusion (ICF) (*1*–*3*), a primary approach to achieving nuclear fusion ignition at the National Ignition Facility (NIF). Properties of the x-ray drive are also of fundamental scientific importance for a wide range of basic and applied high-energy-density physics (HEDP), including laboratory astrophysics, space physics, and materials sciences (*4*, *5*). Conventionally, diagnosing drive and implosions in these experiments has relied on techniques using x-rays, ultraviolet or visible light, and fusion neutrons. Although they have inherent sensitivity to both plasma density and field structures (*6*–*9*), charged particles have not previously been used because of practical limitations and challenging complexities.

We present experiments using monoenergetic proton radiography (*10*) and charged-particle spectroscopy (*11*) to study the x-ray drive and capsule implosions in gold (Au) hohlraums [a hohlraum is an enclosure that creates an environment filled with a nearly blackbody (Planckian) radiation field when it is irradiated by high-power lasers (*2*, *3*)].

[1]Plasma Science and Fusion Center, Massachusetts Institute of Technology, Cambridge, MA 02139, USA. [2]Lawrence Livermore National Laboratory, Livermore, CA 94550, USA. [3]CEA, DAM, DIF, F-91297 Arpajon, France. [4]Laboratory for Laser Energetics, University of Rochester, Rochester, NY 14623, USA. [5]General Atomics, San Diego, CA 92186, USA.

*To whom correspondence should be addressed. E-mail: cku@mit.edu

These measurements have allowed a number of important phenomena to be observed. In particular, three types of spontaneous electric (E) fields, differing by two orders of magnitude in strength with the largest approaching the Bohr field ($= e a_0^{-2} \sim 5 \times 10^{11}$ V m^{-1}, where a_0 is the Bohr radius), were observed at different locations (in or outside the hohlraums, and inside the imploded capsules). The experiments demonstrate the absence of stochastic filamentary patterns and striations generally found in laser-driven implosions (*6*). We also observed plasma flow, supersonic jet formation, and self-generated magnetic (B) fields (*12*, *13*); determined the areal density (ρR) and implosion symmetry; and sampled different implosion phases.

The experiments were performed at the OMEGA laser facility (*14*). In the backlighting experiment (Fig. 1A) the hohlraum had a 2.4-mm diameter, 3.8-mm length, and 100% laser-entrance holes (LEH, defined as the ratio of hole size to hohlraum diameter) with a 25-μm-thick Au wall over-coated on the inside with 0.3 μm parylene (C H) liner to effectively impede and tamp the flow of Au plasma off the wall. The hohlraum was driven by 30 laser beams with wavelength 0.351 μm and total laser energy ~11 kJ in a 1-ns square pulse. The laser beams had full spatial and temporal smoothing (*15*), and phase plates SG4 (super Gaussian with power of 4) were used. The capsule was a 30-μm-thick plastic shell of diameter 550 μm filled with 50 atm H_2 or D_2 gas. The designed radiation temperatures (~150 eV) and consequent capsule compression (≈10) were low. The backlighter was a D^3He-gas–filled, glass-shell capsule with a 420-μm diameter and a 2-μm shell thickness, imploded by 30 laser beams. Two types of fusion protons with discrete birth energies of 14.7 and 3.0 MeV are produced in nuclear fusion reactions ($D + {}^3He \rightarrow \alpha + p$ and $D + D \rightarrow T + p$) ~80 ps (the nuclear burn duration). The images were recorded by CR-39 track detectors, and the timing of the proton sampling (i.e., the time when backlighting protons starting to pass through the subject target) was adjustable (*6*–*10*).

Radiographs made by 15-MeV D^3He protons (*16*) covering a typical ICF implosion sequence (Fig. 1) contain both spatial and energy information because the CR-39 detector records the position and energy of each individual proton (*6*–*10*). The images are displayed to show either proton fluence versus position (Fig. 1B) or proton mean energy versus position (Fig. 1C), to provide time-dependent information about field distributions, capsule compression, and hohlraum plasma conditions.

A striking feature shown in both fluence (Fig. 1B) and energy images (Fig. 1C) is a five-pronged, asterisk-like pattern surrounding the imploding capsule, a consequence of the laser beam positions on the hohlraum wall. To explore this structure, a solid CH sphere driven with identical conditions was imploded (Fig. 2). This solid sphere would not implode (*3*), in contrast to the example in Fig. 1. The plasma conditions and five-pronged asterisk-like structure inside the hohlraums remain nearly identical. Figure 2A shows the simulation of the laser intensity distribution associated with the OMEGA 58.8°- and 42.0°-beam configurations [the locations of the laser beams are illustrated in the simulation (Fig. 1A)], viewed from a location just outside the LEH. The ten 58.8° laser beams are grouped to form five pairs. An azimuthal lineout of the fluence image (Fig. 2B) indicates that the asterisk spokes are formed between two expanding plasma bubbles that are generated by "nearest neighbor" (58.8°) laser beam pairs (illustrated in Fig. 2A), whereas the periodic patterns (narrow fingers) between these spokes are associated with the remaining laser beam distributions.

For a physical picture of the formation of the asterisk spokes, the expanding plasma bubbles [electron temperature $T_e \sim 1$ keV, ion temperature $T_i \sim 10$ eV, and electron density n_e (in units of critical electron density at 0.35 μm) $\sim 0.1 n_c$] (*9*) generated on the hohlraum wall near the laser spots are governed by plasma hydrodynamics because the plasma thermal pressure is much larger than the magnetic pressure. Their hydrodynamic expansion is scaled by the sound speeds [$C_s \sim (ZT_e m_i^{-1})^{1/2} \sim 250$ μm ns^{-1} for CH and ~150 μm ns^{-1} for Au, where Z is the average ion charge state]. For an adiabatic rarefaction expansion of an ideal gas, the expansion speed is 3 C_s, close to the observed jet speed (~4 C_s). Furthermore, the hot electrons advancing ahead of the rarefaction expansion due to their high mobility may further boost the motion of leading-edge CH and Au ions ablating off the hohlraum wall by an additional sound speed (~C_s) factor (*9*). With ~200 μm between pairs of bubbles (Fig. 2A), it is observed that adjacent CH bubbles coalesce in ~0.1 ns and reach the hohlraum axis in ~1 ns, with the Au plasma bubble trailing behind (Fig. 2C).

To identify potential mechanisms for generating the spoke-like structure, we consider whether the image features seen in the region between the capsule and the hohlraum wall are due to collisional scattering in the plasma or to proton deflections by E or B fields. This analysis is helped by the fact that nearly simultaneous images are recorded with two different but very accurately known proton energies. For collisional scattering in matter, deflection angles vary inversely with the proton energy ($\theta \propto \varepsilon_p^{-1}$) (*17*). For B fields, it follows from the Lorentz force law that the deflection angles are inversely proportional to the square root of the proton energy ($\theta \propto \varepsilon_p^{-1/2}$) (*17*), whereas those due to E are inversely proportional to the proton energy ($\theta \propto \varepsilon_p^{-1}$) (*17*). The energy scaling due to B is unique, whereas that due to E and collisional scattering is degenerate. Deflections due to collisional scattering are accompanied by an energy loss, whereas those due to transverse E fields are not. Thus, discrimination between the two effects is possible.

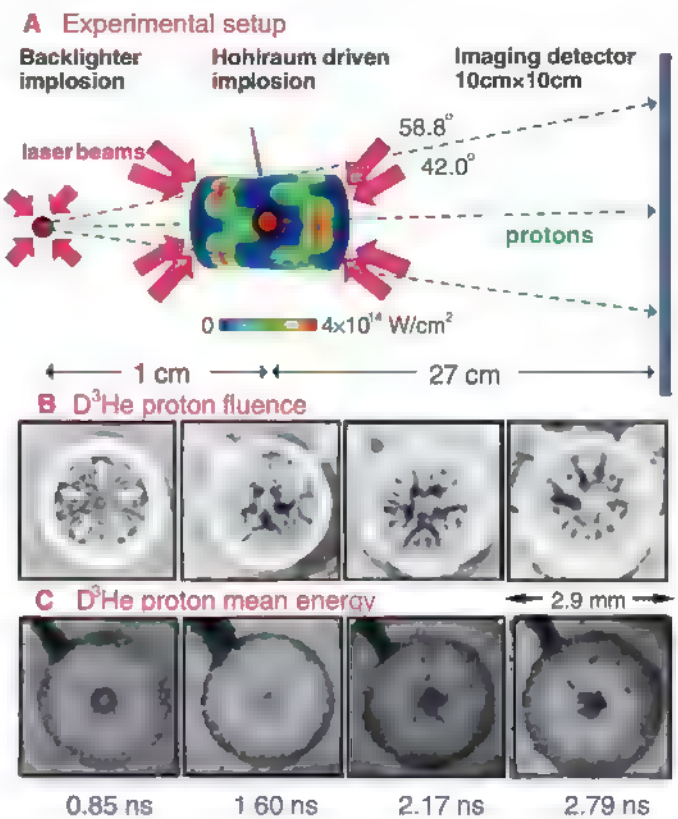

Fig. 1. (**A**) Schematic of the experimental setup, with proton backlighter, hohlraum-driven implosion, CR-39 imaging detector, and laser drive beams. Fifteen laser beams entered each end of the hohlraum: 5 with incident angle 42° and 10 with angle 58.8°. The colors shown on the hohlraum wall indicate the laser intensity distribution [modeled by VISRAD (*26*)]. The proton backlighter was driven by 30 laser beams with total laser energy ~11 kJ in a 1-ns square pulse. The 15 MeV D^3He backlighting protons (*16*) passed through the laser-driven hohlraum, sampling plasma conditions, and capsule implosions at different times. Images in (**B**) show proton fluence (within each image, darker means higher fluence), whereas images in (**C**) show proton energy (within each image, darker means more proton energy loss and therefore more matter traversed). The gray-scale mapping for image display is different in each image. The hohlraum-mounting stalk appears in the upper left corner of each image.

The B field can be excluded by symmetry. The five-pronged asterisk-like pattern in Figs. 1 and 2 provides a constraint that rules out the possibility of self-generated B fields as a major cause for the formation of this structure, because the toroidal B-field topology around the laser spots or radial jets cannot result in azimuthal proton deflections.

With the B field excluded, the other two possible mechanisms for deflecting the proton trajectories are intense, local E fields associated with strong azimuthally oriented electron pressure gradients (∇p_e) in the spokes, and proton collisional scattering in the spokes.

The possibility that the proton deflection is mostly caused by collisional scattering that deflects protons out of the dense spoke can be ruled out through the measurements of the proton energy loss. It can be shown (Fig. 1C, t = 0.85 ns) that there is little energy loss for protons passing through the major spokes. In the regions between the five spokes (Figs. 1C and 2D), there are high-contrast features in the fluence image, including the counterparts of the spokes generated by the "far" beams on the other side of the hohlraum, but very little variation in energy (Fig. 1C) (*18*).

This leaves the electric fields as the remaining cause. Using the spoke widths estimated in the images, the spreading of 15 MeV proton $\delta_{15} \sim 90$ μm (*18*), $\int E \times d\ell \sim 3 \times 10^5$ V (where $d\ell$ is the differential path length along the proton trajectory through the field area). Taking a scale length ~1 mm (the size of laser spot) for field in a jet-spoke results in $E \sim 3 \times 10^8$ V m^{-1} with field directions pointed away from the spoke. This is the first time such strong, local E fields inside the hohlraum have been inferred even though the cavity is effectively a Faraday cage (*9*). The effects of such fields can affect important physics issues, including laser-plasma instabilities, modification of the plasma electron distribution, and implosion symmetry.

Another feature in Fig. 1B of note is that a fluence peak occurs in the capsule center during the early stages of the implosion (t = 0.85 ns), but a fluence dip occurs at later times (t = 1.6 to 2.17 ns). This observation is quantified in the radial lineouts shown in Fig. 3, A and C. Although it has been observed in directly driven spherical implosions (*7*), this is the first time such a phenomenon has been measured in x-ray–driven implosions. In these and the earlier experiments, the deflection of proton trajectories is attributed to self-generated radial E fields with strength 10^9 to 10^{10} V m^{-1} that are initially directed inward and eventually reverse direction (*7*, *19*). Furthermore, the effects of proton collisional scattering in the shell (which sends some of the protons toward the image center and some away) play a minor role. A number of possible sources of such an E field, such as the gradient of plasma electron pressure, acceleration-induced charge separation, and shock-driven plasma polarization, have been proposed to explain the field strength, unique spatial structure, and time evolution (*7*, *19*). This effect will have important implications for ICF implosions; as an example, recent work has demonstrated that such a field leads to a fusion yield anomaly (*20*) through enhanced barodiffusion of different fuel species.

A common feature of the direct-drive implosions is the presence of striations around the capsule or solid CH sphere (*6*). No stochastic filamentary pattern was observed in the fluence images for x-ray–driven implosions, however (Figs. 1 and 2). This result is important for understanding the role of fields in laser and x-ray absorption, instabilities, and thermal transport involved in laser-plasma interactions.

To further characterize the capsule implosion history, quantitative information at different times is extracted from the radial lineouts through the centers of each of the individual images in Fig. 1C. The radial profiles of the mean proton energy (Fig. 3, B and D) [a function of the spatially resolved proton energy loss (*7*, *21*)] are used to infer the capsule ρR, as shown in Fig. 3B, for t = 0.85 ns (~2.5 mg cm^{-2}) and Fig. 3D, t = 2.17 ns (~8 mg cm^{-2}), indicating more energy loss at a later time due to greater compressions.

In summary, backlighting protons provided the direct observations of spontaneously generated fields and plasma flow, and quantitative characterizations of capsule implosions. The identification of strong (~10^8 to 10^{10} V m^{-1}), local E fields and their evolution substantially advance our understanding of both x-ray drive and capsule implosions, and provide critical benchmarks for model validation. Although it provides unique information, this method can be limited sometimes by the directional proton flux and experimental configuration (*22*).

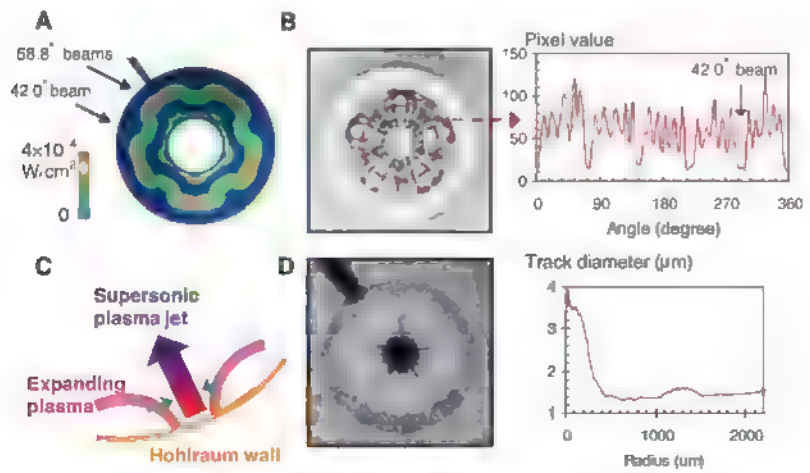

Fig. 2. **(A)** The laser intensity distribution associated with the OMEGA 58.8°-beam and 42°-beam configurations, viewed just outside of the LEH, and modeled by VISRAD. **(B)** An azimuthal lineout of the asterisk fluence image indicates that the periodic pattern is associated with the "near" and "far" laser beam distributions (relative to the detector). **(C)** A cartoon illustrating the formation of a supersonic, radially directed plasma jet as the two laser-driven expanding plasma bubbles approach one another. **(D)** Radial lineout of track diameter from the proton energy image, which indicates the energy-loss-implied areal densities for backlighting protons passing between the hohlraum and the capsule (solid sphere).

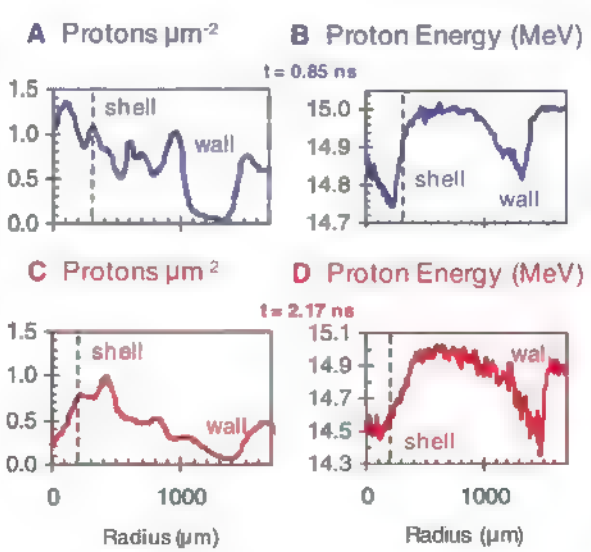

Fig. 3. Radial profiles of proton fluence images and energy images at t = 0.85 ns [blue color, **(A)** and **(B)**], and at 2.17 ns [red color, **(C)** and **(D)**] from Fig. 1, B and C, respectively. The profiles are averaged over azimuthal angle, excluding the stalk region. The dashed lines indicate the positions of the outer shells. The difference in fluence levels outside the two capsules is due to the difference in the backlighter proton yields.

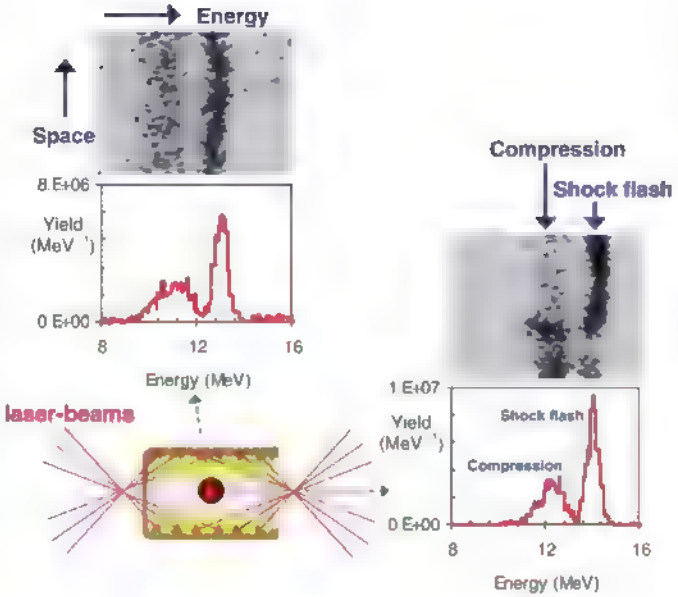

Fig. 4. The spectra and images of self-emitted protons generated from the fusion reaction of D and ^{3}He in an x-ray–driven ICF implosion (OMEGA shot 54744), measured simultaneously at two different directions. The proton yields associated with shock-coalescence burn [the narrow high-energy peak (data bang, in image)] and compression burn [the broad low-energy peak (data bang)] are clearly measured by the energy spectra and spectrally selected images. It is shown that in the direction along LEH, the spatial structure of proton flux is nonuniform (compared with the image along the equator) at both shock flash and compression burn times, with opposing distribution.

To complement the backlighting approach and give further insight into x-ray drive and implosion dynamics and fields, information that cannot be obtained through external backlighting, high-resolution spectrometry of self-emitted charged particles from imploded capsules (*11*) was used. Several important physical quantities, such as ρR at nuclear burn time, fusion yields, and fields around the LEH axis, can be accurately measured through proton self-emission (*22*). As shown in Fig. 4, 14.7-MeV D^{3}He protons generated during the implosion escape the shell and provide information for characterizing implosion performance: first, the charged-particle yield—a fundamental experimental complement to traditional neutron yields; second, measured proton energy loss, which gives information about target areal density [$\rho R = \int \rho (d\varepsilon/dx)^{-1} d\varepsilon$] (*21*); and third, measurements of ρR at different angles to quantify implosion asymmetries (*2*, *3*). These measurements can be used to infer a number of important time-dependent implosion phenomena and parameters, such as fuel-shell mix (*2*, *3*), ion and electron temperatures, convergence ratio [$C_r = Q(\rho R/\rho R_0)^{1/2}$, where Q is a function of mass ablation], and spatially resolved capsule structure (*2*, *3*).

In these experiments, the cylindrical vacuum Au hohlraum was 2.45 mm long, with a 1.6-mm diameter and 50% LEH. The 647-μm diameter CH capsule had a shell thickness of 48.2 μm and was filled with 50 atm of D^{3}He (at equal number densities) gas. The hohlraum was driven by 40 beams with total laser energy of 19.7 kJ in a 1-ns square pulse.

Figure 4 shows data collected from D^{3}He protons produced during the nuclear burn: self-emission, spectrally resolved one-dimensional images and energy spectra. The narrow high-energy peak in each spectrum is associated with shock-flash burn (*23*), and the broad low-energy peak with compression burn. After correcting the proton spectrum seen at the equator for the measured energy loss through the 30-μm hohlraum wall, the two peaks are found to have the same energies as those seen through the LEH. Values of ρR inferred from the measured proton energy losses due to passage through the capsule shell indicate that ~20 mg cm^{-2} is achieved at shock flash time and ~80 mg cm^{-2} at the compression burn time in both the polar (toward LEH) and the equatorial directions.

Whereas the proton fluence in the direction of the equator is spatially uniform, the fluence in the LEH direction shows nonuniformities that are different for the two energy components (Fig. 4). Because they are generated at different times (separated by about ~200 ps between the shock flash and compression burn), the nonuniformities have significantly evolved over this time interval. This distribution is not likely to have been caused by proton collisional scattering off the plasmas, because the measured proton energies along both LEH and the equator are very similar. This suggests that the proton fluence nonuniformity is due to self-generated B or E fields near the LEH that do not cause proton energy loss but deflect their trajectories. As shock-flash protons selected by detector have probed a different line-of-sight than the different compression-generated protons, they might see different static small-scale fields. The strength of this B field is estimated to be ~2.5 × 10^5 Tesla-μm. The scale length (the radius of the laser spot) is about 500 μm, suggesting that the B field is about 500 Tesla (5 megaGauss). If the nonuniformities are due to the E field, the strength required (~5 × 10^{10} V m^{-1}) is about one-tenth of the Bohr field, a fundamental field strength for stripping bound electrons, which effectively enhances and sustains the ionizations after lasers are turned off. This value is about a factor of 10 larger than the strength estimated from Faraday's law ($\partial B/\partial t = \nabla \times E$), based on the above-estimated B field strength and 200-ps time scale, suggesting that the time scale for field variation should be ~10 times as fast. The high fields are likely generated in the region near the LEH where the outward-directed axial plasma becomes increasingly resistive after the laser drive ends, leading to the generation, growth, and saturation of low-mode number magneto-instabilities (*24*). The data suggest that the spatial structure or the directions of such fields undergoes rapid changes between the time of shock flash and compression burn.

We thus have a picture in which radiography-generated data show strong fields with a very well-defined fivefold symmetry between the capsule and the hohlraum walls, as well as an axially symmetric radial field inside the capsule. We also have completely complementary data from self-emission imaging showing a strong, rapidly changing, asymmetric field structure near the hohlraum axis.

References and Notes

1. J. Nuckolls, L. Wood, A. Thiessen, G. Zimmerman, *Nature* **239**, 139 (1972).
2. J. Lindl, *Inertial Confinement Fusion* (Springer, New York, 1999).
3. S. Atzeni, J. Meyer-Ter-Vehn, *The Physics of Inertial Fusion* (Claredon, Oxford, 2004).
4. B. A. Remington, D. Arnett, R. P. Drake, H. Takabe, *Science* **284**, 1488 (1999).
5. R. P. Drake, *High-Energy-Density Physics* (Springer, New York, 2006).
6. J. R. Rygg *et al.*, *Science* **319**, 1223 (2008).
7. C. K. Li *et al.*, *Phys. Rev. Lett.* **100**, 225001 (2008).
8. R. D. Petrasso *et al.*, *Phys. Rev. Lett.* **103**, 085001 (2009).
9. C. K. Li *et al.*, *Phys. Rev. Lett.* **102**, 205001 (2009).
10. C. K. Li *et al.*, *Phys. Rev. Lett.* **97**, 135003 (2006).
11. F. H. Seguin *et al.*, *Rev. Sci. Instrum.* **74**, 975 (2003).
12. S. I. Braginskii, *Review of Plasma Physics 1* (Consultants Bureau, New York, 1965).
13. M. G. Haines, *Phys. Rev. Lett.* **78**, 254 (1997).
14. J. M. Soures *et al.*, *Phys. Plasmas* **3**, 2108 (1996).
15. D. D. Meyerhofer *et al.*, *Phys. Plasmas* **8**, 2251 (2001).
16. A slight upshift from its birth energy is caused by positive charging of the backlighter target.
17. J. D. Jackson, *Classical Electrodynamics* (Wiley, New York, 1975).
18. The measured width (FWHM) in Fig. 1B is Δ_{15} ~ 260 μm (t = 0.85 ns), which includes both the width W of the jet itself and the spreading δ_{15} of the 15-MeV protons. $\Delta_{15}^2 = W^2 + \delta_{15}^2$. Because $\delta_3 = (15/3)\,\delta_{15} = 5\,\delta_{15}$, $\Delta_3 \approx 2\,\Delta_{15}$, and $\Delta_3^2 = W^2 + \delta_3^2$, it follows that $\delta_{15} \approx 90$ μm. Taking the plasma scale length (laser spot size on the wall) L ~ 1.2 mm, the scattering angle in radians can be estimated as ~ $0.5\delta_{15}/L \approx 0.037$. This amount of spreading can be shown to require about $\rho L \approx \rho L_{rad}\,(pv/15\text{MeV})^2\langle\theta\rangle^2$ ~ 33 mg cm^{-2} of Au, where pv = 30 MeV and ρL_{rad} ~ 6 × 10^3 mg cm^{-2} for Au (*25*). If the five-spoke structure in the images is caused primarily by proton collisional scattering in the spokes, this amount of ρL would lead to ~1 MeV energy loss for 15-MeV protons, which is substantially more than observed in Fig. 1C [energy loss consistent with collisional scattering if we assume that CH in the spoke would be even greater (≈15 MeV)].
19. P. A. Amendt *et al.*, *Plasma Phys. Contr. Fusion* **51**, 124048 (2009).
20. J. R. Rygg *et al.*, *Phys. Plasmas* **13**, 052702 (2006).
21. C. K. Li, R. D. Petrasso, *Phys. Rev. Lett.* **70**, 3059 (1993).
22. The backlighting proton fluence is reduced or even blocked along the hohlraum axis due to the deflection

and/or collisional scattering in the compressed capsule core (Figs. 1 to 3).
23. R. D. Petrasso *et al.*, *Phys. Rev. Lett.* **90**, 095002 (2003).
24. C. K. Li *et al.*, *Phys. Rev. E* **80**, 016407 (2009).
25. T. A. Lasinski *et al.*, *Rev. Mod. Phys.* **45**, S1 (1973).
26. J. J. MacFarlane, *J. Quant. Spectrosc. Radiat. Transf.* **81**, 287 (2003).

27. This work was supported in part by the U.S. Department of Energy and the Laboratory for Laser Energetics (LLE) National Laser User's Facility (DE-FG52-07NA28059 and DE-FG03-03SF22691), Lawrence Livermore National Laboratory (B543881 and LDRD-ER-898988), CEA/DIF (France, Cooperative agreement DE-FC52-08NA28302), LLE (414090-G), Fusion Science Center at University of Rochester (412761-G), and General Atomics (DE-AC52-06NA27279).

9 December 2009; accepted 15 January 2010
Published online 28 January 2010;
10.1126/science.1185747
Include this information when citing this paper.

Deglacial Meltwater Pulse 1B and Younger Dryas Sea Levels Revisited with Boreholes at Tahiti

Edouard Bard,* Bruno Hamelin, Doriane Delanghe-Sabatier

Reconstructing sea-level changes during the last deglaciation provides a way of understanding the ice dynamics that can perturb large continental ice sheets. The resolution of the few sea-level records covering the critical time interval between 14,000 and 9,000 calendar years before the present is still insufficient to draw conclusions about sea-level changes associated with the Younger Dryas cold event and the meltwater pulse 1B (MWP-1B). We used the uranium-thorium method to date shallow-living corals from three new cores drilled onshore in the Tahiti barrier reef. No significant discontinuity can be detected in the sea-level rise during the MWP-1B period. The new Tahiti sea-level record shows that the sea-level rise slowed down during the Younger Dryas before accelerating again during the Holocene.

Understanding the behavior and predicting the fate of large ice sheets can be done in parallel by studying recent and ongoing changes in the climate system (*1*, *2*) and by studying the dramatic sea-level changes that occurred during the last deglaciation [21,000 to 5000 years before the present (yr B.P.)]. To date, the most complete record of deglacial sea level is based on reef cores drilled at Barbados, which have yielded ages from both ^{14}C (*3*–*5*) and mass spectrometric U-Th methods (*5*–*8*). The Barbados record is characterized by two periods of sea-level acceleration [meltwater pulses (MWP) 1A and 1B] that occurred around 14,000 calendar yr B.P. (cal yr B.P.) and 11,300 cal yr B.P., respectively. During each MWP event, the sea level apparently rose by several meters per century, leading to a major hydrological perturbation that probably impacted the ocean circulation [e.g., (*9*, *10*)]. Both the amplitude and the localization of injection into the ocean are crucial in understanding the climatic impact of a MWP event [e.g., (*11*)]. However, several first-order questions remain unresolved on the precise characterization of these events, despite the intensive research carried out over the last decade (see SOM text 1).

The precise timing and amplitude of MWP-1A and 1B are still open questions, because both of these events were originally detected as hiatuses between individual drill cores collected at different depths off Barbados (see SOM text 2 and map in fig. S2). Several other records have been interpreted later as direct or indirect evidence of the occurrence of MWP-1A (*12*–*16*). One of the main goals of the recent Integrated Ocean Drilling Program (IODP) Leg 310 at Tahiti was specifically to collect an additional coral record over the MWP-1A time window. The new suite of coral samples collected during this IODP campaign successfully confirms the existence of MWP-1A and leads to a reassessment of its age and amplitude (*17*).

However, MWP-1B is even more controversial and still needs to be confirmed, both at Barbados and at other far-field sites. Indeed, subsequent coral studies at Huon Peninsula (*18*) and Tahiti (*12*) questioned the timing and amplitude of this freshwater pulse. Additional doubts were also raised about the existence of MWP-1B by a study of sea level in northwest Scotland based on the so-called "marginal basin isolation" technique (*19*). However, the interpretation of this Scottish record is complex due to its proximity to former ice sheets in a region where the postglacial rebound contribution is dominant, which explains why the local sea level continued to fall during most of the deglaciation. So far, the sample coverage and depth resolution of these different studies are still insufficient to reach a definitive conclusion about MWP-1B. Unfortunately, the new IODP sample collection from Tahiti is of little help in studying MWP-1B, because the depth range of the drill cores was targeted on MWP1-A and the earliest part of the deglaciation (i.e., 90 to 120 m). At these depths, only deep-living coral species persisted in the reef at the levels corresponding to the age of MWP-1B.

To settle the issue, we dated by U-Th 47 pristine coral samples from three new reef cores (P8, P9, and P10) drilled onshore of the Papeete barrier reef in Tahiti, close to the location of our previous study (23 U-Th dated corals from P6 and P7 cores) (*12*). P8 is at about the same position as P7 (*12*) but was drilled at an angle of 33° toward the sea, whereas P9 and P10 were collected in the inner part of the barrier reef toward the Papeete Pass (fig. S1).

Figure 1B shows a comparison of the new U-Th data from P8, P9, and P10 cores with the previous Tahiti record (*12*). Unlike the Barbados cores, each of these Tahiti cores yields an uninterrupted record of the time window corresponding to MWP-1B. The new U-Th data (Fig. 1B and table S1) provide an unprecedented resolution and can be compared to the other sea-level records from Barbados (*7*, *8*), Papua New Guinea (Huon Peninsula) (*18*, *20*), and Vanuatu (Urelapa) (*21*) (Fig. 1, C and D). The North Greenland Ice Core Project (NorthGRIP) isotope record is also plotted in Fig. 1A using its most recent time scale (*22*). This is done to compare the sea-level records with climatic transitions such as the inception and the end of the Younger Dryas (YD), which marks the start of the Holocene period.

The large number of data points derived from the four cores provides a very accurate constraint on the sea-level rise during this period, defined by the coherent upper envelope of the paleo-depths of the samples. The small scatter of the data reflects the inherent uncertainty linked to the paleo-bathymetry of corals and associated shallow-living biological assemblages (*23*, *24*). Part of this overall scatter is also related to the different positions of the drill cores on the barrier reef (SOM text 2 and fig. S1). P9 and P10 record the upper reef crest on the inner part of the barrier. By contrast, P8 was drilled on the outer part of the barrier reef, with a deviation of 33° toward the sea. Therefore, in the lower sections of P8 below 65 m, the corals (red points in Fig. 1B) plot slightly lower than those from P7, P9, and P10, a difference that remains small (<6 m) but fairly systematic.

The rate of sea-level rise at Tahiti can be calculated by means of linear fits over the three specific climatic intervals: before, during, and after the YD event (thick lines in Fig. 1B) (see SOM text 2 and table S2 for details). Taken together, the Tahiti data define a relatively smooth sea-level rise, with no significant acceleration during the time interval corresponding to

Centre Européen de Recherche et d'Enseignement des Géosciences de l'Environnement (CEREGE), UMR 6635 CNRS, University Aix-Marseille, Institut de Recherche pour le Développement, College de France, Europôle de l'Arbois, BP 80, F-13545 Aix-en-Provence Cedex 4, France.

*To whom correspondence should be addressed. E-mail: bard@cerege.fr

MWP-1B at Barbados (11,400 to 11,100 cal yr B.P.; area shaded green in Fig. 1). This conclusion is based on *Acropora* and *Pocillopora* samples from the four cores P7, P8, P9, and P10 (table S1), which exhibit a rather small scatter (<6 m) (see Fig. 1B). In contrast to the Tahiti record, the MWP-1B event appears as a prominent step of ~15 m between two drill cores at Barbados, implying an apparent rise of ~40 mm/year (Fig. 1D). In the Huon record, the time interval of MWP-1B falls within a time gap of about a millennium (12,100 to 11,100 cal yr B.P.). The Vanuatu record has only two coral samples in this interval, but even considering the few samples below (older) and above (younger), it remains difficult to pick out a step or pause during the 13,000 to 10,000 yr B.P. interval. Therefore, both records from Pacific far-field sites agree with the higher resolution record from Tahiti: None of these reconstructions shows an abrupt 15-m step around 11,300 cal yr B.P., in contrast to the Barbados record.

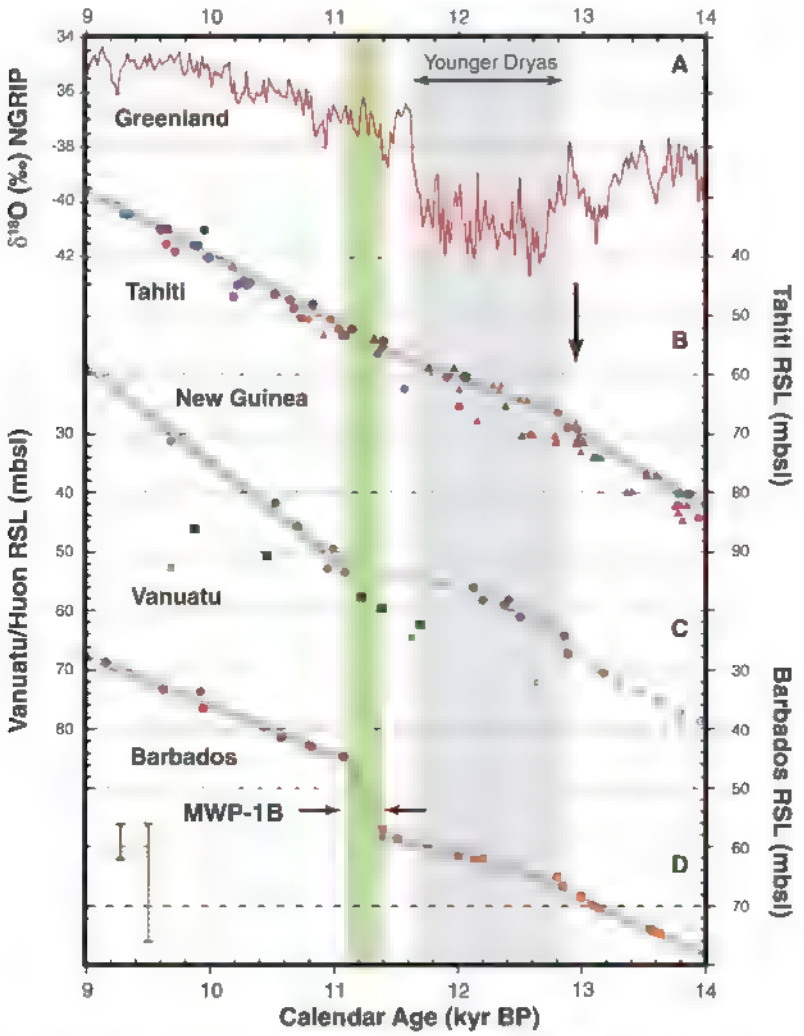

Fig. 1. Deglacial records over the 14,000 to 9000 yr B.P. time window. (**A**) $\delta^{18}O$ record of the NorthGRIP Greenland core plotted on its most recent time scale (*22*). (**B**) Tahiti corals: depth in meters below present sea level versus U-Th ages in thousand years B.P. (core P6, dark blue; P7, light blue; P8, red; P9, orange; P10, green) (see table S1). (**C**) Pacific corals from Huon Peninsula, Papua New Guinea [brown dots (*18*), blue dots (*20*)] and from Urélapa, Vanuatu [light and dark green squares correspond to two different cores (*21*)]. (**D**) Barbados *A. palmata* corals [core #12, orange squares; core #7, red dots; core #16, green diamonds (*8*)]. All depths have been corrected for subsidence (Tahiti) and uplift (all other sites) as described in SOM text 2. Shaded time windows correspond to the YD [boundaries based on (A)] and to the MWP-1B event [boundaries based on (D)]. For Tahiti, the species and/or genus of the dated corals are provided in table S1. The bathymetric habitat of *Acropora* with *Pocillopora* [dots in (B)] is more restricted (about 6 m, a range shown by the short brown bar in the lower left corner) than those of *Porites* or *Favidea* corals [triangles in (B)], which can live in the top 10 to 20 m (a range shown by the longer brown bar in the lower left corner). Dark gray lines correspond to linear fits of sea-level data (SOM text 2 and listed in table S2). For Tahiti, the calculations exclude samples from the base of the P8 core deviated toward the shore (red dots below −65 m) and samples made of *Porites* or *Favidea* corals. Using other assumptions would not change significantly the calculated rates of sea-level changes and would not change our conclusions (SOM text 2 and table S2). For New Guinea, dashed lines are used when data are scarce (gap starting in the middle of the YD and period before YD).

The new Tahiti record includes many samples covering the YD cold period, in particular from cores drilled in the inner part of the outer reef (P9 and P10). An important observation based on this data set is that the deglacial sea-level rise slowed down during the YD event and reaccelerated during the early Holocene (7.5 ± 1.1 mm/year during the YD, compared with 11.7 ± 0.4 mm/year after and 12.1 ± 0.6 mm/year before). Similar conclusions can be derived (see details in SOM text 2 and table S2) by considering the data obtained on the shallow-living corals (*Acropora* and *Pocillopora*, dots in Fig. 1B) or by looking at the entire data set, including those measured on more ubiquitous corals (*Porites* and *Favidea*, triangles in Fig. 1B). The Barbados record also suggests that the rate of sea-level rise was reduced to 5.6 ± 0.4 mm/year (Fig. 1D and table S2), in agreement with the slowing down observed for Tahiti. The case for a slower sea-level rise during the YD event than during the period immediately before (9.3 ± 0.4 mm/year) is particularly strong because all *A. palmata* samples come from the very same Barbados drill core #12 (in contrast to MWP-1B, which occurs between Barbados cores #12 and #7). The existence of a transient pause in the deglacial sea-level rise was also suggested by considering samples older and younger than the 12,100 to 11,100 cal yr B.P. data gap in the Huon record (*18*). Between 12,100 and 11,100 cal yr B.P., the sea-level rise clearly slowed down, although the data gap in the Huon record does not correspond exactly to the YD event and makes it difficult to compare with records from other sites.

In addition, the coral data plotted in Fig. 1 could suggest a small step (<6 m) in sea level near the onset of the YD event at around 13,000 yr B.P. (arrow in Fig. 1). This small step also corresponds to a rate change in both the Barbados and Tahiti records. At Huon, this period is covered by only a few corals that could possibly be fitted with a small step. However, the existence of such a structure is within the overall uncertainty of the approach (see details in SOM text 2) and thus remains speculative.

Relative sea level (RSL) differences between the records obtained for different sites should be interpreted with caution because isostatic effects are not the same everywhere on the planet. Therefore, a more complete comparison between these reconstructions of local sea-level records requires geophysical modeling. Milne and Mitrovica (*25*) drew up a comprehensive comparison by using a wide range of mantle viscosity and lithospheric models forced by different ice-sheet histories. These model simulations illustrate systematic differences in RSL between the different sites. In the time window of interest, the shallowest sea level should be

observed at Huon and the deepest at Barbados, whereas Tahiti RSL falls in between. This is in good agreement with the observations: At 12,000 cal yr B.P., the RSL is situated at 62, 59, and 55 m below modern sea level for Barbados, Tahiti, and Huon, respectively.

Geophysical processes, such as gravitational and rotational effects, can also affect the relative amplitude of abrupt sea-level changes expressed as steps in RSL records (*26*). Clark *et al.* (*11*) even proposed that comparing such steps at different sites could serve to identify the ice sheet(s) that released large amount of icebergs or meltwater. The apparent discrepancy between the Barbados and Tahiti records over the MWP-1B period around 11,300 cal yr B.P. may be reconciled by assuming that the ice was released exclusively from the Pacific sector of the Antarctic ice sheet (*11*, *26*). However, in this scenario, the model predicts that a small residual step should be expected at Tahiti. Our data suggest that this step would be masked by the inherent uncertainty linked to the coral approach (less than 6 m). Further postglacial rebound modeling simulations such as (*11*, *26*) should be performed to investigate whether such a scenario could generate steps larger than 10 m at Barbados and less than 6 m at Tahiti, a relative gradient even larger than the one caused by a release from the West Antarctica Ice Sheet (*11*, *26*). This hypothetical scenario would also require that the Antarctic ice sheet was much larger than today during the glacial period. This issue has been controversial, but recent numerical modeling of the Antarctic ice sheet (*27*) is compatible with a total loss of ice of 17.5 m of equivalent sea level since 15,000 yr B.P. (including both contributions of MWP-1A and MWP-1B). However, specific attempts of geophysical modeling focused on the specific contribution to MWP-1B (*28*, *29*) failed to reconcile the observed contrast in RSL with a reasonable contribution from the Antarctic ice sheet [see figure S3 in (*29*)]. Another puzzling aspect of MWP-1B is the lack of clear signals in marine sediments, from the Southern Ocean or the North Atlantic, for a large freshwater release to the Ocean that should have been similar to the Heinrich events.

Otherwise, we should consider the alternative possibility that MWP-1B might have been overestimated at Barbados. Mapping site locations on the Barbados south coast shows that cores defining MWP-1B are drilled in different environments: submerged fossil barrier reef for the deepest cores #12 and 16, and fringing reef for the shallow core #7 (map in fig. S2). A systematic bathymetric difference between both environments could be invoked, but this hypothesis would imply that, during the sea-level transition, the depth tolerance of *A. palmata* exceeded its 5-m limit, observed during the modern period characterized by sea-level stability. An additional cause of the bias might be the local tectonics of Barbados. Due to its location on the accretionary prism at the convergent boundary between the Caribbean and South American plates, Barbados is characterized not only by a general uplift of varying amplitude around the island but also by several faults and tectonic flexures (*30*). It is thus probably an oversimplification to apply a constant uplift rate to all samples. Indeed, the position of cores #12 (#16) and #7 suggests that they may belong to different neotectonic segments (map in fig. S2) and thus were affected by different uplift rates. Nevertheless, it seems very unlikely that this tectonic factor could explain the full amplitude of the jump observed in the coral record, since even tripling the differential uplift correction between the cores would only contribute to half of the 15-m sea-level step observed at Barbados (see SOM text 2 for a full discussion of this issue). In principle, the different explanations invoked to explain the Barbados step (East Antarctic release and local biases at Barbados) are not mutually exclusive and could have been superimposed, but it seems rather unlikely that all these independent processes occurred within the same time window of a few centuries.

In addition to the absence of a detectable MWP-1B step at Tahiti, the other conclusion of our study, that the rate of sea-level rise was reduced during the YD period and reaccelerated during the early Holocene, has often been overlooked. This scenario would resolve the long-standing controversy between the observation of a slower rate of sea-level rise during the YD and the hypothesis that this millennium-long cold event was triggered by a meltwater pulse that slowed the Atlantic meridional overturning circulation. Our new record is compatible with previous modeling work (*10*) mentioning a reduced sea-level rise during the YD and briefly discussing the climatic implications with respect to freshwater forcing. The detection of a small sea-level change just before the start of YD at ~13,000 yr B.P. is tempting but remains difficult to prove. The reduced rate of sea-level rise observed during the following millennium (i.e., the YD event) would then correspond to a return of glacial conditions that interrupted the deglaciation process and, in some cases, even favored glacier readvances in Europe (*31*–*33*).

Our results on the final stages of the last deglaciation illustrate the complexity of the melting of ice sheets that once covered a large fraction of the northern hemisphere continents. Modeling this retreat, together with the associated icebergs and freshwater drainage history, will help in quantifying the complex impact of ice-sheet melting on ocean circulation and, more generally, Earth's climate over the first half of the Holocene period (*34*, *35*). In addition, the observed long-term sea-level changes will allow geophysicists to extract the isostatic "memory" component from modern satellite data to quantify recent processes such as oceanic thermal expansion, melting of mountain glaciers, and loss of ice from the Greenland and West Antarctica ice sheets (*36*).

References and Notes

1. W. T. Pfeffer, J. T. Harper, S. O'Neel, *Science* **321**, 1340 (2008).
2. Materials and methods are available as supporting material on *Science* Online.
3. R. G. Fairbanks, *Nature* **342**, 637 (1989).
4. E. Bard, M. Arnold, R. G. Fairbanks, B. Hamelin, *Radiocarbon* **35**, 191 (1993).
5. R. G. Fairbanks *et al.*, *Quat. Sci. Rev.* **24**, 1781 (2005).
6. E. Bard, B. Hamelin, R. G. Fairbanks, A. Zindler, *Nature* **345**, 405 (1990).
7. E. Bard, B. Hamelin, R. G. Fairbanks, *Nature* **346**, 456 (1990).
8. W. R. Peltier, R. G. Fairbanks, *Quat. Sci. Rev.* **25**, 3322 (2006).
9. P. U. Clark, N. G. Pisias, T. F. Stocker, A. J. Weaver, *Nature* **415**, 863 (2002).
10. A. J. Weaver, O. A. Saenko, P. U. Clark, J. X. Mitrovica, *Science* **299**, 1709 (2003).
11. P. U. Clark, J. X. Mitrovica, G. A. Milne, M. E. Tamisiea, *Science* **295**, 2438 (2002).
12. E. Bard *et al.*, *Nature* **382**, 241 (1996).
13. S. L. Kanfoush *et al.*, *Science* **288**, 1815 (2000).
14. T. Hanebuth, K. Stattegger, P. M. Grootes, *Science* **288**, 1033 (2000).
15. J. M. Webster *et al.*, *Geology* **32**, 249 (2004).
16. J. D. Stanford *et al.*, *Paleoceanography* **21**, PA4103 (2006).
17. P. Deschamps *et al.*, *Geophys. Res. Abstr.* **11**, EGU2009-10233 (2009).
18. R. L. Edwards *et al.*, *Science* **260**, 962 (1993).
19. I. Shennan, *J. Quat. Sci.* **14**, 715 (1999).
20. K. B. Cutler *et al.*, *Earth Planet. Sci. Lett.* **206**, 253 (2003).
21. G. Cabioch *et al.*, *Quat. Sci. Rev.* **22**, 1771 (2003).
22. S. O. Rasmussen *et al.*, *J. Geophys. Res.* **111** (D6), D06102 (2006).
23. L. F. Montaggioni *et al.*, *Geology* **25**, 555 (1997).
24. G. Cabioch, G. F. Camoin, L. F. Montaggioni, *Sedimentology* **46**, 985 (1999).
25. G. A. Milne, J. X. Mitrovica, *Quat. Sci. Rev.* **27**, 2292 (2008).
26. J. X. Mitrovica, N. Gomez, P. U. Clark, *Science* **323**, 753 (2009).
27. G. Philippon *et al.*, *Earth Planet. Sci. Lett.* **248**, 750 (2006).
28. J. Okuno, M. Nakada, *Palaeogeogr. Palaeoclimatol. Palaeoecol.* **146**, 283 (1999).
29. S. E. Bassett, G. A. Milne, J. X. Mitrovica, P. U. Clark, *Science* **309**, 925 (2005).
30. F. W. Taylor, P. Mann, *Geology* **19**, 103 (1991).
31. B. G. Andersen *et al.*, *Quat. Int.* **28**, 147 (1995).
32. J. I. Svendsen, V. Gataullin, J. Mangerud, L. Polyak, *Dev. Quat. Sci.* **26**, 369 (2004).
33. V. R. Rinterknecht *et al.*, *Science* **311**, 1449 (2006).
34. H. Renssen *et al.*, *Nat. Geosci.* **2**, 411 (2009).
35. Z. Liu *et al.*, *Science* **325**, 310 (2009).
36. G. A. Milne, W. R. Gehrels, C. W. Hughes, M. E. Tamisiea, *Nat. Geosci.* **2**, 471 (2009).

37. The authors thank G. Cabioch for help with coring and sampling; G. Ménot and W. Barthelemy for help with U-Th analyses; D. Borschneck for help with x-ray diffraction analyses; P. Deschamps for age calculations and drafting Fig. 1; P. Dussouillez and J.-J. Motte for help with maps, and F. Antonioli, G. Cabioch, P. Clark, P. Deschamps, and F. Taylor for useful technical and scientific discussions. Numerical data are available in table S1 and also at the National Oceanic and Atmospheric Administration's National Geophysical Data Center public data repository. Paleoclimate work at CEREGE is supported by grants from the Gary Comer Foundation for Science and Education, the European Science Foundation (EuroMARC), the CNRS, and the College de France.

Supporting Online Material

www.sciencemag.org/cgi/content/full/science.1180557/DC1
SOM Text
Figs. S1 and S2
Tables S1 and S2
References

13 August 2009; accepted 5 January 2010
Published online 14 January 2010.
10.1126/science.1180557
Include this information when citing this paper.

Geodynamo, Solar Wind, and Magnetopause 3.4 to 3.45 Billion Years Ago

John A. Tarduno,[1,2]* Rory D. Cottrell,[1] Michael K. Watkeys,[3] Axel Hofmann,[3] Pavel V. Doubrovine,[1,4] Eric E. Mamajek,[2] Dunji Liu,[5] David G. Sibeck,[6] Levi P. Neukirch,[2] Yoichi Usui[1,7]

Stellar wind standoff by a planetary magnetic field prevents atmospheric erosion and water loss. Although the early Earth retained its water and atmosphere, and thus evolved as a habitable planet, little is known about Earth's magnetic field strength during that time. We report paleointensity results from single silicate crystals bearing magnetic inclusions that record a geodynamo 3.4 to 3.45 billion years ago. The measured field strength is ~50 to 70% that of the present-day field. When combined with a greater Paleoarchean solar wind pressure, the paleofield strength data suggest steady-state magnetopause standoff distances of ≤5 Earth radii, similar to values observed during recent coronal mass ejection events. The data also suggest lower-latitude aurora and increases in polar cap area, as well as heating, expansion, and volatile loss from the exosphere that would have affected long-term atmospheric composition.

The oldest record of Earth's magnetic field strength, based on a thermoremanent magnetization (TRM), is from silicate crystals hosting single domain–like magnetite inclusions separated from plutons from the Kaapvaal craton, South Africa; these plutons have been dated to 3.2 billion years ago (Ga) (*1*). This record suggests an intensity that is within 50% of the modern field value. The geomagnetic field may be truly ancient, starting shortly after core formation, but several hypotheses suggest otherwise. A null or weak field at 3.8 to 3.9 Ga is predicted from a hypothesis seeking to explain lunar nitrogen values through transport from Earth's atmosphere by the solar wind (*2*). A delayed onset of the geodynamo, to ages as young as 4.0 to 3.4 Ga, has been predicted from a model for cooling of a dense liquid layer at the base of the early Earth's magma ocean (*3*). However, testing these null-field models is difficult because of the ubiquitous metamorphism that has affected Paleoarchean terrestrial rocks.

Some of the least metamorphosed Paleoarchean rocks, having experienced peak temperatures of <350°C [e.g., (*4*)], are found in the Barberton Greenstone Belt (BGB) in South Africa. Chemical remagnetization associated with Fe mobilization during metamorphism is also a concern. Paleomagnetic and rock magnetic studies suggest that some dacitic rocks of the BGB have largely escaped this problem, probably because of a relatively low Fe content. Specifically, dacite clasts pass a conglomerate test, indicating magnetization prior to 3.42 Ga (*5*). The ~3.45-Ga dacite parent body for the clasts, however, reveals a high unblocking temperature magnetization with scatter greater than that seen in younger rocks. The simplest explanation for the large dispersion of magnetic directions is the presence of multidomain magnetic grains in the dacite, seen in thin section (*5*), that are susceptible to carrying magnetic overprints. Alternatively, the scatter could reflect magnetization in the absence of a geodynamo, in a field related to solar wind interaction with the atmosphere. A good discriminator of external versus internal terrestrial fields is paleointensity. Using modern Venus as an example of a planet lacking a dynamo (*6*), we expect that solar wind–atmosphere interaction will create a field that is highly variable in direction and at least an order of magnitude weaker than the post 3.2 Ga dynamo-driven field recorded on Earth.

We tested the nondynamo magnetization scenario by sampling dacites from two Kaapvaal craton localities for paleointensity analysis: the Hooggenoeg Formation in the BGB (*7*) and the Witkop Formation in the Nondweni Greenstone Belt (NGB) (*8*, *9*); the latter is located ~300 km south of the BGB. Several authors have reported ages of ~3.445 Ga for the BGB dacite (*5*, *10*), whereas new SHRIMP Pb-Pb zircon data reported here (*10*) (fig. S1 and table S1) indicate an age of 3.409 ± 0.004 Ga for the NGB dacite site used in our study. The BGB dacite is a shallowly emplaced body that likely once linked to extrusive (now eroded) counterparts. Our samples were collected within 1 km of the contact with the overlying Buck Reef Chert (*7*), but the dacite body appears to represent the accumulation of many smaller intrusions. We assume that our BGB site represents a sample of one of these 100- to 200-m-thick intrusive events. The NGB site is from a flow or very shallow sill that is 100 m thick where sampled. Hand samples were collected from topographic lows of exposures of both dacites to avoid the effects of modern lightning strikes. A field test for the age of remanence similar to that reported for the BGB dacite (*5*) is unavailable for our NGB site, but the high–unblocking temperature in situ magnetic direction seen in whole rock samples is far removed from later overprint directions (fig. S2).

Single silicate crystals can host magnetic carriers with single domain–like behavior, avoiding complexities posed by the presence of multidomain grains [e.g., (*11*, *12*)]. We isolated quartz phenocrysts, 0.5 to 2 mm in size, as oriented and unoriented samples. Preparation and selection followed prior studies (*1*, *13*) and included the provision that samples could not show visible inclusions under low magnification, thereby excluding samples with larger multidomain magnetic inclusions. This required a search through hundreds of BGB crystals; the NGB dacites, however, yielded cleaner quartz crystals suitable for paleomagnetic and rock magnetic measurements.

Magnetic hysteresis data measured with an alternating gradient force magnetometer (Princeton Measurements Corp.) confirmed the presence of single-domain to pseudo–single-domain carriers in the quartz crystals, whereas whole rocks clearly contained multidomain contributions (fig. S3). Thellier-Coe paleointensity measurements were carried out on unoriented crystals, using both heating with a thermal demagnetization oven and a CO_2 laser (*10*). Natural remanent magnetizations (NRMs) were measured with a 2G DC 755R superconducting quantum interference device (SQUID) magnetometer with high-resolution sensing coils or with a new 2G DC SQUID magnetometer with a small (diameter 6.3 mm) room-temperature access bore optimized for single-crystal studies. Demagnetization data showed the removal of one or more components at unblocking temperatures less than ~450°C; this agrees with theory predicting the temperature range where an overprint acquired under low-grade metamorphism should contaminate the magnetization (*14*). At higher unblocking temperatures, the magnetization showed univectorial decay and linear NRM/TRM characteristics (Fig. 1), with maximum unblocking characteristics consistent with a magnetite carrier. Paleointensity data that met acceptance criteria (*10*, *15*) (tables S2 and S3) were available from 12 BGB and seven NGB quartz crystals; these yield average field intensities of 28.0 ± 4.3 and 18.2 ± 1.8 μT, respectively. The paleointensity values showed strengths that are unexpected from magnetization mechanisms in the absence of a geodynamo [e.g., (*5*)]. Thus, these data extend the record of a geodynamo back in time 250 million years, from 3.2 (*1*) to ~3.45 Ga.

We applied the thin-section technique to obtain oriented quartz crystals (*13*) from NGB samples, yielding a paleoinclination of −42.4° ± 5.9° (n = 7, table S4). Only two samples prepared from BGB dacite thin sections met the selection

[1]Department of Earth and Environmental Sciences, University of Rochester, Rochester, NY 14627, USA. [2]Department of Physics and Astronomy, University of Rochester, Rochester, NY 14627, USA. [3]School of Geological Sciences, University of KwaZulu-Natal, Durban 4000, South Africa. [4]Physics of Geological Processes, University of Oslo, Oslo 0316, Norway. [5]Beijing SHRIMP Centre, Chinese Academy of Geological Sciences, 26 Baiwanzhuang Road, Beijing 100037, China. [6]Code 674, NASA/Goddard Space Flight Center, Greenbelt, MD 20771, USA. [7]Department of Earth Sciences, Tohoku University, Sendai, Miyagi 980-8578, Japan.

*To whom correspondence should be addressed. E-mail: john@earth.rochester.edu

criteria (*10*). Nonetheless, analyses of these samples (table S4) suggest a paleoinclination (44.5° ± 11.1°) similar to that of the NGB dacite, which implies that the two greenstone belts formed in close proximity. Paleolatitude data (*1*) from 3.2-Ga BGB rocks (~29°), when compared to the NGB (~25°) and BGB (~26°) data, yield a minimum long-term plate velocity of <1 cm/year, hinting at the slow rates suggested by some models of mantle cooling (*16*). When referenced to these paleolatitudes, the paleointensity data suggest a virtual dipole moment (VDM) of 3.8 (±0.4) × 10^{22} A m^2 for the NGB dacite and 5.8 (±0.9) × 10^{22} A m^2 for our BGB site, corresponding to 48 and 73% of the modern value, respectively.

Unlike paleointensity estimates from 3.2-Ga plutons of the Kaapvaal craton (*1*), which cooled over tens of millions of years, our paleointensity data should be less affected by cooling rates because of the relatively shallow (or surface) emplacement of the dacites. The cooling time (*17*) to reach 450°C, the approximate starting point of our paleointensity data calculations, is ~30 years for the NGB dacite and ~90 to ~400 years for our BGB sample site (*10*).

If the magnetic inclusions are adequately represented by some theoretical considerations of cooling rate effects on single-domain particles (*18*), our paleointensity estimates could overestimate the true paleointensity by 26 to 35% (*10*) (table S5). However, our magnetic hysteresis data point toward grains having single-domain to pseudo–single-domain characteristics; micromagnetic modeling suggests that the latter will slightly underestimate field strength if they are locked in a vortex state on geological time scales and blocked in the single-domain state in the laboratory (*19*). The net effect of these contrasting cooling rate effects is probably small. Although the shallow emplacement of the dacites lessens the potential influence of cooling rates on paleointensity values relative to more deeply emplaced rocks [e.g., (*1*)], it also implies that the units record less time. A potential limitation of the VDMs, therefore, is that they represent field averages only over decades (NGB) and centuries (BGB).

We next examined the implications of our paleointensity data with respect to shielding of radiation from the young Sun. We again used the dipole assumption because this maximizes the magnetic shielding (*20*) and hence provides a conservative estimate of conditions at >3.4 Ga. The magnetopause standoff distance (r_s) at the subsolar point is determined by the balance of the solar wind pressure and Earth's magnetic field (*21*)

$$r_s = \left[\frac{\mu_0^2 f_0^2 M_E^2}{4\pi^2(2\mu_0 P_{sw} + B_{IMF}^2)}\right]^{1/6} \quad (1)$$

where M_E is Earth's dipole moment, P_{sw} is solar wind ram pressure, f_0 is a magnetospheric form factor (= 1.16 for Earth), μ_0 is the permeability of free space, and B_{IMF} is the interplanetary magnetic field, contributions from the latter are minor. We used two approaches to assess the ancient solar wind. Changes in solar wind ram pressure can be related to changes in mass loss rate ($\dot{m}$) and solar wind velocity (v_{sw}) [e.g., (*22*, *23*)]. Studies of young solar analogs (*23*) suggest a power-law mass loss from which we can derive a relationship between current (t_0, P_{sw0}, $\dot{m}_0$, v_{sw0}) and past values

$$\frac{P_{sw}}{P_{sw0}} \frac{\dot{m}v_{sw}}{\dot{m}_0 v_{sw0}} \sim \left(\frac{t}{t_0}\right)^{2.33} \quad (2)$$

This suggests a mass loss at 3.45 Ga of 2.4 × 10^{-13} $M_\odot$/year, where $M_\odot$ is the present solar mass. In the resulting model A (*10*), wind pressure change with time leads to estimates of magnetopause standoff distance as a function of dipole moment (Fig. 2). Our paleointensity estimates at >3.4 Ga suggest a considerable decrease of the standoff distance, to between 45 and 51% of the present 10.7 Earth radii (R_E). The solar wind pressure changes (Fig. 2) also imply that standoff reductions are robust on a time scale of millions to tens of millions of years, assuming that our paleointensity values sample secular variation broadly similar to that of the younger geomagnetic field (*10*).

In another approach, we started with stellar evolution models and predicted that the Sun at 3.45 Ga would appear to be a G6V star with a rotational period of ~12 days (*10*, *24*). Mass loss rates among solar-type stars correlate with x-ray

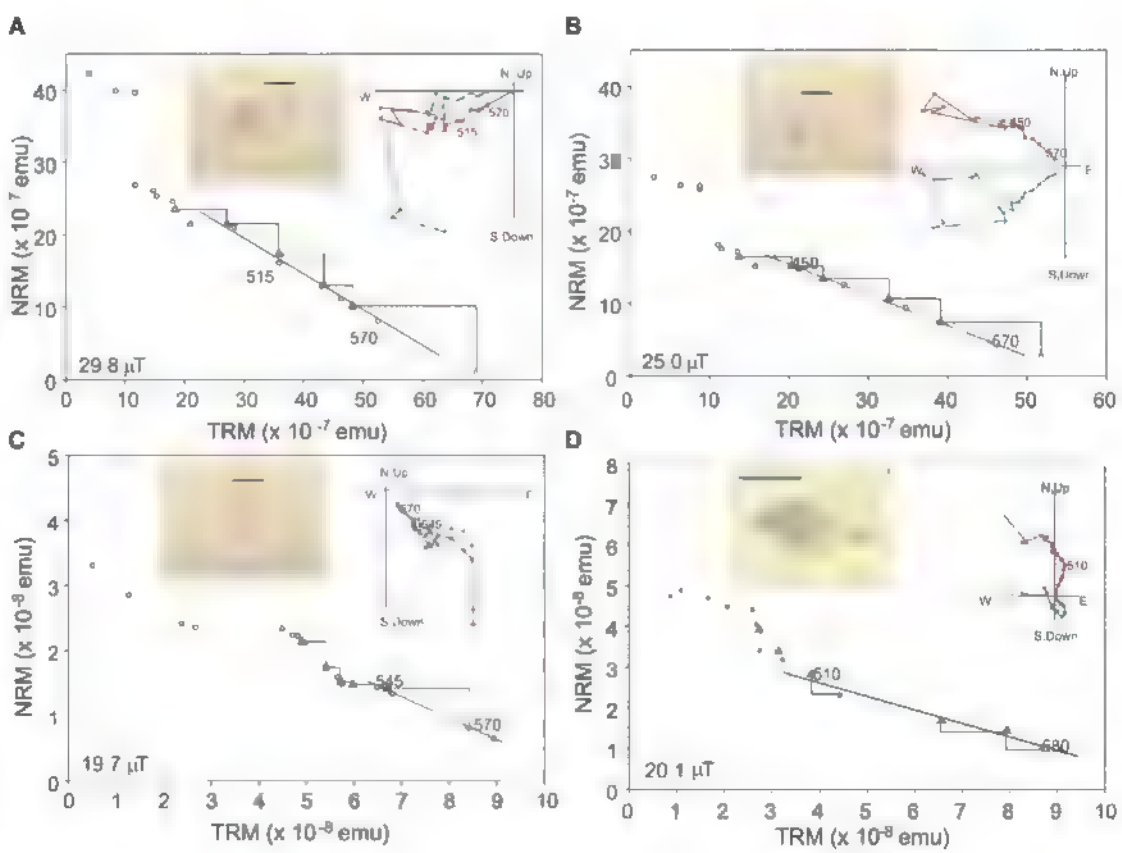

Fig. 1. Paleointensity data examples. For each panel, inset image shows crystal as measured (scale bar, 1 mm); inset at upper right is orthogonal vector plot of field-off magnetization (red, inclination; blue, declination; unoriented samples shown). Main panels are plots of natural remanent magnetization (NRM) versus thermal magnetization (TRM); plotted values are circles, with partial TRM checks shown as triangles (*10*). Line fit shows data used for paleointensity calculation (numerical value at lower left). (**A** and **B**) Examples from Barberton Greenstone Belt locality, using thermal demagnetization oven heating. (**C**) Example from Nondweni Greenstone Belt, using thermal demagnetization oven heating. (**D**) Example from Nondweni Greenstone Belt, using CO_2 laser heating (*1*) of grain from oriented thin section in geographic coordinates.

emission (f_X), which in turn correlates with rotation. We estimated mass loss as

$$\dot{m} = \dot{M}_\odot \left(\frac{R}{R_\odot}\right)^2 \left(\frac{f_X}{f_{X_\odot}}\right)^{1.34\pm0.18} \quad (3)$$

where R is solar radius, $R_\odot$ is the modern value, and $f_{X_\odot}$ is the modern soft x-ray surface flux. This yields a higher mass loss of 1.5×10^{-12} $M_\odot$/year (model B) and an even smaller standoff distance, between 3.6 and 4.2 R_E. The reductions in standoff distance are similar to (model A) or greater than (model B) those characterizing extreme modern events, such as the Halloween solar storm of 2003 [e.g., (*25*)]. However, these standoffs would have been typical, rather than the exceptional day-long deviations associated with modern coronal mass ejections (CMEs).

The continuous Halloween storm conditions would have resulted in aurora at far lower latitudes than is typically the case today. We used a scaling law derived from the pressure balance between the solar wind and Earth's magnetic field (*26*) to determine the latitude of the aurora, namely the location of the polar cap boundary dividing closed (~dipolar) magnetospheric magnetic field lines from open lines that extend into the magnetotail and thence into interplanetary space

$$\cos(\lambda_p) = \left(\frac{M_E}{M_{E_0}}\right)^{1.6} P^{1.12}\cos(\lambda_{p_0}) \quad (4)$$

where λ_p is the magnetic latitude of the polar cap edge, λ_{p_0} is the present value (71.9°), M_{E_0} is the present dipole moment, and P is the solar wind dynamic pressure normalized to its present value of ~2 nPa. This scaling relationship suggests that at 3.4 to 3.45 Ga, the area of the polar cap increased up to a factor of 3 (model B) relative to the present, allowing solar energetic particles far greater access to Earth's atmosphere.

The smaller standoff distances and larger polar cap area would result in heating and expansion of Earth's exosphere, promoting loss of volatiles and water (*27*). An early, high loss rate of hydrogen may have been an important factor in the transition from a mildly reducing to an oxidizing atmosphere (*28*), whereas an early, high loss rate of water implies that Earth had a greater initial water inventory. We also note that whereas our estimates make use of time-averaged estimates of solar wind pressures, Sun-like stars with ages of ~1 Ga are observed to have more frequent and energetic x-ray flares than those of the current Sun (*29*). Presumably, CMEs would also have been more frequent and energetic. Individual CMEs could decrease standoff to levels much less than time-averaged values, exacerbating any impact on the exosphere. Thus, although a Paleoarchean geodynamo produced a magnetic field that would have prevented whole-scale atmospheric erosion, magnetic field and solar wind strengths suggest important modifications during the first billion years of Earth evolution. The dynamo suggested by our paleointensity data is near the oldest age suggested for inner core growth (*30*). More extensive changes in the atmosphere and Earth's water budget would have occurred if an earlier dynamo driven solely by thermal convection was weaker, or if dynamo action was delayed (*2*, *3*).

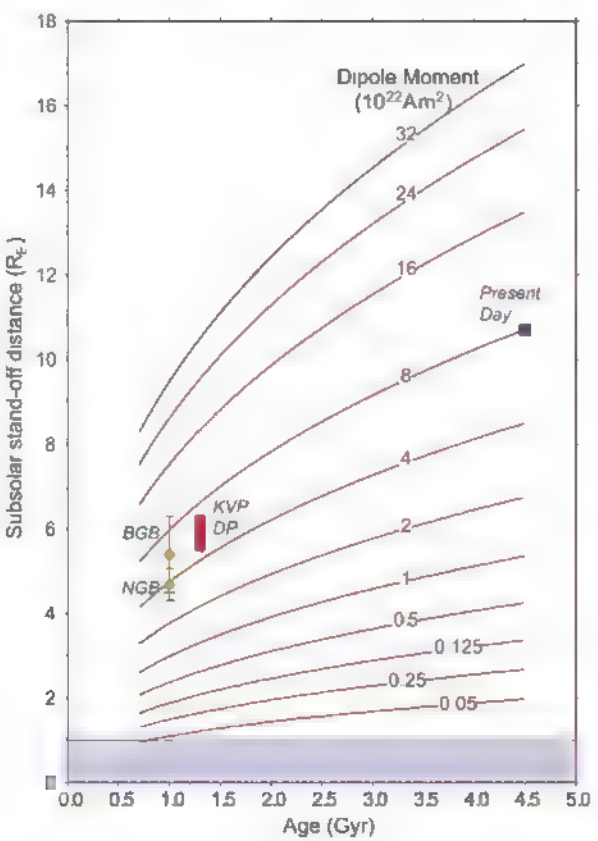

Fig. 2. Subsolar magnetopause standoff distance (expressed in Earth radii) versus dipole moment with respect to the age of Earth (in billions of years), with present-day value (blue square) and estimates from 3.2-Ga Kaap Valley (KVP) and Dalmein plutons (DP) [range from values uncorrected to corrected for cooling rate assuming single-domain behavior shown (*1*)] and virtual dipole moments from the Barberton Greenstone Belt (BGB) and Nondweni Greenstone Belt (NGB) dacite localities.

References and Notes

1. J. A. Tarduno, R. D. Cottrell, M. K. Watkeys, D. Bauch, *Nature* **446**, 657 (2007).
2. M. Ozima *et al.*, *Nature* **436**, 655 (2005).
3. S. Labrosse, J. W. Hernlund, N. Coltice, *Nature* **450**, 866 (2007).
4. M. M. Tice, B. C. Bostick, D. R. Lowe, *Geology* **32**, 37 (2004).
5. Y. Usui, J. A. Tarduno, M. K. Watkeys, A. Hofmann, R. D. Cottrell, *Geochem. Geophys. Geosyst.* **10**, Q09Z07 (2009).
6. T. L. Zhang *et al.*, *Nature* **450**, 654 (2007).
7. D. R. Lowe, G. R. Byerly, *Geol. Soc. Am. Spec. Pap.* **329** (1999).
8. A. H. Wilson, J. A. Versteld, *Precambrian Res.* **67**, 243 (1994).
9. A. Hofmann, A. H. Wilson, in *Earth's Oldest Rocks*, M. J. Van Kranendonk, R. H. Smithies, V. C. Bennett, Eds. (Elsevier, Amsterdam, 2007), pp. 571–605.
10. See supporting material on *Science* Online.
11. R. D. Cottrell, J. A. Tarduno, *Earth Planet. Sci. Lett.* **169**, 1 (1999).
12. J. M. Feinberg, G. R. Scott, P. R. Renne, H. R. Wenk, *Geology* **33**, 513 (2005).
13. J. A. Tarduno, R. D. Cottrell, A. V. Smirnov, *Rev. Geophys.* **44**, RG1002 (2006).
14. D. J. Dunlop, K. L. Buchan, *Phys. Earth Planet. Inter.* **13**, 325 (1977).
15. R. D. Cottrell, J. A. Tarduno, *J. Geophys. Res.* **105**, 23579 (2000).
16. J. Korenaga, *Rev. Geophys.* **46**, RG2007 (2008).
17. J. C. Jaeger, in *Basalts: The Poldervaart Treatise on Rocks of Basaltic Composition*, H. H. Hess, A. Poldevaart, Eds. (Wiley-Interscience, New York, 1967), vol. 2, pp. 503–536.
18. S. E. Halgedahl, R. Day, M. Fuller, *J. Geophys. Res.* **85**, 3690 (1980).
19. M. Winklhofer, K. Fabian, F. Heider, *J. Geophys. Res.* **102**, 22695 (1997).
20. G. L. Siscoe, D. G. Sibeck, *J. Geophys. Res.* **85**, 3549 (1980).
21. J.-M. Grießmeier *et al.*, *Astron. Astrophys.* **425**, 753 (2004).
22. G. Newkirk Jr., *Geochim. Cosmochim. Acta Suppl.* **13**, 293 (1980).
23. B. E. Wood, *Space Sci. Rev.* **126**, 3 (2006).
24. E. E. Mamajek, L. A. Hillenbrand, *Astrophys. J.* **687**, 1264 (2008).
25. L. Rosenqvist *et al.*, *J. Geophys. Res.* **110**, A09S23 (2005).
26. G. L. Siscoe, C.-K. Chen, *J. Geophys. Res.* **80**, 4675 (1975).
27. Y. N. Kulikov *et al.*, *Space Sci. Rev.* **129**, 207 (2007).
28. H. Lammer *et al.*, *Space Sci. Rev.* **139**, 399 (2008).
29. A. Telleschi *et al.*, *Astrophys. J.* **622**, 653 (2005).
30. D. Gubbins, D. Alfè, G. Masters, G. D. Price, M. Gillan, *Geophys. J. Int.* **157**, 1407 (2004).

31. We are grateful to the late William Goree for his encouragement and design of the small-bore SQUID magnetometer and to the staffs of William Goree Inc. and Applied Physics for final construction of the instrument. We thank J. Hopkins for assistance in the laboratory and G. Kloc for sample preparation. Supported by NSF grants EAR 0738844 and EAR 0619467 and the John Simon Guggenheim Foundation (J.A.T.).

Supporting Online Material

www.sciencemag.org/cgi/content/full/327/5970/1238/DC1
Materials and Methods
Figs. S1 to S3
Tables S1 to S5
References

16 October 2009; accepted 15 January 2010
10.1126/science.1183445

Calibrating the Cryogenian

Francis A. Macdonald,[1]* Mark D. Schmitz,[2] James L. Crowley,[2] Charles F. Roots,[3] David S. Jones,[4] Adam C. Maloof,[5] Justin V. Strauss,[6] Phoebe A. Cohen,[1] David T. Johnston,[1] Daniel P. Schrag[1]

The Neoproterozoic was an era of great environmental and biological change, but a paucity of direct and precise age constraints on strata from this time has prevented the complete integration of these records. We present four high-precision U-Pb ages for Neoproterozoic rocks in northwestern Canada that constrain large perturbations in the carbon cycle, a major diversification and depletion in the microfossil record, and the onset of the Sturtian glaciation. A volcanic tuff interbedded with Sturtian glacial deposits, dated at 716.5 million years ago, is synchronous with the age of the Franklin large igneous province and paleomagnetic poles that pin Laurentia to an equatorial position. Ice was therefore grounded below sea level at very low paleolatitudes, which implies that the Sturtian glaciation was global in extent.

Middle Neoproterozoic or Cryogenian strata [850 to 635 million years ago (Ma)] contain evidence for the breakup of the supercontinent Rodinia, widespread glaciation (*1*, *2*), high-amplitude fluctuations in geochemical proxy records (*3*), and the radiation of early eukaryotes (*4*); however, both relative and absolute age uncertainties have precluded a better understanding of the nature and interrelationships of these events. Several first-order questions remain: How many Neoproterozoic glaciations were there? How were they triggered? What was their duration and extent? How did the biosphere respond? Answers to all of these questions hinge on our ability to precisely correlate and calibrate data from disparate stratigraphic records around the world.

The snowball Earth hypothesis (*1*, *2*) was developed in response to strong paleomagnetic evidence for low-latitude glaciation from the Elatina Formation in Australia (*5*, *6*). The Elatina Formation and its distinct cap carbonate have been correlated with chemo- and lithostratigraphy to Marinoan-age glacial deposits in the Ghaub Formation in Namibia (635.5 ± 0.6 Ma) (*7*); the Nantuo Formation in South China (636.3 ± 4.9 Ma) (*8*), which underlies the cap carbonate of the basal Doushantuo Formation (635.2 ± 0.2 Ma) (*9*); and other glacial deposits around the globe, including the Ice Brook Formation in northwestern Canada (*10*). In contrast, a paucity of robust paleomagnetic poles and precise age constraints from volcanic rocks directly interbedded with early Cryogenian glacial deposits has precluded tests of the snowball Earth hypothesis for the Sturtian glaciation. The global nature of the Sturtian glaciation has been inferred from the ubiquitous occurrence of glacial deposits that are stratigraphically below Marinoan diamictite units (*10*) as well as banded iron formation within these deposits (*1*).

We present four high-precision U-Pb isotope dilution–thermal ionization mass spectrometry (ID-TIMS) dates from intrusive and volcanic rocks within Neoproterozoic strata of northwestern Canada. These dates, coupled with high-resolution $\delta^{13}C$ profiles (*11*), allow us to synthesize Cryogenian geological, geochemical, paleomagnetic, and paleontological data both regionally and globally. The accurate integration of these records places hard constraints on the timing and extent of the Sturtian glaciation and its relationship to the Franklin large igneous province (LIP) and the Cryogenian microfossil record.

Neoproterozoic strata are exposed in erosional windows (inliers) through Paleozoic carbonate rocks in northwestern Canada for more than 1500 km, from the Alaska border

[1]Department of Earth and Planetary Sciences, Harvard University, Cambridge, MA 02138, USA. [2]Department of Geosciences, Boise State University, Boise, ID 83725, USA. [3]Geological Survey of Canada, Whitehorse, YT Y1A 1B5, Canada. [4]Department of Earth and Planetary Sciences, Washington University, St. Louis, MO 63130, USA. [5]Department of Geosciences, Princeton University, Princeton, NJ 08544, USA. [6]555 East Simpson Street, Jackson, WY 83001, USA.

*To whom correspondence should be addressed. E-mail fmacdon@fas.harvard.edu

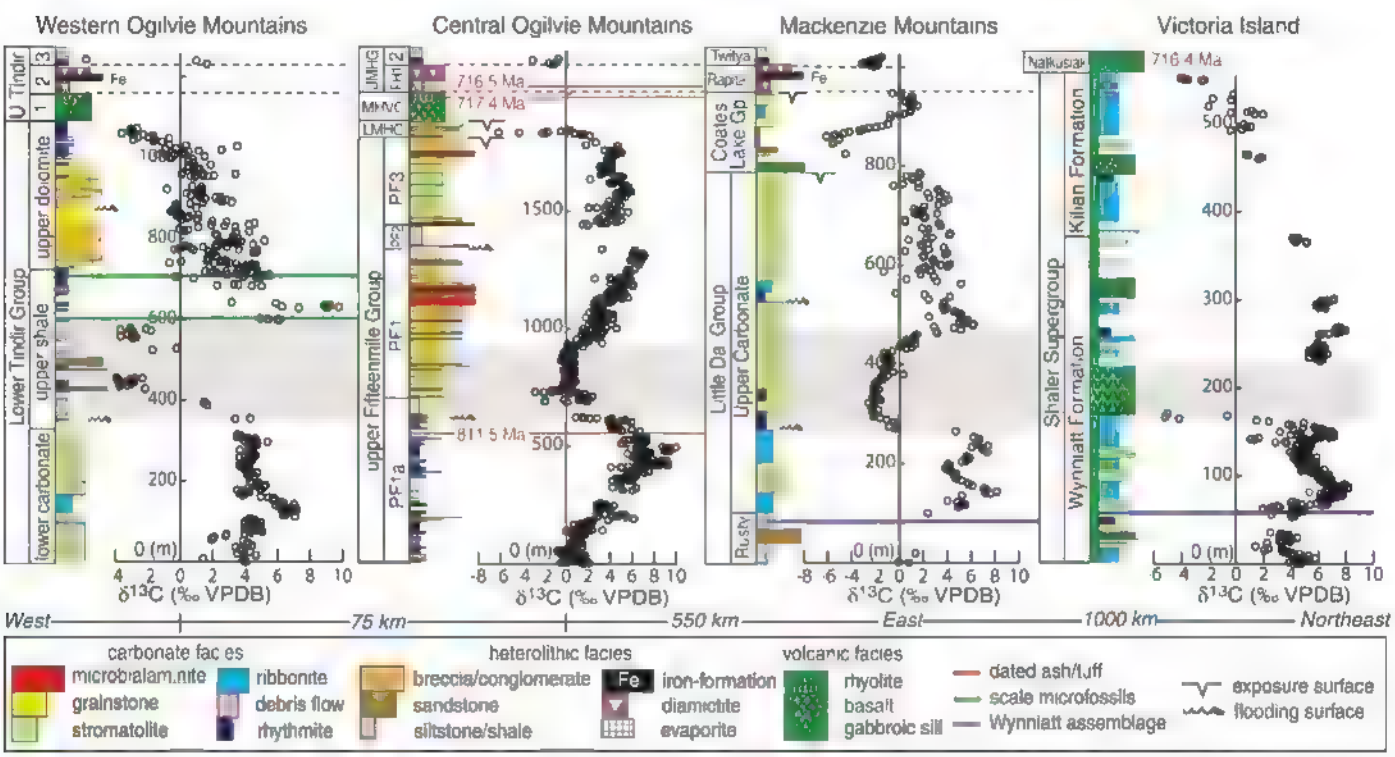

Fig. 1. Composite chemo- and lithostratigraphy of Neoproterozoic strata in northwestern Canada, including the Upper and Lower Tindir Groups (*13*), the Fifteenmile and Lower Mount Harper Group (table S2), the Little Dal Group (*3*), the Coates Lake Group (table S2), the Twitya Formation (*3*), and the Shaler Supergroup (*18*). Shaded area represents the Bitter Springs isotopic stage (*3*).

east through the Ogilvie and Wernecke Mountains of Yukon, to the Mackenzie Mountains of the Northwest Territories, and north to Victoria Island of Nunavut (fig. S1A). Exposures in the Coal Creek inlier of the central Ogilvie Mountains consist of mixed carbonate and siliciclastic rocks of the upper Fifteenmile and Lower Mount Harper Groups (LMHG), bimodal volcanic rocks of the Mount Harper volcanic complex (MHVC) (*12*), and glacial diamictite of the Upper Mount Harper Group (UMHG) (Fig. 1). A glacial origin for the UMHG is inferred from bed-penetrating dropstones with impact margins and outsized clasts in fine, laminated beds, and by striated clasts in exposures in the Hart River inlier of the eastern Ogilvie Mountains (fig. S2). Evidence for grounded ice is provided by glacial push structures and soft-sedimentary deformation (fig. S2). The UMHG and the iron-rich unit 2 of the Upper Tindir Group in the western Ogilvie Mountains are correlative with the Sturtian-age Sayunei Formation of the Rapitan Group in the Mackenzie Mountains (*13*, *14*). The broad distribution of massive diamictite and stratified glacial deposits with coarse-grained ice-rafted debris in the Rapitan Group of the Northwest Territories (*14*, *15*) and its correlatives in Yukon and Alaska (fig. S3) suggests the proximity to a marine ice grounding line.

The MHVC previously was dated with multigrain U-Pb ID-TIMS analyses at 751^{+26}_{18} Ma (*16*). We collected a quartz-phyric rhyolite of member D from the same site (fig. S1) that yielded a weighted mean ^{206}Pb-^{238}U zircon date of 717.43 ± 0.14 Ma, interpreted as the eruptive age of this unit (fig. S4). This ~33-million-year age revision is likely due to inherited cores in the previously dated multigrain zircon fractions, resulting in an artificially old age. Below the MHVC, a green, flinty, bedded tuff within allodapic dolostone beds near the top of unit PF1a of the Fifteenmile Group yielded a weighted mean ^{206}Pb-^{238}U zircon date of 811.51 ± 0.25 Ma, interpreted as the time of deposition (fig. S4). Above the MHVC, a green to pink brecciated tuff within glacial deposits of the UMHG yielded a weighted mean ^{206}Pb-^{238}U zircon date of 716.47 ± 0.24 Ma, interpreted as the deposition age (fig. S4).

In the Minto inlier on Victoria Island (fig. S1), zircon and baddeleyite from gabbroic sills and dikes from the Franklin LIP previously were dated at 723^{+4}_{-2} Ma and 718 ± 2 Ma (*17*). Our Franklin LIP sample is from a coarse-grained diabase sill, >20 m thick, intruding the middle of the Wynnatt Formation (*18*), which yielded a weighted mean ^{206}Pb-^{238}U baddeleyite date of 716 33 ± 0 54 Ma (fig. S4). We interpret the apparent discrepancy between our result and previous ages (*17*) as an artifact of comparing upper intercept and $^{207}Pb/^{206}Pb$ dates with our $^{206}Pb/^{238}U$ dates in light of recently recognized systematic error in the U decay constant ratio (*11*, *19*).

This geochronology reveals the >3000-km extent of the Franklin LIP (~716.5 Ma), from the Yukon-Alaska border to Ellesmere Island, where mafic dikes have been dated at 716 ± 1 Ma (*20*). Although no evidence for prevolcanic extension and rifting is present on Victoria Island (*21*), conspicuous normal faulting exists within the LMHG and the lower suite of the MHVC (*12*), temporally linking the Franklin LIP to extension on the northwestern Laurentian margin.

Several paleomagnetic studies on strongly magnetized mafic dikes, sills, and lavas have demonstrated that the Franklin LIP was emplaced when northwestern Laurentia was within 10° of the equator (*6*, *22*, *23*). The dated sill and the sediments that it intrudes on Victoria Island yield paleomagnetic data that are consistent with the previous low-latitude results (*18*). The age of the tuff interbedded with glacial deposits of the UMHC, 716.47 ± 0.24 Ma, is indistinguishable from the date of the Franklin LIP, 716.33 ± 0.54 Ma. Therefore, grounded ice was present on the northwestern margin of Laurentia at ~716.5 Ma, when it was situated at equatorial latitudes. Climate models have long predicted that if the ice line advanced equatorward of ~30° to 40°, an ice-albedo feedback would drive global glaciation (*24*, *25*). Thus, we conclude that the Sturtian glaciation at ~716.5 Ma was global in nature.

It is uncertain whether the Sturtian glacial epoch consisted of one discrete glaciation that lasted tens of millions of years, or multiple glacial episodes including the low-latitude glaciation at ~716.5 Ma. Prior to this study, minimum and maximum age constraints on the Sturtian glaciation were provided by a sample from South China dated at 662.9 ± 4.3 Ma (*26*) and the Leger Granite in Oman dated at 726 ± 1 Ma (*27*), respectively. We suggest that our age from member D of the MHVC, 717.43 ± 0.14 Ma, provides a maximum age constraint on the low-latitude Sturtian glaciation not only because glacial deposits have not been identified below member D, but also because models suggest extremely rapid ice advance once ice is below 30° latitude (*24*, *25*), such that glaciation of equatorial latitudes should be synchronous around the globe. Evidence for a pre-Sturtian glaciation at ~750 Ma (referred to as the Kaigas glaciation) was reported in southern Namibia (*28*), Zambia (*29*), and northwestern China (*30*). However, at these localities the contact relationship of the purported glacial deposit with the dated unit and the glacial origin of the deposit are sus-

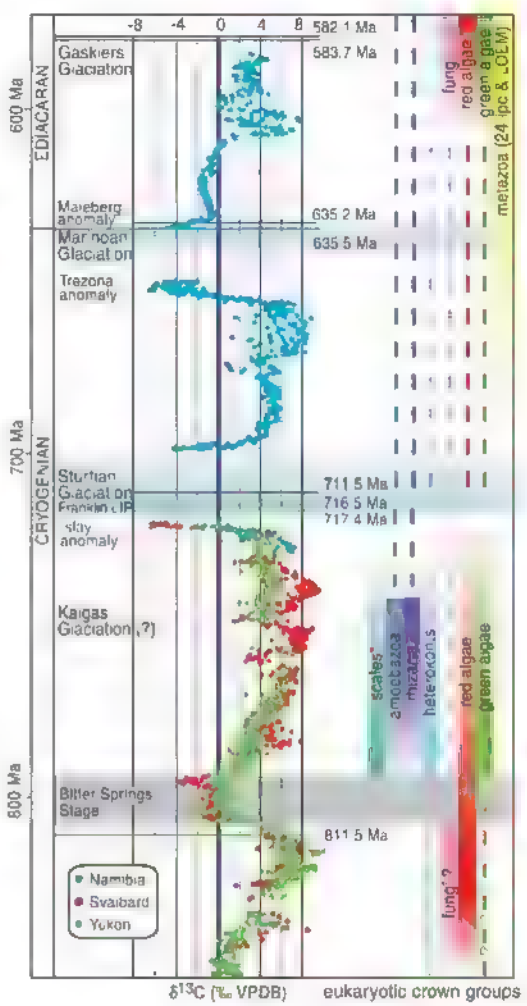

Fig. 2. Neoproterozoic composite carbonate $\delta^{13}C$ chemostratigraphy with U-Pb ID-TIMS ages that are directly linked to isotopic profiles (*11*). Bars indicate the time spans of fossil assemblages representing eukaryotic crown groups. Asterisks indicate fossil groups of uncertain taxonomic affinity. Bars faded upward reflect uncertainty in the minimum age constraint; bars faded downward reflect uncertainty in the maximum age constraint. Dashes represent the time span where a fossil record has not been identified but for which the eukaryotic group's presence is inferred from its occurrence in Ediacaran or Phanerozoic strata. Dashes with question marks indicate that earlier records have been proposed but the relationships between these fossils and the crown groups are uncertain.

pect (*10*). Moreover, because there are no robust paleolatitude constraints on these rocks, the Kaigas glaciation may have been regional in extent. Previous Sturtian synglacial constraints at ~685 Ma were reported from Idaho (*31*, *32*). However, these results have been questioned because the glacial nature of these deposits is uncertain, contacts between dated volcanic rocks and diamictites are tectonic, and repeated analyses have given different results (*10*). A ^{206}Pb-^{238}U ID-TIMS date of 711.52 ± 0.20 Ma was reported from volcaniclastic rocks interbedded with glacigenic deposits within the Ghubrah Formation in Oman (*27*). Thus, if the Ghubrah Formation is recording the same glacial episode as the UMHG, the Sturtian glaciation lasted a minimum of 5 million years.

Using a recalibrated and expanded $\delta^{13}C$ record, we can place the record of eukaryotic evolution in the context of geochemical perturbations and global glaciation (Fig. 2). The tuff dated at 811.5 Ma provides a maximum constraint on the Bitter Springs isotopic stage (*3*) and a useful benchmark for the calibration of early Neoproterozoic microfossil record. For instance, the chemostratigraphic position of the mineralized scale microfossils in the Lower Tindir Group of the western Ogilvie Mountains is above the Bitter Springs isotopic stage and below glacial deposits with banded iron formation that were previously correlated with the Rapitan Group (*13*). The Tindir microfossils are thus broadly coeval with complex microbiota described from the Chuar Formation in the Grand Canyon (older than 742 ± 6 Ma), the preglacial Beck Spring Formation of Death Valley, and the Svanbergfjellet Formation of Spitsbergen (*11*). Collectively, the calibration of these diverse microfossil records indicates that between the onset of the Bitter Springs isotopic stage (~811.5 Ma) and the Sturtian glaciation (~716.5 Ma), many major eukaryotic crown groups—members of Rhizaria, Amoebozoa, green and red algae, and vaucheriacean algae—had diverged and diversified. In contrast, the microfossil record between the Sturtian glaciation and the Marinoan glaciation (i.e., between ~716.5 and ~635 Ma) is depauperate: only simple acritarchs of unknown phylogenic affinity have been described (*4*, *11*). This apparent bottleneck might be due in part to poor preservation and limited sampling, and/or the survival of some groups as cryptic forms. It is clear that a diverse biosphere persisted through the Neoproterozoic glaciations (*4*), but the impact of global glaciation on eukaryotic evolution remains unresolved.

With high-precision ages directly tied to the stratigraphic record we can begin to address the mechanisms behind Neoproterozoic environmental change. The presence of the Islay $\delta^{13}C$ anomaly in the pre-Sturtian LMHG suggests a relationship between global carbon cycling and climate degradation (Figs. 1 and 2). Moreover, the synchrony among continental extension, the Franklin LIP, and the Sturtian glaciation is consistent with the hypothesis that the drawdown of CO_2 via rifting and weathering of the low-latitude Franklin basalts could have produced a climate state that was more susceptible to glaciation (*25*, *33*). However, even with the updated age constraints, it is unclear whether the bulk of the magmatism preceded or occurred during the glaciation.

References and Notes

1. J. L. Kirschvink, in *The Proterozoic Biosphere*, J. W. Schopf, C. Klein, Eds. (Cambridge Univ. Press, Cambridge, 1992), pp. 51–52.
2. P. F. Hoffman, A. J. Kaufman, G. P. Halverson, D. P. Schrag, *Science* **281**, 1342 (1998).
3. G. P. Halverson, in *Neoproterozoic Geobiology and Paleobiology*, S. Xiao, A. J. Kaufman, Eds. (Springer, New York, 2006), pp. 231–271.
4. A. H. Knoll, E. J. Javaux, D. Hewitt, P. A. Cohen, *Philos. Trans. R. Soc. Lond. Ser. B Biol. Sci.* **361**, 1023 (2006).
5. L. E. Sohl, N. Christie-Blick, D. V. Kent, *Geol. Soc. Am. Bull.* **111**, 1120 (1999).
6. D. A. D. Evans, *Am. J. Sci.* **300**, 347 (2000).
7. K. H. Hoffmann, D. J. Condon, S. A. Bowring, J. L. Crowley, *Geology* **32**, 817 (2004).
8. S. Zhang, G. Jiang, Y. Han, *Terra Nova* **20**, 289 (2008).
9. D. J. Condon *et al.*, *Science* **308**, 95 (2005).
10. P. F. Hoffman, Z. X. Li, *Palaeogeogr. Palaeoclimatol. Palaeoecol.* **277**, 158 (2009).
11. See supporting material on *Science* Online.
12. P. S. Mustard, C. F. Roots, *Geol. Surv. Canada Bull. 492* (1997).
13. F. A. Macdonald, P. A. Cohen, F. O. Dudas, D. P. Schrag, *Geology* **38**, 143 (2010).
14. G. M. Yeo, *Geol. Surv. Canada Pap. 81-10*, 25 (1981).
15. G. H. Eisbacher, *Geol. Surv. Canada Pap. 77-35* (1978), p. 1.
16. C. F. Roots, R. R. Parrish, *Geol. Surv. Canada Pap. 88-2* (1988), p. 29.
17. L. M. Heaman, A. N. LeCheminant, R. H. Rainbird, *Earth Planet. Sci. Lett.* **109**, 117 (1992).
18. D. S. Jones, thesis, Harvard University (2009).
19. B. Schoene, J. C. Crowley, D. J. Condon, M. D. Schmitz, S. A. Bowring, *Geochim. Cosmochim. Acta* **70**, 426 (2006).
20. S. W. Denyszyn, D. W. Davis, H. C. Halls, *Can. J. Earth Sci.* **46**, 155 (2009).
21. R. H. Rainbird, *J. Geol.* **101**, 305 (1993).
22. J. K. Park, *Precambrian Res.* **69**, 95 (1994).
23. H. C. Palmer, W. R. A. Baragar, M. Fortier, J. H. Foster, *Can. J. Earth Sci.* **20**, 1456 (1983).
24. G. R. North, R. F. Cahalan, J. A. Coakley Jr., *Rev. Geophys. Space Phys.* **19**, 91 (1981).
25. J. Bendtsen, *Clim. Dyn.* **18**, 595 (2002).
26. C. Zhou *et al.*, *Geology* **32**, 437 (2004).
27. S. A. Bowring *et al.*, *Am. J. Sci.* **307**, 1097 (2007).
28. H. E. Frimmel, U. S. Klötzli, P. R. Siegfried, *J. Geol.* **104**, 459 (1996).
29. R. M. Key *et al.*, *J. Afr. Earth Sci.* **33**, 503 (2001).
30. B. Xu *et al.*, *Precambrian Res.* **168**, 247 (2009).
31. K. Lund, J. N. Aleinikoff, K. V. Evans, C. M. Fanning, *Geol. Soc. Am. Bull.* **115**, 349 (2003).
32. C. M. Fanning, P. K. Link, *Geology* **32**, 881 (2004).
33. Y. Donnadieu, Y. Goddéris, G. Ramstein, A. Nédélec, J. Meert, *Nature* **428**, 303 (2004).

34. We thank the Yukon Geological Survey for assistance with logistics and helicopter support, T. Petach and S. Petersen for assistance in the field, and D. Pearce and H. Yntema for preparing samples. Supported by the Polar Continental Shelf Project and NSF Geobiology and Environmental Geochemistry Program grant EAR 0417422.

Supporting Online Material

www.sciencemag.org/cgi/content/full/327/5970/1241/DC1
Materials and Methods
Figs. S1 to S4
Tables S1 and S2
References

14 October 2009; accepted 11 December 2009
10.1126/science.1183325

The Role of Sulfuric Acid in Atmospheric Nucleation

Mikko Sipilä,[1,2,3]* Torsten Berndt,[1] Tuukka Petäjä,[2] David Brus,[4,5] Joonas Vanhanen,[2] Frank Stratmann,[1] Johanna Patokoski,[2] Roy L. Mauldin III,[6] Antti-Pekka Hyvärinen,[5] Heikki Lihavainen,[5] Markku Kulmala[2,7]

Nucleation is a fundamental step in atmospheric new-particle formation. However, laboratory experiments on nucleation have systematically failed to demonstrate sulfuric acid particle formation rates as high as those necessary to account for ambient atmospheric concentrations, and the role of sulfuric acid in atmospheric nucleation has remained a mystery. Here, we report measurements of new particles (with diameters of approximately 1.5 nanometers) observed immediately after their formation at atmospherically relevant sulfuric acid concentrations. Furthermore, we show that correlations between measured nucleation rates and sulfuric acid concentrations suggest that freshly formed particles contain one to two sulfuric acid molecules, a number consistent with assumptions that are based on atmospheric observations. Incorporation of these findings into global models should improve the understanding of the impact of secondary particle formation on climate.

Nucleation of particles in the atmosphere has been observed to be strongly dependent on the abundance of sulfuric acid (H_2SO_4) (*1*–*4*). Sulfur dioxide (SO_2), the precursor of H_2SO_4, has both natural and anthropogenic sources. Anthropogenic SO_2 emissions can have large indirect effects on climate if H_2SO_4 is responsible for atmospheric nucleation, but laboratory experiments have systematically failed to reproduce ambient new-particle formation rates as well as the nucleation rate dependence on the H_2SO_4 concentration (Table 1) (*5*–*15*).

Reasons for these apparent differences have been unclear. Berndt *et al.* (*5*) reported laboratory experiments with nucleation occurring at nearly ambient concentrations of H_2SO_4 (10^7 molecules cm^{-3}), whereas other experiments (performed with H_2SO_4 produced from a liquid sample) have, until now, required much higher onset vapor concentrations (~10^9 molecules cm^{-3}) (*6*–*9*). This observation revived an old idea (*11*) that other compounds, such as HSO_5, that were formed in the OH + SO_2 reaction were responsible for nucleation (*13*). Recent experiments (*14*, *15*) with in situ–produced H_2SO_4 have also been used to support the idea that the nature of the nucleating species can differ from H_2SO_4.

Even though nucleation has been observed to occur just slightly above ambient atmospheric H_2SO_4 concentrations (*5*), none of the experiments performed to date have succeeded in producing the atmospherically relevant relation ("slope") between the nucleation rate (J) and H_2SO_4 concentration. This slope, according to nucleation theorem, corresponds to the number of molecules in critical cluster (*16*, *17*). $n_{crit} = d(\ln J)/d(\ln[H_2SO_4])$. Atmospheric observations (*2*–*4*) suggest this slope to be between 1 and 2. In contrast, the slopes obtained from the previous laboratory experiments (*5*–*15*) are in the range of 2 to 21.

Here, we report observations of H_2SO_4 nucleation in the presence of water vapor for ambient H_2SO_4 concentrations starting from 10^6 molecules cm^{-3}. Experiments were performed in the Leibniz-Institute for Tropospheric Research laminar flow tube (IfT-LFT) and in the Finnish Meteorological Institute (FMI) laminar flow tube (*17*). We used a chemical ionization mass spectrometer (CI-MS) (*18*) for H_2SO_4 measurements, a modified pulse height–analyzing ultrafine-condensation particle counter (PHA-UCPC) (*19*), and a mixing type particle-size magnifier (PSM) (*17*, *20*) for detecting particles down to ~1.3 to 1.5 nm in mobility-equivalent diameter (~1.0 to 1.2 nm mass diameter). With these instruments, a direct comparison with field measurements becomes possible because field observations typically apply a CI-MS for the H_2SO_4 measurement and because nucleation rates calculated from field data are given for particles with a mass diameter of 1 nm (*2*–*4*), which is close to our estimated smallest detectable particle size.

The growth rate of freshly nucleated particles because of H_2SO_4 condensation close to ambient concentrations is assumed to be small: ~1.5 nm h^{-1} at $[H_2SO_4] = 10^7$ molecules cm^{-3} (*21*). Even in the atmosphere, where several condensing vapors obviously participate in the growth process, total growth rates typically do not exceed 20 nm h^{-1} (*22*). Exceptions are coastal areas, where oxidation of iodine-containing organic vapors can rapidly produce large amounts of condensable matter (*23*), and also highly polluted environments of megacities (*24*). In order to grow nucleated particles from ~1 to 3 nm, which is the lowest detection limit of modern commercial condensation particle counters, high H_2SO_4 concentration and long growth times are required.

The detection efficiency of the present modified PHA-UCPC for <2-nm-diameter particles is several orders of magnitude higher than that of the state-of-art commercial particle counters (*19*). The PHA-UCPC allows also the determination of the particle size and the detection efficiency with which the particles are counted. Particles that are <2 nm in diameter are detected also with the PSM with an efficiency close to unity, allowing us to meet the challenge of slow growth. Figure 1 shows an example of a measurement series using three different counters: a commercial TSI-3025A condensation particle counter (CPC) (with a stated 50% detection limit of 3 nm) (TSI, St. Paul, MN), PHA-UCPC, and PSM. In the case of the PHA-UCPC, both raw data and detection efficiency–corrected data are depicted. The experiment was performed in the IfT-LFT using in situ–produced H_2SO_4. Within the residence time of 115 s, only a tiny fraction of particles grow to sizes detectable with the TSI-3025A CPC, which is a commonly used instrument in nucleation studies. The use of an improper counter clearly affects the apparent onset H_2SO_4 concentration needed for nucleation and also the slope $d(\ln N)/d(\ln[H_2SO_4])$, where N is the observed particle number concentration.

Nucleation rates obtained from different experiments are presented in Fig. 2. All series show similar behavior. For photolysis experiments, the H_2SO_4 concentrations are average concentrations from kinetic modeling (*12*). End concentrations measured with the CI-MS matched the modeled end concentrations well, with only some minor deviations for high concentrations and long residence times (fig. S1) (*17*). In the case of the H_2SO_4 from the liquid sample, the initial concentration measured by the CI-MS is shown. Separate fittings of $\ln(J)$ versus $\ln([H_2SO_4])$ to different data series (Fig. 2) yield slopes between 1.0 and 2.1, with an average value of 1.5. This is, to our knowledge, the first time that nucleation of H_2SO_4 from a liquid sample has been reported at concentrations in the range of 10^7 to 10^8 molecules cm^{-3}. This is also the first experiment showing the atmospherically relevant slope. It should be noted that in the experiment performed with the FMI laminar flow tube, the temperature was 25°C and relative humidity (RH) was 30%, whereas the IfT-LFT experiments were performed at the temperature of 20°C and RH of 22%. A 5°C higher temperature can probably explain the slightly smaller nucleation rates in the FMI experiment.

A slope of 2 can be explained by collision-controlled or kinetic nucleation (*10*), in which $J = K[H_2SO_4]^2$, where K is the kinetic coefficient. A slope of unity might, however, require an additional stabilizing and/or condensing vapor participating in the initial growth of the H_2SO_4 clusters, under the assumption that the role of water condensation is small. The slope of unity can also be explained by the activation of existing clusters (*25*), described by $J = A[H_2SO_4]$, where A is the activation coefficient, but we had no indication of preexisting clusters or gaseous impurities in our experiment (*17*). Application of kinetic or activation nucleation theory to our IfT data yields prefactor values of $K \approx 5 \times 10^{-14}$ cm^3 s^{-1} and $A \approx 3 \times 10^{-6}$ s^{-1}. This is consistent with ambient data, in which K ranges from 10^{-14} to 10^{-11} cm^3 s^{-1} (*2*–*4*) and A ranges between 10^{-7} and 10^{-5} s^{-1} (*2*, *4*).

The growth of the nucleated particles was also investigated. Figure 3 shows the mean particle diameter (d_p) determined with the PHA-

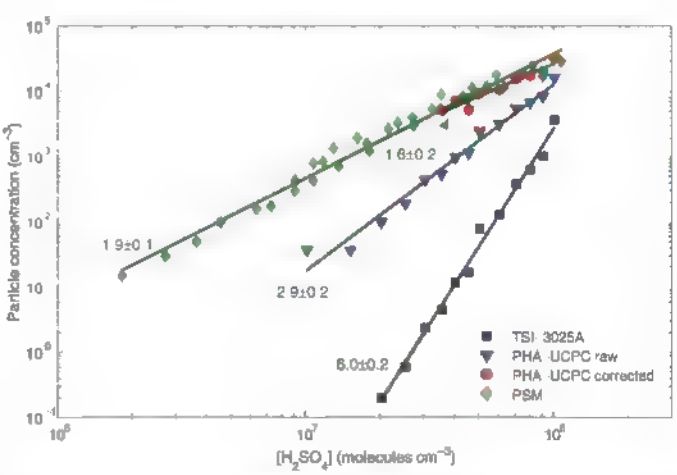

Fig. 1. Comparison of TSI-3025A, PHA-UCPC, and PSM data. In the case of PHA-UCPC, both raw data—in which the diameter-dependency of the counting efficiency is neglected—and the final, corrected data are shown. With a particle size approaching 3 nm, the different series merge. Slopes of the fittings are given in the figure. The experiment is performed in the IfT-LFT with a 115 s residence time and in situ–produced H_2SO_4. The match of the PSM data and the corrected PHA-UCPC data suggests that PSM has a close-to-unity detection efficiency for the particle size range of 1.5 to 3 nm.

[1]Leibniz-Institut für Troposphärenforschung e.V., Leipzig 04318, Germany. [2]Department of Physics, 00014 University of Helsinki, Finland. [3]Helsinki Institute of Physics, 00014 University of Helsinki, Finland. [4]Laboratory of Aerosol Chemistry and Physics, Institute of Chemical Process Fundamentals Academy of Sciences of the Czech Republic, Prague 18502, Czech Republic. [5]Finnish Meteorological Institute, Helsinki 00101, Finland. [6]National Center for Atmospheric Research, Boulder, CO 80307, USA. [7]Department of Applied Environmental Science, Stockholm University, Stockholm 10691, Sweden.

*To whom correspondence should be addressed. E-mail: mikko.sipila@helsinki.fi

UCPC for the photolysis experiments as a function of H_2SO_4 concentration for four different residence times. For comparison, the data taken with a commonly used differential mobility particle sizer (DMPS) system (with a TSI-3025A CPC) are also depicted. From the linear fittings to the data, we get an estimate of the growth rate, which is $(6 \pm 2) \times 10^{-11}$ [H_2SO_4] cm^3 molecule^{-1} $nm\ s^{-1}$. Theoretically, the growth rate from pure H_2SO_4 condensation at ~2-nm particle sizes is ~4×10^{-11} [H_2SO_4] cm^3 molecule^{-1} $nm\ s^{-1}$ (*21*). The agreement can be considered good, and the small difference between measurement and theory can possibly be explained by co-condensation of water. Thus, additional condensing vapors are not necessarily needed to explain the growth in our experiments. The particle diameter after growth represents the sum of the diameter of critical cluster (d_0) and the contribution of growth. The fittings (Fig. 3) intercept the mobility diameter axis at the size d_0, suggesting a critical cluster diameter of (1.2 ± 0.2) nm, which corresponds to a mass diameter of (~0.9 ± 0.2) nm (*26*). However, it should be noted that the PHA-UCPC calibration is based on charged particles, and thus, because of the neutrality of the investigated particles, an additional positive error of ~0.3 nm can be assumed (*17*), yielding the final estimate of the critical cluster mass diameter as ~0.7 to 1.4 nm. The lower limit of this estimation corresponds to approximately 200 atomic mass units (*26*). This is reasonably well in line with our observed slope, which suggests that critical cluster probably contains up to two molecules of H_2SO_4. Furthermore, the size of critical clusters observed in our experiment is about the same as the starting size in atmospheric nucleation events (*27*).

Table 1. Comparison of the parameters describing nucleation. The onset [H_2SO_4] for a nucleation rate of unity ($J = 1$ cm^{-3} s^{-1}) and the slope observed in the laboratory experiments using in situ–produced H_2SO_4 or H_2SO_4 from the liquid sample have previously diverged from atmospheric observations. Results of our present study match well with atmospheric observations.

	Onset [H_2SO_4] molecule cm^{-3}	Slope, d(ln*J*)/d(ln[H_2SO_4])
Atmospheric (*1–4, 28, 29*)	~10^6	1–2
Lab, liquid sample (*6–9*)	10^9–10^{10}	7–21
Lab, OH+SO_2 (*5, 10–15*)	10^7–10^9	2–8
This study, liquid sample and OH+SO_2	~10^6	1–2

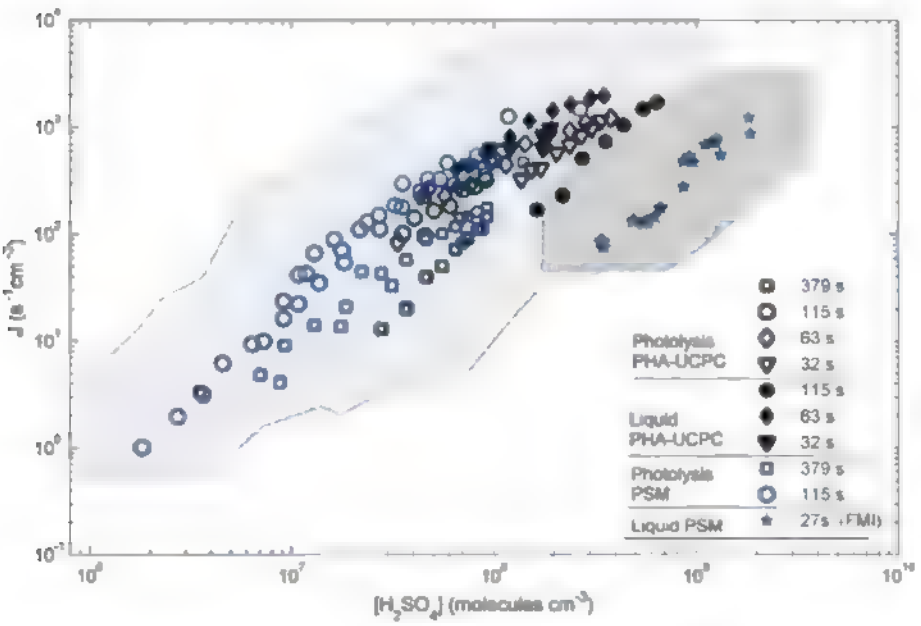

Fig. 2. Nucleation rate as a function of [H_2SO_4]. Fittings to different data series yield slopes ranging from 1.0 to 2.1 with an average slope of 1.5. The experiment in the FMI laminar flow tube was performed at +25°C and RH of 30%, whereas the data from the IfT-LFT are taken at +20°C and RH = 22%. Light and dark gray–shaded areas show the range of the error estimates in the IfT-LFT experiment and the FMI experiment, respectively. An error of (+100/–50)% for [H_2SO_4] was assumed. Error estimates in the nucleation rate comprise the inaccuracy in the determination of the nucleation zone and the error from particle counting.

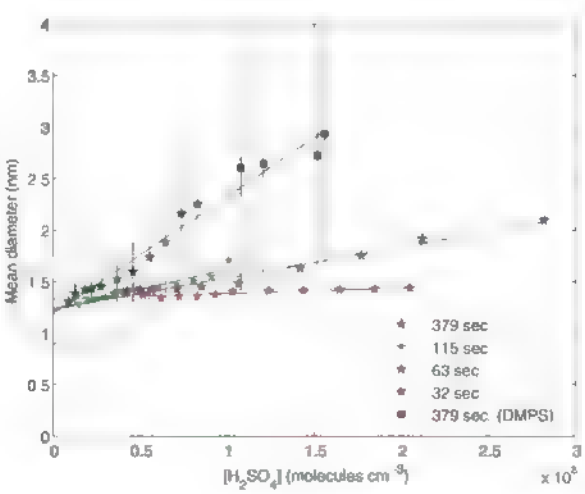

Fig. 3. Measured particle diameter for different residence times as a function of [H_2SO_4] at IfT-LFT, temperature (T) = 20°C, and RH = 22%. Data are mean mobility diameters determined with the PHA-UCPC and with the DMPS in photolysis experiments. The particle diameter is a sum of the diameter of the critical cluster and the contribution of growth. The y intercepts of the fittings suggest a critical cluster diameter of ~1.2 nm (~0.9-nm geometric diameter). Error bars represent SD of particle size distributions (for clarity, they are only shown for the 379-s series).

Our experimental results regarding the onset sulfuric acid concentration as well as the slopes for H_2SO_4 from the liquid sample are clearly in contradiction with other studies performed to date. A probable explanation for the disagreement is as follows. Our data show that high concentrations of H_2SO_4 and proper residence time are needed to allow the particles to grow to ~3 nm in diameter, which is the lowest detection limit of commercial CPCs. The detection efficiency curve of a CPC is typically very steep close to the 50% cutsize of the detector and therefore very sensitive to particle size. According to our data at RH = 22%, the growth rate was ~6×10^{-11} [H_2SO_4] cm^3 molecules^{-1} $nm\ s^{-1}$, which provides evidence that without a suitable detector and long residence times the growth of the freshly nucleated particles is not efficient enough so that they can be observed at [H_2SO_4] below ~10^8 to 10^9 molecules cm^{-3} (Fig. 3). For the most experiments performed to date, the insufficient growth rate together with insufficient counting efficiency can explain a large fraction of the discrepancy between those and our present study. To summarize, it is possible that all of the experiments cited here (including our earlier studies) have been affected either by a short residence time, size-sensitive counting efficiency of particle detectors, unexpected additional loss of H_2SO_4, or all of the above.

Explanation for the mysterious disagreement between experiments performed with in situ–produced H_2SO_4 (*5*) and H_2SO_4 from a

liquid sample (*6*–*9*) lies at least partly in the different H_2SO_4 profiles. Because of nearly uniform H_2SO_4 concentrations in case of in situ experiments (*5*, *12*, *13*), particles have much more time to grow to detectable sizes. In the case of a point source, $[H_2SO_4]$ decreases rapidly with time (fig. S3) (*17*), and the growth is not efficient enough. We have conducted experiments with these two approaches by using the same flow tube and detectors. Therefore, the differences arising from different experimental geometries and different detectors are eliminated in our study.

In conclusion, we have shown that the mystery concerning the apparent disagreement of several orders of magnitude in the nucleation rates and 2 to 3 orders of magnitude in the onset $[H_2SO_4]$ between the in situ–produced H_2SO_4 and the H_2SO_4 from a liquid sample does not exist. Therefore, the role of other sulfur-containing species (*13*), like HSO_5, seems to be of minor importance in the nucleation process, even though these other pathways cannot be completely excluded. Furthermore, we showed that nucleation occurs at atmospherically relevant H_2SO_4 concentrations. The relation between the nucleation rate and H_2SO_4 concentration [$d(\ln J)/d(\ln[H_2SO_4]) = 1.0$ to 2.1] from our experiment is consistent with the corresponding atmosphere observations. A nucleation rate of unity is observed at a $[H_2SO_4]$ slightly above 10^6 molecules cm^{-3}, which is well in line with most atmospheric data (*1*, *4*, *28*, *29*). However, in certain locations co-occurrence of nucleation mechanisms involving other species is plausible. We also showed that H_2SO_4 condensation has a dominating contribution to the observed particle growth in our experiment. The growth rate of $(6 \pm 2) \times 10^{-11}$ $[H_2SO_4]$ cm^3 molecules^{-1} nm s^{-1} obtained from our data is close to the theoretical estimate of pure H_2SO_4 condensation and is smaller than ambient growth rates, which supports the findings that in the atmosphere, compounds like organics (*30*, *31*) or ammonia (*32*) are involved in the early growth process. Even though the exact nucleation mechanism remains an open question, our results show that H_2SO_4 at atmospheric concentrations can explain atmospheric nucleation rates in most locations even without clear participation of ammonia or organic substances. Therefore, our findings can be used straightforwardly in further model studies, including climate models.

References and Notes

1. R. J. Weber *et al.*, *Chem. Eng. Commun.* **151**, 53 (1996).
2. S.-L. Sihto *et al.*, *Atmos. Chem. Phys.* **6**, 4079 (2006).
3. C. Kuang, P. H. McMurry, A. V. McCormick, F. L. Eisele, *J. Geophys. Res.* **113**, (D10), D10209 (2008).
4. I. Riipinen *et al.*, *Atmos. Chem. Phys.* **7**, 1899 (2007).
5. T. Berndt, O. Böge, F. Stratmann, J. Heintzenberg, M. Kulmala, *Science* **307**, 698 (2005).
6. B. E. Wyslouzil, J. H. Seinfeld, R. C. Flagan, K. Okuyama, *J. Phys. Chem.* **94**, 6842 (1991).
7. Y. Viisanen, M. Kulmala, A. Laaksonen, *J. Chem. Phys* **107**, 920 (1997).
8. S. M. Ball, D. R. Hanson, F. L. Eisele, P. H. McMurry, *J. Geophys. Res.* **104** (D19), 23709 (1999).
9. R. Zhang *et al.*, *Science* **304**, 1487 (2004).
10. P. H. McMurry, *J. Colloid Interface Sci.* **78**, 513 (1980).
11. J. P. Friend, R. A. Barnes, R. M. Vasta, *J. Phys. Chem.* **84**, 2423 (1980).
12. T. Berndt, O. Böge, F. Stratmann, *Geophys. Res. Lett.* **33**, L15817 (2006).
13. T. Berndt *et al.*, *Atmos. Chem. Phys.* **8**, 6365 (2008).
14. L.-H. Young *et al.*, *Atmos. Chem. Phys.* **8**, 4997 (2008).
15. D. R. Benson, *Geophys. Res. Lett.* **35**, L11801 (2008).
16. D. Kashchiev, *J. Chem. Phys.* **76**, 5098 (1982).
17. Materials and methods are available as supporting material on *Science* Online.
18. F. Eisele, D. Tanner, *J. Geophys. Res.* **98**, (D5), 9001 (1993).
19. M. Sipilä *et al.*, *Aerosol Sci. Technol.* **43**, 126 (2009).
20. L. A. Sgro, J. Fernández de la Mora, *Aerosol Sci. Technol.* **38**, 1 (2004).
21. K. E. J. Lehtinen, M. Kulmala, *Atmos. Chem. Phys.* **3**, 251 (2003).
22. M. Kulmala *et al.*, *J. Aerosol Sci.* **35**, 143 (2004).
23. C. D. O'Dowd *et al.*, *J. Geophys. Res.* **107**, 8108 (2002).
24. K. Iida, M. R. Stolzenburg, P. H. McMurry, J. N. Smith *J. Geophys. Res.* **113**, (D5), D05207 (2008).
25. M. Kulmala, K. E. J. Lehtinen, A. Laaksonen, *Atmos. Chem. Phys.* **6**, 787 (2006).
26. B. K. Ku, J. Fernandez de la Mora, *Aerosol Sci. Technol* **43**, 241 (2009).
27. M. Kulmala *et al.*, *Science* **318**, 89 (2007).
28. R. J. Weber *et al.*, *Geophys. Res. Lett.* **26**, 307 (1999).
29. W. Birmili, A. Wiedensohler, C. Plass-Dülmer, H. Berresheim, *Geophys. Res. Lett.* **27**, 2205 (2000).
30. J. N. Smith *et al.*, *Geophys. Res. Lett.* **35**, L04808 (2008).
31. C. D. O'Dowd, P. Aalto, K. Hämeri, M. Kulmala, T. Hoffmann, *Nature* **416**, 497 (2002).
32. J. N. Smith *et al.*, *J. Geophys. Res.* **110**, (D22), D22S03 (2005).

33. We thank K. Prelok and A. Rohmer for technical assistance and J. Hertzenberg, K.E.J. Lehtinen, V.-M. Kerminen, and M. McGrath for help preparing the manuscript. C. D. O'Dowd is acknowledged for providing the PHA-UCPC instrument. K. Lehtipalo is acknowledged for assistance with the PHA-UCPC, J. Mikkilä and E. Siivola for constructing the PSM, R. Taipale for help with the PTR-MS, J. Hakala and K. Neitola for assistance with experiments, and T. Nieminen for useful discussions. This work was partially funded by European Commision 6th Framework program project European Integrated Project on Aerosol, Cloud, Climate, and Air Quality Interactions (EUCAARI), contract 036833-2. Financial support from Kone foundation, Väisälä foundation, Otto Malm foundation, the Academy of Finland and European Research Council is acknowledged.

Supporting Online Material

www.sciencemag.org/cgi/content/full/327/5970/1243/DC1
Materials and Methods
SOM Text
Figs. S1 to S4

7 August 2009; accepted 5 January 2010
10.1126/science.1180315

Extensive Methane Venting to the Atmosphere from Sediments of the East Siberian Arctic Shelf

Natalia Shakhova,[1,2]*† Igor Semiletov,[1,2]* Anatoly Salyuk,[2] Vladimir Yusupov,[2] Denis Kosmach,[2] Örjan Gustafsson[3]

Remobilization to the atmosphere of only a small fraction of the methane held in East Siberian Arctic Shelf (ESAS) sediments could trigger abrupt climate warming, yet it is believed that sub-sea permafrost acts as a lid to keep this shallow methane reservoir in place. Here, we show that more than 5000 at-sea observations of dissolved methane demonstrates that greater than 80% of ESAS bottom waters and greater than 50% of surface waters are supersaturated with methane regarding to the atmosphere. The current atmospheric venting flux, which is composed of a diffusive component and a gradual ebullition component, is on par with previous estimates of methane venting from the entire World Ocean. Leakage of methane through shallow ESAS waters needs to be considered in interactions between the biogeosphere and a warming Arctic climate.

The terrestrial and continental shelf regions of the Arctic contain a megapool of carbon in shallow reservoirs (*1*–*3*), most of which is presently sequestered in permafrost (*4*, *5*). Sustained release of methane (CH_4) to the atmosphere from thawing Arctic permafrost is a likely positive feedback to climate warming (*5*, *6*). Arctic CH_4 releases are implied in both past climatic shifts (*7*, *8*) and the renewed growth of contemporary atmospheric CH_4 (*9*, *10*). Observed Arctic warming in early 21st century is stronger than predicted by several degrees (fig. S1A) (*11*–*14*), which may accelerate the thaw-release of CH_4 in a positive feedback. Investigations of Arctic CH_4 releases have focused on thawing permafrost structures on land (*2*, *4*–*6*, *15*, *16*) with a scarcity of observations of CH_4 in the extensive but inaccessible East Siberian Arctic Seas (ESAS), where warming is particularly pronounced (fig. S1A) (*11*).

The ESAS (encompassing the Laptev, East Siberian, and Russian part of the Chuckchi seas) occupies an area of 2.1×10^6 km^2, three times as great as that of terrestrial Siberian wetlands. It is a shallow seaward extension of the Siberian tundra that was flooded during the Holocene transgression 7 to 15 thousand years ago (*17*, *18*). The ESAS sub-sea permafrost (fig. S1B), which is frozen sediments interlayered with the flooded peatland (*18*), not only contains comparable amounts of carbon as still land-fast permafrost in the Siberian tundra but also hosts permafrost-related seabed deposits of CH_4 (*19*). Moreover, ESAS sub-sea

permafrost is potentially more vulnerable to thawing than terrestrial permafrost. In contrast to on-land permafrost, sub-sea permafrost has experienced a drastic change in its thermal regime because of the seawater inundation. The annual average temperature of ESAS bottom seawater (−1.8° to 1°C) is 12° to 17°C warmer than the annual average surface temperature over on-land permafrost (*18*, *19*). A physical implication of combined bottom-up geothermal and top-down seawater heat fluxes is the partial thawing and failure of sub-sea permafrost and thus an increased permeability for gases. We consequently hypothesized that CH_4 is released from seabed deposits to vent extensively to the Arctic atmosphere.

To test our hypothesis, we have undertaken annual field campaigns (August to September, 2003 to 2008, six cruises in total), one helicopter survey (September 2006), and one over-ice winter expedition (April 2007) (*20*, *21*). On the basis of a more limited coverage, we previously demonstrated that CH_4 is released from ESAS sediments to the overlying water column (*22*, *23*). The objective of the present study is an integrated assessment of multiple years of observations for the whole of the ESAS in order to provide an estimate of the venting flux of CH_4 to the atmosphere over the entire ESAS. It is this estimate of CH_4 flux to the atmosphere that has been missing and has prohibited a quantitative evaluation of the putative climate impact of ESAS CH_4. The CH_4 flux estimates are based on 5100 seawater samples from 1080 stations—a larger database than for any previous ocean CH_4 study (*24*) geographically distributed over the ESAS (Fig. 1A). The "landscape" of coastal waters is fortunately less heterogeneous than the terrestrial tundra counterpart. Hence, this assessment of coastal CH_4 fluxes may be contrasted with upscaling challenges facing estimates of greenhouse gas emissions from the tundra, which nonetheless are usually limited to measurements at a few sites (*4*–*6*, *15*, *16*).

The dissolved CH_4 concentrations in ESAS during summers of 2003 to 2008 demonstrate a ubiquitous supersaturation over large spatial scales. Although there are some spatial and vertical gradients, the emerging picture is that most of the ESAS is supersaturated with CH_4 in the near-bottom waters (Fig. 1B), with >50% of the ESAS surface waters being supersaturated (Fig. 1C). The median summertime supersaturation was 880% in background areas and 8300% in hotspot areas [supporting online material (SOM) text] (*21*). Besides the vertical profiles with maximums near the seafloor, which is common to the oceanic water column (*25*), the dissolved CH_4 distribution in the ESAS varied to maximum near the surface and had uniform distribution throughout the water column.

Both the bottom- and surface-water dissolved CH_4 concentrations in winter (~5° to 7°C colder than in summer), which were measured in the studied area beneath the sea ice (Fig. 2A), were 5 to 10 times higher than in summer yet had the same distribution within the water column (Fig. 2B). Such vertical profiles point to a rapid transport mechanism such as ebullition, which is considered to be a predominant mechanism of CH_4 transport in shallow waters and particularly when CH_4 releases from seabed deposits (*26*). Large bubbles of gas entrapped within the fast (annual) sea ice were observed in winter (Fig. 2C), with CH_4 concentrations of up to 11,400 parts per million by volume (ppmv). Manifestations of ebullition were furthermore registered acoustically as bubble clouds, which rose from the seabed throughout the entire water column or, at deeper locations, to subsurface layers (fig. S2). Taken together, the observations demonstrate that the ESAS—the world's largest continental shelf sea—is perennially laden with CH_4 all the way up to the sea surface.

The horizontal and vertical CH_4 distributions indicate a sedimentary source, yet other sources were considered. Riverborne export of CH_4 was excluded on the basis of measurements in, for example, the Bykovskaya Channel, which is the main outflow of the Lena River (fig. S3). Dissolved CH_4 concentrations decreased downstream through the delta channel and then increased again in coastal waters, suggesting separate sources. Production of CH_4 in the water column was also deemed unlikely to account for the high ESAS concentrations. Mixed-layer maxima of CH_4 in

[1]International Arctic Research Center, University of Alaska, Fairbanks, AK 99709, USA. [2]Russian Academy of Sciences, Far Eastern Branch, Pacific Oceanological Institute, Vladivostok 690041, Russia. [3]Stockholm University, Bert Bolin Centre for Climate Research and Department of Applied Environmental Science, Stockholm S-10691, Sweden.

*These authors contributed equally to this work.
†To whom correspondence should be addressed. E-mail: nshakhov@arc.uaf.edu

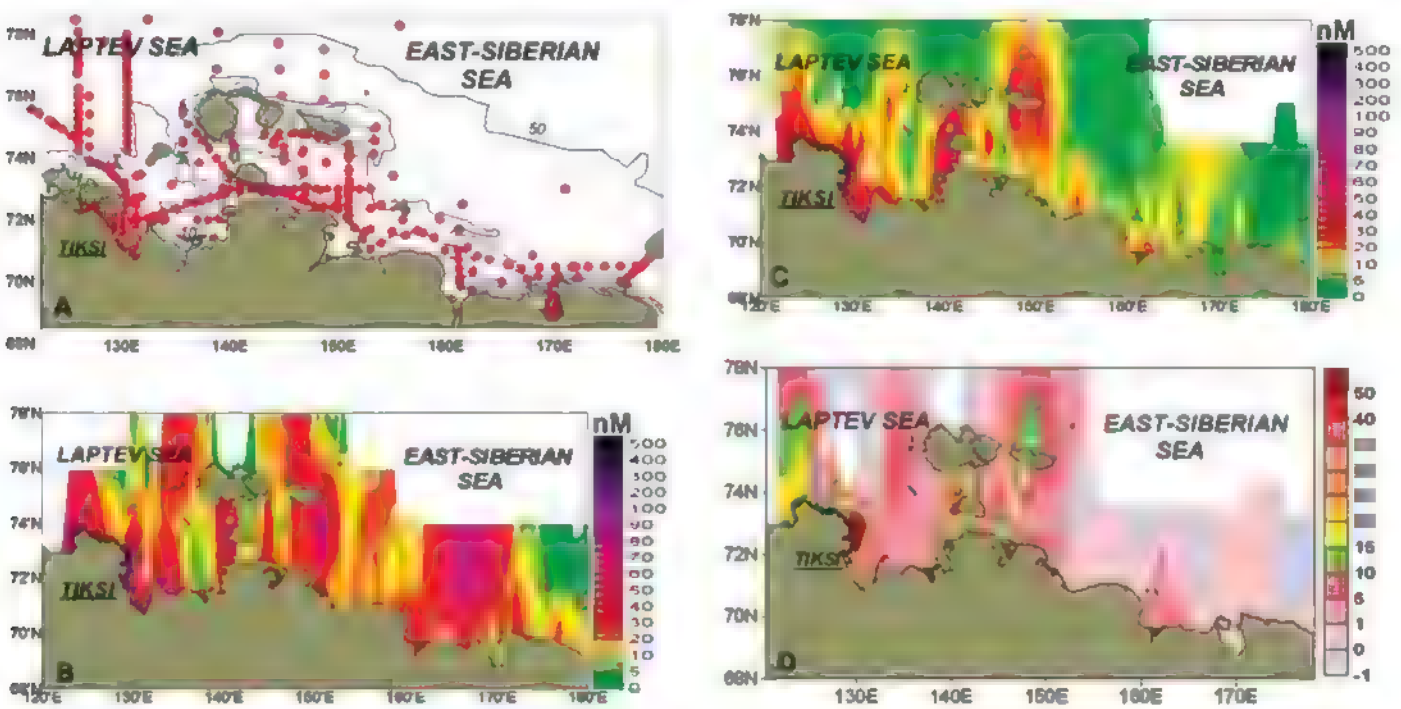

Fig. 1. Summertime observations of dissolved CH_4 in the ESAS (*21*). (**A**) Positions of oceanographic stations in the eastern Laptev Sea and East Siberian Sea; bathymetry lines for 10, 20, and 50 m depth are shown in blue. (**B**) Dissolved CH_4 in bottom water. (**C**) Dissolved CH_4 in surface water. (**D**) Fluxes of CH_4 venting to the atmosphere over the ESAS.

the open ocean in the 4-to 10-nM range have been suggested to be associated with either high rates of primary production, methanogenesis inside anaerobic microenvironments of sinking particles (*25*, *27*), or through decomposition of methylphosphonates in the tropical ocean (*28*). ESAS primary production is suppressed by factors of 100 to 1000 as compared with that of the open ocean because of lack of sunlight and highly turbid waters, whereas CH_4 levels are 10-fold larger (Fig. 1, B and C). The acoustic-geophysical record combined with the vertical CH_4 profiles suggest that the water column inventory in the ESAS stems from sedimentary release. Because the ESAS average depth is only 45 m, the water column provides a short conduit for bottom-released CH_4 to be vented to the overlying atmosphere (Fig. 1D). This distinguishes CH_4 venting in the ESAS from sedimentary releases in deeper waters, in which the bulk of CH_4 would be oxidized before reaching the sea surface (*25*, *29*).

Mixing ratios of CH_4 in the atmospheric boundary layer provide direct evidence for CH_4 escape. For instance, high-frequency surveying along the >4000-km Northeast Passage demonstrates a consistently elevated mixing ratio of CH_4, relative to the latitude-specific monthly mean (LSMM) (*30*), and with extreme variability (Fig. 3A), as is expected near sources. From values averaging 2.10 ± 0.02 parts per million (ppm) (1 SD) through the Kara Sea, the CH_4 mixing ratio increased markedly after passage through the Vilkitskyi Strait and entering the ESAS, averaging 2.97 ± 0.15 ppm in the Laptev Sea and 2.66 ± 0.09 ppm in the East Siberian Sea, with spikes in the 6.4 to 8.2 ppm range. A helicopter-mounted survey over the Laptev Sea during September 2006 demonstrated that the CH_4 mixing ratio in the atmosphere was elevated by 5 to 10% up to 1800 m in height (Fig. 3B).

To estimate the total annual CH_4 flux (F_t) from the ESAS, six separate components of the total flux budget were considered to account for differences in ice coverage [summer (F_{ts}) versus winter (F_{tw})] and mechanism of water column transfer [diffusive-dissolved (F_{td}) versus ebullition-bubbles (F_{te})] integrated over the areal extent of the two regions with different source strengths [background (F_{tb}) versus hotspots (F_{th})] (*31*).

Mean diffusive fluxes were estimated by means of the surface-film model for each population (*32*). The summertime ebullition component was taken as the difference between the total flux as measured directly with eddy covariance techniques (*33*–*35*), and this calculated the diffusive flux. Hence, the averaged CH_4 flux, based on mean daily actual wind speed for the 90 percentile of the data set, yielded a mean flux of 3.67 mg m^{-2} d^{-1}, which was prorated to the background area of 1.9×10^6 km^2. A mean flux of 11.8 mg m^{-2} d^{-1} was prorated to the area of the hotspots (0.2×10^6 km^2). Summertime diffusive contribution of the background area was thus composed of 0.69 Tg C-CH_4, and hotspots added 0.24 Tg C-CH_4 to the total summertime diffusive flux of 0.93 Tg C-CH_4 ($F_{ds} = F_{dsb} + F_{dsh}$) (Table 1). The total summer flux in background areas (F_{tsb}) was 1.56 Tg C-CH_4, which thus constrains the ebullition component (F_{esb}) to 0.87 Tg C-CH_4 ($F_{tsb} = F_{dsb} + F_{esb}$). The total summertime CH_4 flux in hotspot areas (F_{tsh}) was 0.63 Tg C-CH_4, with 0.39 Tg C-CH_4 as the ebullition component (F_{esh}) (F_{tsh} $F_{dsh} + F_{esh}$). Total CH_4 flux for the period of open water thus reaches 2.19 Tg C-CH_4 ($F_{ts} = F_{tsb} + F_{tsh}$)

For the winter period, dissolved CH_4 concentrations beneath the sea ice were 5 to 10 times higher than in the summer (Figs. 1 and 2). Hence, we assume that CH_4 concentrations, accumulating beneath the sea ice, represent the sum of the diffusive (potentially accumulated) winter flux component (F_{dw}) and ebullition winter flux component (F_{ew}, potentially accumulated as increased CH_4 from dissolution of most bubbles during storage under the ice) (Table 1). Given a constant rate of CH_4 release from the seabed throughout the year, the 265-days-long ice-covered period in

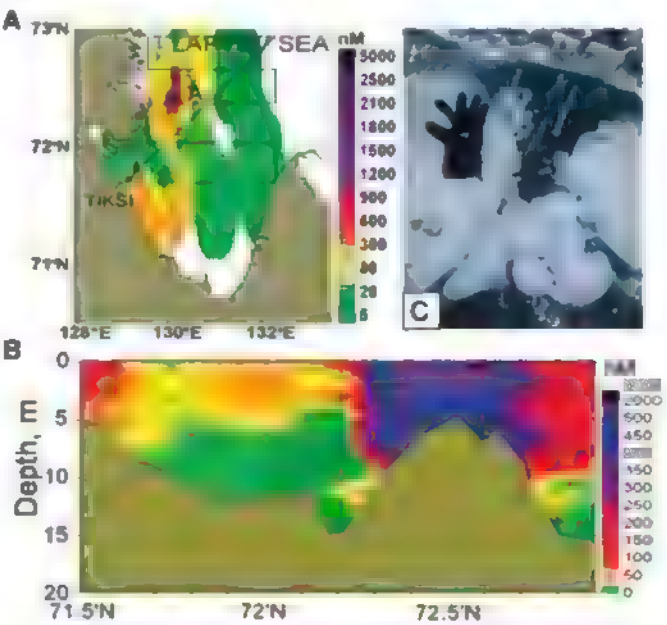

Fig. 2. Wintertime observations of dissolved CH_4 in the ESAS (*21*). (**A**) Dissolved CH_4 measured beneath the sea ice. (**B**) Vertical distribution of dissolved CH_4 along the transect, shown as a blue dotted line in (A). (**C**) Bubbles of gas entrapped within the sea ice were ubiquitously observed [the diameter of the borehole is ~37 cm (72.59°N, 130.11°E), April 2007]. The black-arrow raster line shows the route of the helicopter-based air CH_4 survey in September 2006.

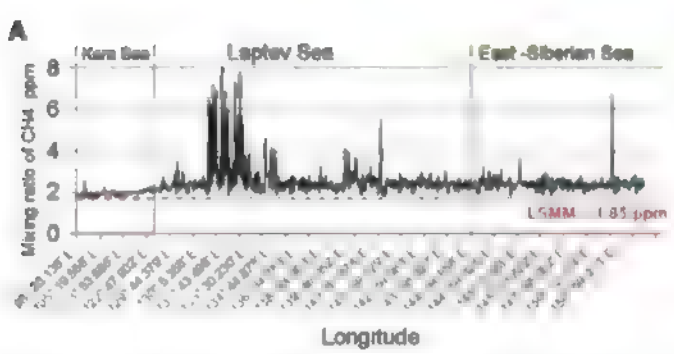

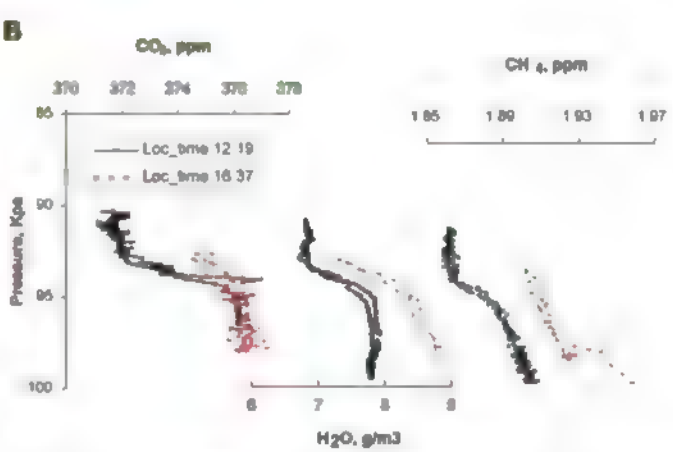

Fig. 3. Survey of CH_4 mixing ratio in the atmospheric boundary layer along the northern Eurasian seaboard (*21*). (**A**) Mixing ratio of CH_4 in the air above the water surface measured along the ship route in September 2005 (red dotted line shows the LSSM of 1.85 ppmv established for the Barrow, Alaska, USA, monitoring station at 71° 19′ N, 156° 35′ W (www.cmdl.noaa.gov/ccgg/insitu.html). The position of the transects are shown as color dotted lines in fig. S1B. Red, the Kara Sea; black, the Laptev Sea; orange, the East Siberian Sea. (**B**) Vertical mixing ratio of CH_4 in the atmosphere above southeast Laptev Sea (72.49°N, 130.51°E) as measured during a helicopter survey in September 2006 (the helicopter route is shown as black-arrows in Fig. 2A).

Table 1. Components of the annual CH_4 flux in the ESAS. In a^b_c, a is the mean, b is the 95% upper confidence limit of the flux, and c is the 95% lower confidence limit of flux. F_{dsb}, diffusive summer flux in background areas; F_{dsh}, diffusive summer flux in hotspots; F_{ds}, total diffusive summer flux ($F_{ds} = F_{dsb} + F_{dsh}$); F_{esb}, ebullition summer flux component in background areas; F_{esh}, ebullition summer flux component in hotspots; F_{es}, total ebullition summer flux component ($F_{es} = F_{esb} + F_{esh}$); F_{dwb}, diffusive winter flux in background areas; F_{dwh}, diffusive winter flux in hotspots; F_{dw}, total diffusive winter flux ($F_{dw} = F_{dwb} + F_{dwh}$); F_{ewb}, ebullition winter flux component in background areas; F_{ewh}, ebullition winter flux component in hotspots; F_{ew}, total ebullition winter flux component ($F_{ew} = F_{ewb} + F_{ewh}$); F_{tsb}, total summer flux in background areas ($F_{tsb} = F_{dsb} + F_{esb}$); F_{tsh}, total summer flux in hotspots ($F_{tsh} = F_{dsh} + F_{esh}$); F_{ts}, total summer flux ($F_{ts} = F_{tsb} + F_{tsh}$); F_{twb}, total winter flux in background areas ($F_{twb} = F_{dwb} + F_{ewb}$); F_{twh}, total winter flux in hotspots ($F_{twh} = F_{dwh} + F_{ewh}$); F_{tw} total winter flux ($F_{tw} = F_{twb} + F_{twh}$); F_{tb}, total flux in background areas ($F_{tb} = F_{tsb} + F_{twb}$); F_{th}, total flux in hotspots ($F_{th} = F_{tsh} + F_{twh}$); F_t, total annual flux ($F_t = F_{tb} + F_{th}$). The methods to calculate the fluxes and to derive the statistical population parameters for each flux component are presented in (*21*) and the SOM text, and the parameters used for calculations are described in table S2.

Component name	Background	Hotspots	Total
Area (km^2)	1.9×10^6	0.2×10^6	2.1×10^6
Diffusive summer flux (Tg C-CH_4), F_{dsb}, F_{dsh}, F_{ds}	$0.69^{0.71}_{0.51}$	$0.24^{0.31}_{0.17}$	$0.93^{1.01}_{0.68}$
Ebullition summer flux (Tg C-CH_4), F_{esb}, F_{esh}, F_{es}	$0.87^{1.26}_{0.65}$	$0.39^{0.41}_{0.38}$	$1.26^{1.67}_{1.03}$
Total summer CH_4 flux (Tg C-CH_4), F_{tsb}, F_{tsh}, F_{ts}	$1.56^{1.97}_{1.17}$	$0.63^{0.71}_{0.55}$	$2.19^{2.68}_{1.71}$
Diffusive winter (accumulative potential) flux (Tg C-CH_4), F_{dwb}, F_{dwh}, F_{dw}	$1.8^{1.84}_{1.32}$	$0.62^{0.78}_{0.44}$	$2.42^{2.62}_{1.76}$
Ebullition winter flux, (Tg C-CH_4), F_{ewb}, F_{ewh}, F_{ew}	$2.2^{3.2}_{1.69}$	$1.17^{1.23}_{1.14}$	$3.37^{4.43}_{2.83}$
Total winter (accumulative potential) flux (Tg C-CH_4), F_{wb}, F_{wh}, F_w	$4.0^{5.04}_{3.01}$	$1.79^{2.01}_{1.58}$	$5.79^{7.05}_{4.59}$
Total annual flux (Tg C-CH_4), F_{tb}, F_{th}, F_t	$5.56^{7.01}_{4.18}$	$2.42^{2.72}_{2.13}$	$7.98^{9.73}_{6.31}$

the ESAS (F_{dwb}) could thus accumulate 1.8 Tg of C-CH_4 from the background areas and an additional 0.62 Tg C-CH_4 from the hotspots (F_{dwh}) to yield a total diffusive wintertime flux of 2.42 Tg of C-CH_4 ($F_{dw} = F_{dwb} + F_{dwh}$), with a portion vented to the atmosphere through wintertime polynyas and the rest at ice break-up. Because the ice-covered period is only 2.5 times longer than the ice-free period, whereas concentrations of dissolved CH_4 are 5 to 10 times higher, we suggest that contribution of ebullition to annual CH_4 emissions from the ESAS could be significant.

The ebullition component of the flux for the ice-covered period was estimated by applying scaling coefficients according to the relative size of diffusive and ebullition components in the summer. Wintertime ebullition fluxes were thus 2.2 Tg C-CH_4 (F_{ewb}) and 1.17 Tg C-CH_4 (F_{ewh}), which gives 4.0 Tg C-CH_4 in total for the background areas ($F_{twb} = F_{dwb} + F_{ewb}$) and 1.79 Tg C-$CH_4$ for the hotspot areas ($F_{twh} = F_{dwh} + F_{ewh}$). Together with the total summer flux of 2.19 Tg C-CH_4, this corresponds to a total annual venting flux of CH_4 to the ESAS atmosphere of $7.98^{9.73}_{6.31}$ Tg C-CH_4 (Table 1), which does not include nongradual ebullition. Although such releases of strong CH_4 pulses occur (Fig. 3A and fig. S2, the "spikes"), this component is not included in the total flux estimate, which thus is conservative because the spatial and temporal pattern of such nongradual "catastrophic event" ebullition is uncertain.

The diffusive flux component was about 40% of the total annual CH_4 flux, with the remainder being vented through gradual ebullition (Table 1). The winter component (including ice break-up) was 2.5 times larger than the summer flux and about one third of the total flux emanated from the hotspot areas covering ~10% of the ESAS area. The annual outgassing from the shallow ESAS of $7.98^{9.73}_{6.31}$ Tg C-CH_4 is of the same magnitude as existing estimates of total CH_4 emissions from the entire world ocean (*1*, *25*). Although the oceanic CH_4 flux should be revised, the current estimate is not alarmingly altering the contemporary global CH_4 budget. These findings do change our view of the vulnerability of the large sub-sea permafrost carbon reservoir on the ESAS; the permafrost "lid" is clearly perforated, and sedimentary CH_4 is escaping to the atmosphere.

There remains substantial uncertainty regarding several aspects of the CH_4 release from the ESAS. To make predictions of future development of these CH_4 releases, there needs to be progress in the comprehension of the forms and locations of the sedimentary CH_4 sources as well as how each may respond to Arctic change. Multidimensional isotopic analysis of the released CH_4 is one method to apportion the CH_4 sources and to constrain the flux attenuation that is attributable to microbial CH_4 oxidation. The relative importance of the various flux components may also be independently approached by means of detailed observations of atmospheric mixing ratios throughout the year because enhanced venting may be expected during fall breakdown of water column stratification (September to October) and ice breakup (May to July). To discern whether this extensive CH_4 venting over the ESAS is a steadily ongoing phenomenon or signals the start of a more massive CH_4 release period, there is an urgent need for expanded multifaceted investigations into these inaccessible but climate-sensitive shelf seas north of Siberia.

References and Notes

1. Intergovernmental Panel on Climate Change (IPCC), *The Scientific Basis* (Cambridge Univ. Press, New York, 2007).
2. C. Tamocai *et al.*, *Global Biogeochem. Cycles* **23**, GB2023 (2009).
3. I. S. Gramberg, Yu. N. Kulakov, Yu. E. Pogrebitsky, D. S. Sorokov, *Proc. World Pet. Congr.* **11**, 93 (1983).
4. S. A. Zimov, E. A. G. Schuur, F. S. Chapin III, *Science* **312**, 1612 (2006).
5. E. A. G. Schuur *et al.*, *Nature* **459**, 556 (2009).
6. K. M. Walter, S. A. Zimov, J. P. Chanton, D. Verbyla F. S. Chapin III, *Nature* **443**, 71 (2006).
7. E. G. Nisbet, J. Chappellaz, *Science* **324**, 477 (2009).
8. V. V. Petrenko *et al.*, *Science* **24**, 506 (2009).
9. W. C. Oechel *et al.*, *Nature* **361**, 520 (1993).
10. M. Rigby *et al.*, *Geophys. Res. Lett.* **35**, L22805 (2008).
11. www.eoearth.org/article/State_of_the_Arctic_Report
12. F. W. Zwiers, *Nature* **416**, 690 (2002).
13. V. M. Kattsov *et al.*, *Arctic Climate Impact Assessment (ACIA) Scientific Report 2004, chap. 4, Future Climate Change: Modeling and Scenarios* (Cambridge Univ. Press, New York, 2005), pp. 99–150.
14. R. W. Lindsay, J. Zhang, A. J. Schweiger, M. A. Steele, H. Stern, *J. Clim.* **22**, 165 (2009).
15. I. P. Semiletov, *J. Atmos. Sci.* **56**, 286 (1999).
16. M. Mastepanov *et al.*, *Nature* **456**, 628 (2008).
17. V. A. Soloviev, Sixth International Conference on Gas in Marine Sediments, St. Petersburg, Russia, 5 to 9 September 2000, abstr. pp. 123–125.
18. N. N. Romanovskii, H.-W. Hubberten, A. V. Gavrilov, A. A. Elseeva, G. S. Tipenko, *Geo-Mar. Lett.* **25**, 167 (2005).
19. V. A. Soloviev, G. D. Ginzburg, E. V. Telepnev, Yu. N. Mikhaluk, *Cryothermia of Gas Hydrates in the Arctic Ocean* (VNIIOkeangeologia, St. Petersburg, 1987).
20. We deployed our field laboratories on ice-strengthened small- and mid-sized ships that were suitable for operation in shallow ESAS waters. Seawater samples were immediately drawn from conductivity-temperature-depth (CTD)–Niskin bottles and analyzed onboard with gas chromatography (*21*).

21. Materials and methods are available as supporting material on *Science* Online
22. N. Shakhova, I. Semiletov, G. Panteleev, *Geophys. Res. Lett.* **32**, L09601 (2005)
23. N. Shakhova, I. Semiletov, *J. Mar. Syst.* **66**, 227 (2007)
24. All the seawater-dissolved CH_4 concentration data are publicly and freely available at http://research.iarc.uaf.edu/SSSS/. A description of this large database as compared with previous ocean CH_4 studies is presented in table S3.
25. W. S. Reeburgh, *Chem. Rev.* **107**, 486 (2007)
26. I. Leifer, B. Luyendyk, J. Boles, J. Clark, *Global Biogeochem. Cycles* **20**, GB3008 (2006)
27. N. J. P. Owens, C. S. Law, R. F. C. Mantoura, P. H. Burkill, C. A. Llewellyn, *Nature* **354**, 293 (1991)
28. D. M. Karl *et al.*, *Nat. Geosci.* **1**, 473 (2008)
29. G. K. Westbrook *et al.*, *Geophys. Res. Lett.* **36**, L15608 (2009)
30. LSMM closest to the study area is established for the Barrow, Alaska, USA, monitoring station at 71° 19′ N, 156° 35′ W (www.cmdl.noaa.gov/ccgg/insitu.html); it is equal to 1.85 ppmv
31. The division into two subpopulations for background and hotspot areas within the ESAS was based on a statistical approach detailed in SOM text S2.1 and displayed graphically in fig. S4. These two resolved populations were then first subjected to an empirical distribution function (EDF) test (SOM text S1.1). The results of the EDF test (table S1) yielded that a lognormal distribution function best fit the data. This function was hence used when applying the maximum likelihood (ML) method to calculate the statistical population parameters mean and variance [expressed as upper and lower 95% confidence limits (equations are provided in SOM text S1.1)]. The derived population parameters, displayed in table S2, were then used to estimate the overall ESAS CH_4 fluxes as summarized in Table 1.
32. R. Wanninkhof, *J. Geophys. Res.* **97** (C5), 7373 (1992)
33. D. D. Baldocchi, *Glob. Change Biol.* **9**, 479 (2003)
34. J. B. Edson, A. A. Hinton, K. E. Prada, J. E. Hare, C. W. Fairall, *J. Atmos. Ocean. Technol.* **15**, 547 (1998)
35. T. Fujitani, *Pap. Meteorol. Geophys.* **36**, 157 (1985)

36. We thank V. Sergienko, G. Golitsyn, S. Akasofu, L. Hinzman, and V. Akulichev for their support of our work in the Siberian Arctic. This research was supported by the International Arctic Research Centre through a National Oceanic and Atmospheric Administration Cooperative Agreement, the Far Eastern Branch of the Russian Academy of Sciences, the Russian Foundation for Basic Research, NSF, the Swedish Research Council, and the Knut and Alice Wallenberg Foundation

Supporting Online Material

www.sciencemag.org/cgi/content/full/327/5970/1246/DC1
Materials and Methods
SOM Text
Figs. S1 to S4
Tables S1 to S3
References

21 September 2009; accepted 21 January 2010
10.1126/science.1182221

Hippocampal Short- and Long-Term Plasticity Are Not Modulated by Astrocyte Ca^{2+} Signaling

Cendra Agulhon,[1]* Todd A. Fiacco,[2] Ken D. McCarthy[1]

The concept that astrocytes release neuroactive molecules (gliotransmitters) to affect synaptic transmission has been a paradigm shift in neuroscience research over the past decade. This concept suggests that astrocytes, together with pre- and postsynaptic neuronal elements, make up a functional synapse. Astrocyte release of gliotransmitters (for example, glutamate and adenosine triphosphate) is generally accepted to be a Ca^{2+}-dependent process. We used two mouse lines to either selectively increase or obliterate astrocytic G_q G protein–coupled receptor Ca^{2+} signaling to further test the hypothesis that astrocytes release gliotransmitters in a Ca^{2+}-dependent manner to affect synaptic transmission. Neither increasing nor obliterating astrocytic Ca^{2+} fluxes affects spontaneous and evoked excitatory synaptic transmission or synaptic plasticity. Our findings suggest that, at least in the hippocampus, the mechanisms of gliotransmission need to be reconsidered.

Calcium transients in astrocytes are physiologically driven by metabotropic G_q G protein–coupled receptors (G_q GPCRs), which can be activated after neurotransmitter release from presynaptic terminals (*1*, *2*). At Schaffer collateral-CA1 (SC-CA1) synapses in acute hippocampal slices, astrocytes can modulate neuronal activity by elevations in Ca^{2+} that are evoked by the following: (i) uncaging IP_3 or Ca^{2+} in individual astrocytes, (ii) repetitive depolarization of the astrocyte membrane, (iii) mechanical stimulation of an astrocyte, or (iv) bath application of endogenous G_q GPCR agonists. With these pharmacological approaches, astrocyte Ca^{2+} elevations have been reported to trigger gliotransmitter release from astrocytes, resulting in the modulation of synaptic transmission and plasticity through the activation of presynaptic [for example, group I metabotropic glutamate receptors (mGluRs) or adenosine A(1) receptors (A_1Rs)] or postsynaptic receptors [*N*-methyl-D-aspartate receptors (NMDARs)] (*3*–*11*). To circumvent a number of caveats associated with the pharmacological approaches described above (*12*–*15*), we have recently developed and characterized two genetically modified mice [the MrgA1$^+$ and IP_3R2 knockout (KO) mice] that enable either selective activation or inactivation of G_q GPCR Ca^{2+} signaling in astrocytes (*13*, *16*, *17*). Within the hippocampus, the stimulation of transgenic MrgA1 G_q GPCRs leads to astrocyte-specific Ca^{2+} responses that mimic the "Ca^{2+} fingerprint" response that is elicited by endogenous G_q GPCRs (*13*). In hippocampal slices derived from IP_3R2 KO mice (*17*), G_q GPCR Ca^{2+} signaling is obliterated selectively in 100% of astrocytes without affecting neuronal Ca^{2+} responses (*16*).

We first tested the possibility that astrocytic G_q GPCR Ca^{2+} is involved in the modulation of spontaneous excitatory postsynaptic currents (sEPSCs). In these and the following experiments, a high percentage of astrocytes (~90 to 100%) were stimulated so that each CA1 neuron has the vast majority of its synapses embedded in astrocyte processes that elevate Ca^{2+} upon G_q GPCR agonist application. Control experiments showed that MrgA1R expression by itself in astrocytes does not affect basal neuronal activity in a nonspecific manner [supporting online material (SOM) text S1]. MrgA1R agonist Phe-Met-Arg-Phe-NH_2 amide (FMRF, 15 μM) was applied to trigger Ca^{2+} elevations in ~90% of mature MrgA1$^+$ passive astrocytes (*13*) in cell bodies as well as fine processes (Fig. 1, A and B, boxes/traces 1 to 5, SOM text S2, and movie S1). No significant effect of astrocyte Ca^{2+} elevations on sEPSC frequency and amplitude in CA1 neurons from MrgA1$^+$ mice was found (Fig. 1C and SOM text S3, $n = 7$, $P > 0.05$). To test the possibility that this lack of effect might be caused by the stimulation of a transgenic G_q GPCR, we also stimulated endogenous astrocytic endothelin G_q GPCRs (ETRs), which were selected as optimal candidates because they evoke gliotransmitter release in vitro (*18*), they are thought to be very weakly expressed by neurons and heavily expressed by brain astrocytes at postnatal day 1 to 30 (*19*), and no direct effects on neuronal activity have been reported when stimulating ETRs (*13*). Astrocytic ETR-mediated Ca^{2+} increases in ~100% of astrocytes from wild-type (WT) hippocampal slices [endothelin 1 (ET1) and ET3, 10 nM each; SOM text S4, and fig. S1) had no effect on the frequency or amplitude of sEPSCs (Fig. 1, D to F, and SOM text S5, $n = 5$, $P > 0.05$).

Previous studies using conventional pharmacological approaches have suggested that postsynaptic NMDARs might be preferential targets for glutamate release from astrocytes (*3*–*7*, *9*, *10*), prompting us to examine the possibility that astrocytic G_q GPCR Ca^{2+} elevations modulate the NMDAR-mediated component of evoked whole-cell EPSCs (eEPSCs). FMRF does not produce a nonspecific effect on NMDA eEPSCs (Fig. 2, A and A1, and SOM text S6). FMRF or ETs were

[1]Department of Pharmacology, University of North Carolina at Chapel Hill, Genetic Medicine Building, CB 7365, Chapel Hill, NC 27599, USA. [2]Department of Cell Biology and Neuroscience, University of California Riverside, Riverside, CA 92521, USA.

*To whom correspondence should be addressed. E-mail: cendra.agulhon@med.unc.edu

applied to MrgA1$^+$ or WT slices, respectively, and the amplitude of NMDA eEPSCs was unaffected during agonist-mediated Ca^{2+} increases in astrocytes (Fig. 2, B and B1, and SOM text S7, MrgA1$^+$, $n = 11$, $P > 0.05$; Fig. 2, C and C1, and SOM text S7, WT, $n = 7$, $P > 0.05$).

Uncaging IP_3 or Ca^{2+} in astrocytes produces a transient enhancement of the probability of neurotransmitter release at a fraction of the SC terminals (*10*, *20*). We directly tested whether activating or inactivating astrocytic G_q GPCR Ca^{2+} signaling affects presynaptic release probability and short-term plasticity by measuring the paired-pulse facilitation (PPF) index of evoked field potentials (fEPSPs). Astrocytic MrgA1R expression by itself did not have a nonspecific effect on PPF (Fig. 2D and SOM text S8). No overall PPF profile changes were observed in association with astrocyte MrgA1R- or ETR-mediated Ca^{2+} elevations in MrgA1$^+$ or WT slices, respectively (Fig. 2E, MrgA1$^+$, $n = 7$, $P > 0.05$; Fig. 2F, WT, $n = 6$, $P > 0.05$). We reasoned that if astrocytic Ca^{2+} elevations regulate gliotransmitter release, then the removal of astrocytic G_q GPCR Ca^{2+} signaling should affect tonic and activity-induced gliotransmitter release and, consequently, PPF. Therefore, PPF was measured in IP_3R2 KO mice versus WT littermate controls. Again, no changes in PPF profiles were observed between the two groups (Fig. 2G, IP_3R2 KO, $n = 9$; WT, $n = 9$; $P \sim 0.73$).

A recent study has shown that temporal coincidence of astrocyte Ca^{2+} elevations (evoked by Ca^{2+} uncaging) and transient depolarization of CA1 neurons can induce a presynaptic form of long-term potentiation (LTP) in SC-CA1 synapses (*10*). Therefore, stimulating astrocytic G_q GPCR Ca^{2+} signaling simultaneously with depolarization of large ensembles of CA1 neurons should either directly induce LTP or at least modulate the baseline slope of fEPSPs through gliotransmitter activation of presynaptic group I mGluRs, or, alternatively, A_1Rs (*10*, *21*). Our data do not support these predictions (fig. S2, B, B1, C, C1, and SOM text S9).

We also directly tested whether astrocytic G_q GPCRs regulate LTP magnitude as well as post-tetanic potentiation (PTP). Similar to PPF, PTP is a form of short-term plasticity (*22*). First, a battery of control experiments clearly demonstrated that neither the selective astrocytic expression of MrgA1Rs nor the application of FMRF to WT slices affected input-output (I/O) curves, PTP, or LTP (Fig. 3, A and D, and SOM text S10). A prerequisite for the involvement of astrocytes in LTP is that their activation precedes the induction of LTP. After establishing a 15-min baseline recording of fEPSPs, Ca^{2+} elevations in astrocytes were induced by bath application of either FMRF to MrgA1$^+$ slices or ETs to WT slices. LTP was induced ~2.5 min after agonist application, when the peaks of Ca^{2+} responses in astrocytes reached their maximum (Fig. 3, B and C). LTP magnitudes obtained from MrgA1$^+$ slices

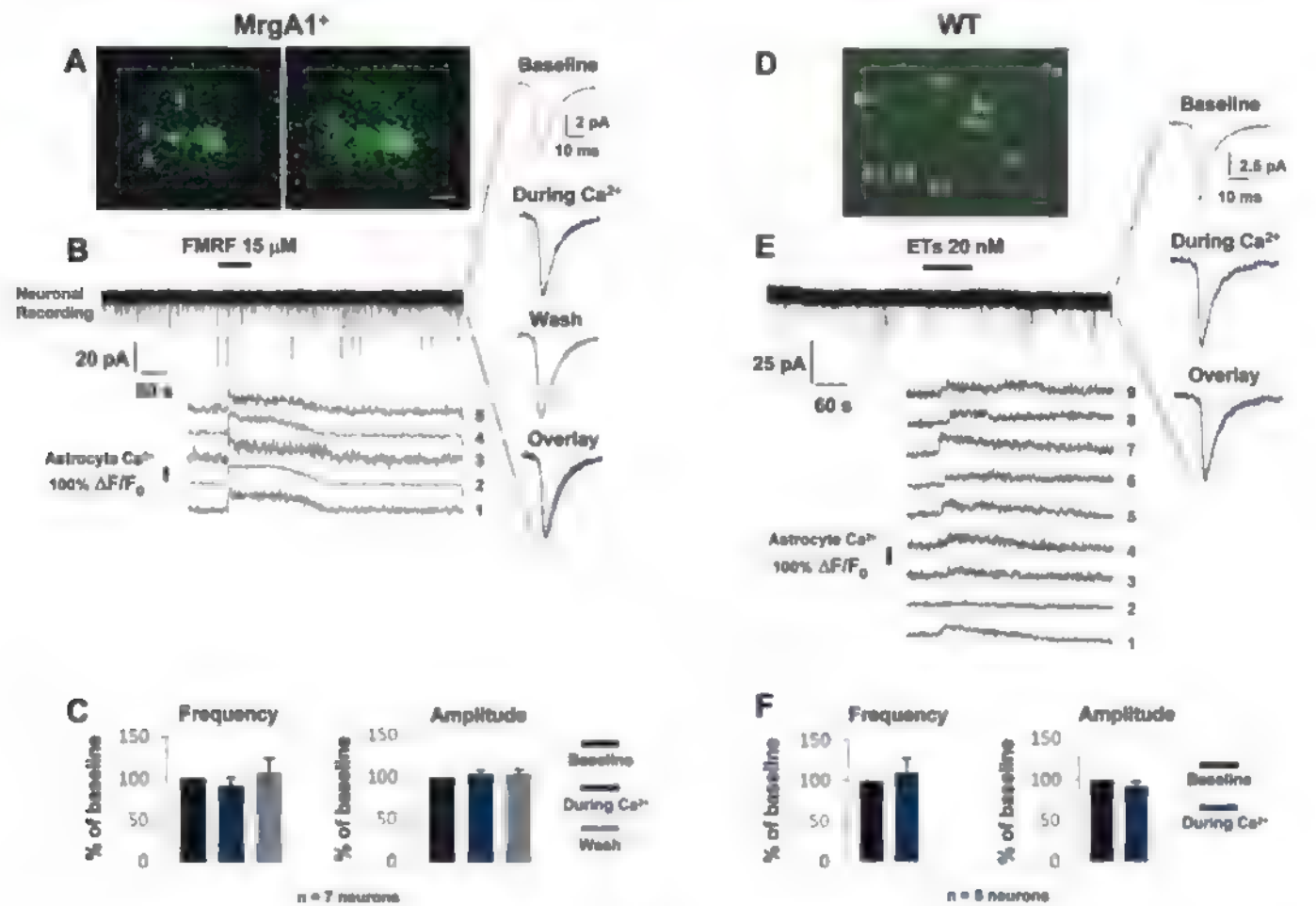

Fig. 1. Stimulation of astrocytic G_q GPCRs does not affect sEPSCs in CA1 pyramidal neurons. (**A**) Typical MrgA1$^+$ astrocyte in stratum radiatum (s.r.), filled with Oregon-Green-BAPTA-1 (OGB1), before (left) and after (right) stimulation of MrgA1Rs with FMRF (15 μM). Astrocyte Ca^{2+} responses are included as representative responses of the ~90% of responsive astrocytes within the slice and were used to monitor the beginning of Ca^{2+} elevations relative to neuronal activity. (**B** and **C**) sEPSCs frequency and amplitude remain unchanged [(B), upper] during astrocyte Ca^{2+} increases [(B), traces 1 to 5]. To the right are the averaged sEPSCs from the trace in (B). (**D**) Astrocytes (1 to 9) bulk-loaded with Ca^{2+} green 1-AM in s.r. from WT slices. (**E** and **F**) sEPSCs frequency and amplitude were unchanged during astrocyte ETR-mediated Ca^{2+} increases (ET1 and ET3, 10 nM each). Due to long-tailing ETR Ca^{2+} increases, sEPSCs were analyzed only during the first 120 s of astrocyte Ca^{2+} increases. Scale bars in (A) and (D) indicate 10 and 20 μm, respectively. Error bars indicate SEM.

stimulated with FMRF (137.97 ± 5.58%, n = 14 slices) or WT slices stimulated with ETs (133.13 ± 7.62%, n = 9), respectively, were no different from LTP magnitudes obtained in matching controls (Fig. 3, E and F, and SOM text S11, $P > 0.05$). Furthermore, PTP was also not affected (Fig. 3, E and F, and SOM text S11, $P > 0.05$).

Next, we examined whether the obliteration of astrocytic G_q GPCR Ca^{2+} signaling would affect basal synaptic transmission as well as PTP and LTP. No significant difference was found in I/O curves performed in IP_3R2 KO versus WT littermate control mice (Fig. 3G, IP_3R2 KO, n = 21; WT, n = 18; P = 0.94). These results indicate that both the pre- and postsynaptic responses, and thus the basal SC-evoked synaptic transmission, are intact in IP_3R2 KO mice, even though astrocytes are completely incapable of producing G_q GPCR Ca^{2+} elevations. No significant alteration in PTP and LTP was detected between IP_3R2 KO and control mice, demonstrating that astrocytic G_q GPCR–mediated Ca^{2+} signaling does not account for a tonic form nor an activity-induced form of short- and long-term synaptic plasticity (Fig. 3H and SOM text S12, IP_3R2 KO, n = 10; WT, n = 8, $P > 0.05$). To validate these IP_3R2 KO data, we showed that the LTP stimulation protocol used is sufficient to induce Ca^{2+} increases in astrocytes from WT slices (fig. S3). Finally, we also found that stimulating or removing astrocytic G_q GPCR Ca^{2+} signaling in MrgA1$^+$ or IP_3R2 KO mice, respectively, does not significantly alter LTP and PTP induced by theta-burst stimulation (SOM text S13).

Previous studies have demonstrated that activation of synaptic group I mGluRs, A_1Rs, or NMDARs depotentiates LTP at SC-CA1 synapses (*23*, *27*). These three receptors have all been reported to be the targets of astrocytic Ca^{2+}–dependent sources of glutamate or adenosine triphosphate (ATP)/adenosine under certain conditions (*12*). To further test whether astrocytic G_q GPCR Ca^{2+} signaling is sufficient to induce gliotransmitter release to affect synaptic transmission through the activation of synaptic mGluRs, A_1Rs, or NMDARs, we investigated the role of astrocyte Ca^{2+} signaling in the maintenance of LTP. Fifty minutes after LTP induction, astrocyte Ca^{2+} increases were elicited by applications of FMRF to MrgA1$^+$ slices or of ETs to WT slices. This did not lead to a significant change in the slope of fEPSPs (Fig. 4, A, B, and D, and SOM text S14, n = 9 MrgA1$^+$ slices, n = 16 WT slices, $P > 0.05$). As a positive control for agonist-induced depotentiation, we applied (RS)-3,5-dihydroxyphenylglycine (DHPG, 50 μM), which exerted a significant depotentiation of the slope in all slices tested (Fig. 4, A and D; MrgA1$^+$, 74.82 ± 3.45%, n = 12, $P <$

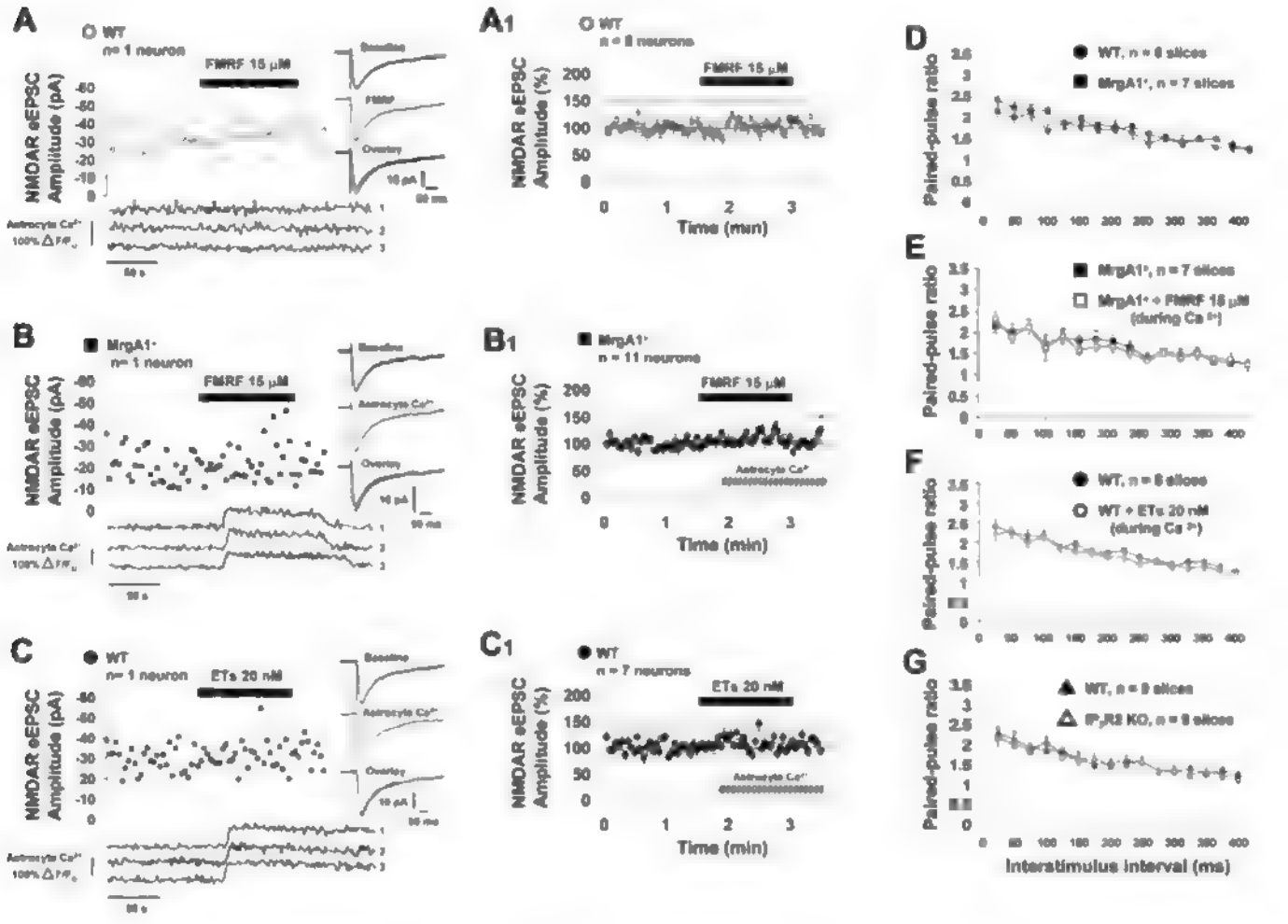

Fig. 2. Astrocytic G_q GPCR Ca^{2+} signaling does not modulate the NMDA eEPSC peak amplitude or PPF in CA1 pyramidal neurons. (**A** and **A1**) WT astrocytes were not activated by FMRF [(A) lower Ca^{2+} traces from three astrocytes surrounding recorded neuron]. FMRF did not nonspecifically affect NMDA eEPSC peak amplitude in WT mice. Representative example (A) and pooled data (A1). (**B**, **B1**, **C**, and **C1**) Activation of MrgA1$^+$ (B and B1) or WT astrocytes (C and C1) by FMRF or ETs, respectively, did not affect NMDA eEPSC peak amplitude. (**D**) MrgA1R expression in astrocytes of MrgA1$^+$ mice did not have a nonspecific effect on PPF ratio compared with WT littermate mice. (**E** and **F**) PPF ratios in MrgA1$^+$ slices before (solid squares) and during (open squares) FMRF-evoked astrocyte Ca^{2+} elevations (E) or in WT slices before (solid circles) and during (open circles) ET-evoked astrocyte Ca^{2+} increases (F) were not significantly different. (**G**) PPF is not altered in IP_3R2 KO mice compared with WT littermate control mice.

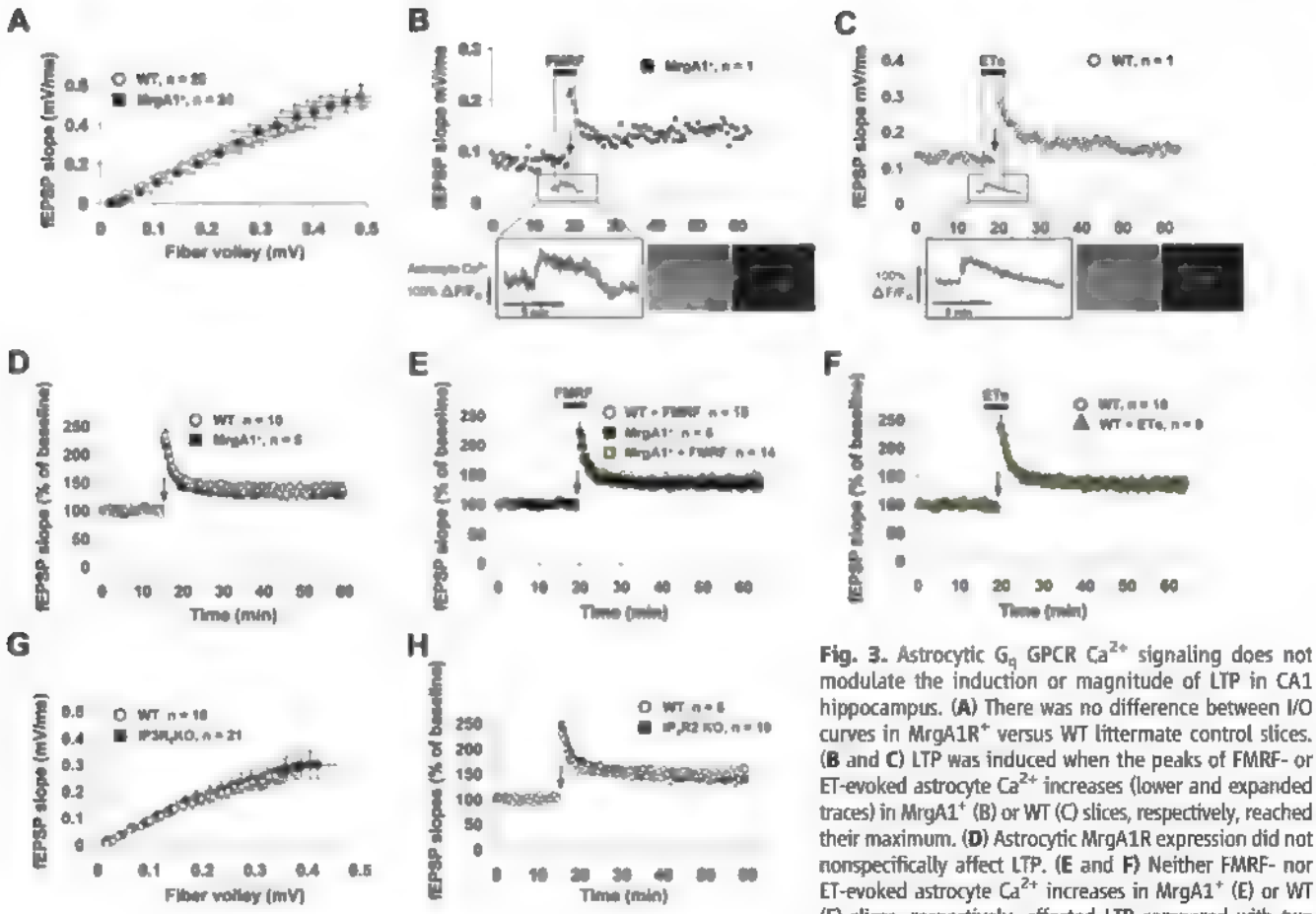

Fig. 3. Astrocytic G_q GPCR Ca^{2+} signaling does not modulate the induction or magnitude of LTP in CA1 hippocampus. (**A**) There was no difference between I/O curves in MrgA1R$^+$ versus WT littermate control slices. (**B** and **C**) LTP was induced when the peaks of FMRF- or ET-evoked astrocyte Ca^{2+} increases (lower and expanded traces) in MrgA1$^+$ (B) or WT (C) slices, respectively, reached their maximum. (**D**) Astrocytic MrgA1R expression did not nonspecifically affect LTP. (**E** and **F**) Neither FMRF- nor ET-evoked astrocyte Ca^{2+} increases in MrgA1$^+$ (E) or WT (F) slices, respectively, affected LTP compared with two sets of control slices [(E), MrgA1$^+$ slices without FMRF application, WT littermate slices with FMRF application; (F), WT slices without ET application]. (**G** and **H**) I/O curves (G) and LTP (H) in IP$_3$R2 KO mice are not affected compared with WT littermate control mice. Arrows indicate LTP induction (2 × 100 Hz).

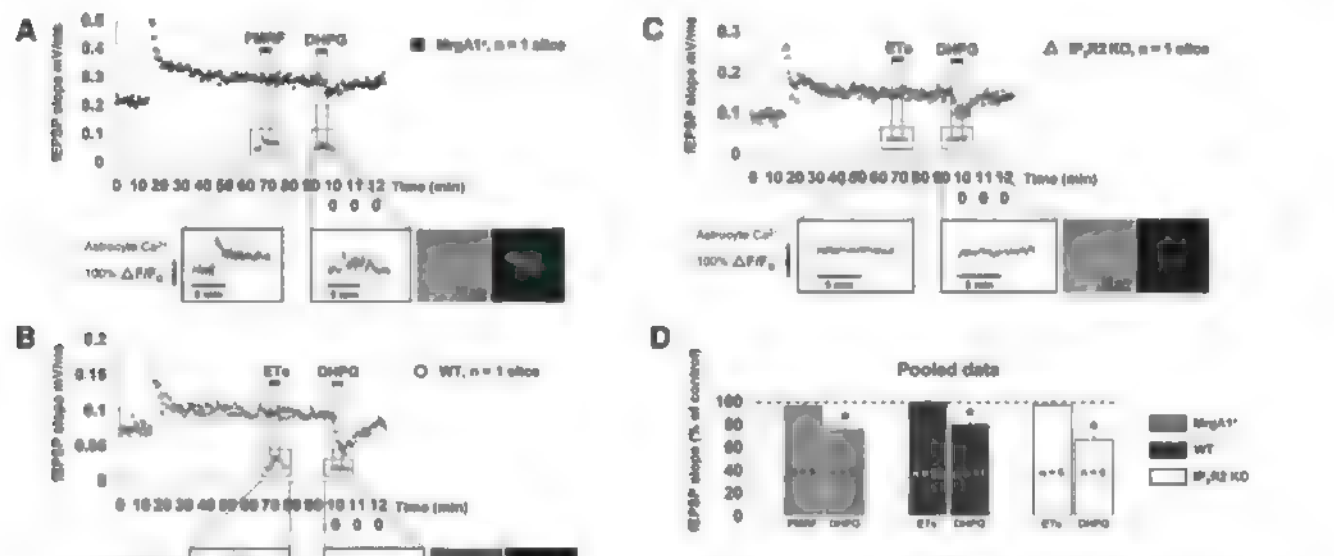

Fig. 4. Astrocytic G_q GPCR Ca^{2+} signaling does not modulate the maintenance of LTP (2 × 100 Hz) in CA1 hippocampus. (**A** and **B**) Neither FMRF- nor ET-evoked astrocyte Ca^{2+} increases (lower and expanded traces) in MrgA1$^+$ slices (A) or WT slices (B), respectively, modulated the maintenance of LTP. As a control for modulation of LTP maintenance, DHPG (50 μM) was applied. (**C**) ETs and DHPG did not evoke any astrocyte Ca^{2+} increases in IP$_3$R2 KO slices. Whereas ETs did not modulate the maintenance of LTP, DHPG induced a clear depotentiation independent of astrocyte Ca^{2+} elevations. (**D**) Summary histogram showing that DHPG, but not FMRF or ETs, affected the maintenance of LTP in MrgA1$^+$, WT, or IP$_3$R2 KO slices. Asterisks indicate statistical significance ($P < 0.0001$).

0.0001; Fig. 4, B and D; WT, 79.54 ± 2.03%, n 11, $P < 0.0001$). To address the possibility that the DHPG-mediated depotentiation could be due in part to astrocyte Ca^{2+}, we performed the same experiments using IP_3R2 KO mice. The magnitude of DHPG-induced depotentiation in IP_3R2 KO slices was not only significant ($P < 0.0001$), it was also similar to the magnitude of depotentiation that was recorded in WT littermate slices ($P = 0.43$), indicating that depotentiation does not rely, even in part, on Ca^{2+}-dependent gliotransmitter release from astrocytes (Fig. 4, C and D; IP_3R2 KO, 66.95 ± 2.79%, $n = 6$, WT, 72.70 ± 5.72%, $n = 8$). These results demonstrate and confirm previous data that DHPG-induced modulation of neuronal activity (*28*, *29*), such as depotentiation (*26*), is due to the direct action of DHPG on neuronal group I mGluRs (*26*), and not to astrocytic group I mGluR-mediated Ca^{2+} elevations and putative gliotransmitter release.

We provide here strong evidence that G_q GPCR Ca^{2+} signaling in astrocytes does not affect spontaneous and evoked excitatory action potential (AP)-mediated synaptic transmission or short- and long-term plasticity at the SC-CA1 synapse. We used two molecular tools (the MrgA1$^+$ and IP_3R2 KO mouse models), as well as the activation of endogenous astrocytic G_q GPCRs, to manipulate Ca^{2+} in astrocytes. A battery of eight electrophysiological protocols (sEPSCs, NMDA eEPSCs, evoked AMPA fEPSPs, I/O curves, PPF, PTP, and two forms of LTP) were studied, all of which point to a lack of modulation of excitatory AP-mediated synaptic transmission by astrocytic G_q GPCR Ca^{2+} signaling. The most logical conclusion from the present analysis is that astrocytic G_q GPCRs and Ca^{2+} signaling activity are not tied to the release of gliotransmitters affecting synaptic transmission or short and long-term plasticity. Therefore, our results suggest that gliotransmission reflects the pharmacological approaches that were used in previous studies (*3*, *10*, *12*) and, at least within the hippocampus, does not occur when the endogenous regulators of astrocyte Ca^{2+}, the G_q GPCRs, or the IP_3R2 themselves are stimulated or inactivated in a cellular-selective manner. These findings suggest that the mechanisms of gliotransmitter release should be reconsidered. These results have profound implications for our understanding of synaptic transmission and should affect the interpretation of a broad range of findings. Thus, the purpose of neuron-to-astrocyte G_q GPCR Ca^{2+} signaling in neurophysiology remains an open question.

References and Notes

1. X. Wang *et al.*, *Nat. Neurosci.* **9**, 816 (2006).
2. J. T. Porter, K. D. McCarthy, *J. Neurosci.* **16**, 5073 (1996).
3. M. C. Angulo, A. S. Kozlov, S. Charpak, E. Audinat, *J. Neurosci.* **24**, 6920 (2004).
4. T. Fellin *et al.*, *Neuron* **43**, 729 (2004).
5. C. J. Lee *et al.*, *J. Physiol.* **581**, 1057 (2007).
6. M. Navarrete, A. Araque, *Neuron* **57**, 883 (2008).
7. L. Pasti, A. Volterra, T. Pozzan, G. Carmignoto, *J. Neurosci.* **17**, 7817 (1997).
8. G. Perea, A. Araque, *J. Neurosci.* **25**, 2192 (2005).
9. E. Shigetomi, D. N. Bowser, M. V. Sofroniew, B. S. Khakh, *J. Neurosci.* **28**, 6659 (2008).
10. G. Perea, A. Araque, *Science* **317**, 1083 (2007).
11. A. Serrano, N. Haddjeri, J. C. Lacaille, R. Robitaille, *J. Neurosci.* **26**, 5370 (2006).
12. C. Agulhon *et al.*, *Neuron* **59**, 932 (2008).
13. T. A. Fiacco *et al.*, *Neuron* **54**, 611 (2007).
14. T. A. Fiacco, C. Agulhon, K. D. McCarthy, *Annu. Rev. Pharmacol. Toxicol.* **49**, 151 (2009).
15. N. X. Tritsch, D. E. Bergles, *Neuron* **54**, 497 (2007).
16. J. Petravicz, T. A. Fiacco, K. D. McCarthy, *J. Neurosci.* **28**, 4967 (2008).
17. X. Li, A. V. Zima, F. Sheikh, L. A. Blatter, J. Chen, *Circ. Res.* **96**, 1274 (2005).
18. Y. Sasaki *et al.*, *J. Neurochem.* **68**, 2194 (1997).
19. M. Andersson, F. Blomstrand, E. Hanse, *J. Physiol.* **585**, 843 (2007).
20. T. A. Fiacco, K. D. McCarthy, *J. Neurosci.* **24**, 722 (2004).
21. O. Pascual *et al.*, *Science* **310**, 113 (2005).
22. R. S. Zucker, *Neuron* **17**, 1049 (1996).
23. H. J. Chung *et al.*, *Proc. Natl. Acad. Sci. U.S.A.* **106**, 635 (2009).
24. C. C. Huang, Y. C. Liang, K. S. Hsu, *J. Biol. Chem.* **276**, 48108 (2001).
25. R. Li, F. S. Huang, A. K. Abbas, H. Wigström, *BMC Neurosci.* **8**, 55 (2007).
26. W. M. Zho, J. L. You, C. C. Huang, K. S. Hsu, *J. Neurosci.* **22**, 8838 (2002).
27. Y. Izumi, C. F. Zorumski, *J. Neurosci.* **28**, 9557 (2008).
28. G. Mannaioni, M. J. Marino, O. Valenti, S. F. Traynelis, P. J. Conn, *J. Neurosci.* **21**, 5925 (2001).
29. M. G. Rae, A. J. Irving, *Neuropharmacology* **46**, 1057 (2004).

30. We thank K. Casper for making MrgA1$^+$ mice; J. Chen for providing IP_3R2 KO mice; and B. Djukic, B. Philpot, A. Roberts, and J. de Marchena for valuable help and discussions. This work was supported by NIH grants NS033938 and NS020212.

Supporting Online Material

www.sciencemag.org/cgi/content/full/327/5970/1250/DC1
Materials and Methods
SOM Text S1 to S14
Figs. S1 to S3
References
Movie S1

17 November 2009; accepted 19 January 2010
10.1126/science.1184821

RTEL-1 Enforces Meiotic Crossover Interference and Homeostasis

Jillian L. Youds,[1] David G. Mets,[2] Michael J. McIlwraith,[3] Julie S. Martin,[1] Jordan D. Ward,[1]* Nigel J. O'Neil,[4] Ann M. Rose,[4] Stephen C. West,[3] Barbara J. Meyer,[2] Simon J. Boulton[1]†

Meiotic crossovers (COs) are tightly regulated to ensure that COs on the same chromosome are distributed far apart (crossover interference, COI) and that at least one CO is formed per homolog pair (CO homeostasis). CO formation is controlled in part during meiotic double-strand break (DSB) creation in *Caenorhabditis elegans*, but a second level of control must also exist because meiotic DSBs outnumber COs. We show that the anti-recombinase RTEL-1 is required to prevent excess meiotic COs, probably by promoting meiotic synthesis-dependent strand annealing. Two distinct classes of meiotic COs are increased in *rtel-1* mutants, and COI and homeostasis are compromised. We propose that RTEL-1 implements the second level of CO control by promoting noncrossovers.

Homologous recombination repair of meiotic DNA double-strand breaks (DSBs) is regulated to ensure the correct number and placement of meiotic crossovers (COs). One CO per chromosome ensures that homologous chromosomes are held together, can orient toward opposite spindle poles, and thereby segregate correctly at the first meiotic division. Crossover interference (COI) ensures appropriate distribution of COs among chromosomes because the formation of one CO reduces the likelihood of other COs occurring nearby. Meiotic COI is "complete" in *Caenorhabditis elegans*: Only a single CO occurs on each chromosome (*1*, *2*). COI is regulated in part by the condensin I complex, which limits meiotic DSB formation (*3*). Because the average number of meiotic DSBs per chromosome is 2.1 (*3*), and only one of these is repaired as a CO, a second tier of CO control must exist downstream of meiotic DSB formation that channels about half of all DSBs into noncrossovers (NCOs). However, the proteins involved in generating a meiotic CO versus NCO are not well understood.

Human RTEL1 (and *C. elegans* RTEL-1, by homology) negatively regulates recombination by disassembling D loop–recombination intermediates during DNA repair (*4*). If RTEL1 acts similarly on meiotic recombination intermediates, it could be the key protein required to execute NCOs by promoting meiotic synthesis-dependent strand annealing (SDSA). By genetic measurements, recombination in *C. elegans rtel-1* mutants was significantly increased in five genetic intervals on three chromosomes, including both chromosome center and arm regions (Fig. 1A and table S1).

[1]DNA Damage Response Laboratory, London Research Institute, Cancer Research UK, Clare Hall, South Mimms, EN6 3LD, UK. [2]Howard Hughes Medical Institute, Department of Molecular and Cell Biology, University of California at Berkeley, Berkeley, CA 97420, USA. [3]Genetic Recombination Laboratory, London Research Institute, Cancer Research UK, Clare Hall, South Mimms, EN6 3LD, UK. [4]Department of Medical Genetics, Faculty of Medicine, University of British Columbia, Vancouver, BC, V6T 1Z4, Canada.

*Present address: Department of Cellular and Molecular Pharmacology, University of California, San Francisco, San Francisco, CA, 94518–2517, USA.
†To whom correspondence should be addressed. E-mail: simon.boulton@cancer.org.uk

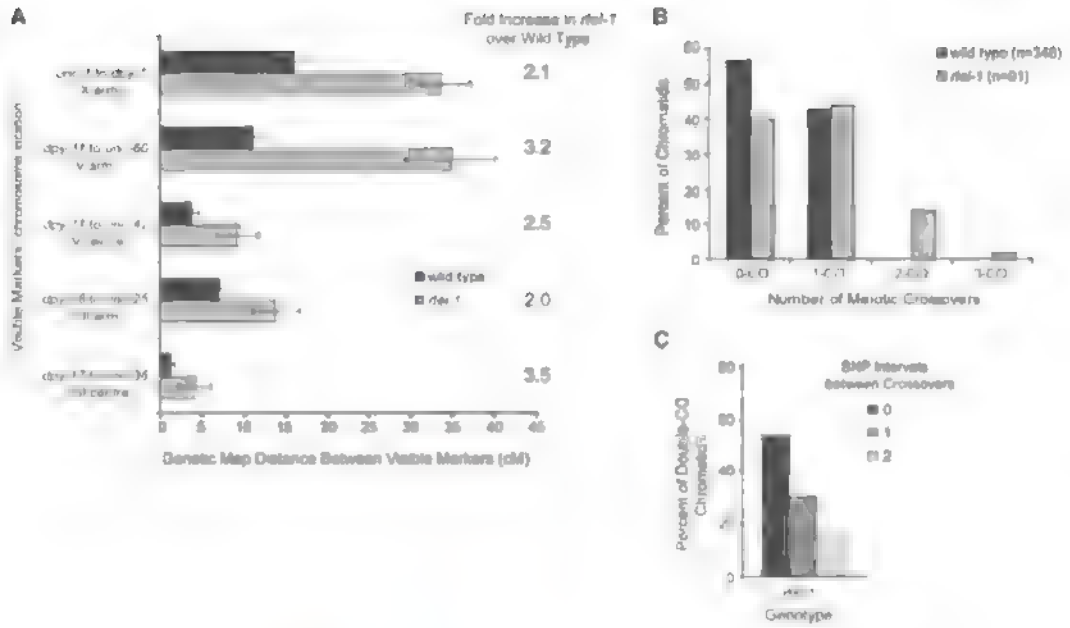

Fig. 1. Recombination is increased in multiple chromosomal regions in *rtel-1* mutants. **(A)** Recombination as measured by genetic map distance (in centimorgans) between pairs of marker genes in wild-type and *rtel-1* mutants. Error bars are 95% CI. **(B)** Percentage of total chromatids (*n*) with no CO or single, double, or triple COs in wild-type and *rtel-1* mutants. **(C)** Number of SNP intervals occurring between COs on double-CO chromatids.

(*4*, *5*). We used five snip–single-nucleotide polymorphisms (snip-SNPs) distributed along 80% of the X chromosome to track recombination events (Fig. 2B). Of wild-type chromatids, 43% had a single CO, and no double COs were observed, as expected (*3*) (Fig. 1B) [normally, 50% of chromatids have a single CO, as one CO occurs per homolog pair (*6*)]. In *rtel-1* mutants, single, double, and triple CO chromatids occurred at a frequency of 44, 14, and 2%, respectively (Figs. 1B and 2B). The number of chromatids with COs in *rtel-1* mutants was significantly different from that of wild type ($P = 1.68e^{-10}$), which indicated that complete COI is defective in the absence of RTEL-1. The 44% of single CO chromatids in *rtel-1* mutants is consistent with the observation that 38% of bivalents receive only one meiotic DSB (*3*). The number of double-CO chromatids in *rtel-1* mutants is also greater than triple-CO chromatids (Figs. 1B and 2B), consistent with the reported distribution of meiotic DSBs (*3*). Therefore, it is possible that all DSBs in *rtel-1* mutants become COs. Examination of the relative positions of COs on double-CO chromatids suggests that there is no interference between multiple COs in *rtel-1* mutants, because double COs occur in adjacent SNP intervals at a frequency that does not differ from random ($P = 1.00$) (Fig. 1C and fig. S1). This lack of interference agrees with the idea that all DSBs in *rtel-1* mutants become COs.

Condensin I complex mutants, such as *dpy-28*, alter the distribution and increase the overall number of COs that occur on each chromosome because of an increase in meiotic DSB formation (*3*, *7*). To determine whether the increased COs seen in *rtel-1* mutants reflect an elevation in recombination precursors (as does *dpy-28*), we measured the number of DSBs generated in *rtel-1* mutants using RAD-51 protein as a marker (*3*). *rtel-1* mutants had slightly more RAD-51 foci, consistent with RTEL-1 having a role in dis-

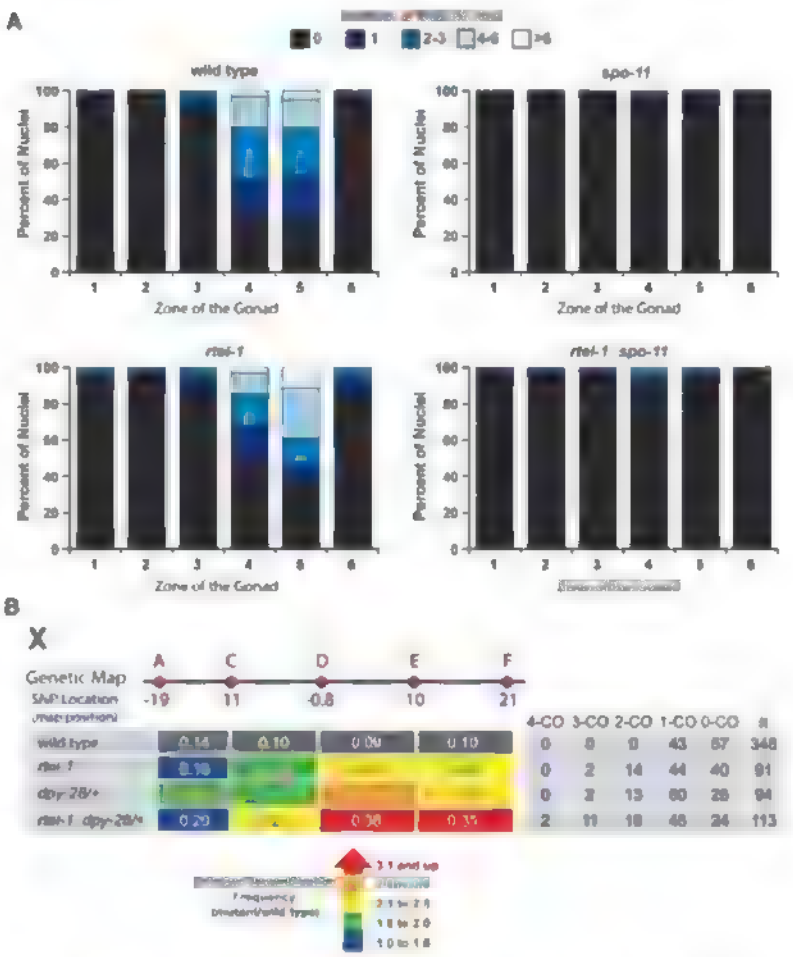

Fig. 2. DSBs are similar in wild-type and *rtel-1* mutants; *rtel-1* and *dpy-28/+* mutations have an additive effect on CO frequency. **(A)** Number of RAD-51 foci in 100 nuclei in each zone of the gonad for each genotype. Zones are as previously defined (*17*). **(B)** Recombination frequencies measured between SNPs A to C, C to D, D to E, and E to F in each genotype. Relative recombination frequencies in each mutant compared with wild type are by color: blue, 1.0- to 1.5-fold; green, 1.6- to 2.0-fold; yellow, 2.1- to 2.5-fold; orange, 2.6- to 3.0-fold; and red, 3.1-fold increase or greater. The table at right shows the percentage of total chromatids (*n*) with no COs or single, double, triple, or quadruple COs.

assembling unstable D loop–repair intermediates (*4*). The distribution of RAD-51 foci in *rtel-1* mutants, as well as dependence on the DSB formation protein SPO-11, was similar to that of wild type (Fig. 2A and fig. S2). Meiotic DSB formation was also quantified in wild-type and *rtel-1* mutants subject to RNA interference (RNAi) with *rad-54*, which stalls recombination intermediates after RAD-51 loading in yeast (*8*) and *C. elegans* (*3*). No significant difference in RAD-51 foci was observed in *rad-54* RNAi treated wild-type and *rtel-1* mutants (average wild type, 11.8 ± 3.2 SD; *rtel-1*, 12.2 ± 4.1 SD). Elevated levels of meiotic DSBs generated in the *dpy-28* mutant are sufficient to partially rescue *him-17* mutants, which are deficient in meiotic DSB formation (*7*). Combining the *rtel-1* mutation with either the *spo-11* or *him-17* mutations did not rescue the *spo-11* or *him-17* mutant phenotypes (fig. S3). Unlike *dpy-28* mutants, the elevated COs in *rtel-1* mutants cannot be explained by an increase in CO precursors, which suggests a breakdown at a second level of CO control distinct from DSB formation.

Because RTEL-1 and DPY-28 appear to control CO formation by different means, we examined the effect on recombination of combining *rtel-1* and *dpy-28* mutations. In *dpy-28(s939)/+* mutants, 60, 13, and 2% of chromatids showed single, double, and triple COs, respectively (*3*) (Fig. 2B). When *rtel-1* mutation was combined with *dpy-28(s939)/+*, quadruple COs were observed in 2% of *rtel-1, dpy-28/+* mutant chromatids (but were not observed in either single mutant), and 45, 18, and 11% of *rtel-1, dpy-28/+* mutant chromatids had single, double, and triple COs, respectively (Fig. 2B). Furthermore, 44% of the total measured intervals had a CO in *rtel-1; dpy-28/+* animals, whereas 32% had a CO in *dpy-28 +*, and 25% had a CO in *rtel-1* mutants. In the *rtel-1; dpy-28/+* mutant, the total CO frequency was significantly different from that of either single mutant ($P = 0.00014$ for *rtel-1* versus *rtel-1, dpy-28*; $P = 0.0097$ for *dpy-28/+* versus *rtel-1, dpy-28 +*). Double COs in *rtel-1; dpy-28/+* double mutants occurred in adjacent SNP intervals at a frequency that did not differ from random ($P = 0.824$), which suggested no residual interference (fig. S1). These data indicate an additive effect of combining *dpy-28/+* and *rtel-1* mutations on meiotic CO frequency, which supports the hypothesis that RTEL-1 and DPY-28 regulate CO formation through distinct mechanisms. These data also reinforce the idea that all DSBs are converted to COs in the absence of RTEL-1.

Meiotic CO homeostasis in yeast maintains COs at the expense of NCOs under conditions where meiotic DSBs are decreased (*9*, *10*). Conversely, beyond the single "obligate" CO per chromosome, most extra DSBs in *C. elegans* appear to be channeled into NCO pathways, such as SDSA. Given that mutation in *dpy-28* causes an increase in meiotic DSBs (*3*, *7*), the additive effect of *rtel-1* and *dpy-28* mutations on meiotic CO frequency suggested that RTEL-1 may function to maintain homeostasis when there are extra DSBs. If additional meiotic DSBs generated by treatment with ionizing radiation (IR) are repaired predominantly through CO pathways in *rtel-1* mutants, this would lead to increased numbers of COs. Treating *rtel-1* mutants with 10 or 75 Gy of IR resulted in a large, dose-dependent increase in COs, up to 6.7-fold over untreated wild-type animals in the intervals measured, whereas relatively small increases in recombination were observed in wild-type animals after IR (Fig. 3A, fig. S2, and table S2). These data indicate that homeostasis is compromised in the absence of RTEL-1.

During *C. elegans* meiosis, the ZHP-3 protein becomes restricted to recombination foci: one focus per chromosome and six spots per nucleus are observed in wild type (*11*). In wild-type nematodes, only 1% of nuclei had greater than six ZHP-3::GFP (ZHP-3 marked with green fluorescent protein) foci, whereas in *rtel-1* mutants, 18% of nuclei had more than six ZHP-3 foci (Fig. 3, B and C). This was a significant, but relatively small, increase compared with the increased COs observed by our genetic and snip-SNP methods.

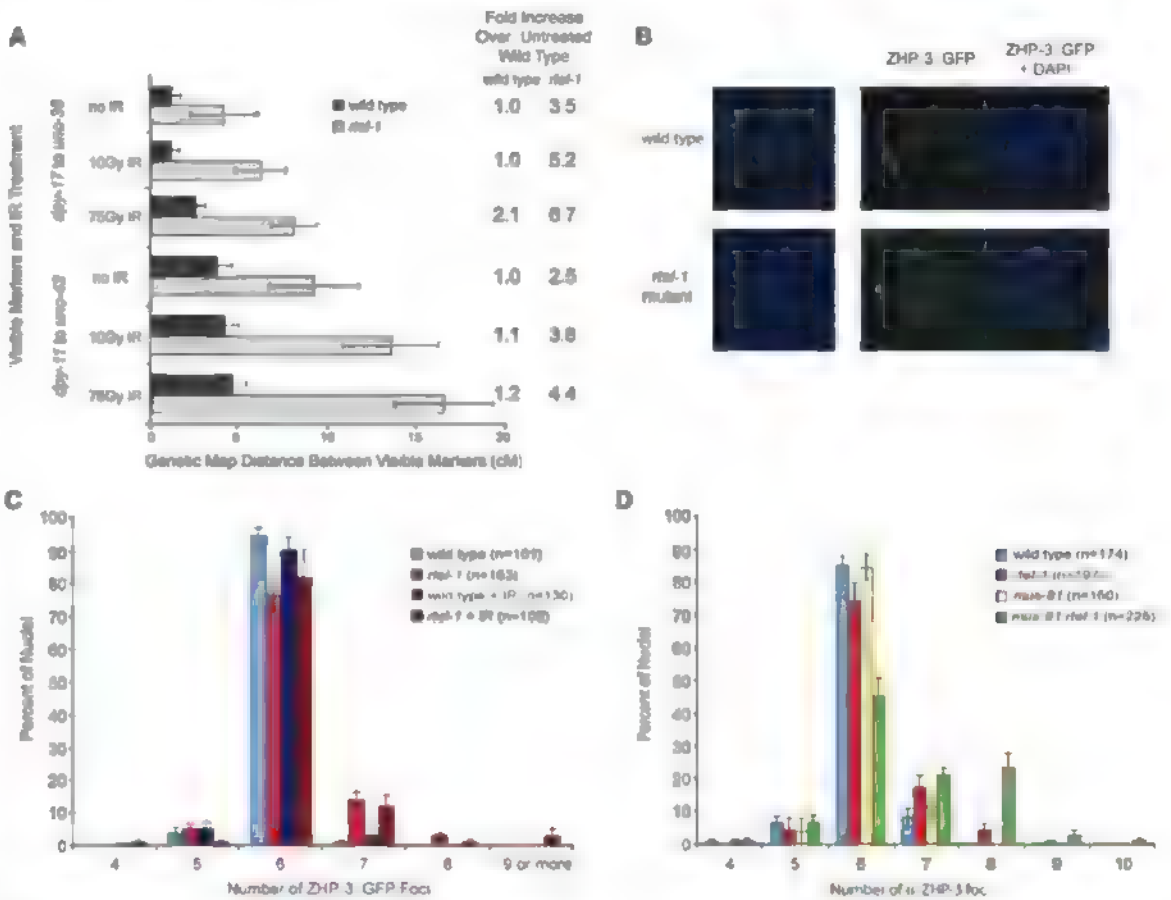

Fig. 3. Recombination increases greatly in *rtel-1* mutants after IR treatment but ZHP-3::GFP foci do not; ZHP-3 foci are increased in *mus-81 rtel-1* mutants. **(A)** Recombination as measured by genetic map distance between pairs of marker genes for two intervals with no IR or 10 or 75 Gy IR in wild-type and *rtel-1* mutants. Fold increase in recombination is compared with untreated wild type. Error bars are 95% CI. **(B)** ZHP-3::GFP foci (green) and 4′,6′-diamidino-2-phenylindole (DAPI)–stained (blue) in wild-type and *rtel-1* mutants at meiotic diplotene. **(C)** Percentage of total nuclei (*n*) with the indicated number of ZHP-3::GFP foci in wild-type and *rtel-1* mutants without treatment and 24 hours after 75 Gy IR. Error bars are SEM. **(D)** Percentage of total nuclei (*n*) with the indicated number of anti–ZHP-3 foci in each genotype. Error bars are SEM.

As recombination greatly increases in *rtel-1* mutants after IR, if ZHP-3 marks all COs, a large increase in ZHP-3 foci should occur after 75 Gy IR. However, ZHP-3 foci remained unchanged in wild-type animals and *rtel-1* mutants after IR (Fig. 3C) [supporting online material (SOM) text]. These data support the hypothesis that ZHP-3 marks only a subset of COs and imply that two classes of meiotic CO events are elevated in *rtel-1* mutants.

In *Saccharomyces cerevisiae*, two classes of COs exist: (i) Those that predominate are dependent on the ZMM proteins (Zip1-4, Mer3, Msh4, and Msh5) and exhibit COI; and (ii) a second class includes those that are independent of the ZMMs, require Mms4 and Mus81, and do not exhibit COI (*12*, *13*). Until now, *C. elegans* was thought to have only class I COs (*14*, *15*). We found COs in the *rtel-1* mutant to fall into two classes: ZHP-3–associated obligate-type COs and COs produced by repair events not associated with ZHP-3 occurring in the absence of RTEL-1. A reliance of COs not associated with ZHP-3 on MUS-81 in *rtel-1* mutants is consistent with the synthetic embryonic lethality of *mus-81 rtel-1* double mutants (*4*). Excess COs generated in wild type after x-ray are similarly dependent on MUS-81 (fig. S4 and SOM text). In *mus-81 rtel-1* double mutants, RAD-51 foci persist (*4*), and ZHP-3 restriction to foci is delayed or does not occur in 65% of nuclei (SOM text), which suggests defects in intermediate processing that may account for the synthetic lethality. In double-mutant nuclei where ZHP-3 foci are observed, foci are increased compared with wild type and with either single mutant (Fig. 3D and SOM text), which indicates that more obligate-type COs are formed in the absence of both RTEL-1 and MUS-81 (fig. S7).

NCO repair of meiotic DSBs in *S. cerevisiae* is thought to occur mainly through the SDSA pathway (*16*). A key step in SDSA is the disruption of the D loop joint molecule. Human RTEL1 can disrupt a preformed D loop in vitro, but the mechanism of RTEL1 action is not well understood (*4*). We considered whether D loop unwinding might require species-specific interactions with RAD51. However, RTEL1 efficiently disrupted D loops preformed by using the *E. coli* RAD51 homolog RecA and single-stranded DNA (ssDNA) binding protein SSB (fig. S5). To determine whether RTEL1 exhibits structural preference for D loops, we generated three substrates: a 3′ ssDNA invasion with a 5′ overhang, a 5′ ssDNA invasion with a 3′ overhang, and a substrate with no overhang. When incubated with RAD51 and replication protein A (RPA), RTEL1 preferentially disrupted the 3′ invasion D loop but showed negligible activity toward D loop substrates with either 5′ invasion or no overhang (Fig. 4, A to C, and fig. S6). Efficient unwinding of the 3′ invasion D loop required incubation with RPA (Fig. 4D). Thus, RTEL1 activity in vitro is consistent with a role in displacing transient strand invasion events in vivo. Taken together, our data support a role for RTEL-1 in meiotic SDSA that enforces COI by preventing further DSBs (beyond the obligate CO) from becoming COs.

In summary, our data support the hypothesis that RTEL-1 regulates meiotic recombination and CO homeostasis in *C. elegans* by physically dissociating strand invasion events and thereby promotes NCO repair by meiotic SDSA (fig. S7). Two levels of meiotic CO control have now been identified in *C. elegans*: regulation of DSB

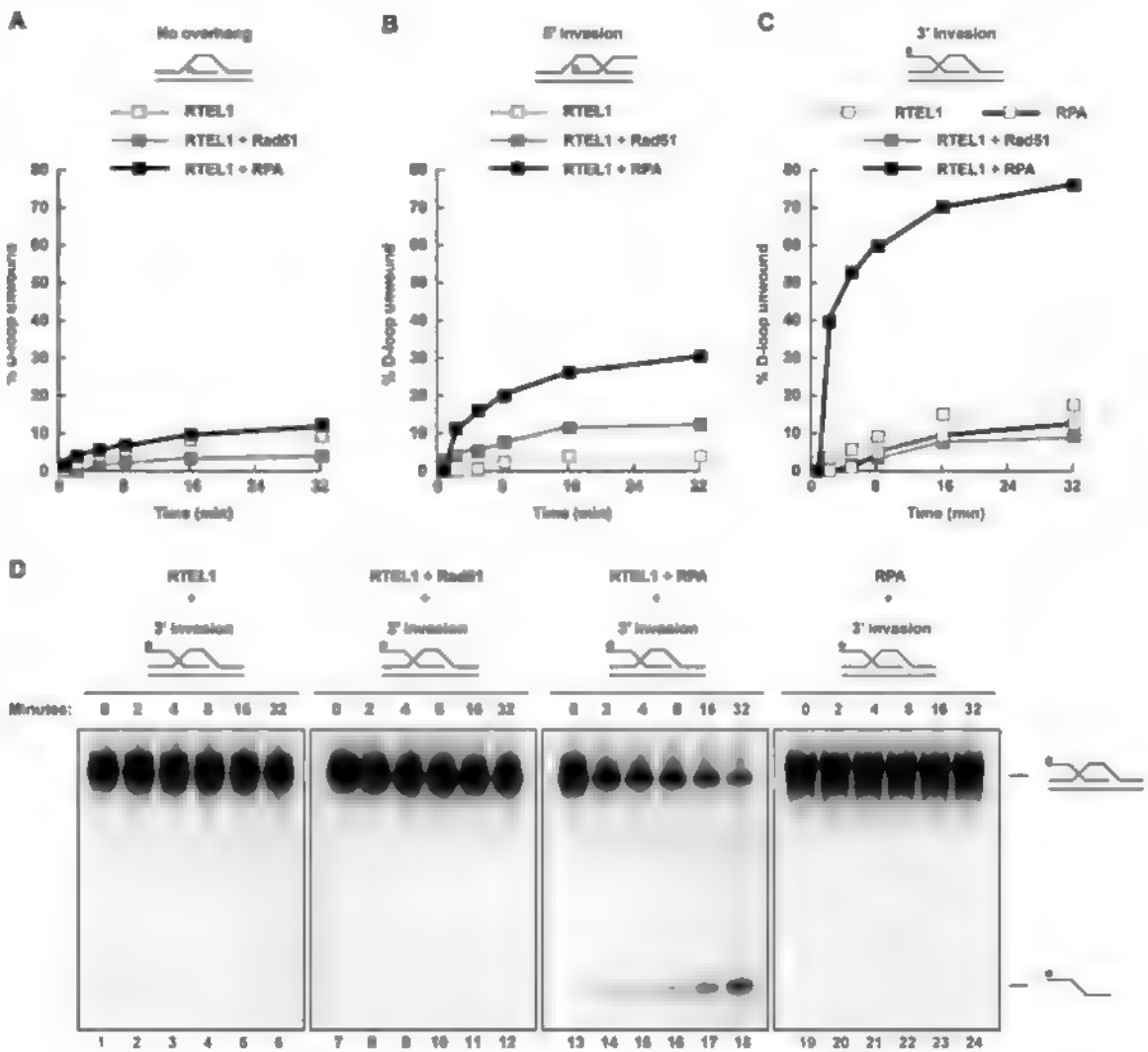

Fig. 4. RTEL1 preferentially dissociates D loops with 3′ invasion and is dependent on RPA. D loop substrates with (**A**) no overhang, (**B**) 5′ invasion, or (**C**) 3′ invasion. Shown is quantification of the percentage of D loop unwound over time. (**D**) Time course of RTEL1 activity toward a D loop substrate with 3′ invasion alone or with the indicated proteins. The fastest migrating band is the displaced radiolabeled (*) ssDNA probe; the slower species is the D loop substrate.

number and distribution by the condensin I complex (*3*) and execution of NCOs by RTEL-1

References and Notes

1. K. J. Hillers, A. M. Villeneuve, *Curr. Biol.* **13**, 1641 (2003)
2. W. Wood, *The Nematode Caenorhabditis elegans* (Cold Spring Harbor Laboratory Press, Cold Spring Harbor, NY, 1988)
3. D. G. Mets, B. J. Meyer, *Cell* **139**, 73 (2009)
4. L. J. Barber *et al.*, *Cell* **135**, 261 (2008)
5. Materials and methods are available as supporting material on *Science* Online
6. P. M. Meneely, A. F. Farago, T. M. Kauffman, *Genetics* **162**, 1169 (2002)
7. C. J. Tsai *et al.*, *Genes Dev.* **22**, 194 (2008)
8. B. O. Krogh, L. S. Symington, *Annu. Rev. Genet.* **38**, 233 (2004)
9. E. Martini, R. L. Diaz, N. Hunter, S. Keeney, *Cell* **126**, 285 (2006)
10. S. Y. Chen *et al.*, *Dev. Cell* **15**, 401 (2008)
11. N. Bhalla, D. J. Wynne, V. Jantsch, A. F. Dernburg, *PLoS Genet.* **4**, e1000235 (2008)
12. D. K. Bishop, D. Zickler, *Cell* **117**, 9 (2004)
13. N. M. Hollingsworth, S. J. Brill, *Genes Dev.* **18**, 117 (2004)
14. T. Garcia-Muse, S. J. Boulton, *Chromosome Res.* **15**, 607 (2007)
15. M. Zetka, *Genome Dyn.* **5**, 43 (2009)
16. M. S. McMahill, C. W. Sham, D. K. Bishop, *PLoS Biol.* **5**, e299 (2007)
17. M. P. Colaiacovo *et al.*, *Dev. Cell* **5**, 463 (2003)

18. This work was supported by Cancer Research UK (S.J.B. and S.C.W.) and the Canadian Institute of Health Research (A.M.R.). B.J.M. is an investigator of the Howard Hughes Medical Institute.

Supporting Online Material

www.sciencemag.org/cgi/content/full/327/5970/1254/DC1
Materials and Methods
SOM Text
Figs. S1 to S7
Tables S1 and S2
References

9 October 2009; accepted 28 January 2010
10.1126/science.1183112

Spatially Ordered Dynamics of the Bacterial Carbon Fixation Machinery

David F. Savage,* Bruno Afonso,* Anna H. Chen, Pamela A. Silver†

Cyanobacterial carbon fixation is a major component of the global carbon cycle. This process requires the carboxysome, an organelle-like proteinaceous microcompartment that sequesters the enzymes of carbon fixation from the cytoplasm. Here, fluorescently tagged carboxysomes were found to be spatially ordered in a linear fashion. As a consequence, cells undergoing division evenly segregated carboxysomes in a nonrandom process. Mutation of the cytoskeletal protein ParA specifically disrupted carboxysome order, promoted random carboxysome segregation during cell division, and impaired carbon fixation after disparate partitioning. Thus, cyanobacteria use the cytoskeleton to control the spatial arrangement of carboxysomes and to optimize the metabolic process of carbon fixation.

Efficient cellular metabolism relies on the compartmentalization of enzymatic reactions. Prokaryotes achieve this organization by using capsidlike protein microcompartments to isolate metabolic pathways from the cellular milieu (*1*–*3*). The best-characterized microcompartment, the carboxysome, is found in cyanobacteria and chemoautotrophs and is responsible for catalyzing more than 40% of Earth's carbon fixation (*2*, *4*). Structurally, the carboxysome consists of an icosahedral proteinaceous shell that encloses the enzymes carbonic anhydrase and ribulose-1,5-bisphosphate carboxylase-oxygenase (RuBisCO) (*5*–*8*). The shell may act as a semipermeable barrier, allowing the passive import of the negatively charged reactants, HCO_3^- and ribulose 1,5-bisphosphate, and excluding the competing substrate O_2. Within the carboxysome, carbonic anhydrase catalyzes the production of CO_2, where it is fixed by RuBisCO into 3-phosphoglycerate. Carbon fixation is the basis of biosynthesis in cyanobacteria, and genetic disruption of the carboxysome is lethal (*9*, *10*). Thus, the proper assembly and function of carboxysomes is fundamental to carbon fixation and cellular fitness.

We developed methods to visualize carboxysomes and to investigate their dynamical behavior in living cells. The carboxysome consists of ~5000 monomers of the shell protein CcmK and ~2000 monomers of RuBisCO (*5*). Expression of these proteins in the cyanobacterium *Synechococcus elongatus* PCC7942 (hereafter *Synechococcus*) (*11*) fused to green, yellow, or cyan fluorescent protein (GFP, YFP, or CFP) yielded fluorescent particles, and the proteins colocalized when coexpressed in the same cell, which indicated assembled carboxysomes (Fig. 1A). The labeled carboxysomes also contained endogenous RuBisCO (Fig. 1B). Electron microscopy showed that all carboxysomes contain RbcL-GFP and that all RbcL-GFP was in carboxysomes (Fig. 1C). Carboxysome morphology and cellular growth rates were unaffected by YFP fusions (fig. S1).

Carboxysomes were evenly spaced along the long axis of *Synechococcus* (Fig. 2A). On average, there were 3.7 ± 1.2 carboxysomes per cell under log phase growth (Fig. 2B). We calculated the pairwise distances between carboxysomes in cells (n = 2508) with four carboxysomes (Fig. 2C). The average spacing between adjacent carboxysomes was 0.66 μm but was proportional to cell length (Fig. 2D). Thus, normalizing by cell length sharpened the pair-

Department of Systems Biology, Harvard Medical School, Boston, MA 02115, USA.

*These authors contributed equally to this work.
†To whom correspondence should be addressed. E-mail: pamela_silver@hms.harvard.edu

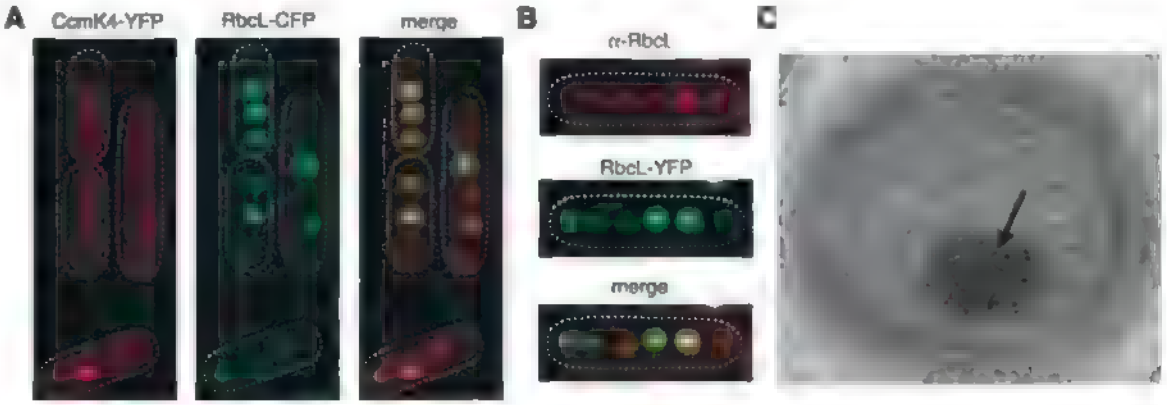

Fig. 1. The carboxysome can be fluorescently labeled. (**A**) Fluorescence colocalization of shell protein CcmK4-YFP and RuBisCO protein RbcL-CFP. (**B**) Immunofluorescence microscopy with an antibody against RuBisCO as a probe and showing RbcL-YFP colocalized to cytoplasmic RuBisCO. (**C**) Transverse cell electron micrograph showing, by means of immunogold labeling with an antibody against GFP, localization of RbcL-GFP to carboxysomes.

wise distance probability distribution (Fig. 2E). This suggested that the spacing of carboxysomes could be actively controlled.

The diffusive dynamics of individual carboxysomes over time was constrained (Fig. 3A). Carboxysomes (n = 350) had an average diffusion coefficient D of $4.58 \times 10^{-5} \pm 4.50 \times 10^{-5}$ μm²/s (Fig. 3A). Using cytoplasmic parameters (*12*) and a mean particle radius of 50 nm, we estimate a theoretical value of $D = 3.85 \times 10^{-1}$ μm²/s, four orders of magnitude greater than the observed. The measured value of D suggests that a carboxysome will diffuse an average distance r [$4 \times 4.58 \times 10^{-5}$ μm²/s × 64,800 s]^{2} = 3.45 μm during the cell cycle. Considering the displacement occurring from cell growth, the carboxysomes do not appear to be diffusing randomly.

Carboxysomes are known to associate with cellular structures, including unidentified filaments (*1*, *13*, *14*). Deletions of the five (*mreB*,

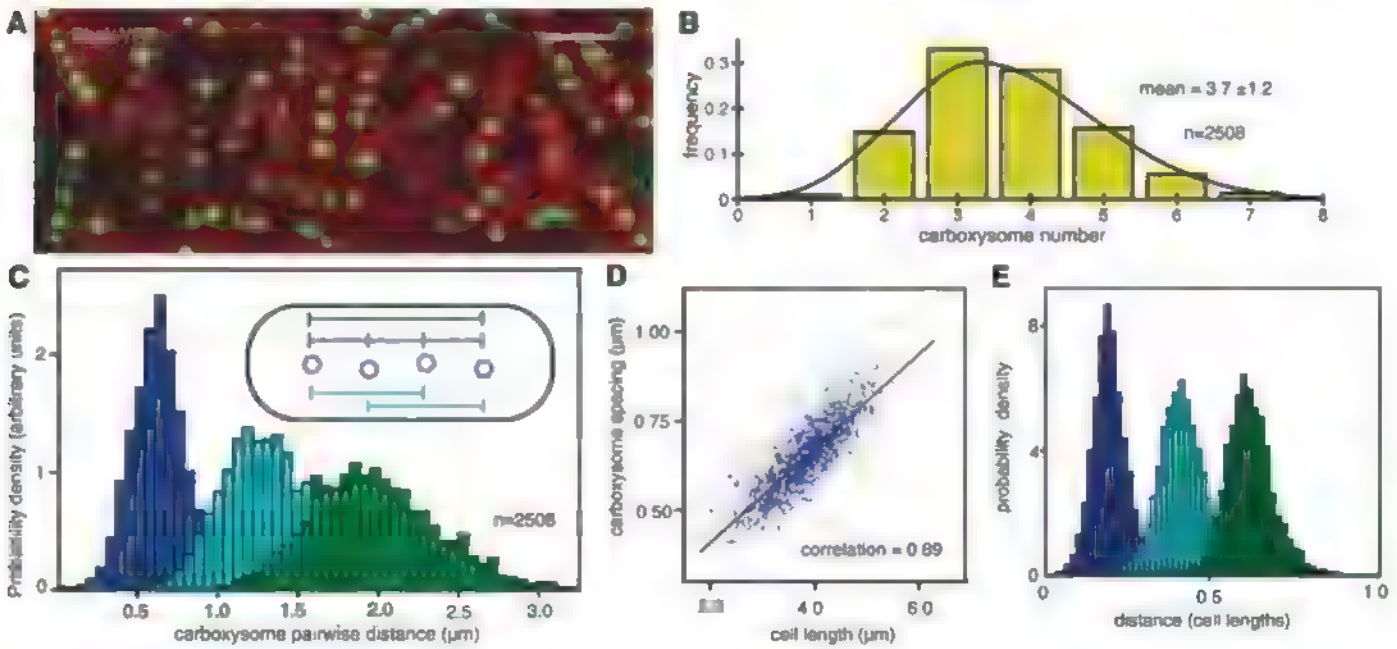

Fig. 2. Carboxysomes are spatially organized in vivo. **(A)** RbcL-YFP (green) expression shows organized carboxysomes. Thylakoid membrane fluorescence is shown in red. **(B)** Average number of carboxysomes per cell. **(C)** Pairwise distance between carboxysomes in cells with four carboxysomes. **(D)** Carboxysome spacing is proportional to cell length. **(E)** Same as (C) except carboxysome distances were normalized for cell length.

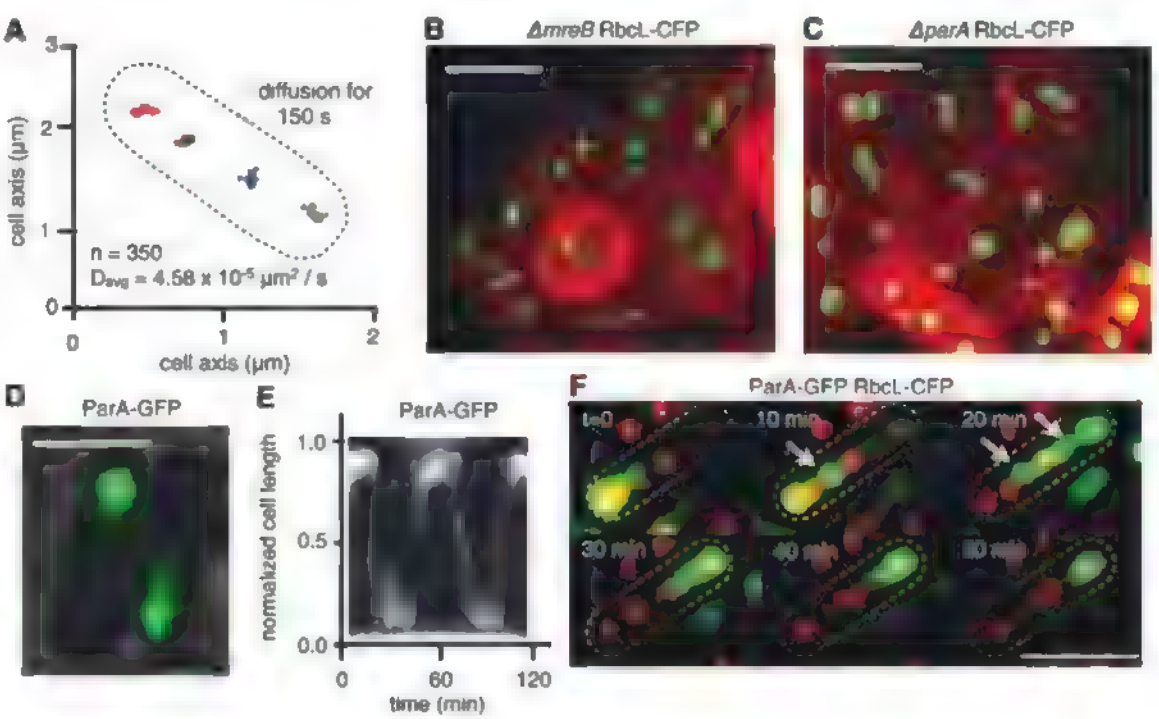

Fig. 3. Carboxysomes are organized by the cytoskeleton. **(A)** Diffusion of four tracked carboxysomes. Trajectories were used to compute D in the two-dimensional diffusion equation $\langle r^2 \rangle = 4Dt$, where t is time. **(B)** RbcL-CFP (green) in *mreB*-deficient cells showing spherical cells and loss of carboxysome spatial organization. Thylakoid membrane fluorescence is shown in red. **(C)** RbcL-CFP (green) in Δ*parA* cells showing the loss of carboxysome spatial organization with no change in morphology. **(D)** Fluorescence image of ParA-GFP overlaid onto phase-microscopy image of cells showing the filament-like nature of ParA. Image is the deconvolved middle focal plane of a z stack. **(E)** Kymograph of the oscillatory behavior of ParA-GFP showing polymer dynamics. **(F)** ParA oscillation in relation to carboxysomes. Arrows denote increased ParA-GFP (green) between carboxysomes (RbcL-CFP, red). Scale bars, 2 μm.

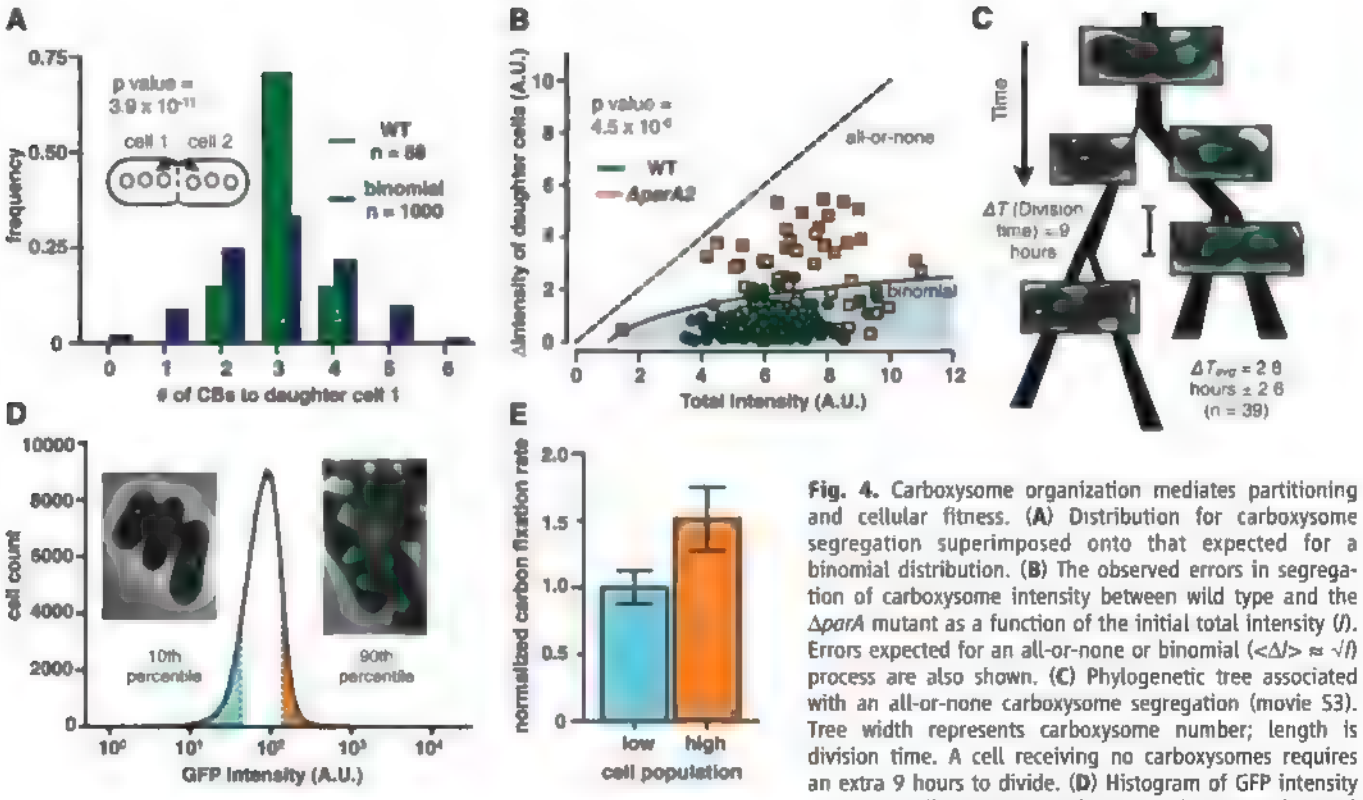

Fig. 4. Carboxysome organization mediates partitioning and cellular fitness. **(A)** Distribution for carboxysome segregation superimposed onto that expected for a binomial distribution. **(B)** The observed errors in segregation of carboxysome intensity between wild type and the Δ*parA* mutant as a function of the initial total intensity (*I*). Errors expected for an all-or-none or binomial ($<\Delta I> \approx \sqrt{I}$) process are also shown. **(C)** Phylogenetic tree associated with an all-or-none carboxysome segregation (movie S3). Tree width represents carboxysome number; length is division time. A cell receiving no carboxysomes requires an extra 9 hours to divide. **(D)** Histogram of GFP intensity in Δ*parA* cells expressing RbcL-GFP. The upper (orange) and lower (cyan) 10% of intensities were sorted and verified by microscopy (inset). **(E)** ^{14}C carbon fixation rates (with standard deviation, $n = 3$) of the populations sorted in (D). The populations are different as judged by an unpaired *t* test ($P = 2.9 \times 10^{-2}$).

fisZ, *minD*, and two *parA*-like genes) annotated cytoskeletal genes present in the *Synechococcus* genome were constructed (*11*). Mutations in *mreB* and the *parA*-like gene *Synpcc7942_1833* (hereafter, *parA*) disrupted carboxysome organization (Fig. 3, B and C). As deletion of *mreB* was pleiotropic, we investigated *parA* (*15*).

Deletion of *parA* showed disruption of carboxysome order with no perturbation of cellular morphology (Fig. 3C). ParA-GFP formed filament-like structures at one pole (Fig. 3D), that depolymerized and reassembled at the opposite pole in an oscillatory manner (period of 33.3 ± 10.6 min, $n = 25$) consistent with other ParA proteins (*16*) (Fig. 3E and movie S1). During oscillations, the filament frequently (68%, $n = 40$) hesitated or left a trail of condensed polymer behind the ParA wavefront. In the latter case, the polymer dissipated but reappeared in the same location after another oscillation. This condensed polymer was found between carboxysomes, which suggested that ParA mediates the connections between adjacent carboxysomes (Fig. 3F and movie S2).

Carboxysomes are essential for carbon fixation, so their organization may function to ensure even segregation during cell division. *Synechococcus* were entrained using a diurnal cycle of light, such that cells divided in synchrony. Single cells were tracked by using phase-contrast microscopy, and fluorescent images of labeled carboxysomes were acquired over several cell cycles. Each daughter cell consistently received an equal number of carboxysomes during division (Fig. 4A). Cytoplasmic proteins are thought to partition randomly (*17*), but segregation of carboxysomes was highly nonrandom (Pearson's chi-square test, $P = 3.9 \times 10^{-11}$). Because of the loss of equal spacing, resolving individual carboxysomes was not possible; instead, we quantified the intensity of carboxysomes partitioning to daughter cells. The *parA* deletion strain exhibited much lower fidelity in partitioning carboxysomes than did wild-type cells (two-tailed Kolmogorov-Smirnov test, $P = 4.4 \times 10^{-6}$) (Fig. 4B).

The loss of carboxysome organization was responsible for reduced fitness. We observed divisions in which one Δ*parA* daughter cell received no carboxysomes. Lineage tracking revealed that these cells divided 2.8 ± 2.6 ($n = 39$) hours later than their corresponding sister cells (Fig. 4C and movies S3 to S5). Populations of newly divided Δ*parA* cells with low or high numbers of carboxysomes were isolated by cell sorting (Fig. 4D). Cells with more carboxysomes fixed ~50% more carbon per unit of time than cells with fewer did (Fig. 4E). Thus, disruption of carboxysome spatial organization compromised the fidelity of carboxysome partitioning and impaired daughter-cell fitness.

The regular spacing of cellular machinery is emerging as a fundamental aspect of bacterial physiology. Vesicular magnetosomes and plasmids distribute regularly along the long axis of the cell (*16*, *18*). Here, an enzymatic complex was observed to behave in a similar manner. The organization of carboxysomes depends on cytoskeletal components, including ParA and MreB. Because MreB is located underneath the inner membrane (*19*), we favor a model in which MreB defines a structure that is used to organize carboxysomes. ParA proteins evenly space plasmids in the cell and mediate the positioning of a pole-localized protein in *Rhodobacter sphaeroides* (*20*). Here, mutation of *parA* affected carboxysome organization, and ParA filaments connected adjacent carboxysomes. Thus, ParA is a specific mediator of carboxysome spacing.

Carboxysomes occur in small numbers such that noise fluctuations during cell division could yield a daughter cell without this essential metabolic complex. It is thus possible that evolutionary pressures have selected for an organizational system—similar to nucleic acid sorting and perhaps derived from it—that ensures that each daughter cell receives a sufficient number of carboxysomes to optimize carbon fixation and cellular fitness.

References and Notes

1. J. M. Shively, F. L. Ball, B. W. Kline, *J. Bacteriol.* **116** 1405 (1973)
2. G. C. Cannon *et al.*, *Appl. Environ. Microbiol.* **67** 5351 (2001)
3. T. O. Yeates, C. A. Kerfeld, S. Heinhorst, G. C. Cannon J. M. Shively, *Nat. Rev. Microbiol.* **6**, 681 (2008)

4. J. Overmann, F. Garcia-Pichel, in *The Prokaryotes*, vol. 2, *Ecophysiology and Biochemistry*, M. Dworkin *et al.*, Eds. (Springer, New York, 2006), pp. 32–85
5. C. V. Iancu *et al.*, *J. Mol. Biol.* **372**, 764 (2007)
6. M. F. Schmid *et al.*, *J. Mol. Biol.* **364**, 526 (2006)
7. C. A. Kerfeld *et al.*, *Science* **309**, 936 (2005)
8. S. Tanaka *et al.*, *Science* **319**, 1083 (2008)
9. H. Ohkawa, M. Sonoda, H. Katoh, T. Ogawa, *Can. J. Bot.* **76**, 1035 (1998)
10. G. D. Price, S. M. Howitt, K. Harrison, M. R. Badger, *J. Bacteriol.* **175**, 2871 (1993)
11. Materials and methods are available as supporting material on *Science* Online.
12. M. B. Ecowitz, M. G. Surette, P. E. Wolf, J. B. Stock, S. Leibler, *J. Bacteriol.* **181**, 197 (1999)
13. T. E. Jensen, R. P. Ayala, *Arch. Microbiol.* **111**, 1 (1976).
14. C. V. Iancu *et al.*, *J. Mol. Biol.* **396**, 105 (2010)
15. M. Thanbichler, L. Shapiro, *Nat. Rev. Microbiol.* **6**, 28 (2008)
16. G. Ebersbach, K. Gerdes, *Annu. Rev. Genet.* **39**, 453 (2005)
17. N. Rosenfeld, J. W. Young, U. Alon, P. S. Swain, M. B. Elowitz, *Science* **307**, 1962 (2005)
18. A. Komeili, *Annu. Rev. Biochem.* **76**, 351 (2007)
19. H. J. Defeu Soufo, P. L. Graumann, *BMC Cell Biol.* **6**, 10 (2005)
20. S. R. Thompson, G. H. Wadhams, J. P. Armitage, *Proc. Natl. Acad. Sci. U.S.A.* **103**, 8209 (2006)
23. We thank R. Milo, R. Ward, R. Losick, S. Stanley, and E. Garner for comments on the manuscript, M. Ericsson and L. Benecchi for electron microscopy, and S. Golden for reagents. D.F.S. is a U.S. Department of Energy Biosciences Fellow of the Life Sciences Research Foundation. B.A. is supported by the Fundação para a Ciência e a Tecnologia and Graduate Program in Areas of Basic and Applied Biology (GABBA). This work was supported by Army Research Office Award W911NF-09-1-0226.

Supporting Online Material

www.sciencemag.org/cgi/content/full/327/5970/1258/DC1
Materials and Methods
SOM Text
Figs. S1 to S4
Tables S1 to S3
References
Movies S1 to S5

17 December 2009; accepted 22 January 2010
10.1126/science.1186090

Retromer Is Required for Apoptotic Cell Clearance by Phagocytic Receptor Recycling

Didi Chen,[1,2*] Hui Xiao,[1,2*] Kai Zhang,[3] Bin Wang,[3] Zhiyang Gao,[1] Youli Jian,[1] Xiaying Qi,[1] Jianwei Sun,[1,2] Long Miao,[3] Chonglin Yang[1]†

The cell surface receptor CED-1 mediates apoptotic cell recognition by phagocytic cells, enabling cell corpse clearance in *Caenorhabditis elegans*. Here, we found that the *C. elegans* intracellular protein sorting complex, retromer, was required for cell corpse clearance by mediating the recycling of CED-1. Retromer was recruited to the surfaces of phagosomes containing cell corpses, and its loss of function caused defective cell corpse removal. The retromer probably acted through direct interaction with CED-1 in the cell corpse recognition pathway. In the absence of retromer function, CED-1 associated with lysosomes and failed to recycle from phagosomes and cytosol to the plasma membrane. Thus, retromer is an essential mediator of apoptotic cell clearance by regulating phagocytic receptor(s) during cell corpse engulfment.

In *Caenorhabditis elegans*, cell corpse engulfment is controlled by two parallel pathways, one that recognizes and transduces engulfing signals, and the other that induces cytoskeleton reorganization (*1*). However, how components of these pathways are regulated and what other factors are involved remain unclear. To identify additional regulators of these pathways we performed genome-wide and candidate-based RNA interference (RNAi) screens (*2*) for genes whose inactivation greatly increased cell corpse numbers in the *C. elegans* germ line. Three genes, *snx-1*, *snx-6*, and *lst-4*, encoding homologs of mammalian sorting nexins 1/2, 5/6, and 9/18/33, respectively, were identified (figs. S1A and S2A and table S1). In mammals, sorting nexins 1/2 and 5/6 are essential components of the intracellular protein sorting complex retromer (*3*–*5*), whereas sorting nexins 9/18/33 regulate endocytosis (*3*). The deletion mutants *snx-1(tm847)* (*6*) and *snx-*

[1]Key Laboratory of Molecular and Developmental Biology, Institute of Genetics and Developmental Biology, Chinese Academy of Sciences, Datun Road, Chaoyang District, Beijing 100101, China. [2]Graduate School, Chinese Academy of Sciences, Beijing 100039, China. [3]National Laboratory of Biomacromolecules, Institute of Biophysics, Chinese Academy of Sciences, Datun Road, Chaoyang District, Beijing 100101, China.
*These authors contributed equally to this work.
†To whom correspondence should be addressed. E-mail: clyang@genetics.ac.cn

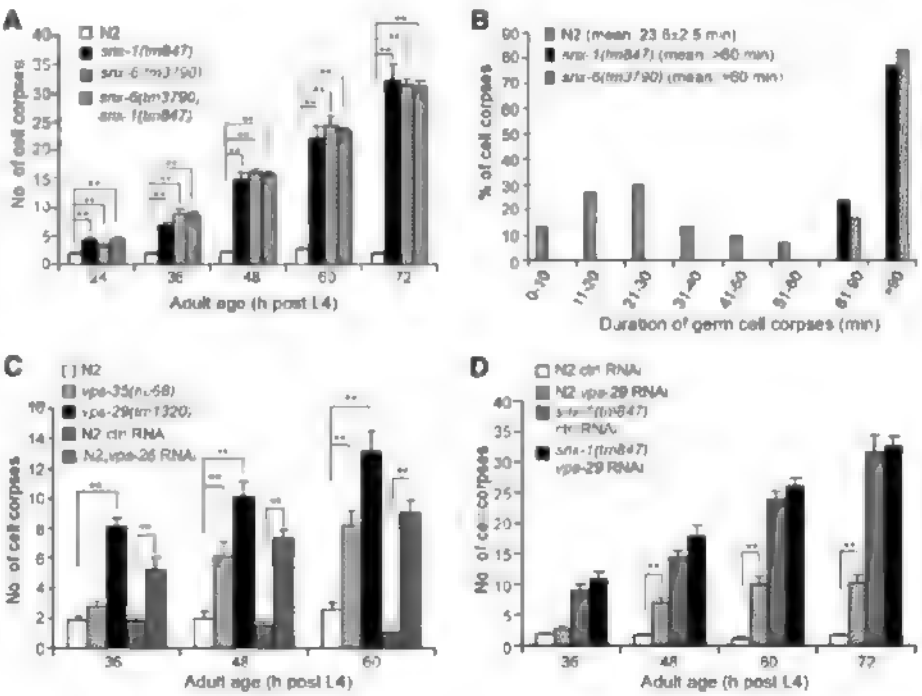

Fig. 1. *C. elegans* retromer affects clearance of apoptotic cells. (**A**) Quantification of germ cell corpses in N2 (wild type), *snx-1(tm847)*, *snx-6(tm3790)*, and *snx-6(tm3790);snx-1(tm847)* mutants. (**B**) Four-dimensional microscopy analysis of germ cell corpse duration in N2, *snx-1(tm847)*, and *snx-6(tm3790)* mutants. Thirty germ cell corpses were recorded for each strain. (**C**) Quantification of germ cell corpses in *vps-26(RNAi)*, *vps-35(hu68)*, and *vps-29(tm1320)* animals. (**D**) Germ cell corpse phenotypes of control RNAi- and *vps-29* RNAi-treated N2 and *snx-1(tm847)* mutants. In (A), (C), and (D), the *y* axis indicates the average number of germ cell corpses. Error bars represent the SEM. Comparisons were performed using unpaired *t* tests. $^{**}P < 0.001$.

6(tm3790), which probably represent strong loss-of-function mutations of *snx-1* and *snx-6* (figs. S1B and S2B), had increased numbers of germline and embryonic cell corpses, which persisted significantly longer than did the wild type (Fig. 1, A and B, and fig. S3). The number of cell deaths in *snx-1(tm847)* and *snx-6(tm3790)* embryos was indistinguishable from that of the wild type; thus, the increased cell corpse numbers result from defective corpse clearance rather than excessive apoptosis.

The retromer mediates retrograde transport of transmembrane cargoes from endosomes to the trans-Golgi network (*4*). SNX-1 and SNX-6 are essential subunits of the retromer sorting nexin dimer (*4*, *5*). In *snx-6(tm3790),snx-1(tm847)* double mutants, germline and embryonic cell corpse numbers were indistinguishable from those of single mutants (Fig. 1A and fig. S3A), suggesting that these genes function in the same genetic pathway. In contrast, *lst-4(tm2423),snx-1(tm847)* double mutants exhibited significantly more germline and embryonic cell corpses than did single mutants (fig. S4). Thus, LST-4 probably acts separately from the retromer during cell corpse clearance. The retromer also contains a Vps26-Vps29-Vps35 trimer (*4*), so we examined *vps-26(tm1523)*, *vps-29(tm1320)*, and *vps-35(hu68)* deletion mutants (*6*). No corpse phenotype was observed in *vps-26(tm1523)* germ lines, probably because of abnormal germline development (*6*, *7*). Partial RNAi inactivation of *vps-26*, however, significantly increased germ cell corpses (Fig. 1C). A similar increase was observed in *vps-29(tm1320)* and *vps-35(hu68)* germ lines (Fig. 1C). Intriguingly, cell corpse numbers in *vps-26(tm1523)*, *vps-29(tm1320)*, and *vps-35(hu68)* embryos were similar to those of the wild type. Thus, loss of individual retromer components affects corpse clearance to different extents. We next asked whether the VPS-26–VPS-29–VPS-35 and sorting nexin subcomplexes acted together in cell corpse removal. *vps-29* RNAi on its own caused an increase in germ cell corpses, but did not further enhance the number of corpses in *snx-1(tm847)* germ lines (Fig. 1D), suggesting that *snx-1* and *vps-29* probably function in the same genetic pathway. Furthermore, in glutathione-*S*-transferase (GST) pull-down assays, SNX-1 and SNX-6 interacted with one another, and with GST-VPS-26, -29, and -35 (fig. S5). Thus, retromer components function together during cell corpse clearance in *C. elegans*.

We next examined germ cell corpse engulfment by transmission electron microscopy. In wild-type animals treated with *gla-3* RNAi, which increases germ cell deaths without affecting corpse clearance (*8*), 10 cell corpses from 4 gonad arms were fully encircled by gonadal sheath cells (Fig. 2), consistent with previous findings that wild-type germ cell corpses are swiftly engulfed (*9*). Of 31 cell corpses from 2 gonad arms in *snx-1(tm847)* mutants, 25 (81%) were only partially encircled by sheath cells, while 6 (19%) were completely engulfed but not properly degraded [Fig. 2, fig. S6, and supporting online material (SOM) text]. Furthermore, engulfing cells required SNX-1/retromer activity for cell corpse removal, and SNX-1 and VPS-29 were recruited and colocalized on the cell corpse surface (SOM text and figs. S7 and S8). Thus, SNX-1/retromer is required for engulfment and degradation of cell corpses.

To determine in which pathway retromer acted, we examined double mutants of *snx-1(tm847)* with strong loss-of-function alleles of engulfment genes. In *C. elegans*, *ced-1*, *ced-6* (GULP), *ced-7* (ABC transporter), and *dyn-1* (Dynamin) function in one pathway to recognize and transduce engulfing signals, whereas *ced-2* (CrkII), *ced-5* (Dock 180), *ced-10* (Rac guanosine triphosphatase), *ced-12* (ELMO), and *psr-1* (phosphatidylserine receptor) act in the other pathway to activate cytoskeleton rearrangement (*1*, *10*). Germline and embryonic cell corpse numbers in double mutants of *snx-1(tm847)* with *ced-1(e1735)* or *ced-6(n2095)* were indistinguishable from those of *ced-1(e1735)* and *ced-6(n2095)* single mutants (Fig. 2G and fig. S9, A to C). Intriguingly, both germline and embryonic cell corpses in *ced-7(n1892),snx-1(tm847)* double mutants were significantly increased compared to *ced-7(n1892)* single mutants (Fig. 2H and fig. S9D). Thus, *snx-1*/retromer probably acts in parallel to *ced-7* in the same pathway as *ced-1* and *ced-6*. Consistent with this, *snx-1(tm847)* significantly enhanced germline and embryonic cell corpse numbers in mutants affecting the other engulfment pathway (Fig. 2, I and J, and fig. S9, E to H).

During phagocytosis, the receptor CED-1 clusters in the phagocytic cup before quickly

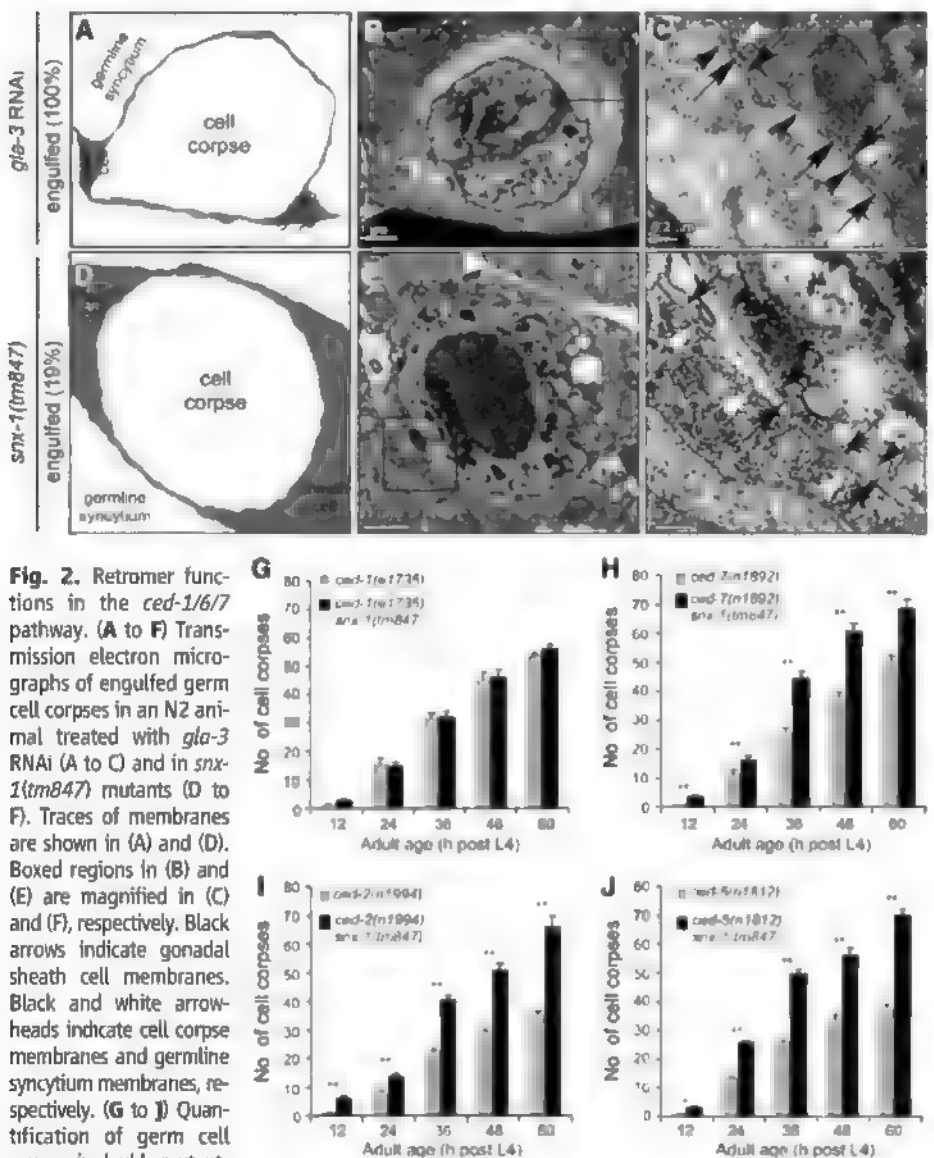

Fig. 2. Retromer functions in the *ced-1/6/7* pathway. (**A** to **F**) Transmission electron micrographs of engulfed germ cell corpses in an N2 animal treated with *gla-3* RNAi (A to C) and in *snx-1(tm847)* mutants (D to F). Traces of membranes are shown in (A) and (D). Boxed regions in (B) and (E) are magnified in (C) and (F), respectively. Black arrows indicate gonadal sheath cell membranes. Black and white arrowheads indicate cell corpse membranes and germline syncytium membranes, respectively. (**G** to **J**) Quantification of germ cell corpses in double mutants of *snx-1(tm847)* with *ced-1(e1735)* (G), *ced-7(n1892)* (H), *ced-2(n1994)* (I), and *ced-5(n1812)* (J) mutants. Data derived from two different genetic backgrounds at multiple stages were compared by unpaired *t* tests. $^{*}P < 0.05$, $^{**}P < 0.001$.

encircling the cell corpse. Recognition of apoptotic cells by CED-1 requires CED-7, loss of which disrupts clustering of CED-1 around embryonic cell corpses (*11*). Because retromer and CED-7 act in parallel in the *ced-1* pathway, we investigated whether retromer regulates CED-1 by time-lapse chasing the association of CED-1::GFP (green fluorescent protein) expressed from an integrated array (*smIs34*) with cell corpses in *snx-1*(*tm847*) embryos, while simultaneously monitoring phagosomal recruitment of lysosomes labeled by the lysosome marker LMP-1..mCherry. In wild-type embryos, CED-1::GFP was quickly recruited to the phagocytic cup and encircled the cell corpse within 3 min (Fig. 3A). Between 3 and 9 min, CED-1 disappeared from the phagosome and reappeared on the plasma membrane of the engulfing cell. As the CED-1 ring formed, lysosomes were simultaneously recruited to the phagosome as indicated by formation of a LMP-1::mCherry ring, which remained associated with the phagosome after CED-1 was released (Fig. 3A). Thus, CED-1 is recycled swiftly from the phagosome to the engulfing cell membrane before the cell corpse is degraded. The mean duration of the CED-1 ring on the phagosome was 10.8 ±1.7 min (n = 6) in wild-type embryos, but in *snx-1*(*tm847*);*smIs34* embryos it was 26.0 ± 1.8 min (n = 6) so that the ring remained associated with the phagolysosome until late in corpse degradation (Fig. 3A). Subsequently, when the corpses had adopted a pit-like structure, the proportion colabeled with CED-1::GFP and LMP-1.::mCherry was <20% in wild-type embryos but >80% in *snx-1*(*tm847*) embryos (Fig. 3B). Thus, loss of retromer inhibits CED-1 recycling from the phagosome to the engulfing cell membrane, and phagosome-associated CED-1 is sent to lysosomes together with cell corpses. Furthermore, whereas *smIs34*-expressed CED-1 GFP was almost exclusively associated with the plasma membrane in wild-type embryos, in *snx-1*(*tm847*) embryos it displayed an intracellular punctate distribution pattern that colocalized with LMP-1..mCherry in addition to its membrane localization in several cell types such as hypodermal cells (Fig. 3C). Thus, CED-1 is internalized from and recycled back to the cell membrane; loss of retromer function causes lysosomal accumulation of CED-1. Consistent with this, CED-1..GFP expression driven by the *vps-33* promoter in macrophage-like coelomocytes was intracellular and partially overlapped with the lysosome marker mCherry::CUP-5 in *snx-1*(*tm847*) and *snx-6*(*tm3790*) mutants, whereas in the wild type it was mainly seen on the plasma membrane (SOM text and fig. S10A).

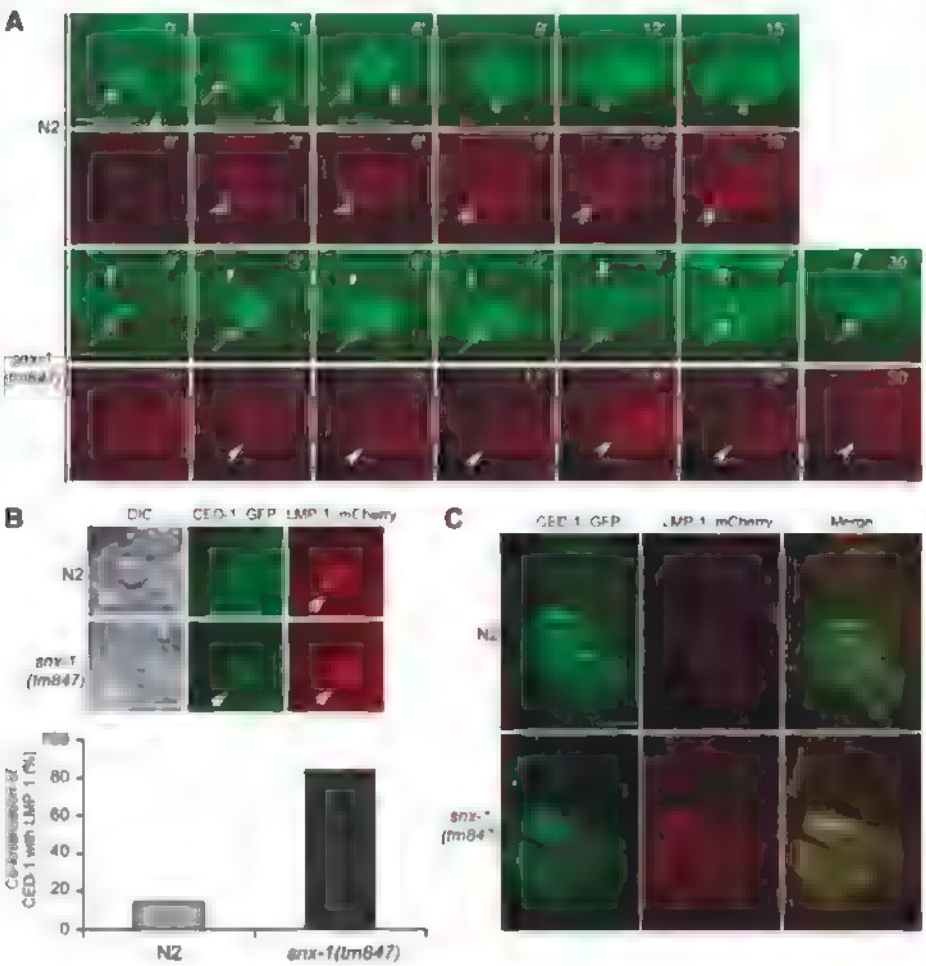

Fig. 3. *snx-1*(*tm847*) causes defective recycling of internalized CED-1. **(A)** Time-lapse chasing of CED-1::GFP (arrows) and LMP-1::mCherry (sharp arrowheads) on phagosomes in N2 and *snx-1*(*tm847*) animals. Clustering of CED-1::GFP on the phagocytic cup was set as 0 min. Blunt arrowheads indicate membranes of engulfing cells. Bars, 5 μm. **(B)** Representative images (top) and quantification (bottom) of CED-1::GFP and LMP-1 ::mCherry colocalization on cell corpses at a late stage of degradation in N2 and *snx-1*(*tm847*) embryos. At least 100 cell corpses in each strain were examined. Arrows indicate cell corpses. DIC, differential interference contrast. Bars, 5 μm. **(C)** Localization of CED-1::GFP and LMP-1::mCherry in hypodermal cells in N2 and *snx-1*(*tm847*) embryos. Bars, 10 μm.

The increased association of CED-1 with lysosomes suggests that CED-1 undergoes lysosome-mediated degradation. CED-1::GFP signal from *smIs34* was reduced in *snx-1*(*tm847*) mutants compared to the wild type (fig. S10B). CED-1::GFP protein abundance was significantly lower in *snx-1*(*tm847*),*smIs34* and *snx-6*(*tm3790*),*smIs34* animals (Fig. 4A). CED-1 :GFP was also reduced in *vps-29*(*tm1320*);*smIs34* worms, though to a lesser extent. In contrast, CED-1::GFP was not reduced in *lst-4*(*tm2423*),*smIs34* animals (Fig. 4A). Using a CED-1 C-terminal–specific antibody, we found that endogenous CED-1 was strongly reduced in *snx-1*(*tm847*) and *snx-6*(*tm3790*) animals, slightly reduced in *vps-29*(*tm1320*) mutants, and undetectable in *ced-1*(*e1735*) mutants containing an early stop codon in the *ced-1* gene (Fig. 4B). Furthermore, endogenous CED-1 localized to the plasma membrane in wild-type embryos but not in *snx-1*(*tm847*) or *ced-1*(*e1735*) mutants (Fig. 4C). Thus, in the absence of retromer function, CED-1 fails to localize to the plasma membrane and is probably degraded in lysosomes, becoming limiting for cell corpse engulfment and causing accumulation of cell corpses. Consistent with this, RNAi knockdown of *vps-37*, a component of the ESCRT-I complex (endosomal sorting complex required for transport) (*12*), partially restored CED-1::GFP abundance in *snx-1*(*tm847*);*smIs34* animals (fig. S11). Moreover, the increased germline and embryonic corpse numbers in *snx-1*(*tm847*) mutants were strongly reduced by overexpressing CED-1::GFP driven by the *ced-1* promoter (*smIs34*) (Fig. 4D and fig. S12A). CED-1::GFP driven by the sheath cell-specific *lin-7* promoter (*bcIs39*) similarly decreased the number of *snx-1*(*tm847*) germline corpses (Fig. 4D). Furthermore, *smIs34* greatly reduced the numbers of both embryonic and germline cell corpses in *snx-6*(*tm3790*) single mutants as well as in *snx-6*(*tm3790*),*snx-1*(*tm847*) double mutants, but not in *lst-4*(*tm2423*) mutants (fig. S12, B to G), indicating that CED-1 overexpression specifically rescued the cell corpse phenotypes of retromer mutants and that retromer acts through CED-1 to affect cell corpse clearance.

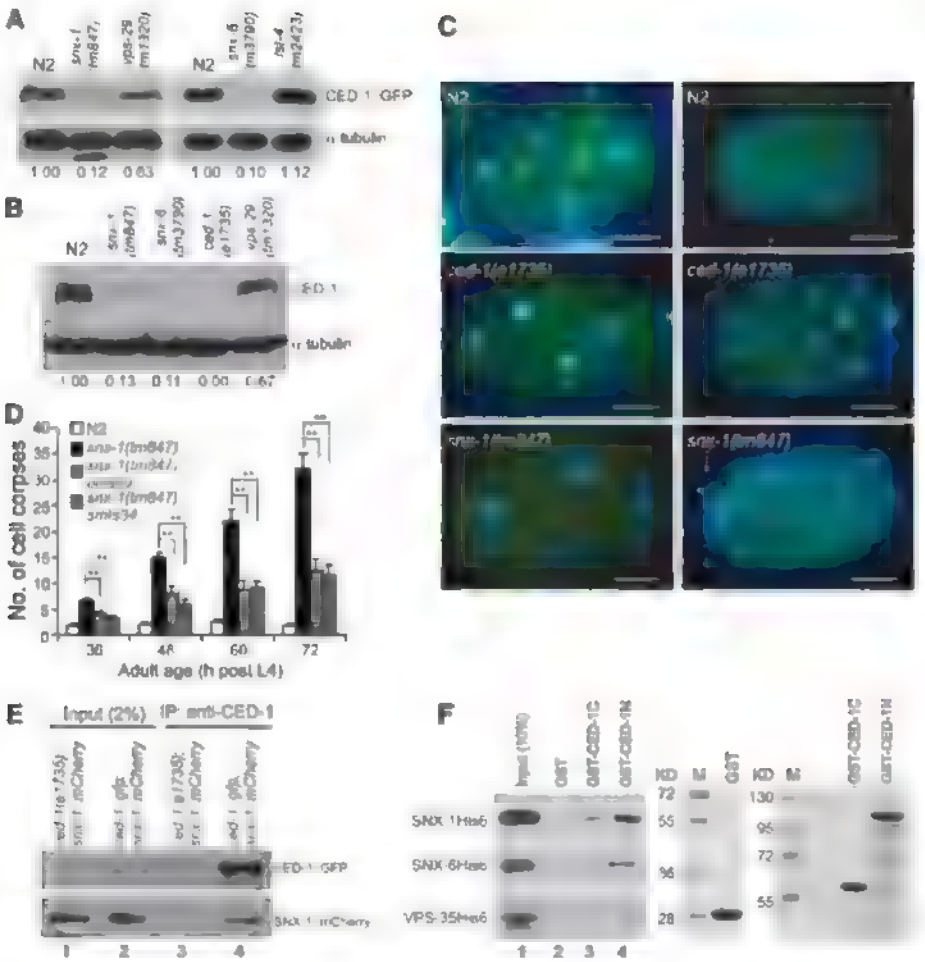

Fig. 4. Retromer acts through CED-1. (**A** and **B**) Immunoblot analysis of CED-1::GFP expression by *smIs34* ($P_{ced\text{-}1}$*ced-1::gfp*) (A) and endogenous CED-1 protein abundance (B) in N2 and different mutants. The relative expression of CED-1 in each strain is indicated. (**C**) Localization of endogenous CED-1 in N2, *ced-1(e1735)*, and *snx-1(tm847)* embryos. Merged images of CED-1–specific antibody staining (green) and nuclear staining (blue) of a four-cell-stage embryo (left) and a ~50-cell-stage embryo (right) are shown. Bars, 10 μm. (**D**) Quantification of germ cell corpses in N2, *snx-1(tm847)*, *snx-1(tm847);smIs34*, and *snx-1(tm847);bcIs39* ($P_{lim\text{-}7}$*ced-1::gfp*) animals. $^{**}P < 0.001$. (**E**) Immunoprecipitations (IP) were performed with CED-1–specific antibody from lysates of *ced-1(e1735)* mutants expressing SNX-1::mCherry (lane 1) and N2 worms expressing both CED-1::GFP and SNX-1::mCherry (lane 2). Proteins were detected with antibodies against GFP and mCherry, respectively. (**F**) His6-tagged SNX-1, SNX-6, and VPS-35 were incubated with immobilized GST, GST-CED-1C, and GST-CED-1N. Bound proteins were detected with antibody to His6 (left). GST fusion proteins used for binding are shown on the right.

Finally, using the CED-1 C-terminal–specific antibody, we immunoprecipitated CED-1::GFP from cell lysates from wild-type animals expressing both CED-1::GFP and SNX-1::mCherry and found that SNX-1::mCherry was associated with CED-1::GFP, whereas no SNX-1::mCherry was coimmunoprecipitated from lysates of *ced-1(e1735)* worms expressing SNX-1::mCherry alone (Fig. 4E). Thus, CED-1 associates with retromer in *C. elegans*. In a pull-down assay, purified SNX-1 interacted with GST-fused CED-1 N terminus (CED-1N, amino acids 1 to 908) and C terminus (CED-1C, amino acids 933 to 1111), and SNX-6 interacted with GST-CED-1N (Fig. 4F). No obvious interaction was detected between CED-1 and VPS-35 (Fig. 4F). Thus, CED-1 cycling is probably achieved by direct interaction with specific retromer subunits.

The retromer mediates a wide range of processes (*4*), including transport of intracellular sorting receptors such as Vps10 in yeast and CI-MPR (cation-independent mannose 6-phosphate receptor) in mammals (*13*, *14*), formation of Wnt gradients in *C. elegans* and *Drosophila* (*6*, *7*, *15*–*19*), and transcytosis of the polymeric immunoglobulin receptor in polarized epithelial cells (*20*). Retromer-mediated cycling of receptors is probably achieved by interaction of cargoes with different retromer subunits (*21*) or between cargoes and a retromer partner like Grd19/Snx3 (*22*). Our findings establish a function of retromer in apoptotic cell clearance in mediating cycling of the phagocytic receptor CED-1 between the plasma membrane and intracellular organelles. CED-1 family phagocytic receptors may be similarly regulated in other organisms.

References and Notes

1. P. W. Reddien, H. R. Horvitz, *Annu. Rev. Cell Dev. Biol.* **20**, 193 (2004).
2. R. S. Kamath, J. Ahringer, *Methods* **30**, 313 (2003).
3. P. J. Cullen, *Nat. Rev. Mol. Cell Biol.* **9**, 574 (2008).
4. J. S. Bonifacino, J. H. Hurley, *Curr. Opin. Cell Biol.* **20**, 427 (2008).
5. T. Wassmer *et al.*, *Dev. Cell* **17**, 110 (2009).
6. D. Y. Coudreuse, G. Roël, M. C. Betist, O. Destrée, H. C. Korswagen, *Science* **312**, 921 (2006).
7. B. C. Prasad, S. G. Clark, *Development* **133**, 1757 (2006).
8. E. A. Kritikou *et al.*, *Genes Dev.* **20**, 2279 (2006).
9. T. L. Gumienny, E. Lambie, E. Hartwieg, H. R. Horvitz, M. O. Hengartner, *Development* **126**, 1011 (1999).
10. X. Yu, S. Odera, C. H. Chuang, N. Lu, Z. Zhou, *Dev. Cell* **10**, 743 (2006).
11. Z. Zhou, E. Hartwieg, H. R. Horvitz, *Cell* **104**, 43 (2001).
12. A. Shi *et al.*, *EMBO J.* **28**, 3290 (2009).
13. C. N. Arighi, L. M. Hartnell, R. C. Aguilar, C. R. Haft, J. S. Bonifacino, *J. Cell Biol.* **165**, 123 (2004).
14. M. N. Seaman, J. M. McCaffery, S. D. Emr, *J. Cell Biol.* **142**, 665 (1998).
15. X. Franch-Marro *et al.*, *Nat. Cell Biol.* **10**, 170 (2008).
16. F. Port *et al.*, *Nat. Cell Biol.* **10**, 178 (2008).
17. T. Y. Belenkaya *et al.*, *Dev. Cell* **14**, 120 (2008).
18. C. L. Pan *et al.*, *Dev. Cell* **14**, 132 (2008).
19. P. T. Yang *et al.*, *Dev. Cell* **14**, 140 (2008).
20. M. Verges *et al.*, *Nat. Cell Biol.* **6**, 763 (2004).
21. B. M. Collins, *Traffic* **9**, 1811 (2008).
22. T. I. Strochlic, T. G. Setty, A. Sitaram, C. G. Burd, *J. Cell Biol.* **177**, 115 (2007).

23. We thank S. Mitani, X. Wang, D. Xue, H. Fares, and *C. elegans* Genetic Center (CGC) for strains, X. Wang and H. Zhang for critically reading the manuscript, and I. Hanson for proofreading services. This research was supported by grants 2007CB947201, 30871266, and KSCX1-YW-R-70 from the Chinese government. C.Y. is supported by the Chinese Academy of Sciences 100-Talents Program.

Supporting Online Material

www.sciencemag.org/cgi/content/full/science.1184840/DC1
Materials and Methods
SOM Text
Figs. S1 to S12
Table S1
References

17 November 2009; accepted 22 January 2010
Published online 4 February 2010
10.1126/science.1184840
Include this information when citing this paper.

LABEL CREATION SOFTWARE

dentLab abel creation software is an intuitive, user-friendly program that allows users to create and print sample dentification labels quickly and easily The software is designed to make legible, durable, and accurate laboratory-specific labels It requires only three steps to create labels from stored temp ates, categorized by common laboratory applications Easy-to-use wizards help create custom labels It includes facilities such as database import, support for two-dimensional barcodes, and automatic number sequencing. IdentiLab is compatible with all Windows-based inkjet and laser printers.

Brady
For info: 01295-228288 | www.bradylab.co.uk

LOW-TEMPERATURE CHILLERS

Designed to maximize bench space, the LS-Series, LM-Series, and MM-Ser es Ch lers provide up to 1,290 watts of cooling at 20°C, mak ng them su table for use with rotary evaporators, jacketed incubators, small reaction vessels, spectrophotometers, chromatography columns, condensers, and other devices that require robust heat remova . The LS-Ser es has a working temperature range of –20°C to +40°C and provides 475 watts of cooling at –10°C. The LM-Series has a working temperature range of –10°C to +30°C and a 230-watt cool ng capac ty at –10°C The MM-Series has a working temperature range of –5°C to +50°C and provides 129 watts of cooling at –5°C A three mode s control temperature within ±0 1°C stab ity and are equ pped with a low-flow-rate alarm, user-adjustable h gh and low temperature alarms, a top-mounted fill port with built-in f ter, ghted f d level ind cator, and washable rigid-frame air filter.

PolyScience
For info: 800-229-7569 | www.polyscience.com

REFRIGERATED MICROCENTRIFUGE

The Centrifuge 5430 R is a refrigerated microcentrifuge that incorporates a m croplate rotor. Like the air-cooled Centrifuge 5430, the refrigerated version accommodates virtually any tube or plate, mak ng it su tab e for a wide range of applications in research and development fac ties, hospitals, and diagnostic laboratories. The 30-place Centr fuge 5430 R combines the rotor options of a benchtop model with the small footprint of a microcentrifuge. The affordable system offers all the capab ties of a high-end microcentrifuge. A choice of e ght rotors gives maximum versatility, enabling the centrifugat on of m cro test tubes, polymerase chain reaction (PCR) tubes and strips, spin co umn kits, cryogenic tubes, 15-ml and 50-ml Falcon tubes, and PCR plates Adapters are available to accommodate every type of commonly used blood collection tube

Eppendorf
For info: 01223-873318 | www eppendorf.co.uk

HEAT SHOCK PROTEIN ANALYSIS

The MultiBead H SP/Chaperone 8-Plex Kit is a new multiplex assay for the analys s of heat shock proteins and molecular chaperones. The bead-based immunoassay enables measurement of heat shock protein c ent proteins and heat shock proteins in cell lysates. The assay makes use of monoclonal antibodies or antigen affinity purified polyclonal antibodies covalently coupled to latex beads The detection antibodies are conjugated to biotin followed by a streptavidin-phycoerythrin conjugate and analyzed on a dual-laser flow cytometer

Assay Designs
For info: 800-833-8651 | www assaydesigns.com

GEL DOCUMENTATION SYSTEM

The Gel Logic 121 Pro Imag ng System is a next generation, fully automated gel imaging system that enables researchers to capture perfectly exposed images in just a few c icks. It features a redesigned user interface, an improved look and feel, and ma or productivity enhancements, includ ng autofocus and autoexposure It is suitable for documenting and analyz ng fluorescent, co orimetric data in sample formats such as gels, membranes, and 96-we plates. It is designed for medium to large labs in which workflow, high sample throughput, safety, and h gh-qua ity image analysis are critical It features a scientific-grade, 1.4-million p xel charge-coup ed device camera that can accumulate up to 12 bits of data, enab ng researchers to detect and quantify very dim as well as very br ght signals in the same image

Carestream Molecular Imaging
For info: 877-747-4357 | www.carestreamhealth.com/gel-logic-systems.html

ASSAY PLATE PRODUCTION SYSTEM

The Coda high throughput automated nanoliter assay plate production system integrates up to three Labcyte Echo 555 liquid handlers to enable fast and efficient processing of up to 300 384-we l plates in 4.5 hours (at 5 nl sample volume) This modular system can be configured to suit any user's sample management programs and typically includes a conventional l quid handler for dispens ng buffer or diluent, a centrifuge for ensur ng liquids are at the bottom of the plate, and The Automation Partnership's spec a ist Echo robot c feeding arm designed to work with the Echo's load ng stages Coda can also have labeling and plate-sea ng modu es integrated, as we as using PlateSafes or plate hotels to ensure full compound track ng and secure plate storage

The Automation Partnership
For info: +44-(0)-1763-227200 | www automationpartnership.com

Electronica y s ubm t your new product desc p.on or product literature information! Go to **www.sciencemag org/products/newproducts dtl** for more information on Newly offered instrumentation, apparatus, and laboratory materials of interest to researchers in all disciplines in academic, industrial, and governmental organizations are featured in th s space Emphasis is given to purpose, chief characteristics, and availability of products and materials. Endorsement by *Science* or AAAS of any products or materials mentioned is not implied. Additional information may be obtained from the manufacturer or supplier.

POSITIONS OPEN

COLLABORATIVE POSTDOCTORAL POSITION
Biological Modeling
California State University, Los Angeles and California Institute of Technology

A Postdoctoral position is open immediately to study the dynamics of layered biological systems with specific applications to the ecology of mussel beds. A Ph.D. is required. Candidates should have experience using mathematical modeling and computer simulation to study biological problems. Knowledge of cellular automata and spatial statistics is desired. Opportunities exist to collaborate with field ecologists and to gain teaching experience. Salary is $42,000 per year plus benefits, renewable for a second year. The position is a joint appointment between California State University at Los Angeles and California Institute of Technology. Inquiries and applications (cover letter, curriculum vitae, and three references) to: **Dr. Robert Desharnais, Biological Sciences, California State University, 5151 State University Drive, Los Angeles, CA 90032. E-mail: rdeshar@calstatela.edu.** *California State University, Los Angeles, CA/AS is an Affirmative Action/Equal Opportunity Employer.*

POSTDOCTORAL SCHOLAR. A Postdoctoral Scholar position in cardiovascular research is available immediately in the Department of Physiology at Brody School of Medicine, East Carolina University in Greenville, North Carolina, in the laboratory of **Dr. David A. Tulis, F.A.H.A.,** Associate Professor. The focus of our research program is vascular smooth muscle physiology and pathology with particular emphasis on molecular, cellular, and functional mechanisms that underlie growth. Specific areas of interest include cyclic nucleotide and transforming growth factor signaling and their regulation, matrix/matrix metalloproteinases and gap junction/connexin biology, and avenues for control of proliferation, migration, and apoptosis. Experimental approaches include whole animal models, in vitro cell culture, and ex vivo tissue explants. Salary and benefits will be commensurate with experience according to NIH guidelines. Review of applications will begin immediately and will continue until the position is filled. Please visit **website: http://www.ecu.edu/cs-dhs/physiology/tulisd.cfm** for more information. Please electronically send an updated curriculum vitae, a statement of research interests, and contact information for three references to **e-mail: tulisd@ecu.edu**, and include Postdoctoral Scholar in the Subject line. *Women and minorities are encouraged to apply.*

PASTEUR FOUNDATION

POSTDOCTORAL FELLOWSHIPS
Institut Pasteur, Paris, France

Come work in Paris at the Institut Pasteur, the world-renowned, private, biomedical research organization. We invite applications from outstanding Fellowship candidates to any of 130 laboratories within our 10 departments. Areas include: developmental and cell biology, epidemiology, immunology, genomics, genetics, microbiology, neuroscience, structural biology, parasitology, mycology and virology. Deadlines vary; see website for details. Annual package is $70,000 for three years. *U.S. citizenship required.*

E-mail: pasteurus@aol.com. Website: http://www.pasteurfoundation.org.

POSITIONS OPEN

SCHOOL OF MEDICINE & DENTISTRY
UNIVERSITY of ROCHESTER

POSTDOCTORAL POSITION

A Postdoctoral position is available in the Center for Oral Biology at the University of Rochester to study salivary gland biology. Specific areas of interest include the development and regeneration of salivary gland, salivary gland stem cells, and salivary gland physiology. Applicants must hold a Ph.D. and/or an M.D. degree with less than five years of postdoctoral experience. Preference will be given to individuals with expertise in one or more of the following areas: animal models, stem cell/developmental biology, molecular biology, epithelial ion and water transport physiology. Please send a brief description of research experience and interests, as well as curriculum vitae containing names and contact information for three references to: **Dr. Catherine Ovitt e-mail: catherine_ovitt@urmc.rochester.edu), University of Rochester Medical Center, Box 611, 601 Elmwood Avenue, Rochester, NY 14642.**

The University of Rochester is an Equal Opportunity Employer. Women and minorities are encouraged to apply.

THE JOHN CALDWELL MEEKER POSTDOCTORAL FELLOW

Applications are invited for the position of the John Caldwell Meeker Postdoctoral Researcher in the Department of Geology at The Field Museum. The successful candidate will be expected to complement, and/or participate in, any one of the ongoing research programs in the Department of Geology. Research projects are being pursued in the areas of vertebrate paleontology, invertebrate paleontology, paleobotany, and meteoritics. Individual curators and their research programs are featured on the Field Museum **website: http://www.fieldmuseum.org/research_collections/geology/research.htm**

A Ph.D. in any field of research represented in the Department of Geology is required. The term for this position is for a maximum of two years. The appointment is anticipated to begin October 1, 2010.

Please send a statement of research interests and experience, curriculum vitae including publications list, and names of three references (with telephone numbers and e-mail addresses) to: **Peter Makovicky, Chair, Department of Geology, The Field Museum, 1400 S. Lake Shore Drive, Chicago, IL 60605-2496 U.S.A. E-mail: pmakovicky1@fieldmuseum.org; telephone: 312 665 7633; fax: 312-665 7641.** Applications must be received by April 30, 2010; applications received after this date may be considered if the position has not been filled.

The Field Museum is an Equal Opportunity Employer.

POSTDOCTORAL POSITION available in the laboratories of **Dr. Ramesh Ramachandran** and **Dr. Regma Vasilatos-Younken,** Pennsylvania State University, University Park, Pennsylvania 16802 to study mechanistic endocrinology and adipose tissue hormones. Research involves recombinant DNA construction, protein purification, and functional assays. Candidates will have a Ph.D. in biological sciences and a strong background in molecular biology and biochemical techniques. Electronically send resume, cover letter with a statement of research interests, and names of three references to **e-mail: rameshr@psu.edu.** *Penn State is an Affirmative Action/Equal Opportunity Employer.*

POSTDOCTORAL POSITIONS are available in the field of autoimmunity to investigate the genetics, mitochondrial dysfunction, activation, and apoptosis signaling of T lymphocytes in lupus patients and experimental model systems. The laboratory is located in the College of Medicine of the State University of New York in Syracuse, New York. Inquiries, statement of research interest, curriculum vitae, and three references should be electronically sent to **Andras Perl, M.D.-Ph.D., e-mail: perla@upstate.edu**

CAREERS BEYOND THE BENCH

After completing their graduate studies, many scientists have moved away from the bench and found rewarding careers in areas from grant administration to venture capital. While still making use of the training and skills gained during graduate school, these "alternative" careers are a better match for many. **By Laura Bonetta**

ANDREA STITH

"I have met so many people who have come to science policy in unique and personal [illegible] points in their careers."

Did You Hear the One about the Former Scientist?

A December 15, 2009, *New York Times* article with that headline described the plight of a biologist who completed his graduate studies at the University of California, Davis before becoming a stand-up comic. Although comedy is an unusual choice, most Ph.D.-trained researchers will eventually pursue, out of choice or necessity, nonacademic careers, according to a survey by the National Postdoctoral Association. In 2003, among Doctorate degree holders who received their degree four to six years previously, only 19.8 percent were in tenure-track or tenured positions at four-year institutions of higher education.

For Ph.D.-trained scientists who do not end up with faculty positions, there are research opportunities in private or government institutions and industry. But increasingly career choices take scientists not just away from academia but away from the bench altogether into areas like science writing and editing, public relations, science policy, scientific program or grant management, science teaching, patent law, and venture capital.

So how do you move beyond the bench?

Find What You Are Good At

Both as a graduate student and postdoc, **Maryrose Franko** took every opportunity to volunteer in science education which made her realize that "I have good people skills that I really enjoy using," she says. "I also discovered that, although I enjoyed doing benchwork, I always looked forward to going into a school or giving a talk or judging a science fair."

While conducting her postdoctoral research at the US National Institutes of Health (NIH) in Bethesda, Maryland, she helped with the Student-Teacher Internship Program run jointly by NIH and the Howard Hughes Medical Institute (HHMI). Through the program she became acquainted with some of the administrative staff at HHMI. "When a position opened up at HHMI, they suggested I apply," she recalls. "I thought that this would be a great way to utilize my people and scientific skills. And this was a wonderful opportunity to make the best out of all my strengths."

She joined HHMI in the spring of 1995 as a program officer and has since moved through the ranks to senior officer in charge of several fellowship programs for graduate students and postdocs. "I spend a lot of time talking to people in the science education community, giving presentations, talking with my grantees, reading reports, and preparing reports," says Franko. To be successful at this job, she adds, "it takes a collaborative person and one who doesn't need or want credit for his or her ideas."

Both private and government-run funding agencies typically hire grant administrators and program officers with graduate degrees. "My job is to evaluate science education needs. I also give feedback to graduate student applicants and make sure that the research they are proposing is fundable by our mechanisms. I assign applications to review based on research area. I organize conferences by grantees and assign talks to different sessions based on research field," says Franko. "I could not perform any of these tasks without a Ph.D."

And Follow That Path

Andrea Stith joined HHMI straight from graduate school. "I met an HHMI investigator during a symposium when I was a biophysics Ph.D. student at the University of Virginia," she recalls. "He helped me set up an informational interview at HHMI, which several months later resulted in my applying for a position administering grant programs."

But after a few years at HHMI, Stith discovered that her true passion was science policy. She is currently at Shanghai Jiao Tong University doing research on higher education and research policy. "I anticipate returning to the United States in the next year. continued »

UPCOMING FEATURES

Faculty 1: Lab Management—March 12

Careers in Bioinformatics/Systems Biology—April 9

Bio/Pharma: Mythbusting about Industry—April 23

Wellcome Trust–Massachusetts Institute of Technology (MIT)

POSTDOCTORAL FELLOWSHIPS

This programme provides four years' support for recently qualified postdoctoral researchers to gain experience of research at the interfaces between biology/medicine and mathematics, engineering, computer, physical or chemical sciences.

You should propose to tackle an important biomedical research question using an interdisciplinary approach in the best laboratories first at MIT (for two to three years) and then in the UK (for two to one years respectively).

You will be a UK/EEA national (or have a relevant UK/EEA connection) with a strong background in a suitable scientific field and should be about to submit your doctoral thesis or have no more than three years' postdoctoral experience.

Deadline for submission of a full application is 7 June 2010.

Further information and application forms are available at **www.wellcome.ac.uk/mit/sci**

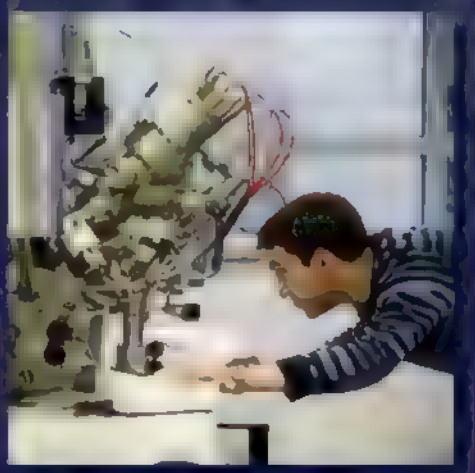

The Wellcome Trust is a global charity dedicated to achieving extraordinary improvements in human and animal health. It supports the brightest minds in biomedical research and the medical humanities.

The mission of MIT is to advance knowledge and educate students in science, technology, and other areas of scholarship that will best serve the nation and the world in the 21st century.

MIT wellcome trust

STONY BROOK

POSTDOCTORAL POSITIONS

The Research Foundation of Stony Brook University/SUNY anticipates the following postdoctoral positions being available.

- **BIOCHEMISTRY AND CELL BIOLOGY**

  The roles of the transcriptional repressor REST in neural development.
  Nurit Ballas, WC-R-6204-10-01-S

  Role of O-linked glycosylation in signaling and development
  Robert Haltiwanger, WC-R-6203-10-01-S

- **CHEMISTRY**

  Ultra nano filtration/reverse osmosis, water purification, multifunctional copolymers, polymer inorganic hybrids, polyoxometalates. Ben Chu, WC-R-6240-10-01-S

  Polymer synthesis, nanocomposites, ultrafiltration nanofiltration/reverse osmosis.
  Benjamin S. Hsiao, WC-R-6239-10-01-S

- **MOLECULAR GENETICS AND MICROBIOLOGY**

  Understanding transcriptional networks in yeast vegetative and meiotic cell cycles.
  A. Bruce Futcher, WC-R-6235-10-01-S

  Informatic analysis of high-throughput data from yeast transcriptional networks
  A. Bruce Futcher, WC-R-6237-10-01-S

  Immunology. Biochemistry of lymphocyte signaling.
  Nicholas Carpino, WC-R-6236-10-01-S

- **MARINE AND ATMOSPHERIC SCIENCE**

  Immunology and functional genomics in marine animals
  Bassem Allam, WC-R-6230-10-02-S

- **PHYSIOLOGY AND BIOPHYSICS**

  Wnt signaling in cell differentiation and early development
  Hsien-yu Wang, HS-R-6218-10-02-S

- **PSYCHIATRY**

  Anatomy of underlying photic sleep and circadian rhythm phase shift induction. Lawrence P. Morin, HS-R-6205-10-02-S

- **PSYCHOLOGY**

  Conduct behavioral experiments on self control with human and nonhuman subjects. Howard Rachlin, WC-R-6209-10-02-S

- **RADIOLOGY**

  Lead the investigation of photon counting detectors for x-ray breast imaging. Wei Zhao, WC-R-6238-10-02-S

To apply online and for information visit *www.stonybrook.edu/jobs* or mail resumés to:
Office of the President, Stony Brook University, Stony Brook, NY 11794-0701.

Stony Brook University/SUNY is an affirmative action, equal opportunity educator and employer.

Life Even Better™

We believe in the power of science to transform life and the power of people to make it happen. Created through the combination of Invitrogen Corporation and Applied Biosystems, Life Technologies is a global biotechnology company dedicated to improving the human condition. We enable people to accelerate scientific exploration, driving to discoveries and developments that make life even better.

Join us in discovering the infinite surprises and solutions that science — and you — can reveal.

www.lifetechnologies.com/careers

EOE

life technologies™

AB applied biosystems | invitrogen

Postdoctoral Fellows

wellcome trust sanger institute

Salary Range £28,000 to £35,000 dependent on experience

The Wel come Trust Sanger Institute is a world leader in genomic research, with an expanding scientific programme dedicated to understanding gene function in health & disease. Two postdoctoral positions are available immediately within the Cancer Genome Project. The Cancer Genome Project (CGP) led by Professor Mike Stratton and Dr Andy Futreal, is at the forefront of applying the latest technologies in genome analysis in the study of human cancer. The central aim is to comprehensively characterize the full repertoire of genomic alterations that can contribute to cancer, thus empowering improvements in the diagnosis and treatment of these diseases.

Postdoctoral Fellow – Cancer Genome Project Core Ref: 80574
We aim to carry out systematic genome wide sequencing, coupled with epigenetic and expression profiles, of human cancer genomes to generate comprehensive catalogues of somatic mutation. We require a self starting postdoctoral fellow to aid the bioinformatic analyses of these mutational catalogues in order to identify new cancer genes and to elucidate the mutational processes that underlie cancer development.

The successful candidate will have a PhD in a scientific discipline, ideally with a substantial component in bioinformatics or computer science (or equivalent experience) and an interest in genomic analysis. As interactions between internal team members and external collaborators will be key, they will have excellent written and verbal communication skills with the ability to prioritise tasks in order to work independently to carry out data analysis.

Postdoctoral Fellow Ref: 80573
The Kay Kendall Leukaemia Foundation have funded a research project led by Dr Peter Campbell entitled "Genome-wide characterisation of somatic mutation in acute lymphoblastic leukaemia and myeloproliferative disorders". This project will use massively parallel sequencing to identify somatic mutations in two contrasting types of haematological malignancy (i) childhood acute lymphoblastic leukaemia (ALL) associated with ETV6-RUNX1 translocations and (ii) the myeloproliferative neoplasms (MPNs).

As part of this exciting project, there is an opportunity for a highly motivated postdoctoral to direct the informatic processing of the sequence data, identification of somatic rearrangements and point mutations from massively parallel sequencing reads, confirmatory capillary sequencing and downstream analyses.

Candidates should have a PhD in a scientific discipline. Interactions between internal team members and external collaborators will be key and as such the successful candidate will exhibit excellent written and verbal communication skills and an ability to organise and prioritise their own workload.
Postdoctoral Fellows are typically in their first or second postdoctoral position as part of a period of early career research training. The posts are three year fixed term contracts. Successful applicant(s) who have submitted their PhD thesis and are awaiting their PhD award to be confirmed will be placed on a transitional pay point, currently £25,845. On confirmation applicants will be moved on to the pay scale above.
For more information on either of these roles and to apply for these positions please go to: **https://jobs.sanger.ac.uk**, to register and apply on line.
Closing date is: 28th March 2010

Postdoctoral Training Program
In Reproductive Biology & Development

KU MEDICAL CENTER

www2.kumc.edu/pdt

- Ageing and oocyte quality - D. Albertini
- Metallothionein gene expression - G. Andrews
- Physiology of sperm ion channels - G. Bianco
- Follicular development - L. Christenson
- Gonadal differentiation & function - L. Heckert
- Immunology of the placenta - J. Hunt
- Signal transduction at fertilization - W. Kinsey
- Hypothalamic-pituitary-gonadal axis - R. Kumar
- MicroRNAs & Uterine physiology - W. Nothnick
- Aryhydrocarbon receptor pathway - B. Petroff
- Maternal immune response to pregnancy - M. Petroff
- Maternal Fetal interactions - M.J. Soares
- Regulation of gonadotrophin genes - M. Wolfe

For more information contact:
William H. Kinsey, Ph.D (wkinsey@kumc.edu)
Department of Anatomy & Cell Biology, University of Kansas Medical Center
3901 Rainbow Boulevard, Kansas City, Kansas, 66160

New Phytologist Tansley Medal
for excellence in plant science

The *New Phytologist* Tansley Medal will be awarded annually in recognition of an outstanding contribution to research in plant science by an individual in the early stages of their career. Submissions are welcomed from both student and post-doctoral researchers with up to five years experience since gaining their PhD. The winner will receive a prize of £2000 GBP and the successful article will be published in *New Phytologist*, which will be accompanied by a comment from the Editor-in-Chief.

Application process

Submit an extended abstract (1000 words, with 1–2 figures) that describes (1) the research conducted, including the rationale, (2) methods, (3) key results and (4) the main conclusion, including key points of discussion. If the work has already been published then you may submit an extended abstract of a mini-review; this will focus on the area to which your publication(s) have contributed and the bullet points of the abstract can be structured to suit the contents of the mini-review. This abstract should be submitted along with your curriculum vitae, and a supporting statement from a scientist who has agreed to act as a referee for your application.

Successful applicants will be notified by July 16 2010 and asked to submit their work as a full research article no later than August 31 2010. These articles will be sent to referees and those accepted will be published in *New Phytologist*. The Tansley Medal winner will then be chosen from these accepted articles and will be announced by December, 2010.
Extended abstracts should be received by **June 18 2010**

To submit your application online or for further details please visit

http://www.newphytologist.org/tansleymedal.htm

New Phytologist — *... promoting plant science*

Roche

Post-doctoral Position in Neuropharmacology Research

Who we are
At Roche, 80,000 people across 150 countries are pushing back the frontiers of healthcare. Working together, we've become one of the world's leading research-focused healthcare groups. Our success is built on innovation, curiosity and diversity, and on seeing each other's differences as an advantage. To innovate healthcare, Roche has ambitious plans to keep learning and growing – and is seeking people who have the same goals for themselves.

The headquarters in Basel is one of Roche's largest sites. It is home to the Corporate Executive Committee, the Pharmaceuticals and Diagnostics Divisions and the global business functions. Roche Basel also covers the entire business chain from research, development and production through to marketing. Over 8,000 people from more than 60 countries work at the site.

The Position
Postdoctoral fellow at Hoffmann-La Roche Ltd in the department of CNS discovery Basel. The position foresees two years of funding. We seek a highly motivated and enthusiastic scientist to join a research group associated with several novel target discovery programs. The main focus of this position will be the characterization of neurodegenerative and psychiatric disease models in the context of the related projects. This task is multidisciplinary and requires a broad understanding of neurobiology. The successful candidate will have access to a wide array of technologies for the characterization of these models and can profit from internal expertise as well as transgenic animal models. The candidate is expected to publish results arising from this project.

Who you are
You're someone who wants to influence your own development. You're looking for a company where you have the opportunity to pursue your interests across functions and geographies, and where a job title is not considered the final definition of who you are, but the starting point.

Applicants require a PhD in neuroscience or neuropharmacology. A comprehensive understanding of neuroanatomy is required and knowledge of behavioral measures is of great advantage. Expertise with rodent handling and with techniques relevant in the fields of biochemistry and immunochemistry is requested. This position offers the unique opportunity to gain first-hand insight into discovery research at one of the leading pharmaceutical companies. We expect outstanding motivation, creativity, analytical thinking and a strong commitment to productivity.

Job ID No.: 19140
Contact Line: L. Ozmen, phone: +41 61 687 02 48

The next step is yours. To apply online today or learn about other exciting positions, please visit http://careers.roche.com

> My position allows me to participate in great science without having to pipette anything.
>
> — Mark Toone

or so and would like to continue pursuing international policy issues, possibly taking a position in the government or in the nonprofit sector," she says.

Stith got her foot in the science policy door through a fellowship at the National Science Foundation's Office of Legislative and Public Affairs through AAAS' Science and Technology Policy Fellow program—but her path is far from typical. "I have met so many people who have come to science policy in unique and personal ways and at very different points in their careers. Some have science backgrounds, others don't," she says. "I can't identify a single best way to get here."

Create Your Own Opportunities

Although a few training programs offer students exposure to different careers—such as science policy and science writing—some people have had to create their own paths.

When **Chris Gunter** was doing her postdoc in the lab of geneticist Huntington Willard, then executive editor of the journal *Human Molecular Genetics,* she approached him with the idea of a fellowship to help him with editorial tasks at the journal. He agreed and she ended up working half time on her postdoctoral research and half time on the journal. And when it came time to apply for a job she decided to pursue a career as a journal editor. "You have to be honest with yourself. Not everyone is going to be an academic PI," says Gunter. "And I was really interested in editing. When I read a paper I would ask myself 'Why is this paper in that journal?'"

At first her postdoc adviser was surprised by her choice. "He cautioned me that, if I were to step off the research track, that would be an irreversible decision," she recalls. "But once he realized that is what I wanted to do, he was very supportive."

Gunter eventually took a post at the journal *Nature* where she spent seven years as the editor responsible for manuscripts in the field of genetics. Those experiences and the wide network of contacts she established then led to a job offer as director of research affairs at the HudsonAlpha Institute for Biotechnology in Huntsville, Alabama. "My job is to make things happen," says Gunter, who is responsible for everything from helping to write grants, to recruiting scientists and students, to writing and editing papers, to publicizing institute discoveries, to organizing seminars and conferences, and fund raising. "You have to be able to multitask because many things have to move forward each day," she says. "And you have to be able to communicate to many different audiences."

Mark Toone went to a similar position straight from the bench. After completing a two-year post as associate scientist at the Paterson Institute for Cancer Research in Manchester, UK, Toone started looking for a permanent position in either academic research or research administration. At that time, Tony Pawson had taken over as director of research at the prestigious Samuel Lunenfeld Research Institute in Toronto, Canada, and was looking for someone to help run the institute. Having completed his graduate studies in Toronto, Toone jumped at the chance.

He was hired by Pawson and then obtained a Master's of Health Administration at the University of Toronto while working full time. That led to his current appointment as director of research operations, where his role is to "oversee laboratory operations, safety, and a range of institutional services, as well as new laboratory design and construction."

Toone first got turned on to the value of research administration during his postdoc at the Imperial Cancer Research Fund (ICRF, currently Cancer Research UK) in London, UK. "At the time ICRF had split its administrative duties between two highly respected scientific leaders, Dr. Paul Nurse, who looked after the scientific side of things, and Dr. John Tooze, who looked after the operations side," says Toone. "After talking with John Tooze, I began to consider a change in career plans."

Toone says that graduate school programs should put more emphasis on preparing students for different careers. "My advice for a grad student or postdoc would be to enhance your research qualifications either through work experience or formal management, project management, computing, intellectual property—whatever interests you—so that you can more easily step into stimulating roles outside of research," he says. "My position allows me to participate in great science without having to pipette anything."

Marrying Different Fields

Many careers paths marry science with a different field. **Mikhail G. Shapiro's** background was originally in business. After he co-founded Cyberkinetics Neurotechnology Systems, he became fascinated by scientific research. "It seemed so cool to actually come up with the innovation," he says. As a result, he completed a Ph.D. in biological engineering at the Massachusetts Institute of Technology. He then joined Third Rock Ventures, a venture capital firm based in Boston, where he works at the intersection of business and science. "We look for innovation in science or medicine and bring that innovation to patients by providing the capital and expertise of building a company," says Shapiro, who is a senior associate at Third Rock. "It is extremely rewarding."

He spends a lot of time talking with thought leaders in different fields, either at conferences or while visiting research institutes and biotech firms. "At our firm we don't just sit at the computer looking at business plans of companies," he explains. "We are more proactive. We will explore a scientific area and talk to experts in that area to understand what is possible. And then we might start up a company." His advice for people who would like to explore this path is to "spend some time in a startup company, even if you are just working at a bench," he says. "At the end of the day, if you are interested in making an impact on society and patients, this is a great way to do it." continued »

CREDIT: PHOTO COURTESY OF MOUNT SINAI HOSPITAL

HOWARD HUGHES MEDICAL INSTITUTE

Laboratory Head Positions at Janelia Farm

We invite applications from biochemists, biologists, chemists, computer scientists, engineers, mathematicians, neurobiologists, and physicists at all career stages who are passionate in their pursuit of important problems in basic scientific and technical research.

Appointments may be made at either of two levels:

Fellows

Fellows are independent scientists with labs of up to two additional members.

Appointments are for five years.

Group Leaders

Group leaders are independent scientists, similar to HHMI investigators, with labs of up to six additional members. The initial appointment is for six years. Thereafter, group leaders will be reviewed for reappointment every five years.

There are two application deadlines per year and the next are:

July 15, 2010 and December 15, 2010.

For more information and to submit an application:

www.hhmi.org/ref/janelia/sci

HHMI janelia farm research campus

At Janelia Farm, we pursue challenging basic biomedical problems for which future progress requires technological innovation. We focus on two research areas: the identification of general principles that govern how information is processed by neuronal circuits; and the development of imaging technologies and computational methods for image analysis. This year we have decided to broaden our foci at the Fellow level – we also seek very promising, early career stage scientists with interests beyond these two major foci. We expect that Janelia would be attractive to people with scientific programs that could benefit from collaborators or technologies already at Janelia. We value people with new perspectives who will contribute to our intellectual community.

Examples might include:

- A cell biologist looking to apply super-resolution optical microscopy to their work.
- A computer scientist interested in machine vision.
- A physicist interested in instrument development.
- A biochemist interested in single-molecule imaging.

Janelia Farm is now home to a growing, multidisciplinary community of 35 research groups, comprising postdoctoral associates, graduate students, and technicians. Our scientists are supported by outstanding shared resource facilities within a unique campus less than an hour from Washington, D.C. All laboratories are internally funded, without extramural grants. Lab heads have no formal teaching duties and minimal administrative responsibilities. Janelia Farm offers a supportive working environment with on-site child care, fitness center, and dining facilities.

Individual research groups are limited in size. We value research collaboration between groups as a mechanism to enable long-range innovative science and encourage the self-assembly of interdisciplinary teams of scientists. In addition we support external collaborative science through a scientific visitor program.

The Howard Hughes Medical Institute is an equal opportunity employer. Women and members of racial and ethnic groups traditionally underrepresented in the biomedical sciences are encouraged to apply.

University of Michigan
Medical School

POSTDOCTORAL
TRAINING OPPORTUNITIES

The University of Michigan is an outstanding training environment that combines world-class faculty and innovative programs of research with a rich academic tradition. For two decades Michigan has ranked among the top 10 medical schools in NIH research funding. This research effort is enhanced by NIH- and industry-sponsored training programs that support Postdoctoral Scholars.

The University of Michigan recognizes the essential contributions Postdoctoral Scholars make to the University's overall research mission. We welcome inquiries from graduate students nearing completion of the Ph.D. degree regarding opportunities for postdoctoral training in the following areas:

- Alcoholism Research
- Biology of Aging
- Biology of Drug Abuse
- Cancer Biology
- Cardiovascular Research
- Cell and Molecular Dermatology
- Clinical and Basic Neuroscience
- Endocrine Dysfunction
- Endocrinology and Metabolism
- Experimental Immunology
- Genome Sciences
- Hearing, Balance and Chemical Senses
- Imaging Science in Biomedicine
- Immunology and Protein Therapeutics
- Lung Disease
- Lung Immunopathology
- Medical Rehabilitation Research
- Microbial Pathogenesis
- Molecular Hematology
- Nephrology Research
- Organogenesis
- Reproductive Sciences
- Research in Gastroenterology
- Substance Abuse
- Tissue Engineering and Regeneration
- Urology Research
- Vision Research

We encourage inquiries from individuals of all backgrounds.

For more information about Sponsored Training Programs, as well as descriptions and contact information for the above programs, visit:
http://www.med.umich.edu/postdoc/sm2010.html

The University of Michigan is an equal opportunity, affirmative action employer

---

Igenica, Inc is a biopharmaceutical company based in the San Francisco Bay Area, and is focused on the creation of breakthrough antibody-based therapeutics to address the unmet medical needs of cancer patients The company has developed innovative technology platforms for discovering novel tumor antigens and cancer antibodies

Postdoctoral Scientists

These are two exciting opportunities for highly motivated individuals to join our research team in either of the following two areas

- Research relating to the application and advancement of our innovative proteomics technologies for the identification and characterization of novel cancer antigens and therapeutic antibody targets This position requires a recent PhD in a relevant discipline with a background in molecular biology, biochemistry and/or cellular signaling ideally in oncology
- Research applying and advancing our leading-edge monoclonal antibody screening technologies for the development of novel antibody therapeutics for cancer The successful candidate will drive antibody lead discovery and characterization efforts, including mechanism of action, *in vivo* proof of concept studies and innovative tumor models. This position requires, a recent PhD in a relevant discipline with a background in monoclonal antibody technologies and/or immunology and in-vivo techn.ques ideally in oncology

Candidates must be able to work independently with strong scientific investigatory skills, have the willingness and expertise to work within a multidisciplinary team of peers and outside experts, and have shown sustained research productivity supported by publications Outstanding written/verbal communication skills are essential

These positions provide an excellent opportunity to contribute significantly to our continued growth We provide a unique work environment, a competitive salary, stock options, and excellent benefits To apply, please include your name and this position title in the subject line of your email, and send your CV to: **careers@igenica.com**

For further information about Igenica please visit our website at **www.igenica.com**. *EOE*

Aalto University
School of Science and Technology

Postdoctoral Positions

Dept. of Biomedical Engineering and Computational Science (BECS) is announcing four postdoctoral research positions

Modeling the human brain: Computational techniques, neuroscience methods (e.g., MRI, TMS or MEG/EEG) and biophysics.

Computational sociology: Quantitative cognitive science, complex social networks, sociology, social psychology, computational analysis and modeling, naturalistic experimenting techniques in

Connecting to the brain: Cellular- and molecular-level experimental science, biological applications of nanotechnology and vision science

Bayesian and computational complex system theory: Computational analysis and modeling, probability theory, statistics, statistical physics

To apply, please send your resume description of research interests, and contact information of 3 persons who can give a recommendation, to Ms. Marita Stenman at the address given below, or by e-mail to marita.stenman@tkk.fi. The closing date is March 31, 2010, after which applications for unfilled positions will be considered monthly

For more information, please visit **www.becs.tkk.fi/en/work/**

BECS, Aalto University
P.O. Box 12200, FI-00076 Aalto, Finland

BECAUSE

We are focused on truly innovative science

Postdoctoral Research Fellows

Genentech is among the world's leading biotech companies, with multiple therapies on the market for cancer and other serious medical conditions.

As a Genentech Postdoctoral Research Fellow you will find yourself collaborating with world-class scientists both at the company and beyond Genentech's walls. Our postdoc positions typically last three years and offer the chance to do cutting edge research in an inspired, purposeful and resource-rich environment.

Our Late Stage Pharmaceutical and Development department currently has the following postdoc fellowships available:

Molecular Engineering and Physical Properties of Antibodies Req #1000026955
This research program has established a link between protein self-association behavior and the viscosity of the Mab formulation. Several charge based mutants have been generated and will be used to further explore the linkage between charge distribution and viscoelastic behavior.

Protein-Protein and Cosolute Interactions – Req #1000028360
The department is investigating the properties of high concentration protein solutions and different strategies for their modification. The objective of the postdoctoral research fellow will be to characterize the self-association of antibodies as well as the interactions between antibodies and co-solutes using a variety of biophysical techniques.

Surface-Protein Interactions – Req. #1000029008
During the manufacture and storage of protein biopharmaceuticals, proteins come in contact with a variety of surfaces and interfaces. The effect of these protein surface interactions on the protein solutions is not well understood especially at high protein solution concentrations. This project aims to utilize surface sensitive techniques (e.g., SPR, QCM-D, TIRF Microscopy, surface enhanced spectroscopy etc.) to examine the dynamics of protein adsorption and the effect of surfaces/interfaces on the structure and conformation of the protein.

Genentech is dedicated to fostering an environment that is inclusive and encourages diversity of thought, style, skills and perspective. To learn more about our current opportunities, please visit **careers.gene.com** and reference the appropriate Req #. Please use "Ad – Science" when a source is requested. Genentech is an equal opportunity employer.

Genentech
A Member of the Roche Group

Faculty Feature: March 12

Lab Management
The Human Elements

Don't miss this special career feature in *Science* or online at **ScienceCareers.org**

Science Careers
From the journal *Science* AAAS

MFPL **Max F. Perutz Laboratories**

Vienna International Post-Doctoral Training in Molecular Life Sciences

With support from the Austrian Ministry of Science and Research and the City of Vienna, the Max F. Perutz Laboratories launch a unique post-doctoral training programme, the Vienna International Post Doctoral Training in Molecular Life Sciences (VIPS).

Join the VIPS

Application Deadline 1st of May 2010

www.mfpl.ac.at/vips

Our Mission:
To promote Post Docs on their way to scientific independence

Our Offer:
- 3-5 years Post-Doctoral training
- Independent research budget
- Travel money
- Mentoring programme
- Career development
- Grant writing support
- Child care

Our profile:
MFPL is part of the Vienna Biocenter Campus. Austria's top address for molecular life sciences. We offer a broad coverage of research areas, ranging from Biochemistry, Cellular Biology and Computational Biology to Organismal Biology and Neurosciences.

Spend your post-doctoral training in a thriving scientific environment in one of the most liveable cities of the world!

Contact: Gabriele Permoser, e-mail: vips@mfpl.ac.at

City of Vienna

Another career that marries science with the business side of science is patent law. **James Dilmore** went from bench to patent law straight after obtaining his Ph.D. in 2000 from the University of Pittsburgh. "The wife of one of my Ph.D. committee members was working at a law firm as a scientific adviser and was about to leave the position, so she introduced me to her boss," he recalls.

But leaving the bench was not an easy decision. "I was very well versed in several areas of cellular neuroscience. I had spent a lot of time and effort developing those skills and knowledge. I recognized that I would not be using the experimental techniques directly and that I might not be working on my specific areas of expertise," he recalls. "It was a bit unnerving, honestly."

Nonetheless, he took the plunge. He first joined the Pittsburgh-based international law firm Reed Smith as scientific adviser. After passing the patent bar exam in April 2002, Dilmore became a patent agent at the firm. His responsibilities include drafting and filing patent applications on behalf of several clients, as well as continuing to assist attorneys involved in litigation cases.

He cannot, however, do things like file appeals from the US Patent and Trademark Office (USPTO) to courts, negotiate licenses to use patented technology, or sue those who breach contracts or infringe patents—tasks that require a law degree. So, Dilmore decided to take the plunge once again and last year started attending law school while working full time. "My kids got to the ages, 12 and 15, where I had somewhat more free time. It also made sense in terms of career progression for me to obtain a law degree," says Dilmore.

"My advice to graduate students and postdocs is to network and know a lot of different people."
—Chris Gunter

Taking a Risk

Dilmore did not have any experience in law before joining his firm, but his career choice turned out to be a good fit. His advice for science Ph.D.s considering a law career is to look at some patent applications that are freely downloadable from USPTO website. Also, most universities offer courses in intellectual property that any student can take. Some universities also have intellectual property or technology transfer offices, where students may volunteer or intern.

Like Dilmore, **Teresa Calzonetti** had not done anything other than research before becoming an instructor at Frederick Community College—a two-year college in Maryland where she teaches an introductory biology course to about 40 students. "I always thought that I would like teaching, but I had no teaching experience," she says.

She called the head of the biology department at the college and applied for a part-time teaching position, which she obtained three weeks before classes started. "I did not sleep for those three weeks," she says. Having taught the class for two years now, Calzonetti has gotten over that initial anxiety and is getting ready to increase her teaching load. "I would like to teach more sessions and new classes," she says. "In addition to enjoying teaching science, the best thing about the job is that I am getting to learn all the stuff again. Its like I am taking a course and every semester I am interested in it all over again."

Making a transition from research can be a scary proposition and one that many students and postdocs will have to make without any support and guidance from their research mentors. "My advice to graduate students and postdocs is to network and know a lot of different people," says Gunter. "And do what appeals to you. Don't just listen to what people say you should do, especially if they think you will be a failure unless you stay in research."

Regardless of the chosen path, says HHMI's Franko, the most important thing is "to make sure you are running *to* a job you really think you will enjoy and be good at—and not running *away* from a job that you are not enjoying or at which you are not currently successful. You should do as much research as possible through informational interviews, volunteering, and internships, to make sure that you do not need to be doing bench research to be challenged and satisfied in your job."

Laura Bonetta is a scientist turned freelance writer based in the Washington, D.C., area.

DOI: 10.1126/science.opms.r1000085

CREDIT: PHOTO BY SCOTT GLASSER

FEATURED PARTICIPANTS

AAAS Science and Technology Policy Fellow Program
fellowships.aaas.org

Cyberkinetics Neurotechnology Systems
www.cyberkinetics.com

Frederick Community College
www.frederick.edu

Howard Hughes Medical Institute
www.hhmi.org

HudsonAlpha Institute for Biotechnology
www.hudsonalpha.org

Imperial Cancer Research (Cancer Research UK)
www.cancerresearchuk.org

Massachusetts Institute of Technology
www.mit.edu

National Postdoctoral Association
www.nationalpostdoc.org

National Science Foundation
www.nsf.gov

Paterson Institute for Cancer Research
www.paterson.man.ac.uk

Reed Smith
www.reedsmith.com

Samuel Lunenfeld Research Institute
www.lunenfeld.ca

Shanghai Jiao Tong University
www.sjtu.edu.cn/english/index/index.htm

Third Rock Ventures
www.thirdrockventures.com

University of California, Davis
www.ucdavis.edu

University of Pittsburgh
www.pitt.edu

University of Toronto
www.utoronto.ca

University of Virginia
www.virginia.edu

US National Institutes of Health
www.nih.gov

POSTDOC OPPORTUNITIES

BIPM

Bureau international des poids et mesures

Research Fellow
Quantification of complex analytes for Laboratory Medicine

Background
The International Bureau of Weights and Measures (BIPM) in Sèvres, France, is an intergovernmental scientific organization whose mandate is to provide the basis for a coherent system of measurements throughout the world, traceable to the International System of Units (SI). It has an international staff of over 70 and an annual budget of about 13 million euros. Further information about the BIPM can be found on the website **www.bipm.org.**
The Chemistry Department of the BIPM organizes international comparisons related to organic substance purity determination. An extension of this program is being developed to support the establishment of Reference Measurement Systems in the field of diagnostics and therapeutics.

The closing date is 31 March 2010

Duties
The BIPM has a vacancy for a Research Fellow for the development of analytical methods for the quantification of complex analytes (amino acids, peptides, and small proteins).

The successful candidate will undertake projects to develop and improve qualitative and quantitative analytical methods, with a focus on high-performance liquid chromatography – mass spectrometry (LC-MS/MS), to identify impurities and to provide precise and accurate measurements for traceable mass fraction value assignments.

Qualifications
Applicants should have:
- a Ph.D. degree in a relevant field (chemistry, biochemistry or laboratory medicine),
- experience in LC-MS/MS of complex molecules relevant to therapeutics/diagnostics,
- a fluent level of spoken and written English;
- the ability to work in a multicultural environment and
- the ability to maintain good working relations inside and outside the organization.

Previous experience with peptide/protein chemistry (hydrolysis, digestion, modification, labeling and purification) and familiarity with the operation of other relevant analytical instrumentation would be advantages.

Employment conditions
The BIPM offers a full-time 2-year fixed-term appointment. The BIPM offers remuneration and conditions of employment detailed in its *Staff Regulations, Rules and Instructions*, which are comparable with those of other international organizations based in France. It manages its own contributory pension scheme and subscribes to a private medical insurance for its staff and their families.

Applications
The BIPM encourages applications from both women and men with relevant qualifications. A full *Curriculum Vitae* (C.V.) and covering letter should be sent by paper mail to the Director, BIPM, Pavillon de Breteuil, F-92312 Sèvres Cedex, France, by **31 March 2010**, with a copy by email to: ldelloro@bipm.org. The selected applicants may be requested to take a written test and only shortlisted applicants will be invited for an interview. Applications should include the names of two referees who will be asked to comment upon the candidate's suitability for the post.
Requests for additional information may be addressed to Dr Robert Wielgosz, Director of the Chemistry Department, **rwielgosz@bipm.org.**

Joining the USF Team is now easier than ever with our on-line application!

DEAN
College of Marine Science

The University of South Florida seeks a dynamic and visionary leader to take the helm of the College of Marine Science. The College of Marine Science is committed to addressing a myriad of societal issues, such as overfishing, coastal erosion, red tides, ocean pollution, ocean noise, declining coral reefs, hurricane predictions, sea level rise, floods, ocean acidification, and drought, in order to build better, more environmentally-sustainable and safe communities. It is the University's goal to have the College of Marine Science recognized as one of the pre-eminent institutions of its kind in the world. Toward this end, we seek a proven leader who can help shape and articulate the vision for the College, develop a compelling strategy to achieve that vision, and possess the charisma and communication necessary to work effectively with a wide range of stakeholders to build a program and foster a team that are second to none.

The College of Marine Science has an extensive array of active research programs encompassing pure and applied science and the development of new technology. College faculty engage in research supported by a variety of federal and state agencies and other organizations. In addition, teams of researchers and technical experts partner with engineers to develop innovative instrumentation for oceanographic research through the College's Center for Ocean Technology. Students at the College of Marine Science pursue interdisciplinary graduate degrees in all aspects of oceanography. Activities in the College are exemplary of the university's strategic priorities which include research and innovation; student success; integrated interdisciplinary inquiry; global literacy and impact; and community engagement.

As the chief executive and academic officer for the College, the Dean sets the standard for intellectual engagement and accomplishments by providing strategic vision for and operational leadership of the academic programs. The dean works to advance marine science scholarship and education - promoting initiatives within and outside of USF, enhancing excellence through diversity in educational programs and faculty and student recruitment, and linking the work of the marine science faculty and students to other disciplines, such as the natural sciences, engineering, education, public health and the arts. The Dean also serves as the College's public voice, articulating its contributions to local, state, regional, national, and international agencies and communities and pursuing an aggressive development program to build the College's resources. The Dean of the College of Marine Science reports directly to the USF Executive Vice President and Provost.

The location of the College in St. Petersburg, Florida, affords ready access to Tampa Bay and the Gulf of Mexico. With the Center for Coastal Geology and Regional Studies of the U.S. Geological Survey, the Southeast Regional Office of NOAA's National Marine Fisheries Service, the Research Institute of the Florida Fish and Wildlife Conservation Commission, Mote Marine Laboratory, SRI International and the office of the Tampa Bay Estuary Program, St. Petersburg has one of the largest concentrations of marine scientists in the southeastern United States. Bayboro Harbor is homeport to the R/V Bellows and the R/V Weatherbird II research vessels operated by the Florida Institute of Oceanography (FIO) which shares space in one of the two principal laboratory-office buildings of the College.

Minimum qualifications include: an earned doctorate in a discipline relevant to the College of Marine Science, demonstrated leadership and administrative experience, and a solid reputation and record of scholarship in a field of science associated with the ocean.

Preferred qualifications include: a demonstrated ability to attract and manage resources from a variety of public and private sources, evidence of understanding of the processes required for outstanding graduate education and student success, proven ability to facilitate collaborative, interdisciplinary work involving university and community partners, strong interpersonal communication skills and a demonstrated commitment to diversity.

Please send applications to the attention of: **Dr. Eric M. Eisenberg, Chair of the Search Committee for the Dean of Marine Science.**

Applicants should apply through the University's online application system, which may be accessed at **https://www.usf.edu/jobs**. Applicants will be asked to submit a letter stating interest in the position and the extent to which they meet the minimum and preferred qualifications; curriculum vitae; and the names, addresses, phone numbers, and e-mails of five professional references. References will not be contacted until the advanced stages of screening, and candidates will receive prior notification. Applications will be accepted until the position is filled. The initial review of applications will commence April 4, 2010. If you have any questions regarding this position or this process, please contact **Maryhelen Shuman-Groh at mshumangroh@usf.edu or 813-974-5567.**

For additional information regarding the University of South Florida and the College of Marine Science please visit the following websites: **http://www.usf.edu** and **http://www.marine.usf.edu**

The University of South Florida is one of the nation's top public research universities and one of only 25 public research universities nationwide with very high research activity that is designated as community engaged by the Carnegie Foundation for the Advancement of Teaching. USF was awarded $380.4 million in research contracts and grants in FY 2008/2009. The university offers 232 degree programs at the undergraduate, graduate, specialist and doctoral levels, including the doctor of medicine. The USF System has a $1.8 billion annual budget, an annual economic impact of $3.2 billion, and serves more than 47,000 students on institutions/campuses in Tampa, St. Petersburg, Sarasota-Manatee and Lakeland. USF is a member of the Big East Athletic Conference.

The University of South Florida is an equal opportunity, affirmative action, equal access institution. For disability accommodations contact Maryhelen Shuman-Groh at (813) 974-5567 or TDD (813) 974-1510 at least five working days in advance of need.

USF UNIVERSITY OF SOUTH FLORIDA

• TAMPA • ST. PETERSBURG • SARASOTA - MANATEE • POLYTECHNIC

FDA Commissioner's Fellowship Program

Touch the Lives of All Americans!

The FDA Commissioner's Fellowship Program is a two-year training program designed to attract top-notch health professionals, food scientists, epidemiologists, engineers, pharmacists, statisticians, physicians and veterinarians. The Fellows work minutes from the nation's capital at FDA's new state-of-the-art White Oak campus in Silver Spring, Maryland or at other FDA facilities. The FDA Commissioner's Fellowship offers competitive salaries with generous funds available for travel and supplies.

Coursework and Preceptorship

The FDA Commissioner's Fellowship program combines coursework designed to provide an in-depth understanding of science behind regulatory review with the development of a carefully designed, agency priority, regulatory science project.

Who Should Apply?

Applicants must have a Doctoral level degree to be eligible. Applicants with a Bachelor's degree in an Engineering discipline will also be considered. Candidates must be a U.S. citizen, a non-citizen national of the U.S., or have been admitted to the U.S. for permanent residence before the program start date. For more information, or to apply, please visit: **www.fda.gov/commissionersfellowships/default.htm**.

Applications will be accepted from January 1, 2010 – March 15, 2010

POSTDOC OPPORTUNITIES

Postdoctoral Associate Laboratory of Dr. Hsien-Yu Wang

Stony Brook University's NIDDK Training Program is seeking a postdoctoral associate in stem cell research who holds US Citizenship/permanent residency and a Ph.D. in a related field or foreign equivalent in biological sciences.

The function and regulation of Frizzled signaling and its control of early development will be explored by using powerful techniques of molecular and cell biology, proteomics, and biosensors technology.

For a full position description, application procedures, or to apply online, visit *www.stonybrook.edu/jobs*
Job Reference # HS R 6218.10-02.SI
or submit a cover letter and resume/C.V. to
Cathy Arrighetta, Postdoctoral Associate
(6218) Search, Human Resources Department
390 Administration Building
Stony Brook University
Stony Brook, NY 11794-0751

Fax (631) 632-2338

Equal Opportunity/Affirmative Action Employer. Women, people of color, individuals with disabilities, and veterans are encouraged to apply.

STONY BROOK

Medical Research Council Cancer Cell Unit Cambridge, UK

Programme leader & Programme leader-track appointments

Applications are invited for group leader positions in the MRC Cancer Cell Unit (CCU) to lead independent research programmes supported by the Medical Research Council. Funding is available for the salary of the group leader, research staff and laboratory consumables.

Applications are invited from non-clinical or clinical candidates with experience in cellular and molecular studies of cancer, who wish to investigate mechanisms in epithelial carcinogenesis and apply their research to cancer diagnosis and treatment. Areas of particular interest include oncogenic signaling in cancer pathogenesis and therapy, genome maintenance in cancer cells, and cell-cell interactions during carcinogenesis.

Applicants with other relevant interests will also be considered. We encourage and can support approaches involving genetically engineered mouse models, chemical tools, or translational research with clinical application. We expect applicants to demonstrate how their research contributes to the Unit's strategy, and integrates with existing programmes.

The CCU provides an outstanding environment for cancer research, supporting some 8 research groups and a total of 80 bench scientists.

It offers an excellent range of core facilities and expertise in molecular, cellular and clinical sciences, providing multiple opportunities for collaborative studies (www.hutchison-mrc.cam.ac.uk/).

The CCU is a key participant in the Cambridge Cancer Centre, enabling access to a wide range of laboratory and clinical infrastructure, and the opportunity to engage in interdisciplinary collaborations with Cambridge colleagues in the biological, physical, chemical and engineering sciences.

Candidates for programme leader positions should have an internationally strong track record of relevant independent research, and a proven ability to lead a research team, pursuing original approaches to long term research goals. Programme leader track appointments will be made for those who demonstrate the potential to develop into programme leaders within six years.

Salary within the MRC's pay structure will be in excess of £44,314 pa for non-clinical appointments commensurate with achievements and experience. Honorary clinical appointments, with an associated clinical salary, will be sought for clinical scientists.

Benefits include a flexible pay and reward policy, optional MRC final salary Pension Scheme, and excellent on-site sports and social facilities. Assistance with relocation expenses is also available.

Further information is available from Professor Ashok Venkitaraman **lks27@hutchison-mrc.cam.ac.uk**

If you would like to receive the advert for this post in large print, Braille, audio, or electronic format/hard copy, please contact the Recruitment team at the MRC Shared Service Centre on the telephone number below or at **recruitment@ssc.mrc.ac.uk.**

Applications for this role should be made online at **jobs.mrc.ac.uk.** Please upload a full CV, a brief statement of no more than 3 A4 pages describing research accomplishments, proposed future research and its relevance, and the names and addresses of three referees.

If you do not have internet access or you experience technical difficulties please call +44 (0)1793 301260 quoting the reference CCU10/060.

Closing date: 1 April 2010.

For further information on the MRC visit **www.mrc.ac.uk**

The Medical Research Council is an Equal Opportunities Employer and operates a strict no smoking policy 'Leading science for better health
The MRC is an Equal Opportunities Employer

Assistant Professor
Molecular Immunology or Cell Signaling

Stony Brook University's The Department of Molecular Genetics and Microbiology in the School of Medicine invites applications for a tenure-track faculty position at the assistant professor level. Applicants must have a Ph.D. or M.D./Ph.D. and have at least three years of postdoctoral experience. The successful candidate will participate in the Department's educational mission of graduate and medical school teaching, establish a vigorous extramural research program, and perform University and Departmental service as needed. Outstanding candidates working in molecular immunology or cell signaling as they relate to infection or cancer are encouraged to apply. The Department of Molecular Genetics and Microbiology, and the adjacent Center for Infectious Diseases and the Stony Brook Cancer Center, provide a highly interactive scientific community with world-class research facilities. The School of Medicine and Stony Brook University maintain state-of-the-art core facilities that provide support in the following areas: microscopy and imaging, flow cytometry, proteomics, microarray analysis, bioinformatics, animal maintenance, monoclonal antibody production, DNA sequencing, cell/tissue culture support, and BSL-3 containment. To ensure full consideration, applications should be received by March 31, 2010. The review of applications will continue until the position is filled.

For a full position description or application procedures, visit ***www.stonybrook.edu/jobs*** (Jobs Reference #: F-6252 10-02). To apply, candidates should submit electronically a curriculum vitae, a three-page summary of accomplishments and future research interests, and the names and addresses of three references as a compiled PDF to *SBUH_MGM_Faculty_Search@notes.cc.sunysb.edu*. Alternatively, submit materials to: Dr. James B. Bliska, Chair of Assistant Professor (6252) Search, Department of Molecular Genetics and Microbiology, 130 Life Sciences Building, Stony Brook University, Stony Brook, NY 11794-5222.

STONY BROOK UNIVERSITY MEDICAL CENTER

Equal Opportunity/Affirmative Action Employer. Call 631-444-4700 for a disability-related accommodation.

USC
Tenure Track Assistant Professor
CELL and DEVELOPMENTAL BIOLOGY/ REGENRATIVE MEDICINE/GENETICS

The University of Southern California (USC) Ostrow School of Dentistry and Keck School of Medicine are jointly recruiting two tenure-track Assistant Professors to conduct cutting-edge research in the areas of cell and developmental biology, tissue regeneration, cell signaling and/or gene regulation. The successful candidates will establish research programs with relevance to craniofacial and skeletal biology. Examples include molecular mechanisms of organogenesis, stem cell biology, and genetics of craniofacial malformations. Competitive salary and start-up package, access to core facilities at USC, and participation in graduate training are available for broadly trained PhD, MD, DDS/PhD, or MD/PhD. The successful candidates are expected to develop independent extramurally funded research programs, which complement our interests as described in **http://www.usc.edu/hsc/dental/ccmb/** and **http://www.usc.edu/programs/pibbs/site/**

Applicants should send their curriculum vitae, including current and future research directions, and arrange to have three letters of reference sent to

Dr. Yang Chai
Chair of the Search Committee
c/o Ms. Patricia Thompson
Center for Craniofacial Molecular Biology
School of Dentistry
University of Southern California
2250 Alcazar Street, CSA 103
Los Angeles, CA 90033
pathomps@usc.edu
Fax (323)442-2981

The University of Southern California values diversity and is committed to equal opportunity in employment

Edward E. Whitacre Jr. College of Engineering

The Maddox Chairs *in Energy* at Texas Tech University

The Edward E. Whitacre Jr. College of Engineering at Texas Tech University is committed to expanding these **two exceptionally large endowed chairs at over $7 million each**, to become one of the nation's leaders in finding solutions to the world's energy challenges. The college is seeking world-class researchers in solar and sustainable energy as candidates for the Maddox Chairs.

Donovan Maddox Distinguished Engineering Chair *in Solar Energy*

Candidates are expected to have national and international reputation in solar energy based on research publications. In addition, a record of acquiring external resources to support research, team building, and mentoring of associates and graduate and undergraduate students is necessary. The holder of the Donovan Maddox Chair will be expected to not only bring his or her own research activities to the Whitacre College of Engineering, but also to build a collaborative community of scholars at Texas Tech Industrial to solar energy research, thereby building a world-class research program. The appointment will be as a full professor in the Whitacre College of Engineering.

Jack Maddox Distinguished Engineering Chair *in Sustainable Energy*

Candidates with exceptional and diverse backgrounds in energy sciences and engineering are sought for this endowed position. The successful candidate will demonstrate a national and international reputation for contributions to the solution or advancement of the state of the art on a variety of research issues in the sustainable energy fields including energy efficiency, biofuels, wind power, tidal power, geothermal, and energy storage. The successful candidate along with the Donovan Maddox Chair in Solar Energy, will set the tone, vision, and the path in order to build a nationally and internationally recognized program at Texas Tech University in sustainable energy research. The appointment will be as a full professor in the Whitacre College of Engineering.

Screening will begin upon the receipt of applications and will continue until the position is filled. Candidates' names will not be made public until the final stages of the search.
Curriculum vitae and the names and contact information of at least four references should be submitted at www.coe.ttu.edu/maddox. To nominate a colleague for these chairs, visit www.coe.ttu.edu/maddox. Nominations can be made anonymously.

Questions about the Jack Maddox or Donovan Maddox Chairs should be directed to:
Jack Maddox and Donovan Maddox Search Committees
Texas Tech University · Whitacre College of Engineering
Box 43103 · Lubbock, Texas 79409-3013 · engineeringdean.coe@ttu.edu · 1.800.528.5583

Texas Tech University | Whitacre College of Engineering
1.800.528.5583 | www.coe.ttu.edu/maddox

THE HONG KONG UNIVERSITY OF SCIENCE AND TECHNOLOGY

Departments of Biochemistry and Biology
FACULTY POSITIONS

HKUST is a publicly-funded research university with strong graduate programs. The Departments of Biochemistry and Biology are two dynamic departments with well-equipped modern facilities and have active research programs in the following areas.

Department of Biochemistry: cellular regulation and signaling, biotechnology & medicinal biochemistry, and macromolecular structure and function

Department of Biology: cell biology, developmental biology, synaptogenesis, signal transduction in cell and animal models, plant biotechnology, and marine and environmental sciences

Applications are invited for tenure-track positions at Assistant Professor and Associate Professor levels, specifically in the areas of

Department of Biochemistry (http://www.ust.hk/bich/)
molecular and cellular biology with research focus in neuroscience using animal models, and structural biology using X-ray crystallography

Department of Biology (http://www.ust.hk/~webbio/)
cellular and organismal biology (e.g. ecology, marine biology, plant biology, microbiology, immunology etc.)

Scientists prominent in other areas will also be considered by the Departments based on their research interests.

Applicants should have a PhD degree, postdoctoral experience and the ability to establish an independent research program. Teaching responsibilities include undergraduate and postgraduate courses.

Starting salary will be commensurate with qualifications and experience. Fringe benefits including medical/dental benefits and annual leave will be provided. Housing benefits will also be provided where applicable. Initial appointment will normally be on a three-year contract, renewable subject to mutual agreement. A gratuity will be payable upon successful completion of contract.

Applications indicating the department and areas applied for, together with a curriculum vitae, a short statement on research interests and the names and addresses of 3 referees should be sent to the respective search committees before **31 March 2010**. Review of applications will start from April 2010 and will continue until the positions are filled.

Department of Biochemistry: The Chair of the Search and Appointments Committee (Prof. Mingjie ZHANG), c/o The Secretary of SAC, Department of Biochemistry, The Hong Kong University of Science and Technology, Clear Water Bay, Kowloon, Hong Kong. (email: bcamy@ust.hk)

Department of Biology: The Chair of the Search and Appointments Committee (Prof. Peiyuan QIAN), Department of Biology, The Hong Kong University of Science and Technology, Clear Water Bay, Kowloon, Hong Kong. (email: bopeqian@ust.hk)

(Information provided by applicants will be used for recruitment and other employment-related purposes.)

One focus: join our shared commitment to improve the lives of cancer patients everywhere.

The innovative science of a leading American biopharmaceutical company plus the global assets of Takeda, Japan's largest pharmaceutical company, equal one global commitment to oncology.

Millennium: The Takeda Oncology Company is developing an extensive pipeline — among the top in oncology worldwide — with more than 17 compounds in development for a broad range of solid and hematological cancers.

Come to where lifesaving science meets lifechanging opportunities. At Millennium, you'll help develop breakthrough treatments that can make a difference in patients' lives. All in a dynamic, collaborative environment where you can be yourself — and do your best science. To learn more or apply, visit us at **millennium.com**.

Millennium has opportunities in the following areas:

- Clinical Development
- Clinical Informatics
- Clinical Operations
- Clinical Pharmacology
- Clinical Research – Oncology
- Formulations
- Global Investigational Supply Operations
- Product Safety
- Regulatory CMC
- Regulatory Operations
- Regulatory Therapeutics

MILLENNIUM
THE TAKEDA ONCOLOGY COMPANY

CHAIR
Department of Microbiology and Immunology
Vanderbilt University School of Medicine

Vanderbilt University School of Medicine is actively searching for a new Chair for the Department of Microbiology and Immunology to succeed **Dr. Jacek Hawiger** who is stepping down after 20 years as chair. This is an outstanding opportunity for a visionary new department chair to build upon a substantial base of existing excellence in the Department of Microbiology and Immunology, as well as in the Divisions of Infectious Diseases in the Departments of Medicine and Pediatrics.

We seek outstanding candidates with Ph.D., M.D., M.D./Ph.D., or equivalent, degrees that have a demonstrated track record of seminal research accomplishments coupled with outstanding interpersonal skills and leadership ability. The ideal candidate should be able to articulate a compelling vision for the future of research and educational opportunities in the field. Our institution is committed to providing the resources needed to execute on that vision.

Review of applications is effective immediately, and the position will remain open until filled. Applicants should submit a cover letter describing their interest along with a full curriculum vitae and names and addresses of three references to:

Samuel A. Santoro, M.D., Ph.D.
Chair, Microbiology & Immunology Search Committee
C/o Sherrie Leach, Committee Assistant
Vanderbilt University School of Medicine
320 Light Hall
Nashville, TN 37232-0260
Telephone: 615-936-2287
Fax: 615-936-2296
E-mail: samuel.santoro@vanderbilt.edu

Vanderbilt University is an Equal Opportunity/Affirmative Action Employer.

UNIVERSITY OF LIVERPOOL

School of Physical Sciences
Stephenson Institute for Renewable Energy

Chair of Chemistry

Salary Negotiable

The University of Liverpool invites applications for a Chair in the area of chemistry and energy. Possible disciplines are Materials Chemistry, Electrochemistry, or a closely related field. The Stephenson Institute is an interdisciplinary research institution within the School of Physical Sciences, which focuses on energy research. It will be creating a strong presence in the North West of England. You will be expected to be an internationally leading scientist in chemistry with applications in the energy area, for example in photovoltaics, carbon capture and storage, sustainable feedstocks, batteries, fuel cells, hydrogen generation and storage. You will also be expected to take a leading role in the Institute in extending existing research networks within the University, in building new networks internationally and in contributing to the strategic leadership of the Institute. The Department of Chemistry has research groupings in organic and biomolecular chemistry, catalysis, materials chemistry, surface science, theoretical and computational chemistry, and chemistry on the nanoscale. The Materials Chemistry group has a strong presence in the fields of polymers, oxides and porous materials for energy applications.
For information about the Department visit www.liv.ac.uk/chemistry **Job Ref: A-571742/S**

Chair of Condensed Matter Physics

Salary Negotiable

The University of Liverpool invites applications for a Chair in Condensed Matter Physics or a closely related field. The Stephenson Institute is an interdisciplinary research institution within the School of Physical Sciences, which focuses on energy research. It will be creating a strong presence in the North West of England. You will be expected to be an internationally leading scientist in an area of condensed matter related to energy, for example, photovoltaics, solar harvesting, or energy transport. You will also be expected to take a leading role in the Institute in extending existing research networks within the University, in building new networks internationally and in contributing to the strategic leadership of the Institute. The Department of Physics has research groupings in Particle Physics, Nuclear Physics, Condensed Matter and Accelerator Physics. The Condensed Matter group has a strong presence in the fields of nanoscale and surface physics of materials, and cellular and molecular biophysics. There is strong involvement at current and future UK and international facilities. For information about the Department visit www.liv.ac.uk/physics **Job Ref: A-571741/S**

Closing date for both posts: 29 March 2010

For full details, or to request an application pack, visit www.liv.ac.uk/working/job_vacancies/ or e-mail jobs@liv.ac.ukTel 0151 794 2210 (24 hr answerphone) please quote job ref in all enquiries.

COMMITTED TO DIVERSITY AND EQUALITY OF OPPORTUNITY

Stonewall DIVERSITY CHAMPION

POSITIVE ABOUT DISABLED PEOPLE

POSITIONS OPEN

ASSISTANT/ASSOCIATE PROFESSOR
The University of Maryland, College Park

The Virginia-Maryland Regional College of Veterinary Medicine at the University of Maryland in College Park, Maryland, invites applications from qualified individuals for two (2) tenure/tenure-track faculty positions in the area of bacterial or viral diseases of zoonotic and/or public health implications. Areas of interest include host-pathogen interactions and immunological mechanisms involved in responses to bacterial or viral infections. The successful candidate is expected to establish an independent, externally funded research program. Both positions require 80 percent research and 20 percent teaching responsibilities. The position(s) offers ample laboratory space and access to excellent animal ABSL-2 and ABSL-3 facilities.

A Ph.D. or D.V.M.-Ph.D. with relevant postdoctoral training is required. Candidates applying at the Associate Professor level must show significant past and present funding success. Screening of applicants will begin April 15, 2010. Submit a letter of application, curriculum vitae, statement of research interest, and names of three references electronically in PDF format to: **LaShae Green, Executive Coordinator, Department of Veterinary Medicine, 8075 Greenmead Drive, University of Maryland, College Park, MD 20742. Telephone: 301-314-6834; e-mail: lashae@umd.edu.**

The University of Maryland is an Affirmative Action/Equal Opportunity Employer; women and minorities are encouraged to apply.

HUMIGEN, L.L.C., the Institute for Genetic Immunology (**website: http://www.humigen.org**), invites applicants for a **TEAM LEADER** position. We are interested in candidates dedicated to research in the field of human immunology and immune-mediated diseases. The successful candidate will be expected to develop a strong and independent research program geared toward translational research, with goals directed to biomarker and drug discovery. The Team Leader will join our current research teams which focus on genetic immunology and genomic immunoepidemiology, and take advantage of close ties with the research effort of our sister company, Medical Diagnostic Laboratories (**website: http://www.mdlab.com/html/rd_index.html**) in pharmacogenomics, antigen discovery, cancer biology, and antimicrobial resistance. Publication and presentation of scientific research as well as the creation of intellectual property are strongly encouraged. Qualified candidates will possess Ph.D. and five years of postdoctoral experience. We offer competitive salary, comprehensive benefits including health, life, disability insurance, and 401(k). To apply, please submit cover letter, curriculum vitae, two- to three-page research plan, and three letters of recommendation. Please reference IMMUNO with your electronic submission to **e-mail: jobs@mdlab.com.** *HUMIGEN is an Equal Opportunity Employer.*

FACULTY POSITION IN OBESITY/WEIGHT MANAGEMENT OR RELATED FIELD

The Department of Nutrition and Food Science at Auburn University is seeking an **ASSISTANT/ASSOCIATE PROFESSOR** with a focus on obesity/weight management or related area. Successful candidate must hold a Ph.D. in nutrition, physiology, biochemistry, endocrinology, epidemiology, behavioral sciences, or related field. For more details, please see **website: http://www.humsci.auburn.edu/nufs/nufs-announcements.php.** *Affirmative Action/Equal Opportunity Employer.*

CAREER OPPORTUNITY. Doctor of Optometry (O.D.) degree in 27 months for Ph.D.s in science and M.D.s. Excellent career opportunities for O.D.-Ph.D.s and O.D.-M.D.s in research, education, industry, and clinical practice. This unique program starts in March of each year, features small classes, and has 12 months devoted to clinical care.

Contact the **Admissions Office, telephone: 800-824-5526** at **The New England College of Optometry, 424 Beacon Street, Boston, MA 02115.** Additional information at **website: http://www.neco.edu. E-mail: admissions@neco.edu.**

POSITIONS OPEN

ASSOCIATE PROFESSOR
in Below Ground Ecology

The Department of Plant Biology at the University of Georgia invites applications for the Haines Family Professorship in Below Ground Ecology. This new position will focus on the below ground component of plant ecology: plant roots and their interactions with their environment, other plants, and soil organisms (including fungi, bacteria, and herbivores) and soil processes (including nutrient and water cycling). We seek an individual who addresses fundamental ecological and evolutionary questions and who integrates field- and lab-based research approaches with molecular tools and techniques. The successful candidate will have a Ph.D. degree and a record of scientific productivity appropriate for appointment at the level of Associate Professor. She/he is expected to continue and expand a vigorous, externally funded research program and to teach and train undergraduate and graduate students. To apply, the following should be submitted at **website: http://www.plantbio.uga.edu/positions.html**: (1) a single PDF file containing a cover letter, curriculum vitae, and short statements of research interests and teaching philosophy; (2) a single PDF file containing three reprints of research papers; (3) four letters of recommendation submitted by references. The search will remain open until the position is filled. Complete applications (including letters) received by March 25, 2010, are assured full consideration. *The Franklin College of Arts and Sciences, its many units, and the University of Georgia are committed to increasing the diversity of its faculty and students, and sustaining a work and learning environment that is inclusive. Women, minorities, and people with disabilities are encouraged to apply. The University is an Equal Employment Opportunity/Affirmative Action Institution.*

The Department of Research and Development at Medical Diagnostic Laboratories, L.L.C. (MDL) invites applicants for a neurobiology **TEAM LEADER** position. The successful candidate is expected to develop a strong and independent research program geared toward translational research focused on disease-based biomarkers or drug discovery platforms. The team leader will join our current research teams which focus on aspects of antimicrobial resistance, cancer biomarker discovery, genetic immunology, pharmacogenomics, and antigen discovery. Publication and presentation of scientific research as well as the creation of intellectual property are strongly encouraged. Visit **website: http://www.mdlab.com/html/rd_index.html** for more information about our Department. Qualified candidates will possess Ph.D. and three years of postdoctoral experience. We offer competitive salary, comprehensive benefits including health, life, disability insurance, and 401(k). To apply, please submit cover letter, curriculum vitae, two- to three-page research plan and three letters of recommendation. Please reference NEURO with your electronic submission to **e-mail: jobs@mdlab.com.** *Medical Diagnostic Laboratories is an Equal Opportunity Employer.*

MARKETPLACE

WEBINAR

The Next Generation of Cell Analysis

Gaining Insight with Cytometry

WEDNESDAY
MARCH 24, 2010
12 noon ET
9 am PT
4 pm GMT

REGISTER NOW!

Sign up at
www.sciencemag.org/webinar

PARTICIPATING EXPERTS

Albert Donnenberg, Ph.D.
University of Pittsburgh

John Nolan, Ph.D.
National Cancer Institute
National Institutes of Health

William Telford, Ph.D.
La Jolla Bioengineering Institute

The next generation of cell analysis tools provides scientists with the ability to easily collect cell-by-cell statistics, rapidly differentiate between cell sub-populations, and derive information about the physical, chemical, and molecular nature of each individual cell. Continuous and accurate monitoring of thousands of cells can now be accomplished, allowing for the application of this technology to the measurement of dynamic ion concentration, intracellular pH, transfection efficiency, and RNAi knockdown efficacy. Recent improvements in flow cytometer technology providing simplified user interfaces, rapid analysis, and more accurate results are removing the barriers of cost, size, and complexity, making the next generation discovery phase in cell analysis feasible.

This webinar will:

- bring together cellular and molecular biology experts to share their knowledge of cutting-edge cell analysis techniques
- highlight the latest cytometry technologies available to research scientists
- focus on new applications for flow cytometry devices
- allow viewers to ask questions of the live panel.

Science
AAAS

Brought to you by the
AAAS/*Science* Business Office

Webinar sponsored by Accuri

R&D Systems Bioactive Proteins

High quality proteins aren't a luxury, they are a necessity.

WHAT'S THE RISK? ✓ Missed opportunities ✓ Non-specific results ✓ Experiments that can't be repeated ✓ Weeks or months of wasted time

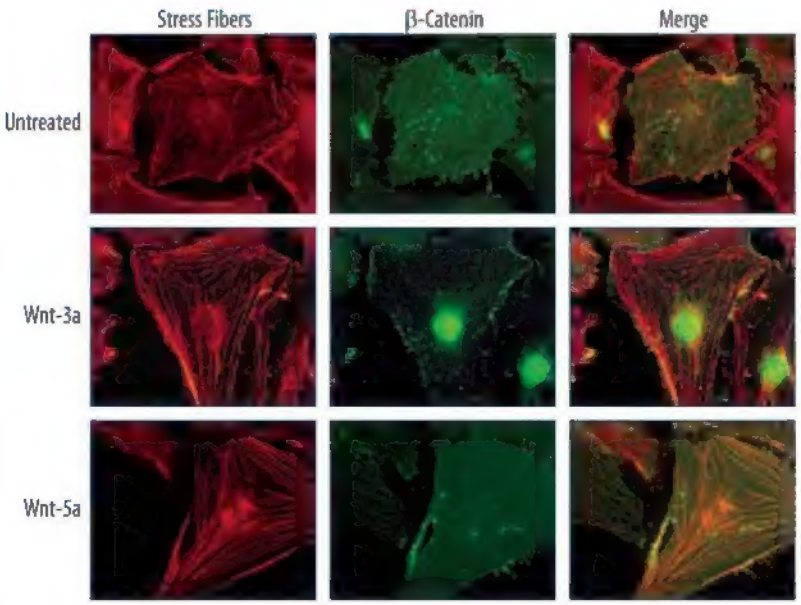

R&D Systems recombinant mouse Wnt-3a (Catalog # 1324-WN) and Wnt-5a (Catalog # 645-WN) promote stress fiber formation in NIH-3T3 cells, while only Wnt-3a promotes nuclear β-Catenin accumulation. Please visit our website for information about our new high purity human Wnt-3a (Catalog # 5036-WNP). *Images Courtesy of Dr. Raymond Habas, Robert Wood Johnson School of Medicine.*

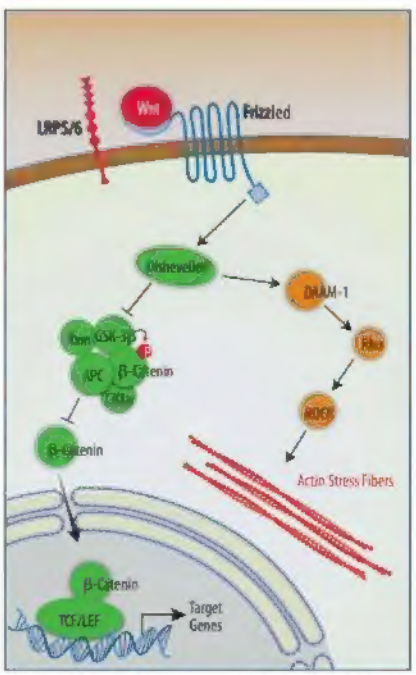

For research use only. Not for use in diagnostic procedures.

R&D Systems has spent almost 25 years building its reputation as a source for high quality proteins.

Every stage of protein development takes place in R&D Systems' laboratories, from cloning of the gene, to protein purification and testing for bioactivity. Because we control all aspects of protein manufacturing, R&D Systems can better control the quality of our products and the technical assistance we offer. Please visit our website at **www.RnDSystems.com/go/Proteins** for more information.

Cancer Development Endocrinology Glycobiology Immunology Neuroscience Proteases Signal Transduction Stem Cells

R&D Systems Tools for Cell Biology Research™

USA & Canada **R&D Systems, Inc.** Tel: (800) 343-7475 info@RnDSystems.com
Europe **R&D Systems Europe, Ltd.** Tel: +44 (0)1235 529449 info@RnDSystems.co.uk
China **R&D Systems China Co., Ltd.** Tel: (800) 988-1270 info@RnDSystemsChina.com.cn

Selection expanding weekly—visit **www.RnDSystems.com/go/request** to sign up for weekly new product updates.

R&D SYSTEMS®